Doctoral Dissertation
博士論文

Long-Term Evolution and Dispersal of Protoplanetary Disks

（原始惑星系円盤の長期進化と散逸過程）

A Dissertation Submitted for the Degree of Doctor of Philosophy
December 2024
令和６年１２月博士（理学）申請

Department of Physics, Graduate School of Science,
The University of Tokyo

東京大学大学院理学系研究科物理学専攻

Ayano Komaki

駒木　彩乃

Abstract

A protoplanetary disk is a circumstellar structure composed of gas and dust grains. Planets form from these disk materials. Disk lifetime sets a strict time limit for planet formation. It is necessary to reveal disk evolution to understand planet formation. There are three major disk dispersal mechanisms: accretion, magnetohydrodynamic (MHD) winds, and photoevaporation. Recent radiation hydrodynamic simulations of photoevaporation suggested that photoevaporation is necessary to explain the observed disk lifetime of a few million years. The timescale and structure of photoevaporation vary depending on physical properties such as stellar mass and metallicity. Since photoevaporation is only one part of disk dispersal, it is necessary to confirm if the trend seen in photoevaporation hold in the simulations which consider all the disk dispersal processes.

We perform radiative hydrodynamic simulations of photoevaporation varying the dust-to-gas mass ratio, $\mathcal{D}$, in the range of 10^{-6}–10^{-1} to clarify the detailed photoevaporation mechanisms in dust-deficient disks. In the case of $\mathcal{D} \geq 10^{-3}$, the disk gas is dominantly heated via photoelectric effect on dust grains. In the case of $\mathcal{D} \leq 10^{-3}$, the disk gas is heated by H_2 pumping and X-ray photons.

Photoevaporation is one of the processes contributing to disk dispersal. A combination of dispersal processes drives the overall evolution. To clarify the role of photoevaporation, we perform long-term disk evolution simulations that include accretion, MHD winds, and photoevaporation, as well as the time variation in FUV luminosity. The photoevaporation rate is influenced by stellar evolution because the disk dispersal timescale and the time until the star reaches the main sequence are similar. Disk fraction, a commonly used parameter in observations of star-forming regions, shows a clear impact from stellar evolution. This highlights the importance of using realistic FUV luminosities for disk evolution around solar- to intermediate-mass stars.

Photoevaporation is most effective in the outer region during the final stage of disk dispersal. Dust grains evolve differently from gas, resulting in a decrease in the dust-to-gas mass ratio over time. To assess the impact of dust evolution on photoevaporation and overall disk dispersal, we perform long-term simulations of gas and dust grains. Dust is removed by growth and strong radial drift in the first $1\,\mathrm{Myr}$, reducing the dust-to-gas mass ratio to 10^{-4} in the outer region, which lowers the photoevaporation rate. Dust growth affects the disk dispersal timescale, while dust growth and entrainment influence the gas distribution in the outer region through photoevaporation.

Table of Contents

1

Introduction

How are planets formed? It is one of the most fundamental and intriguing questions humanity has ever asked. Thanks to recent advances in high-resolution observations, over 5000 exoplanets have been discovered. At the heart of this process lies the protoplanetary disk (PPD), a circumstellar disk around a pre-main sequence star. A protoplanetary disk is made up of gas and dust grains and serves as the birthplace of planets. Increasing numbers of disks are observed with increasingly detailed structures, now resolving features down to scales of $\sim 1\,\mathrm{au}$. Statistical analyses of exoplanet properties reveal significant variations in planet mass, size, semi-major axis, and composition. These differences are thought to originate from the diverse evolutionary pathways of protoplanetary disks, driven by variations in their physical and chemical properties.

Infrared observations suggest that disks disperse within a few million years, providing a strict timeline for planet formation. Understanding how the distribution of disk material evolves and when disks disperse is therefore critical to unraveling the mechanisms of planet formation.

There are three main processes believed to dominate disk dispersal: accretion, magnetohydrodynamic (MHD) winds, and photoevaporation. These processes drive the evolution of the disk gas over time and ultimately determine the possible place and time for planet formation. Table 1.1 summarizes progress in this research field, highlighting the processes incorporated in some theoretical studies. Although each disk dispersal process has been claimed to be the dominant mechanism, no comprehensive simulation has been performed. We aim to reproduce a more realistic disk gas evolution by performing simulations that consider major disk dispersal mechanisms. Additionally, we include stellar evolution and investigate how disk dispersal depends on various properties of star-disk systems. Our simulations also account for dust size and spatial evolution, as shown in Table 1.1, providing a more realistic model of protoplanetary disk evolution.

The observed diversity of exoplanets suggests that protoplanetary disks follow various evolutionary pathways. These differences are thought to be caused by variations in disk properties. We also investigate how disk dispersal depends on the physical parameters of

	Accretion	MHD winds	Photo-evaporation	Stellar evolution	Dust grains
Gorti et al. [2015]	✓		✓		✓
Kunitomo et al. [2020]	✓	✓			
Kunitomo et al. [2021]	✓		✓	✓	
Coleman and Haworth [2022]	✓		✓		
Weder et al. [2023]	✓	✓	✓		
This work	✓	✓	✓	✓	Chapter 5

► **Table. 1.1** The table of previous works which perform long-term disk evolution simulations. The processes each research incorporated is marked with ✓. The processes incorporated in our research are shown in the bottom row. In Chapter 4, we consider accretion, MHD winds, photoevaporation consistently while the stellar evolution is also considered. In Chapter 5, dust size and spatial evolution is considered in addition to the gas evolution calculation introduced in Chapter 4.

the disk.

In the following chapter, we introduce the essential processes of star-disk evolution and planet formation from the onset of star formation. We review the history and recent observational findings related to protoplanetary disks and explain the theoretical mechanisms underlying each disk dispersal process. Additionally, we summarize the general disk evolution pathways and the varied observed disk properties that might influence disk dispersal.

2

Star-Disk-Planet Formation

2.1 Stellar Evolution

A star is a self-luminous object. Although a star and planets form from the same material, called an interstellar medium (ISM), the properties of the star and the planets are vastly different. A star dominates its surrounding materials with its radiation, gravity, and radiation pressure. Understanding star formation and evolution is crucial because these processes strongly influence planet formation and provide the foundation for studying planetary systems.

While my primary interest is in disks, studying star formation is an essential part of this pursuit.

2.1.1 A Molecular Cloud to a Star

A star forms through the gravitational collapse of a dense region within a molecular gas cloud. The typical number density of a molecular cloud is $n_{\rm H} \sim 10^3$–$10^6\,{\rm cm}^{-3}$ and the typical temperature is $T_{\rm gas} \sim 10$–$20\,{\rm K}$. The gas forms a narrow, dense region called 'filaments' by turbulence or the effect of shock waves in the molecular cloud [André et al., 2010, Arzoumanian et al., 2011, Könyves et al., 2015]. In a filament, a dense gas clump is formed, which is called a molecular cloud core [Shimajiri et al., 2019, Zhang et al., 2020]. Stars are formed at the center of the molecular cloud core by its gravitational contraction.

Infrared observations of star-forming regions show that low-mass stars are a common component of star-forming regions. The mass distribution of new-born stars is called Initial Mass Function (IMF), and it is observationally known to be fitted by the power-low relation. Kroupa [2002] derived the IMF as follows:

$$\begin{aligned} \xi(m) &\propto m^{-\alpha} \\ \alpha &= 1.3 \, (0.1\,{\rm M}_\odot < m \leq 0.5\,{\rm M}_\odot) \\ \alpha &= 2.3 \, (0.5\,{\rm M}_\odot < m). \end{aligned} \tag{2.1}$$

This distribution is crucial because it affects the evolution of star-forming regions over time, since low-mass stars are more common and live much longer than high-mass stars.

In the same manner, the mass distributions of molecular cloud cores and filaments are called the Core Mass Function (CMF) and Filament Mass Function (FLMF), respectively. Recent infrared observations indicate that these distributions share a shape similar to that of the IMF. Although the exact process behind the formation of the IMF remains unclear, it is widely believed that the formation of filaments, molecular cloud cores, and stars influences each other.

A molecular cloud core is made up of neutral gas, which is nearly isothermal at $T_{\rm gas} \sim 10$–$20\,\mathrm{K}$. The contraction of the core is described as the gravitational collapse of an isothermal gas sphere. Once the gravitational collapse starts, the gas continues to fall toward the star. This process follows a free-fall motion, and the timescale is called the free-fall time, given by:

$$t_{\rm ff} = \sqrt{\frac{3\pi}{32 G \rho_{\rm ini}}}, \tag{2.2}$$

where $\rho_{\rm ini}$ is the initial density of the core. During this phase, some gas forms a circumstellar structure, called protoplanetary disk (PPD) as a result of its angular momentum.

2.1.2 The Evolution to the Main Sequence

A protostar forms at the center of a molecular cloud through gravitational contraction. During its initial stages, the protostar remains surrounded by a gas envelope. The dense gas in the envelope makes it difficult to directly observe the star at the initial phase. A protostar gains most of its mass through accretion. If a constant and spherical accretion rate is assumed over time, this process is referred to as Bondi accretion.

A star is classified as a pre-main-sequence star once its surrounding envelope disperses. Stars with spectral types F to M are referred to as T Tauri stars, corresponding to masses of 0.1–$2\,\mathrm{M}_\odot$. Stars with spectral types A or B are called Herbig Ae/Be stars. These pre-main-sequence stars continue to contract gravitationally, while radiating thermal energy from their surfaces. The timescale of this process is characterized by the Kelvin-Helmholtz timescale $t_{\rm KH}$, which is given by:

$$\begin{aligned} t_{\rm KH} &= \frac{G M_*^2}{R_* L_*} \\ &\sim 32\,\mathrm{Myr} \left(\frac{M_*}{1\,\mathrm{M}_\odot}\right)^2 \left(\frac{R_*}{1\,\mathrm{R}_\odot}\right)^{-1} \left(\frac{L_*}{1\,\mathrm{L}_\odot}\right)^{-1}, \end{aligned} \tag{2.3}$$

where M_*, R_*, L_* represents the stellar mass, radius, and luminosity respectively.

The bolometric luminosity of the star depends on the internal energy transport processes. Stellar luminosity evolves over time as the stellar internal physical and chemical properties change. The evolution of bolometric luminosity and effective temperature is often plotted on a Hertzsprung-Russell diagram (HR diagram). Figure 2.1 shows the evolution tracks of the stars with $0.3, 0.5, 0.7, 1, 2, 3, 5\,\mathrm{M}_\odot$ in the HR diagram. During

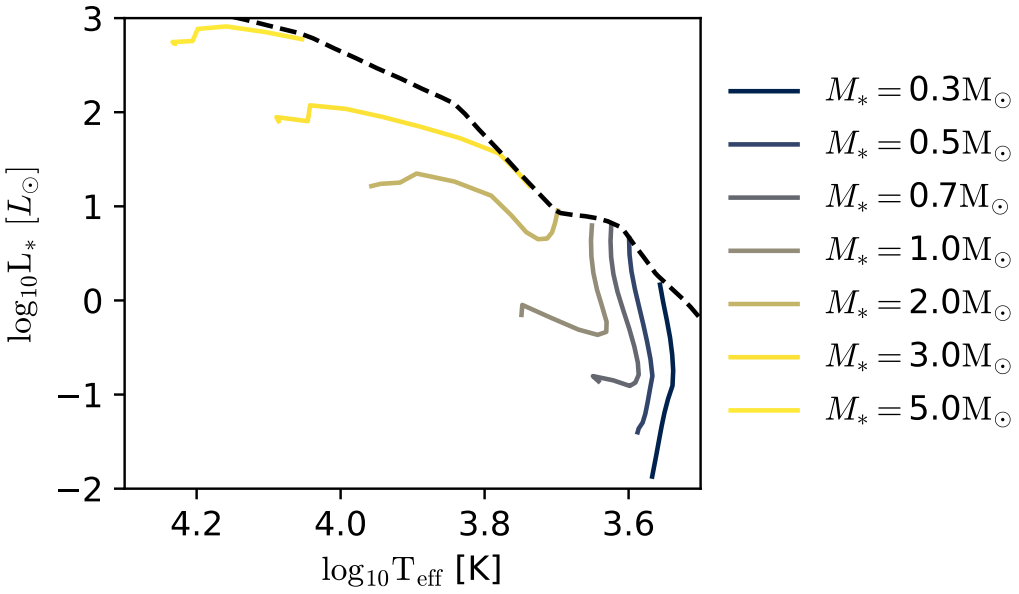

► **Figure. 2.1**

Hertzsprung-Russell diagram (HR diagram). The evolution of the bolometric luminosity and the effective temperature are plotted for $0.3, 0.5, 0.7, 1, 2, 3, 5\,\mathrm{M}_\odot$ stars until the stars reach the main sequence. The color variation from navy to yellow represents the stellar mass range from $0.3\,\mathrm{M}_\odot$ to $5\,\mathrm{M}_\odot$. The evolution is calculated using the stellar evolution code MESA [Paxton et al., 2011]. The birthline is shown in a black dotted line [Stahler and Palla, 2004].

its evolution, the star follows the Hayashi track, which appears as a vertical downward movement on the HR diagram. In the later phase, it follows the Henyey track, characterized by a horizontal leftward movement.

The difference between the Hayashi and Henyey tracks is because of changes in the dominant absorbing species, which affect the temperature dependence of the opacity. During the Hayashi phase, H^- is the primary absorbing material. Its opacity, κ, in several thousand Kelvin is given by Gray [2005]:

$$\kappa \propto \rho^{0.5} T_{\rm gas}^{7.7}, \tag{2.4}$$

where ρ and $T_{\rm gas}$ represent the local gas density and temperature. The high opacity during this phase causes energy to be transported mainly by convection. As the internal temperature increases, the opacity of H^- decreases, leading to more energy being transferred by radiative processes. In the Henyey phase, H replaces H^- as the dominant absorbing material. Massive stars, which have higher temperatures, evolve quickly through the Hayashi track. In contrast, low-mass stars with $M_* < 0.5\,{\rm M}_\odot$ do not experience Henyey track because of the low internal temperature and evolve directly into the main sequence.

When the core temperature becomes high enough to start hydrogen fusion, the star enters the main-sequence phase. This stage is called the Zero Age Main Sequence (ZAMS) [Stahler and Palla, 2004]. Since stars and disks evolve together, understanding how stars change is important for studying disk evolution.

Since it is difficult to estimate the age solely from disk observations, stellar age is often used as a proxy for disk age. Stellar age is estimated using a combination of stellar evolution models and observations. First, the stellar luminosity and spectral type can be derived from observations of the photosphere. By comparing these data with stellar evolution models, the stellar age is derived. Stellar evolution models have been updated over time. For example, Siess et al. [2000] developed a stellar evolution model for pre-main-sequence stars with masses between 0.1–$7.0\,{\rm M}_\odot$. They solved the equation of state for the stellar gas with boundary conditions derived from stellar atmosphere models. Later, Baraffe et al. [2015] updated the model by performing radiation hydrodynamic simulations with improved chemical compositions. The updated composition provides a more accurate opacity and energy transfer inside the star. They resolved the issue in earlier models where the reproduced luminosities were higher than observed.

There are several sources of uncertainty in this method. Observational uncertainties have a larger impact in later stages because luminosity varies less once the star reaches the main sequence. Isochrone lines, which represent stars of the same age on the Hertzsprung-Russell diagram, become closely spaced. This makes it harder to distinguish ages accurately, and the observation error bars span a wider age range [Soderblom et al., 2014]. Age estimates can also vary by a factor of 2–3 depending on the chosen model [White et al., 1999, Dahm and Simon, 2005, Hillenbrand et al., 2008, Bell et al., 2013, Richert et al., 2018]. It is generally assumed that disk age matches system age, meaning that stars and their disks form simultaneously throughout the region. However, observations of star-forming regions suggest that star formation occurs over a few to several Myr [Galli

et al., 2021]. For example, stars in Upper Scorpius show a wide age range from 5–10 Myr. Several explanations have been proposed. Feiden [2016] introduced a new stellar evolution model that incorporates magnetic-field effects. For low-mass stars, magnetic fields inhibit convection, reducing energy transport to the surface. Inefficient energy transport causes energy to accumulate inside the star. This leads to higher luminosity and lower effective temperatures, resulting in longer estimated stellar ages. They concluded that the stars in Upper Scorpius are approximately 10 Myr old. Alternatively, kinematic analysis using CO observations suggests that the region can be divided into two subgroups of different ages [Esplin and Luhman, 2020, Squicciarini et al., 2021]. Estimating stellar age remains challenging but is essential.

Stellar radiation spans a wide range of wavelengths. High-energy radiation, such as far-ultraviolet (FUV), extreme ultraviolet (EUV), and X-ray photons, significantly influences the physical and chemical structure of the circumstellar environment. The following sections will discuss radiation processes and the evolution of FUV and X-ray emission.

The main processes of FUV radiation are accretion, chromospheric emission, and photospheric emission. When gas is accreted onto the star, the released energy is emitted as high-energy photons. Observations confirm that FUV luminosity is proportional to the accretion rate [Gullbring et al., 1998]. Studies of pre-main sequence stars suggest that 4% of the liberated energy is emitted as FUV photons [Calvet and Gullbring, 1998]. The accretion rate decreases with time, with a timescale of a few Myr. Consequently, the FUV luminosity from accretion also decreases.

The chromosphere, the layer just above the photosphere, is a prominent source of FUV radiation. This layer emits specific spectral lines such as Hα and CaII. In stars with high chromospheric activity, such as T Tauri stars, FUV emission can contribute significantly to total luminosity. For instance, in T Tauri stars, the FUV luminosity accounts for approximately $10^{-3.3}$ of the bolometric luminosity. Specific chromospheric lines, such as Lyα and CII, play a critical role in influencing the circumstellar environment. For example, Lyα alone contributes roughly 80% of the total FUV luminosity [Schindhelm et al., 2012] and dominates the FUV emission [Bergin et al., 2003, Herczeg et al., 2004].

The photosphere, located below the chromosphere, typically has a temperature in the range of several to tens of thousands Kelvin. Radiation from the photosphere follows an approximately black-body spectrum, including FUV wavelengths. As stellar mass increases, the effective temperature rises and more photons are emitted at higher energies, including FUV. In the pre-main sequence, photospheric temperatures are generally too low to contribute significantly to FUV radiation. Once stars reach the main sequence, their photospheric temperatures can exceed 10^4 K, leading to a drastic increase in photospheric FUV radiation. Husser et al. [2013] developed the PHOENIX code to model radiation from stellar photospheres, incorporating 81 chemical species to derive spectral energy distributions across different stellar types.

X-ray photons are emitted by stellar internal processes, similar to FUV photons. Magnetic dynamics is induced by rapid rotation and strong convection on the surface of a pre-main sequence star. When magnetic dynamics transforms the internal energy into

magnetic energy, a part of this energy can be seen in a corona. Since the X-ray photons originate from the internal energy, the X-ray luminosity is proportional to the bolometric luminosity. The relation is approximated by $10^{-3}L_{\rm bol}$, where $L_{\rm bol}$ is the bolometric luminosity [Flaccomio et al., 2003, Preibisch et al., 2005, Telleschi et al., 2007, Wright et al., 2011]. An intermediate-mass star has weaker magnetic fields because it does not have a convective zone on the stellar surface, which results in lower X-ray luminosity. In some cases, X-ray photons are also emitted by accretion processes. Gas falls on the star, and the released energy generates localized high-energy X-ray emissions [Kastner et al., 2002].

X-ray flares are another significant source of X-ray radiation. These flares are produced by sudden magnetic reconnection events on the stellar surface [Shibata and Magara, 2011]. X-ray flares are characterized by high-energy photons with $> 10\,{\rm keV}$. Although soft X-ray photons tend to be absorbed by the surrounding gas near the star or on the disk surface, hard X-ray photons can penetrate deeper into the disk, reaching the midplane, where they contribute to gas heating through scattering [Igea and Glassgold, 1999, Bethell and Bergin, 2011]. Each flare event deposits significant energy into the surrounding gas, temporarily altering the thermal structure of the disk.

X-ray observations reveal that X-ray luminosity varies over time [Flaccomio et al., 2003, Hamaguchi et al., 2005, Gregory et al., 2016, Villebrun et al., 2019], as shown by comparisons between young systems [Hamaguchi et al., 2005, Huenemoerder et al., 2009] and relatively older ones [Zinnecker and Preibisch, 1994]. Tracking X-ray luminosity evolution in young stars is challenging because of the variability of magnetic activity, accretion rates, and flare frequency. However, understanding the evolution of FUV and X-ray luminosity is crucial to studying the interactions between the star and PPD.

To summarize, the central star impacts its surrounding environment from the onset of star formation through gravity and irradiation. Irradiation, in particular, alters the physical and chemical conditions of the gas, which constitutes the majority of circumstellar material. Understanding the evolution of a protostar is crucial for comprehending the dispersal of disk gas.

2.2 Protoplanetary Disks: From Formation to Dispersal

More than 5000 exoplanets have been discovered since the first detection. Planets form inside disks out of disk materials (gas and dust grains). Disk evolution is key to understanding the entire process of planet formation. Observations of nearby star-forming regions show that the disk lifetime is a few million years. This timescale is much shorter than the typical lifetime of a solar-mass star, which is about one billion years. During this brief disk lifetime, the structure of the star-planet system is established. We will explore the overview of disk evolution and the latest research.

2.2.1 Introduction to Protoplanetary Disks

A circumstellar disk is composed of gas and dust grains inherited from the interstellar medium (ISM). It orbits the central star, carrying angular momentum from the molecular cloud core. An image of a PPD was first captured in 1993 as a blurry figure against the bright background of Orion [O'Dell et al., 1993]. This image revealed disk material being stripped away by strong radiation from a nearby massive star. Since then, more disks have been observed, and understanding of disk evolution has improved.

A disk consists mainly of gas and dust grains. Most of the disk mass is composed of gas, similar to ISM. The disk is thin in the vertical direction, creating a flattened shape. The balance in the vertical direction is described using cylindrical coordinates (r, z) as

$$\frac{\mathrm{d}P}{\mathrm{d}z} = -\frac{GM_*\rho}{(r^2+z^2)^{3/2}}z, \tag{2.5}$$

where P, ρ, M_* of each denotes the gas pressure, density, and stellar mass. By assuming the gas is ideal and isothermal, the equation above is written below by using $P = \rho c_\mathrm{s}^2$,

$$c_\mathrm{s}^2\frac{\mathrm{d}\rho}{\mathrm{d}z} = -\rho\frac{GM_*}{(r^2+z^2)^{3/2}}z \tag{2.6}$$

The density distribution is derived by solving the equation above as

$$\rho = \rho_0 \exp\left[\frac{GM_*}{c_\mathrm{s}^2}\left(\frac{1}{\sqrt{r^2+z^2}} - \frac{1}{r}\right)\right], \tag{2.7}$$

where ρ_0 represents the midplane density. The equation is approximated as below when $z \ll r$ is assumed:

$$\rho \approx \rho_0 \exp\left(-\frac{v_\mathrm{K}^2}{2c_\mathrm{s}^2 r^2}z^2\right), \tag{2.8}$$

where v_K denotes Keplerian velocity. The scaleheight, H, is defined as

$$H = \frac{c_\mathrm{s}}{\Omega_\mathrm{K}}.$$

Since a disk has a thin structure, the surface density, Σ is often used to depict the gas distribution. The surface density is given by

$$\Sigma(r) = \int \rho(r,z)\mathrm{d}z.$$

The mid plane density is expressed as

$$\rho_0 = \frac{\Sigma}{\sqrt{2\pi}H}$$

The observed gas distribution reflects the chemical structure in addition to the physical

properties introduced earlier. Radiation from the central star plays an important role in determining the temperature profile and drives photon-related chemical reactions [Herczeg et al., 2004, Nomura and Millar, 2005, Qi et al., 2006, Öberg et al., 2010, Walsh et al., 2010]. Radiative transfer calculations that include stellar radiation show that FUV luminosity significantly influences the composition of the disk gas [Bergin et al., 2003].

The dust grains in the disks vary widely in size. It is believed that tiny dust grains grow into kilometer-sized planetesimals and eventually form planets. Observations of ISM attenuation reveal that the size distribution of dust grains follows a power-law relation [Mathis et al., 1977, Draine and Lee, 1984], given by:

$$\mathrm{d}n(a) \propto a^{-3.5}\mathrm{d}a,$$

where $n(a)$ represents the number density of dust grains with the particle radius of a. This distribution is known as the MRN distribution. The size distribution implies that smaller grains are far more abundant than larger ones.

Small dust grains consist of polycyclic aromatic hydrocarbons (PAHs). PAHs are cyclic carbon compounds and are detected by specific infrared emission lines [Cesarsky et al., 1996, Tielens, 2008]. PAHs also emit electrons through the photoelectric effect caused by FUV photons [Bakes and Tielens, 1994]. These electrons transfer energy to the surrounding gas, raising its temperature. The observed spectral lines indicate the degree of gas ionization because the energy distribution of the emitted photons depends on the ionization level [Okuzumi, 2009, Ivlev et al., 2016].

Observations of the Orion Bar confirmed this connection [Knight et al., 2022]. Using data from the Spitzer Space Telescope, observational research focused on the photodissociation region near the Orion Bar and found that the spectral line ratios from PAHs correlate with the distance from the ionization front. The observation also revealed that small PAHs are destroyed by strong radiation from nearby massive stars. These findings suggest that PAH distribution and abundance serve as indicators of environmental conditions, such as FUV radiation fields and ionization parameters.

The temperature of dust grains is determined by the balance between the absorption of stellar radiation and the thermal emission from their surfaces. By assuming a black-body radiation as the dust thermal emission, the energy absorbed and emitted per second is expressed as:

$$\begin{aligned} \Gamma_{\mathrm{dust}} &= \pi a^2 \frac{L_*}{4\pi r^2} \\ \Lambda_{\mathrm{dust}} &= 4\pi a^2 \sigma_{\mathrm{SB}} T_{\mathrm{dust}}^4, \end{aligned} \tag{2.9}$$

where L_* and r represent the stellar luminosity and the distance from the central star. In the equation, T_{dust} is the dust temperature. When the dust temperature reaches equilibrium, it is given by:

$$T_{\mathrm{dust}} \sim 280 \left(\frac{r}{1\,\mathrm{au}}\right)^{-1/2} \left(\frac{L_*}{\mathrm{L}_\odot}\right)^{1/4} \mathrm{K} \tag{2.10}$$

The resulting temperature does not depend on the size of the dust grains. In dense regions of the disk, gas and dust are thermally coupled because of frequent collisions. The temperature decreases with distance from the star, approximately following $\propto r^{-1/2}$. The hot inner region is observed in shorter wavelengths, such as near-infrared, while the cool outer region is observed in longer wavelengths such as submillimeter to micrometer. The region in focus depends on the wavelength that we use to observe [Dullemond et al., 2007, Yasui et al., 2014, Testi et al., 2014].

2.2.2 Observational Properties of Protoplanetary Disks

In this section, we will introduce observational results and their implications for PPDs.

Gas Observations

A PPD is observed across a wide range of wavelengths, from infrared to radio because gas is detected through spectral lines at various wavelengths, while dust grains are observed through thermal emission or scattered light from small grains. A significant challenge in studying the entire disk is that, although the dominant gas component is H_2, it is difficult to observe it under disk conditions. It cannot be observed in the radio range because H_2 lacks a permanent dipole moment. Rotation-vibration transitions occur only in high-temperature environments, which are unlikely in disks where the gas temperature is 10–$100\,\mathrm{K}$ in the midplane. This requires us to understand the physics of PPDs without directly observing their main component.

The other major components of the disk gas are CO and HD, which can be detected. Previous research has attempted to estimate the total disk mass from the observed amounts of these molecules. However, their abundance strongly depends on ongoing chemical reactions within the disk, making the estimated disk mass dependent on the assumed chemical model. This method does not always successfully reproduce the disk mass. For example, the disk mass derived from the CO spectral lines is often lower by a factor of 5–10 compared to the value derived by other methods [Favre et al., 2013, Kama et al., 2016a, Manara et al., 2016, Miotello et al., 2016, 2017]. This discrepancy suggests that the abundance of CO is actually lower than predicted based on the CO/H_2 ratio observed in the ISM. There are several possible factors. At gas temperatures below $20\,\mathrm{K}$, CO freezes on dust grains. The boundary where CO transitions from gas to solid is called the snowline, located at $\sim 30\,\mathrm{au}$ around a solar-type star [Qi et al., 2013]. Similarly, H_2O exists as gas and ice in disks, with its snowline at $\sim 3\,\mathrm{au}$. The chemical composition of the dust grains differs between these snowlines [Qi et al., 2019]. Furthermore, CO is easily dissociated by high-energy radiation, such as FUV photons. Both processes affect the abundance of CO.

Williams and Best [2014] used emission lines of ^{13}CO and C^{18}O to estimate the mass of the disk gas. They developed a model that characterizes disk gas with nine parameters, including the effects of photodissociation and freeze-out. Their results were consistent with independent studies. These discussions highlight the difficulty of accurately estimating the disk mass from gas observations.

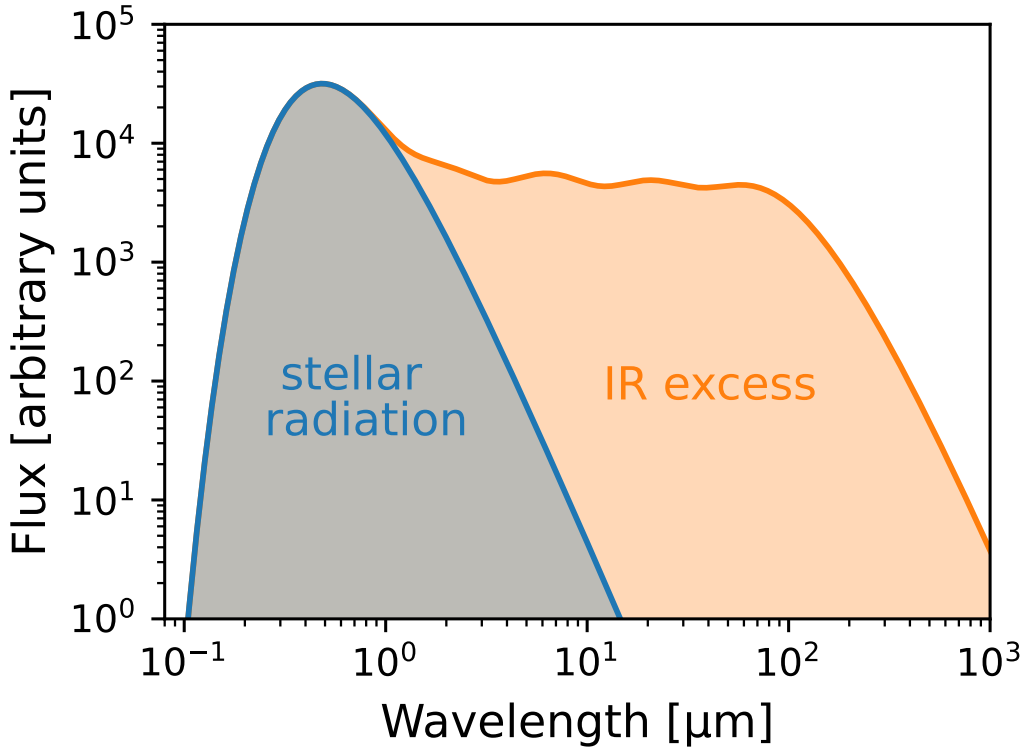

► **Figure. 2.2**

The spectral energy distribution (SED) of a star-disk system. The stellar radiation is shown in blue. The radiation from a disk, referred to as IR excess is shown in orange. The stellar component is approximated by a black-body radiation while the disk component is a combined radiation from dust in various regions with different temperatures.

Dust Observations

Infrared observations of dust grains in PPDs have a longer history than gas observations. JHKL bands are often used in these observations and have provided basic features of PPDs. In these observations, the Spectral Energy Distribution (SED) of a combination of a star and a disk is obtained. Figure 2.2 illustrates a schematic SED of a star-disk system with the effective temperature set to $T_{\rm eff} = 6000\,{\rm K}$. The dust grains emit infrared radiation as a black-body of 10 Kelvin to a few hundred Kelvin, and the temperature depends on the local environment. The radiation from the star is fitted by a black body. The remaining part of the SED is called the 'infrared excess' and corresponds to the dust thermal emissions. As the disk evolves and the shape of the dust disk changes, the structure of the SED also changes. The SED shape changes because of dust-specific processes such as growth and settling in the midplane [D'Alessio et al., 2006, Hernández et al., 2007].

The slope in the range of $2 \leq \lambda \leq 25\mu$m is expressed as:

$$\alpha_{\rm IR} = \frac{{\rm d}\log \nu F_\nu}{{\rm d}\log \nu}.$$

This parameter evolves with the disk and is used to classify the evolutionary stage of Young Stellar Objects (YSO). The system is mainly divided into three stages: Class I, II, and III [Lada, 1987, Williams and Cieza, 2011]. Additionally, $\alpha_{\rm IRAC}$, the slope calculated by the Infrared Array Camera (IRAC) using wavelengths of 3.6, 4.5, 5.8, and 8.0 μm, is also used. The classification has been expanded to the younger stage of Class 0. Class III objects are further divided into Classical T Tauri Stars (CTTS) and Weak-Lined T Tauri Stars (WTTS) based on the presence of Hα spectral lines or UV radiation, indicating an accreting gas. These observations have provided insight into disk evolution. Researchers determine whether a star has a disk by examining whether the SED slope is steep enough. The criterion varies by observation, ranging from -1.8 to 2.2. Although this affects the number of disks identified, [Yasui, 2021] suggests that the impact on disk fraction is negligible.

Some disks lack emission around ~ 10 μm during the Class II and III stages [Strom et al., 1989, Calvet et al., 2005, Espaillat et al., 2014]. These disks are called transitional disks. Based on observation trends, it is believed that these disks lose small dust grains typically observed in the near-infrared. These disks are thought to represent the final stage of disk dispersal.

Substructures of Protoplanetary Disks

One big progress in disk observation was made by the launch of the Atacama Large Millimeter/submillimeter Array (ALMA). The high-quality, high-resolution observations allowed us to observe disks in class 0/I that are embedded in dense envelopes. More detailed structures, such as gaps and spirals, are now observable in disks.

Before ALMA, observations focused on disks later than class II. Although it was theoretically proposed that stars form with disks, there had been no direct evidence of disks around protostars. ALMA observations also provided detailed gas kinematics. In the earliest stage of stellar life, a protostar is surrounded by an envelope, and distinguishing between an envelope and a disk was challenging. An envelope shows strong accretion, while a disk typically follows Keplerian rotation. By analyzing gas kinematics, disks around protostars were discovered [Lindberg et al., 2014, Ohashi et al., 2014, Aso et al., 2017]. Since then, ALMA has identified disks around very young stars, younger than 10^5 years [Rygl et al., 2013]. The estimated disk mass is lower than that of disks around older protostars, suggesting ongoing mass growth from the envelope. This phase is very brief relative to the subsequent disk dispersal, so disk dispersal simulations typically exclude it.

ALMA provided an impressive image of HL Tau, revealing several rings and gaps in the disk [ALMA Partnership et al., 2015]. Observations show that many disks have rings or gaps ranging from a few to a few tens of au wide [Andrews et al., 2016, Isella et al., 2016, Francis and van der Marel, 2020]. The processes forming these substructures

remain unclear, but several mechanisms have been proposed, including secular gravitational instability [Takahashi and Inutsuka, 2014, 2016], magnetorotational instability [Lubow and D'Angelo, 2006, Bai and Stone, 2014], and planet-disk interaction induced by planet formation. Two-dimensional hydrodynamics simulations suggest that a single planet can create multiple gap structures [Bae et al., 2017, Dong et al., 2017, Kanagawa et al., 2021]. Gas pressure bumps may trap dust grains, preventing them from accreting onto the star [Pinilla et al., 2012, Ricci et al., 2012, Ronco et al., 2024], which could make these substructures more prominent. This mechanism may explain the extended high disk fraction observed in some systems. These studies suggest that disks evolve alongside planet formation, making it essential to understand disk evolution to clarify the final planetary system.

Observed Mass of Protoplanetary Disks

The flux emitted from the dust grains allows for an estimate of the disk dust mass. The disk dust mass is given by:

$$M_{\rm disk} = \frac{F_\nu d^2}{\kappa_{\rm dust}(\nu) B_\nu(T_{\rm dust})}, \tag{2.11}$$

where F_ν represents the flux from thermal emissions, and d is the distance to the observer. In this equation, $\kappa_{\rm dust}$ denotes the absorption opacity of the dust grains. The absorption opacity has been calculated in various studies [Weingartner and Draine, 2001, Beckwith et al., 1990, D'Alessio et al., 2001, Birnstiel et al., 2018]. For example, models have been improved by updating dust grain compositions and optical constants for each component. Initially, it was assumed that water ice made up 60% of the volume, but this was revised to 10–20% to better match the observed SEDs [D'Alessio et al., 2006, Espaillat et al., 2010].

Infrared observations show that the disk dust mass decreases over time, corresponding to the reduced flux of infrared excess in SEDs [Ansdell et al., 2017, Andrews, 2020]. Dust grains make up only 1% of the total disk mass, so the entire disk mass is commonly estimated by assuming the dust-to-gas mass ratio, $\mathcal{D}$, is equal to the ISM value of 0.01 [Beckwith et al., 1990, Ansdell et al., 2016]. This method is widely used because estimating mass from gas observations is challenging and heavily dependent on chemical models [Anderson et al., 2022]. Theoretical studies and observations suggest that $\mathcal{D}$ decreases as a result of radial drift and dust collisional growth [Weidenschilling, 1977, Nakagawa et al., 1981, Keller and Gail, 2004, Brauer et al., 2007, Ciesla, 2009]. This reduction can lead to inaccuracies in the derived disk mass [Eisner et al., 2016]. Estimating disk mass remains difficult.

Another approach uses dynamical motion [Veronesi et al., 2021, Lodato et al., 2023]. This method compares the observed rotation curves of ^{12}CO and ^{13}CO with velocity models that include stellar gravity, disk self-gravity, and gas pressure. When the disk lacks complex structures or kinematic perturbations, the estimated mass aligns with the results of dust observations. Since planets are formed from disk materials, knowing the available mass is essential to understand the formation of planets [Testi et al., 2022].

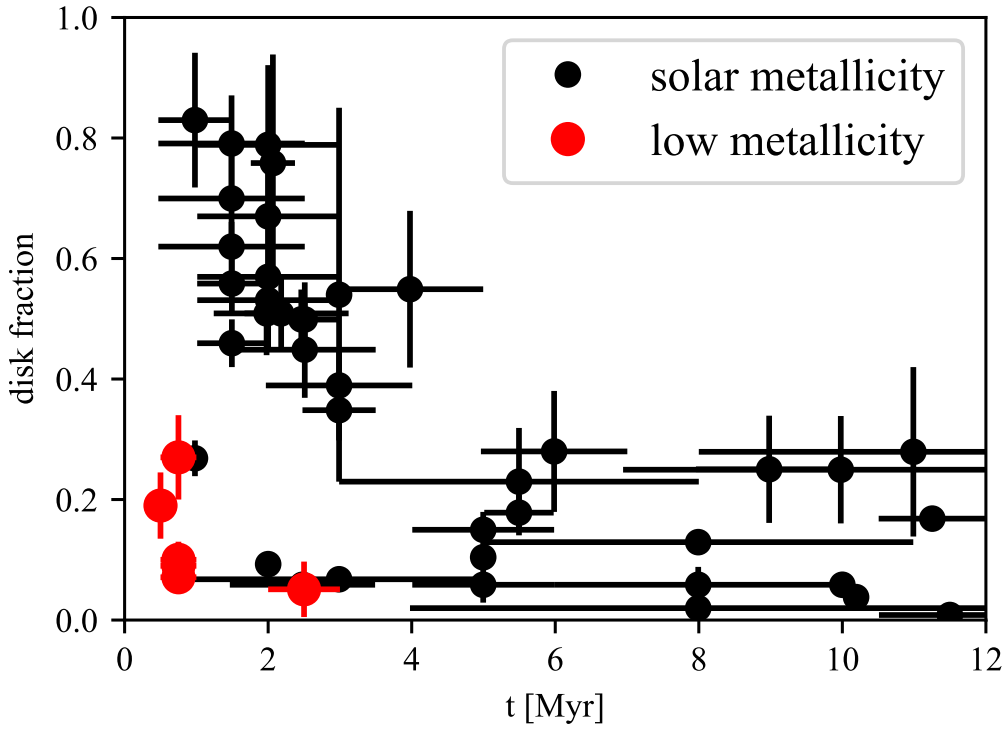

► **Figure. 2.3**

The observed disk fractions toward various stellar clusters. The black plots represent disk fractions in solar-metallicity environments derived from the stellar clusters in the solar neighborhood [Mamajek, 2009, van der Marel and Mulders, 2021, Pfalzner et al., 2022]. The red plots show disk fractions in the outer galaxy, where the metallicity is $[\mathrm{O/H}] \sim -0.7$ [Yasui et al., 2010].

Lifetimes of Protoplanetary Disks

PPDs are often studied as groups within star-forming regions, and the results are interpreted through statistical analyses. One commonly used parameter is the 'disk fraction', which is the ratio of stars that have surrounding disks. The disk fraction is a useful parameter to describe the evolutionary stage of a region. Infrared observations of star-forming regions with various ages reveal that the disk fraction decreases as the system ages [Haisch et al., 2001, Hernández et al., 2008, Mamajek, 2009, Muzerolle et al., 2010]. This is because disks lose mass over time through processes such as accretion onto the central star, outflows driven by magnetic fields, and radiation-driven photoevaporation. Figure 2.3 shows the observed disk fractions for various star-forming regions with a wide range of ages.

Haisch et al. [2001] observed six star-forming regions using JHKL bands and calculated the disk fraction for each region. They showed that the disk fraction decreases within a

few million years and drops to zero by $6\,\mathrm{Myr}$. Since a decrease in disk fraction reflects disk dispersal, the decreasing timescale corresponds to the disk dispersal timescale. The disk fraction is often fitted with an exponential relation:

$$f_{\mathrm{disk}} = \exp(-t/t_{\mathrm{dis}}),$$

where f_{disk} and t_{dis} represent the disk fraction and the estimated disk dispersal timescale, respectively.

Since this initial study, many more star-forming regions have been observed, and observations show variation in disk dispersal timescales. The dispersal timescale is generally estimated to be 1–$3\,\mathrm{Myr}$ [Haisch et al., 2001, Hernández et al., 2008, Mamajek, 2009, Fedele et al., 2010, Ribas et al., 2014, Briceño et al., 2019]. However, recent studies suggest that disk dispersal timescales may be longer, with estimates that extend up to $3.5\,\mathrm{Myr}$ [Richert et al., 2018], $4.7\,\mathrm{Myr}$ [Pecaut and Mamajek, 2016], and even beyond $5\,\mathrm{Myr}$ [Pfalzner et al., 2014, Michel et al., 2021, Pfalzner et al., 2022].

Recent research suggests longer disk dispersal timescales for several reasons [Pfalzner et al., 2022]. Earlier observations were limited and biased toward regions massive stars because of detection limits. Observations of stellar clusters also often focus on their central regions. Over time, the clusters expand and eventually disperse. Disks in the central part of a cluster are more likely to be influenced by strong radiation from nearby massive stars. These factors suggest that previous estimates may have underestimated the disk dispersal timescale.

Dust detection is commonly used to calculate disk survival rates, but Hα detection by spectroscopy is also utilized [Fedele et al., 2010, Richert et al., 2018, Briceño et al., 2019]. Hα emission indicates the presence of accreting gas in the hot inner region of the disk. These methods consistently suggest that PPDs disperse within a few to several million years.

Different wavelengths probe different parts of the disk. Short-wavelength observations focus on the inner regions as a result of higher temperatures. Ribas et al. [2015] compared disk fractions in several star-forming regions using near- and mid-infrared observations. They found no significant differences in the disk dispersal timescales, indicating that disks disperse simultaneously across different regions. This result is consistent with another study [Maeshima et al., 2021].

Stellar Mass Dependence of Lifetimes

Observations toward various star-forming regions have revealed that the disk fraction, and therefore disk dispersal timescale, depends on stellar properties such as stellar mass and metallicity [Yasui et al., 2009, 2010]. Hillenbrand et al. [1992] observed Herbig Ae/Be stars in the near-infrared. They suggested that disk dispersal timescales are shorter around massive stars because no disks were detected. Similarly, multi-wavelength observations have consistently shown that disk fraction decreases as stellar mass increases, indicating that disks around massive stars disperse more rapidly [Carpenter et al., 2006, Lada et al., 2006, Dahm and Hillenbrand, 2007, Kennedy and Kenyon, 2009, Roccatagliata et al., 2011,

Fang et al., 2012, Yasui et al., 2014, Richert et al., 2018].

Bayo et al. [2011, 2012] performed multi-wavelength observations of the λ Orion region and found that the disk fraction decreases as stellar mass increases in the range of $0.1\,\mathrm{M}_\odot \leq M_* \leq 1.7\,\mathrm{M}_\odot$. Their results suggest that disks around low-mass stars generally have longer lifetimes. Similarly, Ribas et al. [2015] conducted infrared observations of eleven star-forming regions. They classified stars by age and stellar mass. They used $3\,\mathrm{Myr}$ as the age threshold and $2\,\mathrm{M}_\odot$ as the mass boundary. They found that disks around stars with $M_* > 2\,\mathrm{M}_\odot$ show lower survival rates, supporting the trend that disks around massive stars disperse more rapidly.

Ansdell et al. [2016] conducted infrared observations and estimated the disk dust mass for stars in the range of $0.1\,\mathrm{M}_\odot \leq M_* \leq 1.0\,\mathrm{M}_\odot$. They found that the relationship between stellar mass and dust mass becomes steep over time, suggesting that disks around low-mass stars do not retain dust mass compared to those around solar-mass stars. The change in slope suggests that disks around low-mass stars lose mass more efficiently. This result also implies that disk dispersal processes vary by stellar mass. Furthermore, Richert et al. [2018] studied young star-forming regions with $\leq 5\,\mathrm{Myr}$ using X-ray observations. They found that the disk fraction does not vary significantly by stellar mass during the first $3\,\mathrm{Myr}$, indicating that the influence of stellar mass on disk dispersal may increase with age.

In summary, these observations indicate that most stars have disks in the first few million years, followed by rapid dispersal influenced by stellar mass. These relationships help us understand disk evolution and highlight the role of stellar mass in determining disk dispersal timescales.

Metallicity Dependence of Lifetimes

Some observations indicate that disk dispersal depends on metallicity in addition to stellar mass. In the Galaxy, metallicity decreases gradually from the inner to the outer regions, in the range of 0.1–$3\,\mathrm{Z}_\odot$, where $\mathrm{Z}_\odot$ represents the solar metallicity. Observational studies of PPDs in the outer Galaxy have found that disk fractions are lower in low-metallicity environments compared to solar-metallicity regions [Yasui et al., 2010, 2016b,a]. Yasui et al. [2010] showed that the disk fractions in low-metallicity environments drop below 20% within $1\,\mathrm{Myr}$ and the disks disappear entirely within a few million years. These results suggest that the disk dispersal timescale in low-metallicity regions may be shorter than that in solar-metallicity environments. Similar trends have been observed in recent work by Guarcello et al. [2021]. One proposed explanation for this trend is enhanced photoevaporation, because the reduced dust grains result in less shielding for disk gas and leads to effective gas heating. A recent study by Patra et al. [2024] observed 18 stellar clusters with metallicities in the range of 0.34–$0.83\,\mathrm{Z}_\odot$ and ages between 0.9 and $2.1\,\mathrm{Myr}$. The observations of various disks allowed them to track the evolution of disk fractions over time. They found that disk fractions in these clusters were consistently lower than those in solar-metallicity environments across all age ranges. This finding suggests that the decline in disk fraction appears to follow a trend similar to that observed in solar-metallicity clusters. In contrast, observations of Hα emission lines emitted from

accreting gas have found the existence of accretion flow around stars in low-metallicity environments, including older systems. This observation suggests that, despite a rapid decrease in disk fraction, some disks in low-metallicity environments may retain gas.

Establishing a clear link between metallicity and disk evolution remains difficult. There are few studies on this topic because observing low-metallicity environments requires targeting stellar clusters in the outer Galaxy. Metallicity decreases with distance from the galactic center, but observations in these regions face challenges because of distance and limited sensitivity. This limits observations to higher-mass disks and stars. Pfalzner et al. [2022] noted that these biases make it harder to estimate a dependence on the metallicity of disk dispersal over a wide range of metallicities. More studies are needed to understand how metallicity impacts disk evolution. This includes investigating physical processes like reduced dust shielding and the initial conditions of disk formation. Understanding these factors is important for building accurate models of disk dispersal in different environments.

2.2.3 Processes and Pathways of Disk Dispersal

PPDs lose mass through accretion and winds and disperse within a few million years. Several processes contribute to gas mass loss, including accretion, magnetohydrodynamic (MHD) winds, photoevaporation, stellar winds, and radiation pressure. In the following, I detail each process.

Viscous Accretion

Due to the viscosity, angular momentum transfers from the inner to the outer disk. As a result, gas in the inner disk moves toward the central star and is accreted onto it. The evolution of gas surface density by accretion is described by Shakura and Sunyaev [1973], Lynden-Bell and Pringle [1974], and Hartmann et al. [1998] as:

$$\frac{\partial \Sigma}{\partial t} = \frac{3}{r}\frac{\partial}{\partial r}\left[r^{1/2}\frac{\partial}{\partial r}(r^{1/2}\nu\Sigma)\right], \tag{2.12}$$

where ν is the kinematic viscosity. This viscosity ν is described in terms of the dimensionless viscous parameter α, which is related to sound speed $c_{\rm s}$ and scale height H of the disk:

$$\nu = \alpha c_{\rm s} H \tag{2.13}$$

This model aligns well with an observed power-law distribution. Accretion rates in pre-main sequence stars are estimated through observations. A portion of the gravitational energy released during accretion is radiated as high-energy photons [Herczeg and Hillenbrand, 2008, Alcalá et al., 2014, Manara et al., 2016, 2017, Alcalá et al., 2017]. Assuming that a fraction ϵ of the accretion energy is radiated, the accretion luminosity is expressed as:

$$L_{\rm acc} = \epsilon\frac{GM_*\dot{M}_{\rm acc}}{R_*}, \tag{2.14}$$

where M_* is the stellar mass, $\dot{M}_{\rm acc}$ is the accretion rate, R_* is the stellar radius, and ϵ represents the efficiency with which gravitational energy is converted into radiation. The luminosity is used in observations to estimate the accretion rate.

Accretion rates can also be estimated from Hα emission lines [White and Basri, 2003, Natta et al., 2004, Flaherty and Muzerolle, 2008, Fedele et al., 2010]. These lines are emitted from high-temperature gas near the star and provide the kinematics structure of the accreting gas.

The observations toward T Tauri stars have suggested that the typical accretion rate is $\sim 10^{-8}\,{\rm M}_\odot\,{\rm yr}^{-1}$ [Cieza et al., 2012, Alcalá et al., 2014, Manara et al., 2017]. Observations show that accretion rates increase with stellar mass, following $\propto M_*^{1.8}$ [Muzerolle et al., 2003, Natta et al., 2006, Herczeg and Hillenbrand, 2008, Alcalá et al., 2014, Manara et al., 2017]. Theoretical studies propose that this steep slope can be explained by the positive correlation between disk mass and stellar mass [Pascucci et al., 2016, Pinilla et al., 2020]. Somigliana et al. [2022, 2024] analyzed this slope and showed that the slope becomes steep when the disk mass grows more steeply than the accretion rate with the stellar mass. They also found that the initial slope lies between 0.7 and 1.5 when comparing their model with observations.

Accretion rates vary by several orders of magnitude even among the same stellar mass stars [Manara et al., 2020]. Accordingly, the viscous parameter α varies from 10^{-4} to 10^{-2} [Andrews et al., 2009, Pinte et al., 2016, Trapman et al., 2020]. Earlier observations estimated α at 10^{-2} [Hartmann et al., 1998, Williams and Cieza, 2011, Rosotti et al., 2020], but recent observations suggest lower values, such as 10^{-3} [Rafikov, 2017] and 10^{-4} [Flaherty et al., 2020]. Subsequent studies have confirmed these lower estimates [Fedele et al., 2018, Trapman et al., 2020].

The origin of viscosity remains an open question. One explanation involves magnetic fields inherited from the molecular cloud. Magnetic fields interact with the gas, inducing magnetorotational instability (MRI), which generates turbulence that enhances viscosity. Theoretical calculations show that MRI can produce an effective viscous parameter of around 10^{-2} [Sano et al., 2004, Suzuki et al., 2010]. This process depends on interactions between the magnetic fields and the ionized gas. In the inner region of the disk ($r \leq 0.3\,{\rm au}$), high temperatures enable thermal ionization [Desch and Turner, 2015], while cosmic rays occasionally ionize gas near the midplane [Simon et al., 2015].

The ionization state of the disk is divided into layers, with accretion processes varying by layer [Gammie, 1996]. In shielded regions with low ionization, called the 'dead zone,' MRI is suppressed both theoretically and observationally [Turner et al., 2014, Mori and Okuzumi, 2016, Flaherty et al., 2017]. ALMA observations of CO line broadening confirm that MRI is less effective in these areas, with the effective viscous parameter estimated to be around 10^{-4} [Flaherty et al., 2015, Nelson et al., 2013].

Magnetohydrodynamics Winds

Magnetic fields contribute to disk dispersal not only through MRI but also by dispersing gas via MHD winds driven by centrifugal force [Suzuki and Inutsuka, 2009, Armitage

et al., 2013]. Theoretical studies have performed shearing-box MHD simulations and have shown that wind torque causes significant mass loss [Fromang et al., 2013, Bai and Stone, 2013a,b]. However, shearing-box simulations have limitations [Lesur et al., 2013]. For example, Fromang et al. [2013] found that the results depend strongly on the box size, with variations in the mass-loss rate reaching up to an order of magnitude. To address this, Suzuki et al. [2016] conducted MHD simulations with a global disk model to provide more realistic mass-loss rates.

MHD winds carry away the angular momentum, enhancing accretion as the gas loses angular momentum [Lesur et al., 2014, Tabone et al., 2022b,a]. Kunitomo et al. [2020] performed 1-dimensional disk evolution simulations that included both accretion and MHD winds. They showed that a disk can disperse within $6\,\mathrm{Myr}$ because of efficient mass-loss driven by MHD winds, even with a low viscous parameter of 8.0×10^{-5}.

Recent observations directly captured outgoing CO gas emissions, likely from MHD winds [Booth et al., 2021]. These observations revealed that the gas flow originates from the inner disk, within $r \leq 4\,\mathrm{au}$. The angular momentum carried away by these winds is comparable to the angular momentum lost by the accreting gas. This finding suggests that accretion driven solely by MHD winds can explain the observed disk dispersal features, making the viscousity unnecessary in such models. These different observational results highlight the variability and complexity of disk models.

Recent observations detected direct emissions from gas in escaping winds. It is proposed that the observed neon spectral lines above the disk originates from the gas in the winds Pascucci and Sterzik [2009], Pascucci et al. [2020, 2023]. Theoretical studies have solved radiative transfer equations coupled with chemical reactions and have predicted the expected image of CII emissions [Weber et al., 2020, Haworth and Owen, 2020]. Small dust grains are carried away by gas flows.Franz et al. [2022] solved hydrodynamics to predict the distribution and trajectory of dust grains. Actually, the James Webb Space Telescope (JWST) observed the forbidden emission lines from several elements Arulanantham et al. [2024]. JWST is expected to detect more signals of disk winds and to lead to the further understanding of disk winds. Understanding the disk dispersal process and pinpointing where mass is lost through winds will guide future observations of MHD winds.

Photoevaporation

The combined model of accretion and MHD winds indicates that the gas in the inner region loses angular momentum rapidly and accretes onto the star. This predicts that disk mass is lost in an inside-out manner. However, observations of disks emitting only from outer regions are rare. This implies that while disk dispersal occurs over a few million years, the final clearing of the disk occurs within a few hundred thousand years. Clarke et al. [2001] proposed that photoevaporation clears gas in the outer region, while processes such as accretion and MHD winds disperse gas in the inner region. Alexander et al. [2006a,b] performed one-dimensional photoevaporation simulations and confirmed that once the inner disk disperses, the outer disk gas is cleared within 10^5 years.

Photoevaporation is a process in which high-energy photons from the central star such

as far-ultraviolet (FUV), extreme-ultraviolet (EUV), and X-rays heat the disk gas enough to gain escape velocity and leave the system. The efficiency and heating mechanism depend on the photon energy:

- Far-ultraviolet photons (FUV; $6\,\mathrm{eV} < h\nu < 13.6\,\mathrm{eV}$) induce the photoelectric effect on dust grains. Electrons ejected from dust grains transfer excess kinetic energy to the surrounding gas, contributing to gas heating.
- Extreme-ultraviolet photons (EUV; $13.6\,\mathrm{eV} < h\nu < 0.1\,\mathrm{keV}$) directly ionize hydrogen atoms. The free electrons from ionization are quickly thermalized, which heats the gas.
- X-ray photons ($h\nu > 0.1\,\mathrm{keV}$) ionize a variety of elements on the disk and often cause secondary ionization events. These ionizations lead to further heating as the electrons are thermalized.

The gas escapes the disk when its kinetic energy is sufficient to overcome the gravitational potential of the star. The radius beyond which gas can escape as a result of photoevaporation is referred to as the gravitational radius, r_g, given by

$$\begin{aligned} r_\mathrm{g} &= \frac{GM_*}{c_\mathrm{s}^2} \\ &\sim 8.9\,\mathrm{au}\left(\frac{M_*}{1\,\mathrm{M}_\odot}\right)\left(\frac{c_\mathrm{s}}{10\,\mathrm{km\,s^{-1}}}\right)^{-2}. \end{aligned} \tag{2.15}$$

This position is approximated by the distance where the gravitational potential and thermal energy are balanced. Liffman [2003] updated this by incorporating internal disk pressure and derived the definition of a "critical radius," r_crit, which is given by

$$r_\mathrm{crit} = \frac{(\gamma-1)}{2\gamma}\frac{GM_*}{c_\mathrm{s}^2} \sim 0.2 r_\mathrm{g}. \tag{2.16}$$

In the equation, γ represents the ratio of specific heats and $\gamma = 5/3$ is assumed. This suggests that photoevaporative mass loss can also occur inside the gravitational radius. This is confirmed in a hydrodynamic calculation by Font et al. [2004]. Their calculations showed that, although the mass loss is limited, photoevaporation affects disk evolution in both inner and outer regions.

The concept of photoevaporation was initially introduced to explain the longevity of the observed H II regions with high-mass stars. Early models suggested that intense EUV radiation from massive stars could maintain an ionized H II region by continuously supplying ionizing photons [Yorke and Welz, 1996].

The first direct imaging of a PPD showed blurred gas around stars [O'Dell et al., 1993, O'Dell and Wen, 1994, McCaughrean and O'Dell, 1996]. FUV photons are not as efficiently absorbed by the gas near the star as EUV photons, so external photoevaporation by FUV photons has been suggested as the cause. Richling and Yorke [2000] conducted radiation

hydrodynamics simulations of external photoevaporation with FUV and EUV radiation. They found that FUV photons are the primary heating source for the gas, which results in wing-shaped evaporative flows.

The radiation flux from the central star is comparable to that from nearby massive stars, so photoevaporation also applies to individual disk evolution. Initial studies on photoevaporation mainly focused on higher-energy photons, such as EUV and X-ray photons. Since atomic hydrogen, the main absorber of EUV photons, is abundant in disk gas, EUV photons are strongly attenuated near the star. Hollenbach et al. [1994] ran photoevaporation simulations that incorporated radiative transfer and found that the efficiency of photoevaporation depends on the strength of the stellar wind. When the stellar wind is weak, photoevaporative flows originate just outside the gravitational radius. These flows block radiation from reaching the outer disk, suppressing the mass-loss rate. The mass-loss rate by photoevaporation is this model is fitted by:

$$\dot{M}_{\rm pe} = 9.2 \times 10^{-10} \left(\frac{\Phi_{\rm EUV}}{10^{40.7}\,{\rm s}^{-1}} \right)^{1/2} \left(\frac{M_*}{1\,{\rm M}_\odot} \right)^{1/2} {\rm M}_\odot\,{\rm yr}^{-1} \tag{2.17}$$

This expression is widely used in studies that incorporate photoevaporation as a disk dispersal process [Kunitomo et al., 2021]. EUV photons, however, are often fully absorbed in the inner regions of the disk, which limits their impact on the outer regions of the disk [Johnstone et al., 1998].

Subsequent studies extended the model to include photons of various wavelengths and to disks around low-mass stars. Ercolano et al. [2008] performed photoevaporation simulations that accounted for both EUV and X-ray radiation. Taking into account hydrostatic conditions, their model estimated a photoevaporative mass-loss rate of approximately $\dot{M}_{\rm pe} \sim 10^{-8}\,{\rm M}_\odot\,{\rm yr}^{-1}$. They further explored the effects of different X-ray spectral energy distributions, finding that soft X-rays ($< 1\,{\rm keV}$) contribute significantly to disk heating because they penetrate deeper into the disk and generate dense photoevaporative winds. More recently, Ercolano et al. [2021] updated their simulations with an enhanced soft X-ray spectrum, confirming that soft X-ray photons are a dominant heating source.

Gorti and Hollenbach [2009] investigated the role of far-ultraviolet (FUV) radiation in driving disk photoevaporation. Their steady-state simulations revealed that FUV-driven photoelectric heating is the dominant heating mechanism at the disk surface. This effect occurs when FUV photons eject electrons from dust grains, transferring energy to surrounding gas molecules and raising the gas temperature sufficiently to initiate a photoevaporative flow. For a solar-mass star ($M_* = 1\,{\rm M}_\odot$), their model estimated a substantial mass-loss rate from photoevaporation, exceeding $10^{-8}\,{\rm M}_\odot\,{\rm yr}^{-1}$, which is comparable to typical accretion rates observed in such systems. In addition to examining the general effect of FUV heating, they explored how photoevaporation rates vary with stellar mass by simulating a wide range of stellar masses, from $0.3\,{\rm M}_\odot$ to $7\,{\rm M}_\odot$. They found that for stars in the range $0.3\,{\rm M}_\odot \leq M_* \leq 3\,{\rm M}_\odot$, the disk dispersal timescale remained relatively stable at $\sim 0.8\,{\rm Myr}$. However, for a $7\,{\rm M}_\odot$ star, the disk dispersal timescale

shortened drastically to under $10^5\,\mathrm{yr}$ because of the intense FUV and extreme-ultraviolet (EUV) radiation from the star. This high-energy radiation rapidly heats and disperses the disk gas, driving fast photoevaporative winds and hastening disk dispersal.

The study by Gorti and Hollenbach [2009] was the first to directly demonstrate how differences in disk dispersal timescales across varying stellar masses could be attributed to photoevaporation. Their findings underscore the importance of FUV radiation in setting disk lifetimes, particularly in more massive stars, where high-energy radiation accelerates disk clearing.

As theoretical studies improve, radiation hydrodynamic simulations have become the standard for modeling photoevaporation because they provide a more realistic structure of gas flows. Ercolano et al. [2009] compared the mass-loss rates of photoevaporation between hydrostatic simulations and those with a fixed vertical structure, finding that the mass-loss rate is approximately ~ 4.9 times higher in the hydrostatic case. This is because a flaring structure exposes a larger region to high-energy radiation from the central star.

Recent theoretical studies use photoevaporation simulations that solve radiative transfer, hydrodynamics, and thermochemistry while considering all FUV, EUV, and X-ray radiation [Wang and Goodman, 2017, Nakatani et al., 2018a,b]. They confirmed that the photoelectric effect on dust grains by FUV radiation is the main heating process on the disk surface. In addition, Nakatani et al. [2018b] varied the X-ray luminosity and clarified the role of photons at different energies. Their series of calculations suggested that X-ray radiation enhances the efficiency of heating by photoelectric effect because X-ray photons ionize various elements and increase the ionization rate.

A series of previous studies provides a detailed insight into the photoevaporation process and how high-energy photons of various energies contribute to mass loss. The latest research has focused on how disk evolution depends on stellar properties, such as mass and luminosity. We ran radiation hydrodynamic simulations of photoevaporation varying a stellar mass in the range of 0.5–$7\,\mathrm{M}_\odot$ [Komaki et al., 2021] (see also Komaki [2022]). In the simulations, we incorporated FUV, EUV, and X-ray radiation and showed that photoelectric heating by FUV photons consistently drives disk surface heating across different stellar masses. The mass-loss rate is $\sim 3 \times 10^{-9}\,\mathrm{M}_\odot\,\mathrm{yr}^{-1}$ around $M_* = 1\,\mathrm{M}_\odot$. We concluded that shorter disk lifetimes with increasing stellar mass can be attributed to higher FUV luminosities of more massive stars.

Furthermore, Picogna et al. [2021] conducted radiation hydrodynamic simulations to investigate the effects of EUV and X-ray photons on mass loss. They showed that the mass-loss rate increases with X-ray luminosity, which also correlates with stellar mass. Despite these advances, there is ongoing discussion as to which wavelength range has the most significant role in driving photoevaporation and disk dispersal. The resulting mass-loss rate of photoevaporation also varies from one simulation to another because of the calculation method relating to stellar radiation and consequent heating.

Sellek et al. [2024] revisited the previous studies by Nakatani et al. [2018b] and Ercolano et al. [2021] to identify which photon energies contribute the most to disk heating and to understand the differences in their simulation results. Earlier simulations

that emphasize X-ray heating did not solve all radiative transfer equations [Owen et al., 2010]. Instead, they used precomputed tables of the ionization parameter and local gas temperature based on independent calculations. These tables overestimated gas temperatures because molecular line cooling was not included. The overestimated temperatures led to higher mass-loss rates in X-ray photoevaporation simulations.

Sellek et al. [2024] suggested that the variation in dominant energy ranges is attributed to differences in the X-ray energy spectra used in simulations, particularly in the soft X-ray range. Ercolano et al. [2021] showed that soft X-rays can drive photoevaporation by depositing energy deeper into the disk. The actual photoevaporation mass-loss rate may be closer to a lower value of $\sim 10^{-9}\,\mathrm{M}_\odot\,\mathrm{yr}^{-1}$. This aligns with recent observational findings suggesting longer disk lifetimes.

The behavior of photoevaporation remains under investigation, particularly its dependence on parameters such as dust amount, stellar luminosity, and stellar spectrum. The physical quantities of the system undergo significant changes throughout disk dispersal. Understanding the effects of both disk dispersal and stellar evolution to the main sequence on photoevaporation is essential.

Combined Model of Disk Gas Dispersal

Previous research has examined how each process (accretion, MHD winds, and photoevaporation) occurs and its contribution to disk mass loss. The observed disks reflect the combined results of these dispersal processes. Theoretical research has used long-term disk evolution simulations that incorporate accretion and photoevaporation [Clarke et al., 2001, Alexander et al., 2006b, Gorti et al., 2009, Owen et al., 2010, Morishima, 2012, Bae et al., 2013, Kimura et al., 2016, Emsenhuber et al., 2021, Kunitomo et al., 2021]. Table 1.1 shows the progress of this research field and describes the process incorporated in each calculation. These studies consistently show that initially accretion drives the mass loss dominantly, but photoevaporation becomes dominant at the final stage. Kunitomo et al. [2020] demonstrated that MHD winds can explain observed disk lifetimes, even with a low viscous parameter. Kunitomo et al. [2021] performed one-dimensional long-term disk evolution simulations incorporating accretion, photoevaporation, and stellar evolution. Their results showed that the high radiation from intermediate-mass stars increases the mass loss rate and shortens the disk lifetimes. Theoretical studies have also demonstrated that disks lose angular momentum through interactions with their host stars [Koenigl, 1991, Shu et al., 1994, Romanova et al., 2009, Hartmann et al., 2016], further emphasizing the multifaceted impact of magnetic fields on disk evolution.

Weder et al. [2023] performed simulations that included accretion, MHD winds, and photoevaporation from EUV and X-ray radiation. They found that weak MHD winds are essential for explaining observed disk dispersal timescales, comparing weak- and strong-wind models. Their results also showed that external photoevaporation drives significant disk dispersal. Kunitomo et al. [2021] demonstrated that as stars evolve and luminosity increases, photoevaporation intensifies and accelerates disk dispersal. These findings highlight the need for simulations that account for all relevant effects to fully

understand disk dispersal.

Theoretical studies have made significant progress in understanding the physics underlying individual disk dispersal processes. These processes are expected to operate in combination. In this thesis, we perform long-term disk evolution simulations that integrate accretion, MHD winds, photoevaporation, and stellar evolution. A unique aspect of our approach is the incorporation of mass-loss rates derived from two-dimensional radiation hydrodynamic simulations, which provide a more accurate representation of photoevaporative effects. The photoevaporative mass-loss rate generally increases with stellar mass. It is necessary to investigate whether this trend also applies to the overall dependence of disk dispersal timescale on stellar mass. To address this, we conduct long-term simulations that incorporate accretion, MHD winds, photoevaporation, and stellar evolution while varying stellar mass in the range of 0.1–$7\,\mathrm{M}_{\odot}$. Understanding disk evolution around various types of stars offers realistic insights into planet-formation processes, helping to explain the observed diversity in exoplanets.

Observations of star-forming regions provide statistical analyses of disks and their evolutionary paths. Disk fraction, defined as the ratio of stars with surrounding disks, is often used to understand population synthesis in regions. Recent studies have attempted to reproduce observed disk fractions by assuming initial dispersions in star-forming regions [Mordasini et al., 2009a,b, Emsenhuber et al., 2021, Weder et al., 2023]. We generate a mock star-forming region containing 10000 disks to calculate the evolution of disk fraction over time using the state-of-the-art disk evolution models, enabling a direct comparison with observational data.

Interactions between Systems

Stars in a star-forming region evolve together and may interact with each other. Some studies suggest that external effects, such as accretion from the envelope and external photoevaporation, might influence disk evolution in certain cases. However, these effects are not confirmed to be significant for all disks. Most disk evolution simulations assume that the disks evolve independently.

Observations of PPDs often show extended gas around the system, suggesting that gas continues to accrete from the envelope even after the star reaches the pre-main-sequence stage. This accretion from the envelope can replenish the disk mass and prolong disk lifetimes.

Kimura et al. [2016] performed one-dimensional diffusion simulations incorporating a source term representing envelope accretion to model more realistic disk evolution. Their results showed that systems with high angular momentum form larger disks, which leads to longer disk lifetimes. This suggests that angular momentum influences both the shape of the disk and the lifetime. In another study, Winter et al. [2024] conducted disk evolution simulations that included Bondi-Hoyle-Lyttleton (BHL) accretion from the envelope. They compared their results with observed disk lifetimes, masses, accretion rates, and radii. Their simulations showed that the disk mass increases during the first $1\,\mathrm{Myr}$ before starting to decline. In the final stages of disk evolution, 20–70% of the disk mass comes from accreted

gas.

External photoevaporation is another important disk dispersal process. High-energy radiation from nearby massive stars heats the disk gas and launches the photoevaporative gas flows. The impacts of nearby massive stars are observed as reduced disk mass [Mann et al., 2014, Ansdell et al., 2017, van Terwisga et al., 2020], smaller disk radii [Eisner et al., 2018, Boyden and Eisner, 2020], and undetectable CO [Ansdell et al., 2017, Boyden and Eisner, 2020]. Observations also suggest that the disk fractions of these regions are low, suggesting shorter disk lifetimes [Mann et al., 2014, Guarcello et al., 2016, Sellek et al., 2020, van Terwisga et al., 2020]. For example, in the Orion star-forming region, disks within a projected separation of 1.5 pc from B-type stars show significant CO dissociation caused by FUV radiation.

Haworth et al. [2018, 2023] developed hydrodynamic simulations of external photoevaporation, which examine an impact of a wide range of FUV fluxes from 10 to $10^5 G_0$, where G_0 is the Habing flux unit and given by

$$G_0 = \frac{u_\nu (6 - 13.6\,\mathrm{eV})}{1.6 \times 10^{-3}\,\mathrm{erg\,cm^{-2}\,s^{-1}}}. \tag{2.18}$$

In the equation, u_ν represents the flux integrated in the wavelength of FUV photons. They found that a disk begins to lose its mass with a significant mass-loss rate of $\geq 10^{-8}\,\mathrm{M_\odot\,yr^{-1}}$ when the FUV field exceeds $1000 G_0$, with mass loss primarily occurring in the outer disk regions where gravitational binding is weaker.

Some disk evolution simulations focus on the collective evolution of disks within star-forming regions. N-body simulations are employed to track the positions of individual stars, modeling their interactions through external photoevaporation. These simulations have shown that the external photoevaporation efficiency is highly environment-dependent [Concha-Ramírez et al., 2019, 2021, Parker et al., 2021]. While 58% of the stars in regions with O/B stars are influenced by FUV radiation, only about 25% experience FUV flux intense enough to cause significant external photoevaporation [Fatuzzo and Adams, 2008]. External photoevaporation plays a critical role in modeling individual systems in dense, massive star-forming regions, but it may not be necessary to understand the general evolution of the disk.

Evolution of Dust Grains

Since most of the disk mass is composed of gas, the physical processes that dominate disk evolution are primarily related to gas behavior. However, most disk observations focus on the distribution of dust grains. To understand the observed trends, it is necessary to study the evolution of dust grains.

Dust grains orbit the star and form part of the PPD, similar to gas. Their motion differs from that of gas because of processes specific to dust grains, such as radial drift, settling, collisional growth, and fragmentation. The evolution of dust grains is given by Clarke and

Pringle [1988] as:

$$\frac{\partial \Sigma_{\rm d}}{\partial t} + \frac{1}{r}\frac{\partial}{\partial r}\left(r\Sigma_{\rm d}u_{\rm d}\right) + \frac{1}{r}\frac{\partial}{\partial r}\left(rF_{\rm d}\right) = 0 \tag{2.19}$$

where $u_{\rm d}$ and $F_{\rm d}$ represent the dust radial velocity and the external forces on dust grains. Simple dynamics predicts that dust grains orbit following a Keplerian motion with no radial velocity, but they deviate from the Keplerian motion because of gas drag. The drift velocity $u_{\rm r}$, which corresponds to the difference from Keplerian motion, is given by:

$$u_{\rm d} = \frac{2St}{St^2+1}v'_{{\rm gas},\phi} + \frac{1}{St^2+1}v'_{{\rm gas},r}, \tag{2.20}$$

where $v'_{{\rm gas},r}$ and $v'_{{\rm gas},\phi}$ denote the deviation of the gas velocity from Keplerian motion. In the equation, St represents the Stokes parameter. Radial drift is an effective process that shapes the morphology of dust disks. Observations show that the radius of the gas component is larger than that of the dust component. In Lupus, more than 60% of the observed disks have a gas-to-dust radius ratio of $R_{\rm CO}/R_{\rm dust} \geq 2$ [Sanchis et al., 2021]. Toci et al. [2021] showed that the large $R_{\rm CO}/R_{\rm dust}$ in the young star-forming region can be attributed to radial drift by performing disk evolution simulations considering viscous evolution, grain growth, and radial drift.

Dust grains also experience diffusion similar to that of gas. Since dust observations are more common than gas observations, dust simulations provide a useful way to compare them with observed data. Some theoretical studies simulate the evolution of dust disks [Garaud, 2007, Hughes and Armitage, 2010], but they often differ in their assumptions. Many calculations assume that the dust size distribution always follows a power-law distribution. For gas, these models typically include viscous accretion and sometimes a simple one-dimensional mass-loss profile for photoevaporation. Dust grains undergo radial drift and growth simultaneously. The dust evolution models have been updated by solving the dust size distributions using continuous distributions [Brauer et al., 2008, Birnstiel et al., 2010]. These models show that the dust size distribution is influenced by the slope of the gas density (pressure) distribution and the strength of turbulence. Birnstiel et al. [2012] provided a simple fit for the dust size distribution calculated in Birnstiel et al. [2010], considering only viscous accretion as a gas dispersal process. Since the resulting dust size distribution is primarily determined by the gas surface density via turbulence, it is crucial to track gas evolution processes to fully understand dust evolution.

Recent advances in disk simulations have allowed us to simultaneously track the evolution of gases and dust [Gorti et al., 2015, Burn et al., 2022, Emsenhuber et al., 2023]. Until recently, models incorporating dust growth were limited to just a few dust-size bins. For example, Burn et al. [2022] developed a one-dimensional disk evolution model that includes accretion, X-ray photoevaporation for gas evolution, and radial drift, diffusion, entrainment by photoevaporative winds and two-size dust growth for dust evolution. As gas surface density evolves, capturing the full distribution of dust sizes becomes a challenge with only two bins.

In response to this limitation, Stammler and Birnstiel [2022] developed a model with a

more detailed dust size distribution in the range of 5.2×10^{-5}–$24\,\mathrm{cm}$ with 120 bins. This comprehensive approach allows for a more accurate description of the evolving dust size distribution. Most previous studies have focused on radial drift and turbulence as the main outcomes of gas-dust interactions. However, other processes also play an essential role, such as dust entrainment in gas flows [Hutchison et al., 2016b] and external photoevaporation [Sellek et al., 2020]. Hydrodynamic simulations reveal that only small dust grains with $\leq 10\,\mu$m are entrained by gas flows [Facchini et al., 2016, Hutchison et al., 2016a]. Settling of dust grains toward the midplane could reduce this size further, limiting the entrainment of larger grains. Sellek et al. [2020] suggested that the dust grains grow rapidly within 10^5 years, becoming too large to be carried by gas flows during this period. Although external photoevaporation significantly reduces the dust mass in the outer disk, the impact on the overall dust distribution remains limited.

While prior research has extensively studied gas evolution and the effects of gas dynamics on dust, there are relatively few studies examining how dust evolution impacts gas. Dust grains play a key role in photoelectric heating, which is one of the primary mechanisms driving photoevaporation through the photoelectric effect of dust grains by FUV radiation. In this paper, we investigate how dust evolution influences gas dispersal.

2.3 Planet Formation

Planets form inside PPDs out of the disk materials. Dust grains settle on the midplane of the disk, where they cluster and undergo coagulation. Through successive collision and growth, these grains gradually grow into larger bodies, eventually reaching kilometer-scale sizes, known as planetesimals. Since the disk lifetime sets a strict upper limit on the time available for planet formation, understanding disk evolution is essential to clarifying how and when planets form.

Over 5000 planets have been discovered since the first detection by Mayor and Queloz [1995]. Observed planets exhibit diversity in their properties, such as mass and distance from their host stars [Howard, 2013, Fulton et al., 2017, Zhang et al., 2018, Zhu and Dong, 2021, Gaudi et al., 2021]. Mulders et al. [2015] analyzed planets around M-, K-, G- and F-type stars observed by the Kepler Space Telescope. They found that planet formation rates are higher around M-type stars compared to G-type stars. Observations also indicate that larger planets are more common around F-, G-, and K-type stars than low-mass stars [Howard et al., 2012, Sabotta et al., 2021]. Johnson et al. [2010] revealed that the occurrence rate of gas giants increases with metallicity and with stellar mass around M to A-type stars. These findings suggest that planet-occurrence rates and properties depend on stellar mass and natal environments influenced by stellar properties.

PPDs, as the birthplace of planets, are believed to influence the diversity of planets. Disk characteristics such as mass [Kokubo and Ida, 2002], metallicity [Petigura et al., 2018], and ring positions [van der Marel and Mulders, 2021] are believed to shape planet formation. Ribas et al. [2015] suggested that shorter disk lifetimes around massive stars explain the lack of hot Jupiters in these systems. By studying how variations in disk mass, metallicity,

stellar mass, and other factors affect disk evolution, we can gain insight into how these initial conditions influence planet formation and help explain the diverse characteristics observed in exoplanet populations.

Theoretically, planets are believed to create substructures such as gaps and rings through interactions with the disk. Observing these gaps provides an estimate of the planet mass, offering valuable insights into ongoing planet formation [Tobin et al., 2020, Tychoniec et al., 2020]. Simulating such gaps requires detailed knowledge of the evolution of the gas surface density.

Previously, planet formation was assumed to occur around class II stars. However, recent observations suggest that planet formation begins earlier. ALMA observations show that disk radius decreases from class 0 to class I phases, because of the loss of angular momentum due to interactions with planets [Tobin et al., 2020]. Understanding disk evolution, especially from the earliest phases, is crucial to fully revealing the process of planet formation. Further evidence suggests that the class I disk has sufficient material for planet formation while the class II disk has insufficient material for the observed planet [Tychoniec et al., 2020]. This result also suggests that planet formation begins in the early stage of disk evolution. Given these findings, understanding disk evolution from the earliest stages is crucial for revealing the complete timeline of planet formation.

Dust grains grow by colliding and sticking together, forming pebbles and eventually planetesimals. The classical model of planet formation suggests that dust grains collide, stick together, and settle toward the midplane. Dust settling facilitates larger grains to coagulate and grow further [Weidenschilling and Cuzzi, 1993]. The dust growth timescale is estimated to be $\sim 10^4\,\mathrm{yr}$ at $r = 5\,\mathrm{au}$. However, there are significant challenges with this theory.

One issue is that coagulated dust grains undergo rapid radial drift toward the central star. For example, cm-sized dust grains accrete to the star within $\sim 100\,\mathrm{yr}$. Another issue is the relative velocity between the dust grains. As dust coagulates and grows, the velocity differences increase, making collisions more likely to result in fragmentation [Brauer et al., 2008]. These challenges suggest a barrier in the classical model, prompting many researchers to investigate alternative processes for planet formation.

To address the radial drift problem, it is necessary to consider a planet formation model that avoids the cm-sized phase. One proposed model involves millimeter-sized grains rapidly condensing through gravitational collapse or instability within the disk [Goldreich and Ward, 1973]. Several mechanisms for inducing this collapse have been proposed. Cuzzi et al. [2008] suggest that turbulence concentrates dust grains within eddies, which then collapse. Another mechanism is the flow instability, where the different motions of gas and dust cause dust grains to clump together [Youdin and Goodman, 2005, Youdin and Johansen, 2007, Jacquet et al., 2011]. Simulations show that this process is enhanced by higher dust-to-gas mass ratios [Chen and Lin, 2020, Gole et al., 2020, Umurhan et al., 2020] and moderate gas pressure gradients [Abod et al., 2019, Gerbig et al., 2020]. These calculations suggest that both gas and dust evolution plays a critical role.

Another pathway is coagulation of fluffy dust [Okuzumi et al., 2012]. Traditional

dust growth simulations often assume a constant solid density for dust grains, typically $1.6\,\mathrm{g\,cm^{-3}}$ or $2.2\,\mathrm{g\,cm^{-3}}$. However, fluffy dust grains, formed through low-density collisions, increase in porosity as they grow. Calculations suggest that fluffy grains can be compressed and grow to km-sized bodies under the influence of gas pressure or self-gravity [Kataoka et al., 2013a,b]. The secular gravitational instability provides another potential route for planet formation. Disk material gathers into planetesimals through this process [Youdin, 2011, Takahashi and Inutsuka, 2014]. Tominaga et al. [2019] showed that a high dust-to-gas ratio, $\mathcal{D} \geq 0.2$, is necessary for this mechanism to occur.

The dominant process for planet formation remains debated. Previous research highlights the need to account for both dust distribution and the effects of gas evolution on dust growth. Long-term disk evolution simulations that incorporate both gas and dust dynamics could provide crucial insights into the conditions under which planets form.

Previous works failed to incorporate accurate gas evolution to dust evolution simulations, even though the gas density profile dominates the motion and growth of dust grains. In this dissertation, we tackle this by performing disk evolution simulations which incorporate both gas and dust evolution by utilizing our original gas evolution simulation which considers all the major disk dispersal processes; accretion, MHD winds, and photoevaporation. At the same time, we also investigate the impact of dust evolution on disk dispersal through photoevaporation because the disk is dominantly heated by the photoelectric effect of dust grains. This is the first work to consider all the above processes at the same time.

2.4 Thesis Overview

When considering the evolution from gas to a star-planet system, the disk is always at the center of attention. Understanding disk evolution is key to determining the conditions under which planets form and the timing of planet formation. Recent observations suggest that planet formation begins earlier than previously thought. This highlights the need for thorough disk evolution simulations starting from the very initial phase.

Recent simulations of photoevaporation show that FUV photons play a significant role in heating disk gas through the photoelectric effect on dust grains. Two important parameters that influence the efficiency of FUV heating are the abundance of dust grains and the FUV luminosity. We have performed radiation hydrodynamic simulations of photoevaporation, varying the FUV luminosity over several magnitudes, and found that the photoevaporative mass-loss rate increases with FUV luminosity, following $\propto L_{\mathrm{FUV}}^{0.55}$. This relationship holds across a wide range of stellar masses, $0.5 \leq M_* \leq 7\,\mathrm{M}_\odot$. It is therefore essential to investigate how the photoevaporation process changes with varying amounts of dust.

In Chapter 3, we perform radiation hydrodynamic simulations of photoevaporation, varying the dust-to-gas mass ratio in the range of $10^{-1} \leq \mathcal{D} \leq 10^{-6}$. These simulations focus solely on gas motion induced by photoevaporation and do not include other disk dispersal processes such as viscous accretion and MHD winds. We include FUV, EUV, and X-ray photons as sources of radiation from the central star. The dust-to-gas mass ratio is assumed

to be spatially uniform throughout the disk. Although the simulation primarily considers the evolution of gas density and temperature, we calculate the dust temperature separately to consistently evaluate the efficiency of the photoelectric effect. From these calculations, we derive the surface mass-loss rate and identify the radii from which photoevaporative flows are launched. This also provides a formula that can be applied in one-dimensional disk evolution simulations, enabling to consider of multiple disk dispersal processes consistently.

Previous theoretical studies demonstrated realistic disk dispersal using simulations that included incomplete sets of processes. As a result, each work claims that the different process is the dominant one. It is essential to perform a long-term disk evolution simulation considering all major disk dispersal processes to fully understand the evolution path of protoplanetary disks.

In Chapter 4, we perform one-dimensional long-term disk evolution simulations incorporating accretion, MHD winds, photoevaporation, and stellar evolution simultaneously. This provides a comprehensive view of disk evolution. The surface mass-loss rate due to photoevaporation is derived from the radiation hydrodynamic simulations presented in Chapter 3. Our work represents the first simulation that includes photoevaporation driven by FUV, EUV, and X-ray photons. This approach enables a more realistic realization of disk gas evolution. Although we assume a constant dust-to-gas mass ratio in this calculation, the evolution of dust grains is discussed in Chapter 5. We run simulations with varying stellar masses to investigate the reasons for differences in disk dispersal timescales and how the distribution of disk material changes with stellar mass. Disk fraction, a widely used parameter to describe the evolutionary stage of disk dispersal, is calculated for a mock star-forming region containing 10,000 disks to enable direct comparisons with observational data. Observations from the outer galaxy suggest a low disk fraction in low-metallicity environments. Although the exact cause is unclear, rapid disk dispersal in these regions is often attributed to enhanced photoevaporation due to reduced attenuation. To investigate this trend, we perform a series of photoevaporation simulations and long-term disk evolution simulations at $Z = 0.1\,\mathrm{Z}_\odot$ to identify the processes contributing to rapid disk dispersal. This is the first study to perform disk evolution simulations incorporating a complete set of disk dispersal processes, aiming to understand the observed trend of low disk fractions in low-metallicity environments.

Most disk observations focus on dust grains, even though the majority of the disk mass is composed of gas. The commonly observed dust-to-gas mass ratio of 0.01 in the ISM is often used to infer the total disk mass from observed dust, but this estimate carries significant uncertainty. This uncertainty arises from the efficient dispersal or coagulation of dust grains and the local and time variations in the dust-to-gas mass ratio. Since disk gas is primarily heated by the photoelectric effect on dust grains, the evolution of dust grains can significantly influence gas dispersal through photoevaporation. To accurately model this process, it is essential to perform disk evolution simulations that consistently account for both gas and dust components. Several previous studies have aimed to understand the detailed mechanisms of photoevaporation during the later stages of disk dispersal. However, the outcomes of these studies often depend on assumptions made about the

evolved state of the disk.

In Chapter 5, we perform simulations that simultaneously solve the evolution of gas and dust. These simulations include processes such as radial drift, diffusion, entrainment by gas flows, and dust collisional growth to study dust evolution in detail. At each time step, we explicitly follow the local dust-to-gas mass ratio. Using the dependence of the photoevaporation rate on the dust-to-gas mass ratio derived in Chapter 3, we consistently estimate the surface mass-loss rate at each location. In addition, we examine the overall effect of dust evolution on disk dispersal. This research is the first to assess the impact of dust evolution on the photoevaporation process. A distinctive aspect of our approach is that we consistently follow the gas and dust co-evolution from the very beginning.

Throughout this dissertation, we focus on photoevaporation and its role in overall disk dispersal. This represents the first and most detailed research on this topic with comprehensive calculations.

3

Photoevaporation of Dust-Deficient Disks

Figures

3.1 Motivation for Studying Dust-Deficient Disks

Photoevaporation is one of the major disk gas dispersal processes. The disk gas is heated by high-energy radiation such as far-ultraviolet (FUV), extreme ultraviolet (EUV), and X-ray photons emitted from the central star. The heated gas with sufficient kinetic energy escapes from the system, and the gas flows result in gradual mass loss from the disk. Previous theoretical research has shown that viscous accretion alone cannot explain the observed disk dispersal timescale of several million years. Adding photoevaporation makes it possible to explain this timescale. For this reason, photoevaporation is often introduced as the dominant process driving disk dispersal in the later stages of disk evolution.

Previous research has studied photoevaporation using $1 + 1$ dimensional simulations, typically assuming hydrostatic equilibrium and focusing primarily on EUV-driven heating. Gorti et al. [2009] advanced these models by including FUV, EUV, and X-ray radiation in their one-dimensional simulations. They demonstrated that the photoelectric effect on dust grains by FUV photons is the primary mechanism for gas heating in a wide range of stellar masses ($0.3\,\mathrm{M}_\odot \leq M_* \leq 7\,\mathrm{M}_\odot$).

Subsequent radiation hydrodynamic simulations revealed that the assumption of hydrostatic equilibrium does not fully capture the dynamics of photoevaporative flows. Gas launched from the inner disk can attenuate radiation from the central star, altering the heating profile and mass-loss rates [Wang and Goodman, 2017, Nakatani et al., 2018a]. We conducted a series of radiative hydrodynamic simulations for stars with masses ranging from $0.5\,\mathrm{M}_\odot$ to $7\,\mathrm{M}_\odot$, confirming that FUV photons dominantly drive photoevaporative flows [Komaki et al., 2021]. These photons heat the gas on the disk surface via the photoelectric effect on dust grains. The emitted electrons thermalize in the gas and increase its temperature. Therefore, the efficiency of FUV heating depends both on the abundance of dust grains and the FUV luminosity.

Nakatani et al. [2018b] showed that the abundance of dust grains plays a crucial role in the photoelectric effect by varying the metallicity in their photoevaporation simulations. Dust grains follow an evolution path distinct from gas because of processes unique to solid particles, including radial drift, settling toward the midplane, entrainment in photoevaporative winds, growth via coagulation, and turbulence. Several theoretical studies have shown that these processes often lead to a faster decrease in dust mass than in gas mass. Furthermore, coagulation reduces the abundance of small dust grains that are critical for photoelectric heating. The photoelectric effect occurs most efficiently on small dust grains with radii in the $15\text{Å} \leq a \leq 100\text{Å}$ range.

Theoretical studies have shown that photoevaporation becomes particularly important in the later stages of disk evolution as accretion rates drop significantly because of the reduced surface density. The relative importance of photoevaporation highlights the necessity of investigating the heating mechanism and resulting mass-loss of photoevaporation with a low dust-to-gas mass ratio.

Another reason for focusing on photoevaporation in dust-deficient disks is the low abundance of polycyclic aromatic hydrocarbons (PAHs) observed around low-mass stars. These observations suggest that the PAH abundance is less than 1% of the abundance in ISM [Geers et al., 2006, 2007, Oliveira et al., 2010, Vicente et al., 2013]. Since low-mass stars are the main components of stellar clusters according to the IMF, photoevaporation of disks with less dust grains is essential to understanding general disk dispersal.

In this chapter, we perform a series of radiation hydrodynamics simulations varying the dust-to-gas mass ratio. We clarify the detailed heating processes for photoevaporation with various dust-to-gas mass ratios in the range of $10^{-6} \leq \mathcal{D} \leq 10^{-1}$. We aim to understand how photoevaporation depends on the dust-to-gas mass ratio and to discuss its impact on overall disk evolution and dispersal.

3.2 Methods

In our simulation, radiation transfer, hydrodynamics, and non-equilibrium thermochemistry are solved simultaneously to understand the physical and chemical structures in evaporating disks. We use the open-source code PLUTO [Mignone et al., 2007] to solve gas hydrodynamics combined with a radiative transfer module Nakatani et al. [2018a]. We update the chemical network module and add it to the radiative hydrodynamic simulation codes. The updated chemical reactions allow us to trace detailed heating related to excitation and de-excitation of H_2. This network captures the detailed chemical reactions and heating mechanisms, including those driven by FUV, EUV, and X-ray radiation.

By solving these three components—radiation transfer, hydrodynamics, and non-equilibrium thermochemistry—simultaneously, we achieve a detailed representation of the physical and chemical structure of an evaporating disk. This approach comprehensively explains how high-energy radiation interacts with the disk material and drives photoevaporative gas flows.

3.2.1 Governing Equations

The governing equations are given in three-dimensional spherical coordinates (r, θ, ϕ) by

$$\begin{aligned}
\frac{\partial \rho}{\partial t} + \nabla \cdot (\rho \mathbf{v}) &= 0, \\
\frac{\partial (\rho v_r)}{\partial t} + \nabla \cdot (\rho v_r \mathbf{v}) &= -\frac{\partial P}{\partial r} - \rho \frac{GM}{r^2} + \rho \frac{v_\theta^2 + v_\phi^2}{r}, \\
\frac{\partial (\rho v_\theta)}{\partial t} + \nabla \cdot (\rho v_\theta \mathbf{v}) &= -\frac{1}{r}\frac{\partial P}{\partial \theta} - \rho \frac{v_r v_\theta}{r} + \rho \frac{v_\phi^2}{r} \cot\theta, \\
\frac{\partial (\rho v_\phi)}{\partial t} + \nabla^l \cdot (\rho v_\phi \mathbf{v}) &= 0, \\
\frac{\partial E}{\partial t} + \nabla \cdot H\mathbf{v} &= -\rho v_r \frac{GM}{r^2} + \rho(\Gamma - \Lambda), \\
\frac{\partial n_{\rm H} y_i}{\partial t} + \nabla \cdot (n_{\rm H} y_i \mathbf{v}) &= n_{\rm H} R_i.
\end{aligned} \tag{3.1}$$

In the equations, P, ρ, E, H, Γ, and Λ represent the pressure, gas density, total energy per unit volume, enthalpy per unit volume, heating rate, and cooling rate, respectively. The first equation describes the continuity equation. The second to fourth equations correspond to the Euler equations, which represent momentum conservation in the r, θ, and ϕ directions in spherical coordinates. The fifth equation is the energy conservation equation. The sixth equation is the equation for chemical evolution. In the equation, $n_{\rm H}$ is the number density of elemental hydrogen, and y_i and R_i denote the abundance and reaction rate of the specific chemical species labeled i. For simplicity, a disk is assumed to be axisymmetric around the z-axis. Equations in the ϕ direction are also solved to clarify the evolution of the angular momentum.

Eleven chemical species are incorporated: H, H^+, H^-, He, H_2, $H_2{}^+$, $H_2{}^*$, CO, O, C^+, and electrons. Atomic carbon (C) is not explicitly included because it is quickly ionized into C^+ by FUV photons right after CO is photodissociated [Nelson and Langer, 1997, Richling and Yorke, 2000].

The elemental abundances of carbon and oxygen in the gas phase are set to $y_{\rm C} = 0.927 \times 10^{-4}$ and $y_{\rm O} = 3.568 \times 10^{-4}$, respectively, following the model to reproduce the solar abundance [Pollack et al., 1994].

Vibrationally excited hydrogen molecules are explicitly incorporated as $H_2{}^*$ to clarify the heating and chemical reactions that involve this species. Although H_2 has hundreds of excitation levels, the vibrational state of $v = 6$ represents all excited states for simplicity Tielens and Hollenbach [1985].

The reaction network between these species is incorporated in the calculation. The rates of these processes depend on the local physical conditions, such as temperature, density, and radiation field intensity. The complete list of rate coefficients is provided in Appendix A.

3.2.2 Heating and Cooling

Major heating and cooling reactions are considered to reproduce the thermal and chemical structure of the disk.

We incorporate EUV and X-ray heating, FUV heating via the photoelectric effect on dust grains, H_2 dissociation, and the de-excitation of vibrationally excited H_2^* for heating processes. For cooling processes, we employ adiabatic cooling, hydrogen recombination, Ly α emission, dust-gas collisional cooling, O I line cooling, C II line cooling, and molecular line cooling of H_2 and CO. Each process will be introduced in later sections.

EUV and X-ray photons contribute to heating primarily by ionizing hydrogen atoms. Hydrogen ionization requires photons with energies exceeding $h\nu \geq 13.6\,\mathrm{eV}$. The excess energy from these photons is converted into the kinetic energy of free electrons, which thermalize the gas. The ionization rate of H I is expressed as:

$$R_{\mathrm{ion}} = \int_{\nu_1}^{\infty} y_{\mathrm{H\,I}} n_{\mathrm{H}}\, \sigma_{\mathrm{H}}\, F_\nu \,\mathrm{d}\nu, \tag{3.2}$$

where σ is the ionization cross-section, and F_ν is the photon flux at a specific frequency ν. The minimum frequency for ionization corresponds to $h\nu_1 = 13.6\,\mathrm{eV}$. The cross-section σ is approximated as shown in Osterbrock and Ferland [2006] and given by

$$\sigma_{\mathrm{H}} = 6.3 \times 10^{-18} \left(\frac{h\nu}{h\nu_1}\right)^{-3} \mathrm{cm}^2 \tag{3.3}$$

The resulting heating rate due to hydrogen ionization is given by:

$$\Gamma_{\mathrm{EUV}} = \int_{\nu_1}^{\infty} y_{\mathrm{H\,I}} n_{\mathrm{H}}\, \sigma_{\mathrm{H},\nu}\, F_\nu\, h(\nu - \nu_1)\,\mathrm{d}\nu \tag{3.4}$$

The local photon flux at a specific frequency is derived by solving a radiative transfer, given by

$$\frac{1}{r^2}\frac{\partial}{\partial r}\left(r^2 F_\nu\right) = -n_{\mathrm{HI}}\sigma_\nu F_\nu. \tag{3.5}$$

The local photon flux at a specific frequency is then obtained by integrating Eq. 3.5 along the line of sight:

$$F_\nu = \frac{\Phi_{\mathrm{EUV},\nu}}{4\pi r^2} \exp\left(-\sigma_\nu N_{\mathrm{H\,I}}\right), \tag{3.6}$$

where $N_{\mathrm{H\,I}}$ denotes the column density of neutral hydrogen, which is given by

$$N_{\mathrm{H\,I}} = \int \mathrm{d}r\, n_{\mathrm{H\,I}}. \tag{3.7}$$

EUV photons are assumed to follow a blackbody distribution with an effective temperature of $T_{\mathrm{eff}} = 10^4\,\mathrm{K}$. At the same time, the X-ray spectrum is based on observational data for TW Hya provided by Nomura et al. [2007].

EUV radiation creates an H II region in the region close to the star. EUV photons are

mainly absorbed near the star, limiting their role in launching photoevaporative flows [Richling and Yorke, 2000]. In contrast, X-ray photons can penetrate deeper into the dense region inside the disk and launch dense neutral photoevaporative flows [Owen et al., 2010].

FUV photons do not have sufficient energy to ionize hydrogen atoms directly. Instead, they contribute to gas heating by inducing the photoelectric effect on dust grains. In this process, FUV photons eject electrons from the surface of dust grains. These emitted electrons must overcome the Coulomb potential of the positively charged dust grains. The electrons thermalize in the surrounding gas and increase the temperature there.

The efficiency of this process depends on the electric charge of the dust grains. The electron emission rate of a single photoelectric effect can be expressed as:

$$\left(\frac{\mathrm{d}N}{\mathrm{d}t}\right) = \int \mathrm{d}\nu \frac{u_\nu c}{h\nu} \pi a^2 Q_{\mathrm{abs}} Y_{\mathrm{pe}}, \tag{3.8}$$

where Y_{pe} represents the yield, the fraction of electrons that successfully escape the dust grain after being excited. The value of Y_{pe} increases with higher photon energy and decreases with higher Coulomb potential of the dust grain [Draine and Bertoldi, 1996, Weingartner et al., 2006]. In the equation, $\mathrm{d}\nu \frac{u_\nu c}{h\nu}$ represents the number of photons with energy $[\nu, \mathrm{d}\nu]$ per unit area, and $\pi a^2 Q_{\mathrm{abs}}$ denotes the absorption cross-section of a dust grain with the radius of a. The heating efficiency of the photoelectric effect is most prominent on small dust grains with sizes in the range of $15\text{Å} \leq a \leq 100\text{Å}$. This is because emitted electrons are more likely to escape the electronic potential of the dust grain and reach the gas phase than from larger grains.

The heating rate due to the photoelectric effect is described by Bakes and Tielens [1994] as:

$$\begin{aligned} \Gamma_{\mathrm{PE}} &= 10^{-24}\,\mathrm{erg\,s^{-1}\,cm^{-3}} \times \epsilon G_0 n_{\mathrm{H}} (\mathcal{D}/0.01) \\ \epsilon &= \left[\frac{4.87 \times 10^{-2}}{1 + 4 \times 10^{-3} (G_0 \sqrt{T_{\mathrm{gas}}}/n_e)^{0.73}} + \frac{3.65 \times 10^{-2} (T_{\mathrm{gas}}/10^4\,\mathrm{K})^{0.7}}{1 + 2 \times 10^{-4} G_0 \sqrt{T_{\mathrm{gas}}}/n_e} \right], \end{aligned} \tag{3.9}$$

where T_{gas} and n_e represent the gas temperature and electron number density. This heating process is significant in the upper layers of protoplanetary disks, where small dust grains are abundant and FUV photons are not attenuated. The heating rate of the photoelectric effect depends on the abundance of small dust grains that are susceptible to the coagulation process.

Lyman-Werner (LW) photons, with energies of $11.2\,\mathrm{eV} \leq h\nu \leq 13.6\,\mathrm{eV}$, excite hydrogen molecules from their electronically ground state to an electronically excited state. Approximately 10% of the excited molecules experience photodissociation and are split into two hydrogen atoms. This process is called photodissociation. The rate of H_2 dissociation is expressed as:

$$R_{\mathrm{H_2,diss}} = 3.4 \times 10^{-11} f_{\mathrm{shield}} G_0 e^{-2.5 A_{\mathrm{V}}}\,\mathrm{s^{-1}}, \tag{3.10}$$

where f_{shield}, G_0, and A_{V} represent the self-shielding factor, the incident FUV flux in Habing units, and the visual extinction, respectively.

The Habing unit is a parameter for the energy density of FUV radiation and is defined as:

$$G_0 = \frac{u_\nu (6 - 13.6\,\mathrm{eV})}{1.6 \times 10^{-3}\,\mathrm{erg\,s^{-1}\,cm^{-2}}}. \tag{3.11}$$

In the solar vicinity, $G_0 \sim 1$. Self-shielding of H_2 is parameterized by $f_{\rm shield}$, as described by Draine and Bertoldi [1996]:

$$f_{\rm shield} = \begin{cases} 1 & (N_{\rm H_2} < 10^{14}\,\mathrm{cm^{-2}}) \\ (N_{\rm H_2}/10^{14}\,\mathrm{cm^{-2}})^{-0.75} & (N_{\rm H_2} \geq 10^{14}\,\mathrm{cm^{-2}}) \end{cases} \tag{3.12}$$

During the process of H_2 photodissociation, $0.4\,\mathrm{eV}$ is deposited in the gas and consequently contributes to the heating.

The remaining 90% of the excited H_2 molecules go through de-excitation and return to the vibrationally excited ground state labeled $H_2{}^*$. The rate of this process is given by:

$$R_d = 3.06 \times 10^{-10} \beta G_0 e^{-2.5 A_{\rm v}}\,\mathrm{s^{-1}}. \tag{3.13}$$

There are four possible pathways for $H_2{}^*$ de-excitation: collision with H I, collision with H_2, direct photodissociation by FUV photons, and spontaneous decay. The reaction rates for collisions with H I and H_2 are given by Tielens and Hollenbach [1985] as

$$\begin{aligned} k_{\rm de}({\rm H}) &\simeq 1.8 \times 10^{-13}\ \mathrm{cm^3\,s^{-1}} \times \left(\frac{T_{\rm gas}}{\rm K}\right)^{1/2} \exp\left(-\frac{1000\,\mathrm{K}}{T_{\rm gas}}\right) \\ k_{\rm de}({\rm H_2}) &\simeq 2.3 \times 10^{-13}\ \mathrm{cm^3\,s^{-1}} \times \left(\frac{T_{e\rm gas}}{\rm K}\right)^{1/2} \exp\left(-\frac{1800\,\mathrm{K}}{(T_{\rm gas} + 1200\,\mathrm{K})}\right). \end{aligned} \tag{3.14}$$

These collisional processes transfer energy amounts of $2.6\,\mathrm{eV}$ to the ambient gas. The heating rate from collisions is expressed as:

$$\Gamma = [n({\rm H}) k_{\rm de}({\rm H}) + n({\rm H_2}) k_{\rm de}({\rm H_2})] n({\rm H_2^*}) \times 4.17 \times 10^{-12}\,\mathrm{erg\,cm^{-3}\,s^{-1}}. \tag{3.15}$$

$H_2{}^*$ molecules also photodissociate into two H I atoms by FUV photons. The dissociation rate is given by

$$R = 10^{-11} \beta G_0 e^{-2.5 A_{\rm v}}\,\mathrm{s^{-1}}. \tag{3.16}$$

This dissociation process deposits $0.4\,\mathrm{eV}$ in the gas.

Finally, $H_2{}^*$ can undergo spontaneous decay, returning to the ground state. This process occurs at a rate of

$$A = 2.0 \times 10^{-7}\,\mathrm{s^{-1}}. \tag{3.17}$$

Although spontaneous decay emits energy, this radiation escapes the system and does not contribute significantly to gas heating.

We incorporate several cooling processes into the calculations; dust-gas collisional cooling [Yorke and Welz, 1996], fine-structure line cooling of C II and O I [Hollenbach and McKee, 1989, Osterbrock, 1989, Santoro and Shull, 2006], molecular line cooling of H_2 and

Stellar mass (M_*)	$1\,\mathrm{M}_\odot$
Disk mass (M_{disk})	$0.03\,\mathrm{M}_\odot$
Metallicity (Z_*)	$\mathrm{Z}_\odot$
Dust-to-gas mass ratio	10^{-6}, 10^{-5}, 10^{-4}, 10^{-3}, 10^{-2}, 10^{-1}
FUV luminosity	$10^{31.7}\,\mathrm{erg\,s^{-1}}$
EUV luminosity	$10^{40.7}\,\mathrm{s^{-1}}$
X-ray luminosity	$10^{30.4}\,\mathrm{erg\,s^{-1}}$

► **Table. 3.1** The stellar parameters used in the simulation. FUV and X-ray luminosities are given in the unit of energy luminosity and EUV luminosity is given in the unit of photon flux.

CO [Galli and Palla, 1998, Omukai et al., 2010], hydrogen Lyman α line cooling [Anninos et al., 1997], and radiative recombination cooling [Spitzer, 1978]. LTE level populations are assumed for C II and O I line cooling.

3.2.3 Simulation Setup

We perform a series of photoevaporation simulations varying the dust-to-gas mass ratio, $\mathcal{D}$, in the range of 10^{-6}–10^{-1}. In all cases, we assume a stellar mass of $M_* = 1\,\mathrm{M}_\odot$ and a gas-phase metallicity of $Z = Z_\odot$. The initial disk mass is set to 3% of the stellar mass, a typical value around a T Tauri star at $1\,\mathrm{Myr}$.

The initial density profile is given by

$$\Sigma(r) = 27.1\,\mathrm{g\,cm^{-2}} \times (r/r_{\mathrm{g}})^{-1}. \tag{3.18}$$

Although the minimum solar system model suggests $\Sigma \propto r^{-1.5}$, we adopt a more gradual distribution. As proposed by Clarke et al. [2001], photoevaporation becomes dominant in the later stages of disk dispersal, while accretion primarily governs mass loss in the earlier stages. In self-consistent accretion models, the surface density profile naturally evolves toward $\Sigma \propto r^{-1}$ after approximately 1 million years. Therefore, we adopt $\Sigma \propto r^{-1}$ as the initial surface density profile.

The initial temperature profile is defined as

$$T_{\mathrm{gas}} = 100\,\mathrm{K} \times (r/0.1r_{\mathrm{g}})^{-1/2}. \tag{3.19}$$

The gas temperature is updated at each timestep, accounting for heating and cooling processes through non-equilibrium thermochemical reactions.

The luminosity of each FUV, EUV, and X-ray radiation and stellar parameters are listed in Table 3.1.

We perform simulations for 8400 years, which is equivalent to ten times the Keplerian orbital period at the gravitational radius. We confirm that the system reaches a quasi-static state during this period, allowing us to analyze the steadily evaporating disk.

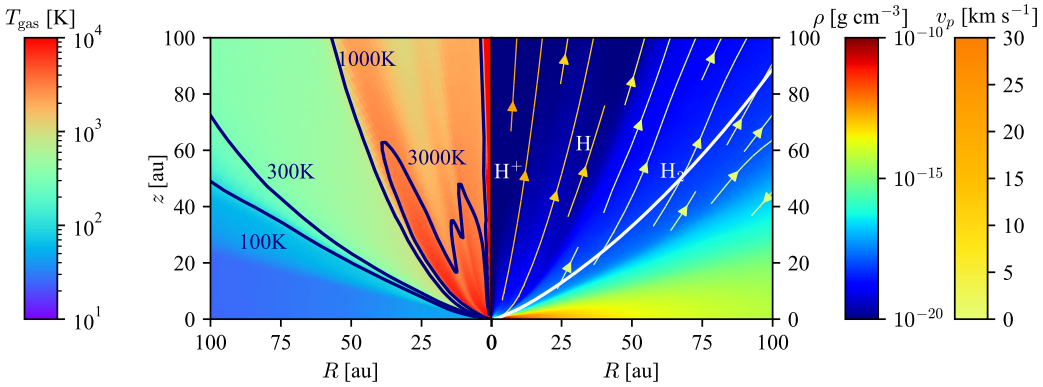

► **Figure. 3.1**

The time-averaged snapshot of the simulation with $\mathcal{D} = 10^{-2}$. The average is taken from 840 to 8400 years. The color map of the left-hand side shows the gas temperature structure, $T_{\rm gas}$. The color variation from purple to red corresponds to the temperature from 10 to 10^4 K. The gas is heated to more than 1000 K in the high-latitude region. The contour lines represent the location with temperatures of 100, 300, 1000, and 3000 K. The color map on the right-hand side shows the gas density structure, ρ. The color variation from black to red corresponds to the density from 10^{-20} to $10^{-10}\,{\rm g\,cm^{-3}}$. The white line represents the base of the photoevaporative gas flows, which is set to the location which corresponds to $N_{\rm H_2} = 10^{20}\,{\rm cm^{-2}}$. The streamlines represent the poloidal velocity of the gas, $v_{\rm p} = \sqrt{v_r^2 + v_\theta^2}$. The color of the streamlines shows the velocity ranging from 0 to 30 $\rm km\,s^{-1}$. The streamline with a velocity lower than $0.1\,{\rm km\,s^{-1}}$ is omitted for clarity. The streamlines originate from the disk surface and extend to the outer region. The primary gas component varies from H^+ to H_2 as the latitude decreases.

The computational domain is set to $[0.1r_{\rm g}, 20r_{\rm g}]$, corresponding to a radial range of $[0.9\,{\rm au}, 176\,{\rm au}]$. This domain captures both the inner and the outer regions of the disk.

3.3 Results

We present the simulation results with various dust-to-gas mass ratios to understand how the photoevaporation process changes in a dust-deficient environment. First, we discuss the results of the fiducial case with $\mathcal{D} = 10^{-2}$. Later, we show the results of photoevaporation simulations with a lower dust-to-gas mass ratio.

3.3.1 Mass-Loss Rate from Photoevaporation

Figure 3.1 shows the time-averaged gas distribution and the temperature structure of the evaporating disk. The average is taken from 840 to 8400 years. We do not include the first

840 years because the abrupt initiation of the calculation causes fluctuations in temperature and gas density. The HII region is formed near the star and at a high latitude. In that region, EUV photons are the primary heating source via hydrogen ionization. The temperature reaches $\sim 3000\,\mathrm{K}$ by the balance between EUV heating and adiabatic cooling.

The photodissociation region (PDR) is formed next to the HII region. The dominant heating process in this region is the photoelectric effect on the dust grains and H_2 pumping. Gas heating by H_2 pumping is especially effective on the photodissociation front, where the transition from the molecular to the atomic state occurs.

The molecular region lies next to the PDR with a higher polar angle. The gas velocity profile shows that the base of the photoevaporative flows is located in this molecular region. The position of the base corresponds to the place where the column density of the hydrogen molecule reaches $N_{\mathrm{H_2}} = 10^{20}\,\mathrm{cm}^{-2}$. The temperature is $\sim 300\,\mathrm{K}$ at the base, and determined by the balance between photoelectric effect by FUV photons and molecular line cooling of H_2. The dominant heating process is the photoelectric effect of dust grains by FUV radiation. O I cooling also contributes to gas cooling in the lower polar angle side.

We calculate the mass-loss rate due to photoevaporation by counting the amount of mass going through a spherical surface set at $r = 100\,\mathrm{au}$, given by

$$\dot{M}_{\mathrm{pe}} = \int_{S,\eta>0} \rho \mathbf{v} \cdot \mathrm{d}\mathbf{S}, \tag{3.20}$$

where $\mathrm{d}\mathbf{S}$ denotes a unit area at $r = 100\,\mathrm{au}$. The boundary is set at $r = 100\,\mathrm{au}$ to avoid reflection at the edge of the calculation domain. In the equation, η expresses the Bernoulli function, given by

$$\eta = \frac{1}{2}v_p^2 + \frac{1}{2}v_\phi^2 + \frac{\gamma}{\gamma-1}c_{\mathrm{s}}^2 - \frac{GM_*}{r}, \tag{3.21}$$

where γ denotes the specific heat ratio, which is set to 1.0 in our calculation. The poloidal velocity, $v_p = \sqrt{v_r^2 + v_\theta^2}$, is used in the equation. The gas with $\eta > 0$ is only counted as the gas leaving the system because it has sufficient energy to escape the gravitational potential of the central star. Setting this condition enables the exclusion of the gas with a subsonic velocity that does not leave the system.

The mass-loss rate is calculated over time. The time-averaged mass-loss rate is

$$\dot{M} = 2.7 \times 10^{-9}\,\mathrm{M}_\odot\,\mathrm{yr}^{-1}. \tag{3.22}$$

The mass-loss rate fluctuates greatly during the calculation, ranging from -13% to $+10\%$ compared to the average value. The fluctuation is caused by reflection at the outer boundary of the computational domain.

The mass-loss rate is consistent with the previous calculations by Komaki et al. [2021], which did not include H_2 pumping in the calculation. The comparison suggests that the heating and cooling process at the base is essential and that the temperature structure above the disk has a limited impact on the overall mass-loss rate by photoevaporation. The comparison suggests that the mass-loss rate is primarily determined by dynamical

structure at the base while the whole disk temperature structure is determined by local thermo-chemical reactions.

3.3.2 Photoevaporation in Dust-Deficient Disks

The photoelectric effect of dust grains caused by FUV radiation contributes to gas heating and plays a crucial role in launching photoevaporative flows. The efficiency of this heating process depends mainly on the dust-to-gas mass ratio, $\mathcal{D}$, and the incident FUV flux. We have already investigated the dependence of photoevaporation on FUV luminosity [Komaki, 2022]. In this section, we focus on the impact of the dust-to-gas mass ratio, $\mathcal{D}$.

Dust grains evolve differently from the gas component; in principle, $\mathcal{D}$ also changes over time and by place. We perform a series of photoevaporation simulations varying the dust-to-gas mass ratio in the wide range of 10^{-6}–10^{-1} to assess the impact of reduced $\mathcal{D}$ on photoevaporation. For simplicity, we assume that a disk has a constant value of $\mathcal{D}$ throughout the disk. We discuss the impact of local dust evolution on photoevaporation and the overall disk dispersal in Chapter 5.

The heating rate of the photoelectric effect increases proportionally with $\mathcal{D}$, as expected from its definition (see Eq. 3.9). As $\mathcal{D}$ decreases, the heating rate of the photoelectric effect reduces, while those from H_2 pumping and X-ray photons remain unchanged. In the case of $\mathcal{D} = 10^{-3}$, the heating rates of the photoelectric effect, H_2 pumping, and X-ray photons become comparable. H_2 pumping is the primary heating process among these three in the inner region of $r \leq 5\,\mathrm{au}$. X-ray photons become the dominant heating source in the outer region, where $H_2{}^*$ deposits energy via spontaneous de-excitation and does not contribute to gas heating.

O I cooling remains to be the dominant cooling mechanism at the base in the cases with low dust-to-gas ratios because the gas-phase metallicity is unchanged while the dust-to-gas mass ratio decreases.

Figure 3.2 shows the density and temperature structure of an evaporating disk in the case of $\mathcal{D} = 10^{-4}$. In the case of $\mathcal{D} \leq 10^{-4}$, the photoelectric effect of the dust grains is ineffective because of the low abundance of the dust grains. Instead, H_2 pumping and X-ray heating are the dominant processes at the base. The heating by H_2 pumping is efficient because of collisional de-excitation in the inner region, and X-ray photons are the dominant heating source in the outer region. The temperature is lower by a factor of 2 compared to the fiducial case in the molecular region, where photoelectric heating is efficient. Consequently, the gas in the whole molecular region shows $\eta \leq 0$, which means that the gas does not have sufficient energy to leave the system and shows $\eta \leq 0$. The low temperature also leads to a low gas scale height in dust-deficient cases, and the gas is concentrated on the disk midplane. The change in temperature structure alters the dynamics of photoevaporative flows. The streamlines of photoevaporative flows mainly originate from the inner region.

The position of the base is located to the place that corresponds to $N_{\mathrm{H_2}} = 10^{19}\,\mathrm{cm}^{-2}$, which is one magnitude lower than the fiducial value because the gas is concentrated on the disk midplane, and the gas density is low in the upper region.

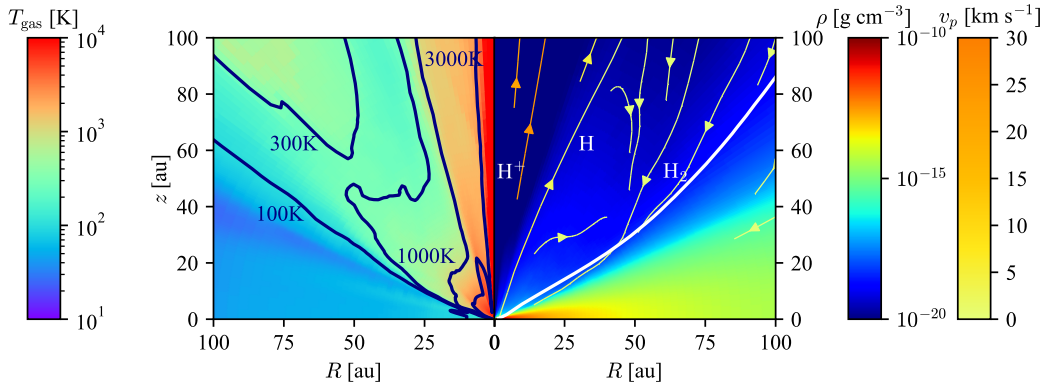

► **Figure. 3.2**

The time-averaged snapshot of the simulation with $\mathcal{D} = 10^{-4}$. This figure is interpreted the same as Figure 3.1. The average is taken from 840 to 8400 years. The left panel shows the gas temperature structure, $T_{\rm gas}$. The color variation from purple to red corresponds to the temperature from 10 to 10^4 K. The right panel shows the gas density structure and the poloidal velocity. The color variation from black to red corresponds to the density from 10^{-20} to $10^{-10}\,{\rm g\,cm^{-3}}$. The white line represents the base of the photoevaporative gas flows, which is set to the location which corresponds to $N_{\rm H_2} = 10^{19}\,{\rm cm^{-2}}$. The color of the streamlines shows the velocity ranging from 0 to $30\,{\rm km\,s^{-1}}$. The streamlines mainly originate from the innermost region. Some streamlines com back to the disk because they do not have sufficient energy to leave the system. This explanation is supported by the fact that the region with $\eta < 0$ is more extended. The dissociation front is positioned on the disk surface in the inner region with $r < 10 r_{\rm g}$, so no distinct heated region appears in the upper layer, unlike the case with $\mathcal{D} = 10^{-2}$.

In the case of $\mathcal{D} = 10^{-1}$, the heating rate of the photoelectric effect is enhanced. This results in a more flared disk geometry, with higher temperatures and an optically thick upper layer. The distribution of the velocity streamlines shows that the base of the photoevaporative flows is located at $N_{\rm H_2} = 10^{19}\,{\rm cm}^{-2}$.

Figure 3.3 shows the time-averaged mass-loss rates. The mass-loss rate becomes the highest at $\mathcal{D} = 10^{-2}$. The mass-loss rate in the range of $10^{-3} \leq \mathcal{D} \leq 10^{-1}$ is fitted by a function of dust-to-gas mass ratio as

$$\dot{M}_{\rm pe} = 6.4 \times 10^{-0.23(\log_{10}\mathcal{D})^2 - 0.73(\log_{10}\mathcal{D}) - 10}\,{\rm M}_\odot\,{\rm yr}^{-1}. \tag{3.23}$$

The fit enables us to assess the mass-loss rate of disks with various $\mathcal{D}$. The mass-loss rates for lower dust-to-gas mass ratios are excluded from the data used to derive the fit. We aim to understand the relation between photoelectric heating and the dust-to-gas mass ratio. Data from dust-deficient disks are omitted because the photoelectric effect does not heat the gas in those cases. The mass-loss rate decreases in the case of $\mathcal{D} = 10^{-1}$ because the gas density at the base is lower than in the fiducial case. The mass-loss rate also decreases with the decreasing dust-to-gas mass ratio in the range of $10^{-5} \leq \mathcal{D} \leq 10^{-3}$. Especially in the case of $\mathcal{D} = 10^{-4}, 10^{-5}$, the whole molecular region, including the outer boundary, is $\eta \leq 0$, which indicates that the gas does not have sufficient energy to leave the system. The gas rarely has a sonic velocity, resulting in spurious gas reflection at the outer boundary.

The shaded region in Figure 3.3 the time variation in the mass-loss rate over time. In the case of $\mathcal{D} = 10^{-6}$, the outer region of the base has $\eta > 0$. This is because the gas is concentrated on the midplane and has higher v_θ because of the pressure gradient at the base. As a result, the mass-loss rate shows less time variation and is higher than in the cases of $\mathcal{D} = 10^{-4}$ and $\mathcal{D} = 10^{-5}$.

Since the heating process of H_2 pumping and X-ray photons do not depend on the abundance of dust grains, the heating process and the resulting mass-loss rate are expected to remain unchanged toward even more dust-deficient cases. The extremely dust-deficient case like $\mathcal{D} = 10^{-6}$ is regarded as a disk dispersal in the early universe with zero metallicity. The most significant difference is the gas-phase metallicity, which contributes to cooling in the molecular region. Since the heating rate does not change, photoevaporation and the resulting mass-loss rate can be approximated by the results of the $\mathcal{D} = 10^{-6}$ case.

The main difference between our dust-deficient case and low-metallicity case conducted by Nakatani et al. [2018b] is the treatment of gas-phase metals. Nakatani et al. [2018b] assume that the amount of gas-phase metals decreases proportionally with the reduction in dust grains, whereas we assume that the gas-phase metal content remains constant even as the dust-to-gas mass ratio in the disk changes. Our calculations show that O I line cooling remains effective on the surfaces of dust-deficient disks, indicating that the temperature structure is strongly influenced by the gas-phase metallicity. This effective cooling prevents the mass-loss rate from increasing in cases with a dust-to-gas mass ratio reduced by a factor of 10, in contrast to simulation with $Z = 0.1\,{\rm Z}_\odot$, which results in a higher mass-loss rate compared to the fiducial case.

Recent spectral observations indicate that the gas-phase metallicity measured by CO is

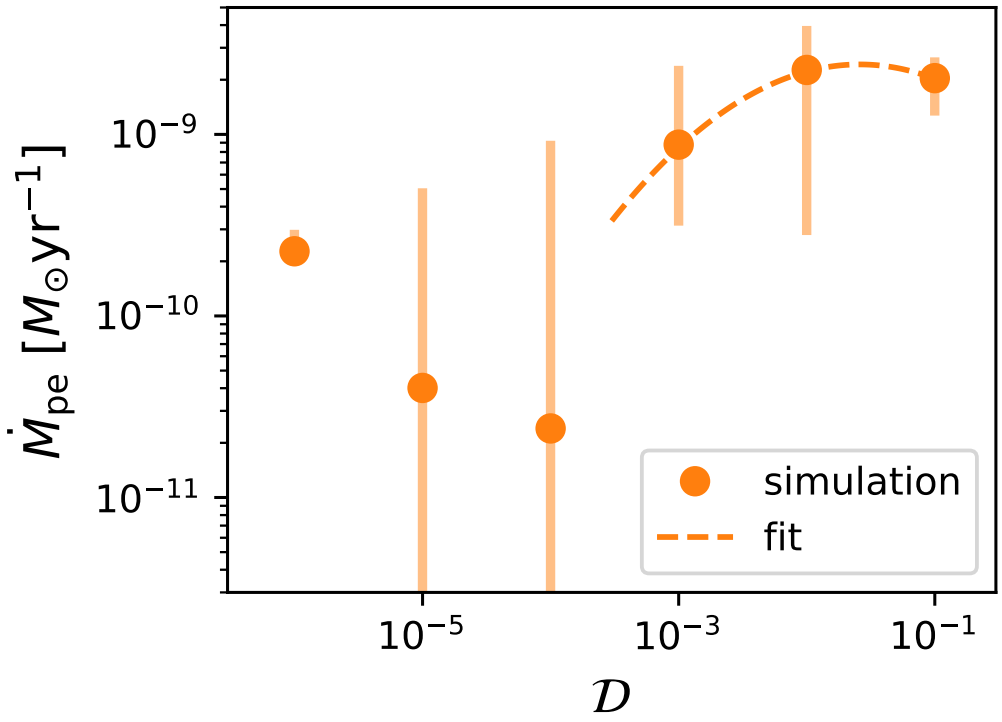

► **Figure. 3.3**

The time-averaged mass-loss rate with each dust-to-gas mass ratio. The plots represent the mass-loss rate calculated based on the simulations. We calculate the mass-loss rate as the amount of gas going out of a spherical surface set at $r = 100\,{\rm au}$. The shaded region represents the range of time variation. The variations in the cases of $\mathcal{D} = 10^{-4}, 10^{-5}$ are relatively large because of the spurious reflection at the outer edge of the computational domain. The dotted line shows the fit for the mass-loss rates in the range of $10^{-3} \leq \mathcal{D} \leq 10^{-1}$, where the photoelectric effect is the most dominant heating process.

often low, sometimes only 1–10% of the ISM value [Kama et al., 2016b, Miotello et al., 2017]. The mechanism behind this reduced gas-phase metallicity remains unclear. Possible explanations include rapid gas dispersal, condensation onto dust grains, or the formation of complex molecules. Wölfer et al. [2019] conducted hydrodynamic simulations of photoevaporation by varying the gas-phase carbon abundance to explore its impact under different conditions. Their simulations incorporated EUV and X-ray photons as high-energy radiation from the central star. Since atomic carbon contributes to X-ray attenuation, a lower carbon abundance results in more efficient heating by X-ray photons. This study highlighted the role of reduced gas-phase metals in enhancing X-ray photoevaporation. In our calculations, FUV photons are the primary heating source for the disk gas, and thus it is crucial to examine their effect on photoevaporation. CO is dissociated into two atoms when exposed to FUV radiation. Consequently, a small amount of carbon and oxygen in gas-phase is expected to increase the FUV flux at the disk surface, potentially leading to a higher photoevaporation rate. Our results provide a lower limit for mass-loss rates driven by photoevaporation.

3.3.3 Surface Mass-Loss Rates with Varying Dust-to-Gas Ratios

The photoevaporation rate is calculated by setting a spherical boundary at a specific radius of $r = 100\,\mathrm{au}$. This allows us to determine the total mass lost from the system. The surface mass-loss rate is more informative than the total mass-loss rate to understand the spatial variation of the photoevaporation process.

We derive the surface mass-loss rate in the same manner from previous works [Owen et al., 2010, Picogna et al., 2021]. There are several steps to follow to derive the surface mass-loss profile. First, the cumulative mass-loss rate is calculated by varying the outer boundary radius of the spherical domain. For instance, the cumulative mass-loss rate at $r = 100\,\mathrm{au}$, as discussed in the previous section, represents the mass lost due to photoevaporation within this radius. Since the mass-loss rate depends on the boundary radius, it can be expressed as a function of the radius. The cumulative mass-loss rate is given by:

$$\dot{M}_{\mathrm{cum}}(r) = \int_{r_{\mathrm{in}}}^{r} \dot{M}_{\mathrm{pe}}(r')\mathrm{d}r'. \tag{3.24}$$

The surface mass-loss rate is calculated by taking the gradient of the cumulative mass-loss rate and dividing it by the area of the ring at each radial position, given by

$$\dot{\Sigma}_{\mathrm{pe}} = \left| -\frac{1}{2\pi r}\frac{\mathrm{d}}{\mathrm{d}r}\dot{M}_{\mathrm{cum}} \right|. \tag{3.25}$$

To ensure the robustness of our method, we integrate the surface mass-loss rate across the entire disk to reconstruct the total mass-loss rate. We confirm that the derived value differs by no more than 10%. This demonstrates that the surface mass-loss rate obtained through this method successfully represents the distribution of mass-loss due to photoevaporation.

Figure 3.4 shows the surface mass-loss rates for cases with $\mathcal{D} = 10^{-2}$, 10^{-4}, and 10^{-6}.

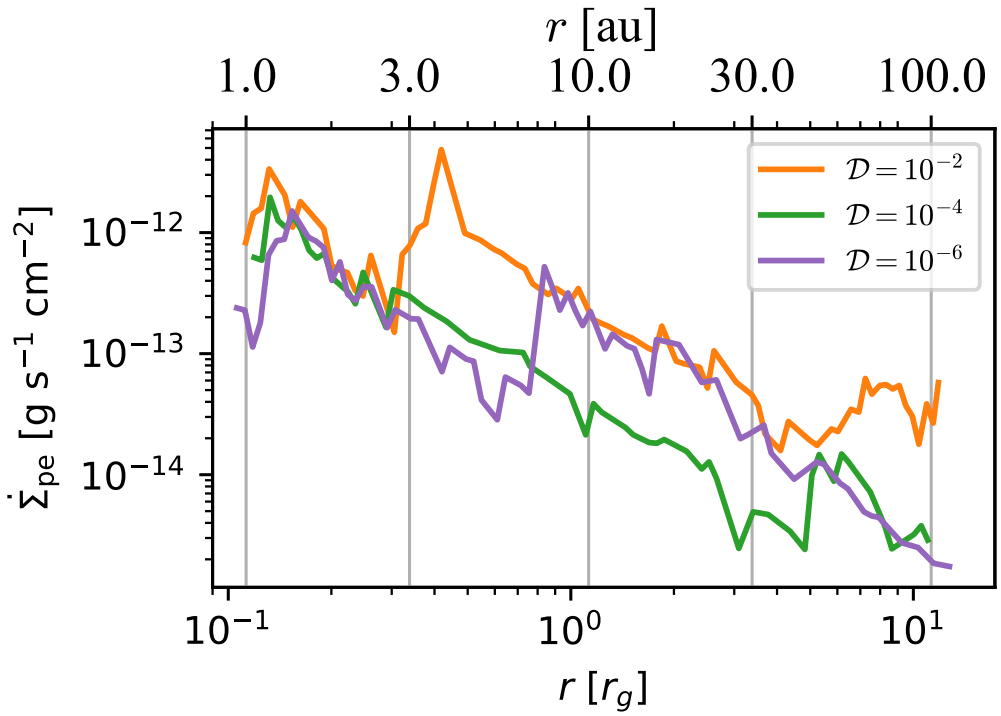

► **Figure. 3.4**

The surface mass-loss rate in the cases of $\mathcal{D} = 10^{-2}, 10^{-4}, 10^{-6}$ calculated based on the photoevaporation simulations. The line color corresponds to $\mathcal{D} = 10^{-2}$ (orange), $\mathcal{D} = 10^{-4}$ (green), and $\mathcal{D} = 10^{-6}$ (purple). In all the cases, a peak is observed at the innermost part. This peak corresponds to the launching point of EUV-driven photoevaporative flows. In the case of $\mathcal{D} = 10^{-2}$, a peak at $\sim 6r_{\rm g}$ corresponds to the launching point of FUV-driven photoevaporative flows. In this scenario, the surface mass-loss rate sustains over $10^{-14}\,{\rm g\,cm^{-2}}$ in the outer region and contributes to the high mass-loss rate. In contrast, the surface mass-loss rate decreases toward the outer region in dust-deficient cases.

All cases show a peak in the innermost region, corresponding to the launching point of EUV-driven photoevaporative flows. In dust-deficient cases, the surface mass-loss rate decreases with distance from the central star, following $r^{-1.5}$, which is steeper than the initial surface density distribution of $\Sigma \propto r^{-1}$. This steep decline indicates that the mass loss is concentrated in the inner region.

A second peak in the surface mass-loss rate is observed for $\mathcal{D} = 10^{-4}$ at $r = 6r_{\rm g}$. Within this radius, the gas in the molecular region has $\eta < 0$, preventing the gas from escaping the system and leading to a low surface mass-loss rate.

In the extreme case of $\mathcal{D} = 10^{-6}$, the second peak appears at $r = 0.8r_{\rm g}$. To explore in more detail which heating process contributes to launching photoevaporation in dust-deficient cases, additional simulations are conducted. First, a simulation excluding FUV and X-ray photons shows a mass-loss rate of $5.5 \times 10^{-11}\,{\rm M}_\odot\,{\rm yr}^{-1}$, 25% lower than the fiducial case. This result highlights the limited contribution of EUV photons because they are absorbed near the star.

We perform a series of simulations varying the X-ray luminosity by 0.01, 0.1, and 10 times the fiducial luminosity, $L_{\rm X,f}$. Reducing X-ray luminosity does not significantly alter the mass-loss rate, which remained at $\sim 6 \times 10^{-10}\,{\rm M}_\odot\,{\rm yr}^{-1}$. In this scenario, H_2 pumping dominated heating throughout the base. When X-ray luminosity is increased by a factor of 10, the mass-loss rate increases by a factor of 2.6. The increase in the mass-loss rate suggests that H_2 pumping and X-ray heating together drive photoevaporation, with the balance between FUV and X-ray luminosities playing a critical role.

In the fiducial case, the surface mass-loss rate is almost constant at $\sim 3 \times 10^{-14}\,{\rm g\,s^{-1}\,cm^{-2}}$ in the outer disk. This efficient mass-loss in the outer region is primarily attributed to FUV-driven photoelectric heating. A secondary peak at $\sim 0.5r_{\rm g}$ corresponds to the launching point of FUV-driven flows, consistent with the radius predicted analytically by Font et al. [2004]. Since the mass loss at each location is proportional to $\dot{\Sigma}_{\rm pe} \times 2\pi r^2$, the contribution of photoelectric heating in the outer region significantly affects the total mass loss rate.

Dust-deficient cases show notable differences in surface mass-loss rates. As the dust-to-gas mass ratio evolves with time and position as a result of processes such as dust growth, the impact of reduced small dust grains must be carefully considered, especially in the outer disk. These results underscore the importance of dust in shaping the photoevaporation process and its implications for disk dispersal. In Chapter 5, we quantitatively examine the impact of changes in dust size and spatial distributions on photoevaporation by conducting disk evolution simulations that consistently account for both gas and dust, utilizing the surface mass-loss rates derived in this section.

3.3.4 Impact of Spectral Energy Distribution on Photoevaporation

In our calculation, $H_2{}^*$ represents the vibrationally excited state of $v = 6$ within the ground electronic state. We assume that $H_2{}^*$ is primarily generated by de-excitation of the electronically excited state. However, this is not the only pathway to form H_2 in the vibrationally excited state.

H_2 can be directly excited into the vibrational states of the ground electronic state by radiation. While the excitation to electronic excited states requires sufficiently high-energy photons with $h\nu \geq 11.2\,\mathrm{eV}$, which are called Lyman-Werner photons, photons with lower energy excite H_2 directly into vibrationally excited states. The spectroscopic observations of T Tauri stars have shown that emission lines, such as Lyman α and CIV bring H_2 into vibrationally excited states [Herczeg et al., 2002, 2004, 2006, Yang et al., 2011]. As $H_2{}^*$ de-excites, it produces an emission that alters the spectral energy distribution.

Our simulation does not include the direct excitation of H_2 into vibrationally excited states. If this process were incorporated, the abundance of $H_2{}^*$ would likely increase, enhancing the associated heating due to H_2 pumping. In our results, the direct dissociation of $H_2{}^*$ by FUV photons is the primary de-excitation process near the base of photoevaporative flows, particularly in the inner region ($r \leq 7r_\mathrm{g}$), where H_2 pumping dominates the heating.

To assess the potential impact of enhanced $H_2{}^*$ dissociation, we conduct an additional photoevaporation simulation with a dissociation rate increased by a factor of 10 in the case of $\mathcal{D} = 10^{-3}$. The fiducial dissociation rate of $H_2{}^*$ is given by Eq. 3.16. X-ray heating remained the dominant heating mechanism in the outer region despite this increase, and the overall mass-loss rate showed no significant change. This result suggests that, while direct excitation of H_2 may increase the efficiency of H_2 pumping, it does not substantially alter the entire photoevaporation process.

We discuss the impact of the X-ray energy spectrum. The penetration depth and the amount of energy deposited in the gas depend on the energy of each X-ray photon. Ercolano et al. [2008] conducted simulations to examine how variations in the X-ray energy spectrum affect photoevaporation. Soft X-ray photons with $\leq 1\,\mathrm{keV}$ are more easily absorbed and contribute significantly to gas heating. In contrast, hard X-ray photons pass through the disk with little interaction with the gas.

Figure 3.5 shows the spectral energy distribution of the X-ray radiation used in our simulation. The X-ray spectrum in our model peaks around $\sim 1\,\mathrm{keV}$. Although our X-ray spectrum lacks photons with energy $\sim 0.1\,\mathrm{keV}$, the spectrum used by Ercolano et al. [2021] includes more than $10^5\,\mathrm{erg\,s^{-1}\,cm^{-2}\,sr^{-1}}$ at $\sim 0.1\,\mathrm{keV}$. Sellek et al. [2024] attributed this difference to the use of different observation telescopes, either ground-based or space-based. This discrepancy highlights the challenge of accurately determining the X-ray flux spectrum experienced by the disk gas.

Estimating the precise energy spectrum of X-rays reaching the disk is difficult because X-rays are absorbed by gas along the line of sight and by the atmosphere of the Earth. Furthermore, the spectrum emitted by the star is altered by absorption and re-emission before it reaches the disk gas. Our X-ray spectrum may underestimate the contribution of soft X-ray photons. This comparison underscores the importance of photoevaporation simulations that account for the evolution of the spectrum from the star to the disk.

High-energy X-ray photons are emitted during magnetic reconnection events on the stellar surface, known as X-ray flares. Washinoue et al. [2024] reconstructed the theoretical X-ray spectrum of a flare with a total energy of $\sim 10^{35}\,\mathrm{erg}$. These flares significantly

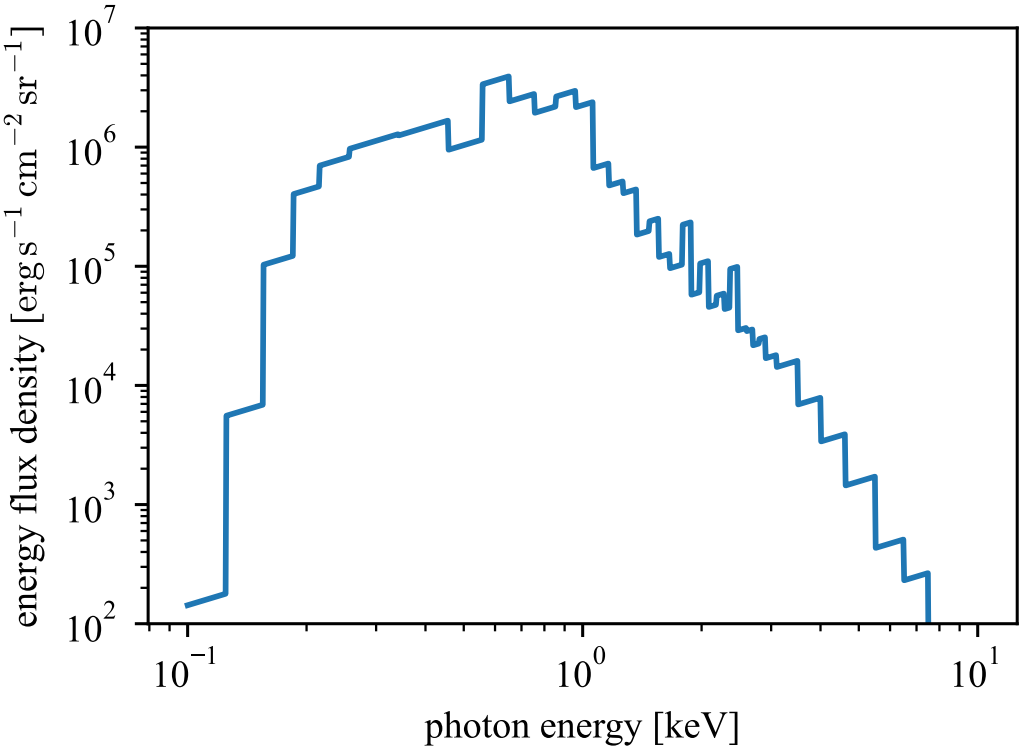

► **Figure. 3.5**

The spectral energy distribution of X-ray radiation we use in our simulation. The distribution is based on observational data for TW Hya provided by Nomura et al. [2007]. The peak is $\sim 1\,\mathrm{keV}$, but drops at the $0.1\,\mathrm{keV}$ end.

contribute to the X-ray flux in the $> 30\,\mathrm{keV}$ range. Considering that Ercolano et al. [2008] demonstrated that X-ray photoevaporation is primarily driven by soft X-ray radiation, X-ray flares are not expected to significantly contribute to mass-loss via photoevaporation. However, as shown by Washinoue et al. [2024], hard X-ray photons can alter the ionization profile above the disk.

3.4 Chapter Summary

Photoevaporation is critical in the dispersal process of a protoplanetary disk. This process is driven by the heating of disk gas by high-energy photons, such as EUV, FUV, and X-ray radiation emitted from the central star. The heated gas escapes from the gravitational potential and results in mass loss of disk material. Recent studies using radiation hydrodynamics simulations have provided a realistic understanding of the physical and chemical structure of evaporating disks.

Theoretical studies with radiation hydrodynamics highlight that FUV photons are the dominant heating source via the photoelectric effect on dust grains. The efficiency of photoevaporation depends on two critical parameters: FUV luminosity and the dust-to-gas mass ratio. Observations suggest that both properties evolve within the typical disk lifetime. We used two-dimensional radiation hydrodynamic simulations to explore the relationship between FUV luminosity and photoevaporation rates [Komaki, 2022]. Investigating the dependence on dust amount is essential to obtain the whole picture of photoevaporation.

We conducted radiation hydrodynamics simulations across a wide range of $\mathcal{D}$ values (10^{-6}–10^{-1}) to investigate photoevaporation during the later stages of disk evolution when small dust grains are depleted. The dominant heating process changes because the photoelectric effect of dust grains is not efficient in dust-deficient cases with $\mathcal{D} < 10^{-3}$. In such cases, H_2 pumping and X-ray heating contribute dominantly to gas heating and drive photoevaporative flows.

This change also leads to notable differences in disk morphology. Dust-deficient disks are less effectively heated than the disk with $\mathcal{D} = 10^{-2}$. As a result, the disk has a vertically thin compressed gas structure in the case of $\mathcal{D} = 10^{-6}$. By deriving the surface mass-loss rate, we analyzed the spatial distribution of disk mass loss. In case with $\mathcal{D} = 10^{-2}$, mass-loss rate is highest, driven by efficient photoelectric heating and significant mass loss from the outer region.

Photoevaporation simulations with a wide range of $\mathcal{D}$ clarifies the dependence of photoevaporation on dust abundance, highlighting the role of small dust grains in disk evolution. We also suggest that the result of the extremely low $\mathcal{D}$ case with $\mathcal{D} \leq 10^{-6}$ offers insight into disk dispersal in zero-metallicity environments.

4

Long-Term Evolution of Protoplanetary Disks

Figures

4.1 Overview of Disk Dispersal Processes

Infrared observations have shown that a protoplanetary disk disperses within several million years. Since a protoplanetary disk is the birthplace of planets, disk evolution is an essential process that determines when and where planets form.

Theoretical research has proposed some disk dispersal processes: accretion, magnetohydrodynamic (MHD) winds, and photoevaporation. Previous researches have focused more on understanding the individual process and its impact on disk dispersal. However, these processes work in combination in the context of actual disk dispersal. Therefore, a calculation that incorporates all these processes at the same time is necessary. We perform a one-dimensional long-term disk evolution simulation, including accretion, MHD winds, photoevaporation, and stellar evolution. In this chapter, we discuss which process dominates mass loss and how the density distribution changes over time.

4.2 Methods

We conduct one-dimensional long-term disk evolution simulations incorporating accretion, magnetohydrodynamic (MHD) winds, photoevaporation, and stellar evolution. Recent observations suggest that class 0 and class I disks contain enough solid mass to form the observed exoplanets [Tychoniec et al., 2020]. Dust coagulation has been confirmed to start during the class 0 stage. These findings indicate that planet formation begins in the early stages of disk evolution. To explore this, we model disk evolution from its initial phase to the end of disk dispersal. This approach helps us to understand the realistic progression of disks.

Our simulations explore a wide range of stellar masses, spanning from $0.1\,\mathrm{M}_\odot$ to $7\,\mathrm{M}_\odot$, to understand the diversity of disk evolution related to stellar mass. We assume that the disk exhibits axisymmetry around the z-axis and employed cylindrical coordinates (r, z) for the calculations. We solve the equation about the evolution of the surface density, Σ.

The following sections provide further details about the calculation setup, initial conditions, and numerical methods.

4.2.1 Governing Equations

We solve the evolution of gas surface density, Σ, over time using the following governing equation:

$$\frac{\partial \Sigma}{\partial t} + \frac{1}{r}\frac{\partial}{\partial r}\left(r\Sigma v_r\right) + \dot{\Sigma}_{\mathrm{w}} + \dot{\Sigma}_{\mathrm{pe}} = 0, \tag{4.1}$$

where $\dot{\Sigma}_{\mathrm{w}}$ and $\dot{\Sigma}_{\mathrm{pe}}$ denote the surface mass-loss rates due to magnetohydrodynamic (MHD) winds and photoevaporation, respectively. The derivations of these surface mass-loss rates are presented in Chapter 4.2.2 and Chapter 4.2.4. In this equation, v_r represents the radial velocity of the gas.

Radial velocity, v_r, is determined by viscous accretion and loss of angular momentum caused by MHD winds. It is expressed as:

$$r\Sigma v_r = -\frac{2}{r\Omega_{\mathrm{K}}}\left[\frac{\partial}{\partial r}\left(r^2\Sigma\overline{\alpha_{r\phi}}c_{\mathrm{s}}^2\right) + r^2\overline{\alpha_{\phi z}}\left(\rho c_{\mathrm{s}}^2\right)_{\mathrm{mid}}\right], \tag{4.2}$$

where Ω_{K} is the Keplerian angular velocity, and c_{s} is the sound speed. The derivation of this equation is given in Appendix C.

In the equation, $\left(\rho c_{\mathrm{s}}^2\right)_{\mathrm{mid}}$, represents the value at the middle of the plane of the gas pressure. It is rewritten under the assumption of hydrostatic equilibrium along the z-axis with the disk scale height H as:

$$\left(\rho c_{\mathrm{s}}^2\right)_{\mathrm{mid}} = \frac{\Sigma\Omega_{\mathrm{K}}}{\sqrt{2\pi}}. \tag{4.3}$$

In the equation, $\overline{\alpha_{r\phi}}$ and $\overline{\alpha_{\phi z}}$ are the mass-averaged viscous parameter and the wind torque, respectively. The calculation of $\overline{\alpha_{\phi z}}$, which quantifies the angular momentum transport by MHD winds will be detailed in the next section.

The viscous parameter, $\overline{\alpha_{r\phi}}$, is estimated based on accretion rates obtained by observations. Observations toward star-forming regions indicate that accretion rates increase with stellar mass [Muzerolle et al., 2003, Calvet et al., 2004, Muzerolle et al., 2005, Hartmann et al., 2006]. The relation is approximately fitted by

$$\dot{M}_{\mathrm{acc}} \propto M_*^2 \tag{4.4}$$

Setting $\overline{\alpha_{r\phi}} \propto M_*$ reproduces the observed relation. Observations of accreting disks reveal that accretion rates vary significantly by a factor of 10^2 within stars of the same stellar masses, and the resulting viscous parameter varies in the range of 10^{-4}–10^{-2}.

4.2.2 Magnetohydrodynamic (MHD) Winds

The equation of disk evolution is derived from the Euler equation with magnetic fields. The mass-loss profile of MHD winds is given by

$$\dot{\Sigma}_{\rm w} = C_{\rm w}(\rho c_{\rm s})_{\rm mid}, \tag{4.5}$$

where $C_{\rm w}$ represents the dimensionless mass-loss rate by MHD winds and is derived in Appendix C. There are two models to describe $C_{\rm w}$: 'strong wind case' and 'weak wind case.' In the strong wind case, all the energy liberated by accretion is transferred to drive MHD winds. In weak wind cases, part of the energy released by gravitational accretion and viscous heating drives the MHD winds, while the rest is radiated from the disk. In this model, we define $\epsilon_{\rm rad}$ as the ratio used for radiation. We employ the weak wind case for our fiducial model because it aligns closer with observations in previous research Weder et al. [2023]. In this case, $C_{\rm w}$ and $F_{\rm rad}$, the energy lost by radiation are given by

$$C_{\rm w} = (1-\epsilon_{\rm rad})\left[\frac{2}{r\Omega_{\rm K}}\overline{\alpha_{\phi z}}c_{\rm s} + 3\sqrt{2\pi}\frac{\overline{\alpha_{r\phi}}c_{\rm s}^2}{r^2\Omega_{\rm K}^2}\right]$$
$$F_{\rm rad} = \epsilon_{\rm rad}\left[\frac{1}{\sqrt{2\pi}}r\Omega_{\rm K}^2\Sigma\overline{\alpha_{\phi z}}c_{\rm s} + \frac{3}{2}\Sigma\Omega_{\rm K}\overline{\alpha_{r\phi}}c_{\rm s}^2\right].$$

Both in accretion and MHD winds, $\overline{\alpha_{R\phi}}$ is an important parameter to determine the mass-loss rates in both processes. Bai and Stone [2013a] conducted MHD simulations and the local $\overline{\alpha_{R\phi}}$ is approximated as

$$\overline{\alpha_{\phi z}} = \overline{\alpha_{\phi z,{\rm ini}}}\left(\frac{\Sigma}{\Sigma_{\rm ini}}\right)^{-0.66}, \tag{4.6}$$

where $\overline{\alpha_{\phi z,{\rm ini}}}$ and $\Sigma_{\rm ini}$ represent the wind torque and surface density at the initial state. In this scenario, the vertical magnetic flux is assumed to be constant throughout the evolution. It is unlikely that magnetic fields remain unchanged as the gas disperses. Some magnetic fields leave the disk along with the gas. To account for this, we set an upper limit for $\overline{\alpha_{\phi z}}$ at 1. The initial wind torque is set to $\overline{\alpha_{\phi z,{\rm ini}}} = 10^{-5}$ based on Bai and Stone [2013a].

4.2.3 Temperature

The gas temperature, $T_{\rm gas}$, is a crucial factor that determines the overall evolution of the protoplanetary disk. In our calculations, we simultaneously solve for the vertically averaged gas temperature and the surface density, Σ. The total gas temperature is expressed as a combination of two primary heating mechanisms: stellar irradiation and viscous heating. The relationship is given by:

$$T_{\rm gas}^4 = T_{\rm irr}^4 + T_{\rm vis}^4, \tag{4.7}$$

where $T_{\rm irr}$ is the temperature due to stellar irradiation, and $T_{\rm vis}$ is the temperature resulting from viscous heating.

We assume that the gas is well mixed with dust grains, meaning that the gas temperature reaches equilibrium with the dust temperature. The dust temperature, which does not depend on the particle size inside disks, is calculated as:

$$T_{\rm irr} = 280\,{\rm K}\left(\frac{L_*}{{\rm L}_\odot}\right)^{1/4}\left(\frac{r}{1\,{\rm au}}\right)^{-1/2}, \tag{4.8}$$

where L_* represents the stellar bolometric luminosity. In the simulations, the stellar L_* is updated as the star evolves.

Viscous heating is a process in which a part of the energy liberated by accretion is transferred to thermal energy. The viscous temperature, $T_{\rm vis}$, is determined from the vertical radiative transfer equation as:

$$2\sigma_{\rm SB}T_{\rm vis}^4 = \left(\frac{3}{8}\tau_{\rm R} + \frac{1}{2\tau_{\rm P}}\right)F_{\rm rad}, \tag{4.9}$$

where $\sigma_{\rm SB}$ is the Stefan-Boltzmann constant, $\tau_{\rm R}$ is the Rosseland mean optical depth, $\tau_{\rm P}$ is the Planck mean optical depth, and $F_{\rm rad}$ is the radiative flux from the disk surface.

The efficiency of viscous heating depends on the amount of energy transported vertically through the disk. We consider the vertical energy transfer through the disk to calculate the viscous temperature. In dense regions, the temperature increases as the optical depth increases. The temperature decreases in low-density regions because less energy is stored inside the disk.

The Rosseland mean optical depth, $\tau_{\rm R}$, is the product of the dust opacity, $\kappa_{\rm R}$, and the surface density. The dust opacity depends on the local temperature and the composition of the dust grains. Following Hueso and Guillot [2005], who assumed dust grains consist of silicates and water ice [Pollack et al., 1985], the dust opacity is given as:

$$\kappa_{\rm R} = \begin{cases} 4.5\left(\frac{T_{\rm gas}}{150\,{\rm K}}\right)^2\,{\rm cm^2\,g^{-1}} & (T_{\rm gas} < 150\,{\rm K}) \\ 4.5\,{\rm cm^2\,g^{-1}} & (150\,{\rm K} \le T_{\rm gas} \le 1500\,{\rm K}) \\ 0\,{\rm cm^2\,g^{-1}} & (T_{\rm gas} > 1500\,{\rm K}) \end{cases}, \tag{4.10}$$

where $T_{\rm gas} = 150\,{\rm K}$ corresponds to the sublimation temperature of the water ice. In our calculation, to avoid abrupt changes that could cause numerical instabilities, we fit this behavior with a smooth function:

$$\kappa_{\rm R} = 2.25\,{\rm cm^2\,g^{-1}}\left[1 - \tanh\left(\frac{T_{\rm gas} - 1500\,{\rm K}}{150\,{\rm K}}\right)\right] \times \min\left[1, \left(\frac{T_{\rm gas}}{150\,{\rm K}}\right)^2\right]. \tag{4.11}$$

This smooth function reproduces the critical features of the temperature dependence while maintaining numerical stability.

At low temperatures, the Planck mean optical depth, $\tau_{\rm P}$, scales proportionally to the Rosseland mean optical depth, as $\tau_{\rm P} = 2.4\tau_{\rm R}$ [Nakamoto and Nakagawa, 1994]. However,

$\tau_{\rm P}$ converges to a lower limit of 0.5 for optically thin regions. Thus, we define $\tau_{\rm P}$ as:

$$\tau_{\rm P} = \max(\tau_{\rm P}, 0.5) \tag{4.12}$$

The dependence of $\tau_{\rm R}$ and $\tau_{\rm P}$ on $T_{\rm vis}$ makes the equation for viscous heating implicit. To solve this equation, we use the robust midpoint method, which ensures convergence for dense and sparse disk regions.

By combining $T_{\rm irr}$ and $T_{\rm vis}$, our calculation provides a vertically averaged gas temperature, $T_{\rm gas}$, that accurately reflects the thermal structure of the disk throughout its evolution.

4.2.4 Mass-Loss Profiles from Photoevaporation

We incorporated a one-dimensional surface mass-loss profile into the disk evolution calculation. This profile is obtained by fitting the results of two-dimensional photoevaporation simulations that solve radiative transfer, hydrodynamics, and non-equilibrium thermochemistry. These simulations include heating by FUV, EUV, and X-ray photons. This work represents the first simulation to integrate the effects of all these photons into a disk evolution model. The surface mass-loss profile is fitted using a combination of a quadratic function and a power-law function with a negative exponent to accurately capture the surface mass-loss rate characteristics (see Figure 4.7).

Previous simulations of photoevaporation have confirmed that the mass-loss rate due to photoevaporation is mainly independent of the disk mass [Wölfer et al., 2019, Nakatani et al., 2021]. Simulations varying the initial disk mass within a range of 10^{-1}–$10^{-3} M_*$ demonstrated that neither the total mass-loss rate nor the surface mass-loss profile are significantly affected by the disk mass. This is because photoevaporation is driven by gas heating on the disk surface, while most of the disk mass is concentrated near the midplane. The density of the midplane has little impact on the thermo-chemical processes occurring on the surface.

As discussed in Chapter 3, photons of different energy ranges contribute to gas heating in distinct ways. Gorti and Hollenbach [2009] first suggested that FUV photons could effectively heat gas via the photoelectric effect on dust grains, even though they do not ionize hydrogen atoms. Recent radiation hydrodynamic simulations that included FUV, EUV, and X-ray photons showed that the photoelectric effect of dust grains by FUV photons is the dominant heating process on the disk surface and plays a vital role in launching photoevaporative flows as long as the dust-to-gas mass ratio is larger than 10^{-3} [Wang and Goodman, 2017, Nakatani et al., 2018b, Komaki et al., 2021] (see also Komaki et al. [2024]).

We performed hydrodynamic simulations of photoevaporation with FUV, EUV, and X-ray photons varying the stellar mass in a wide range of 0.5–$7\,{\rm M}_\odot$ in a master thesis (see Komaki [2022]). Our results showed that the photoelectric effect on dust grains by FUV photons dominates the heating process for all types of stars. We performed a series of photoevaporation simulations varying the FUV luminosity to better understand

the role of FUV luminosity in launching photoevaporative flows. We derived a relationship between the mass-loss rate and the FUV luminosity, given by $\dot{M}_{\rm pe} \propto L_{\rm FUV}^{0.55}$ by performing photoevaporation simulations varying the FUV luminosity over two magnitudes Komaki [2022]. This result highlights the importance of FUV luminosity in photoevaporation.

In our calculation, the FUV luminosity is calculated at each step of the simulation, while the EUV and X-ray luminosities are assumed to be constant throughout the simulation. The following section will provide a detailed method for estimating the FUV luminosity at each step.

We adopt the surface mass-loss rate of photoevaporation from radiation hydrodynamic simulations, assuming a spatially constant dust-to-gas mass ratio of $\mathcal{D} = 10^{-2}$ throughout the simulation. In this callculation, photoevaporation varies with FUV luminosity evolution.

4.2.5 Stellar Evolution and Luminosity Variation

It takes millions of years for protoplanetary disks to disperse. The central star undergoes significant evolution, transitioning from a protostar to a pre-main-sequence star and eventually to a main-sequence star. As seen in the Hertzsprung-Russell (HR) diagram (Figure 2.1), stars exhibit drastic changes in luminosity and effective temperature. We used the stellar evolution code MESA [Paxton et al., 2011] to incorporate the effects of stellar evolution on disk evolution. We performed stellar evolution calculations for stars with various masses in the range of 0.1–$7\,{\rm M}_\odot$.

FUV photons heat gas through the photoelectric effect on dust grains. To model realistic photoevaporation and disk dispersal, we update the FUV luminosity at each time step. In our calculation, we incorporate three major components to estimate the total FUV luminosity: accretion, chromospheric activity, and photospheric emission, expressed as:

$$L_{\rm FUV} = L_{\rm acc} + L_{\rm chr} + L_{\rm ph}, \tag{4.13}$$

where $L_{\rm acc}$, $L_{\rm chr}$, and $L_{\rm ph}$ represent the FUV luminosities from accretion, the chromosphere, and the photosphere, respectively. We calculate the luminosity of each component at each time step to consistently incorporate FUV luminosity evolution.

The accretion-origin FUV luminosity, $L_{\rm acc}$, is updated dynamically at each time step. Observations of pre-main-sequence stars indicate that approximately 4% of the total energy released during accretion is emitted as FUV photons. The accretion rate is calculated at the computational inner radius, $r = 0.01\,{\rm au}$, using:

$$\dot{M}_{\rm acc} = -2\pi r v_r \Sigma, \tag{4.14}$$

where v_r is the radial velocity and Σ is the surface density. This method allows us to incorporate the gradual decrease in accretion-origin FUV luminosity over several million years.

The photospheric FUV luminosity, $L_{\rm ph}$, is calculated with the method proposed by Kunitomo et al. [2021]. Emission from the stellar photosphere is expressed with thermal

M_* [$M_\odot$]	0.1	0.3	0.5	0.7	1.0	1.7	2.0	3.0	5.0	7.0
$L_{\rm bol}$ [$L_\odot$]	0.06	0.26	0.93	1.72	2.34	5.0	6.4	14.9	554.5	1687
log $L_{\rm FUV}$ [erg s^{-1}]	30.7	30.8	30.9	31.3	31.7	32.3	32.4	32.3	36.0	36.5
log $L_{\rm EUV}$ [s^{-1}]	39.7	39.9	40.1	40.5	40.7	41.0	41.0	39.0	40.0	44.1
log $L_{\rm X\text{-}ray}$ [erg s^{-1}]	29.2	29.9	30.3	30.5	30.4	31.1	27.9	28.7	29.3	33.1

► **Table. 4.1** The list of stellar mass, disk mass, disk radius, and luminosities we used for the simulations. FUV and X-ray luminosities are given in the unit of energy luminosity and EUV luminosity is given in the unit of photon flux.

black-body radiation. However, the spectrum is not pure black-body radiation because of the absorption and emission lines. Husser et al. [2013] developed a stellar spectrum model that incorporates more than 90 chemical species, varying parameters such as surface gravity, metallicity, and effective temperature.

For simplicity, we assumed solar metallicity and constant surface gravity throughout the disk dispersal. The fraction of energy emitted as FUV photons depends strongly on the stellar effective temperature. Higher-mass stars emit a larger fraction of their energy as high-energy photons because of their higher effective temperatures. To capture this trend, we derived the ratio $\gamma = L_{\rm ph}/L_{\rm bol}$ as a function of effective temperature and updated $L_{\rm ph}$ at each time step using:

$$L_{\rm ph} = \gamma(T_{\rm eff}) L_{\rm bol}, \tag{4.15}$$

where $L_{\rm bol}$ is the bolometric luminosity and $T_{\rm eff}$ is the effective temperature.

The chromospheric FUV luminosity, $L_{\rm chr}$, also evolves over time. Observations of T Tauri stars have shown that $L_{\rm chr}$ is proportional to the bolometric luminosity, following the relation:

$$L_{\rm chr} = 10^{-3.3} L_{\rm bol}, \tag{4.16}$$

as suggested by Valenti et al. [2003]. The bolometric luminosity, $L_{\rm bol}$, decreases along the Hayashi track and gradually increases during the Henyey track and the main sequence.

The total FUV luminosity is calculated at each time step by summing the contributions from all three components. To isolate the effects of stellar evolution on disk evolution, we also performed photoevaporation simulations in which the stellar luminosities of FUV, EUV, and X-ray photons are assumed to remain constant throughout the disk lifetime. This approach allows us to clarify the role of evolving stellar parameters. The list of stellar parameters, including $L_{\rm bol}$, $T_{\rm eff}$, and the corresponding evolution paths, is provided in Table 4.1.

4.2.6 Simulation Setup

In our model, we assume an initial surface density distribution introduced by Hayashi [1981], expressed as:

$$\Sigma = \Sigma_{1\,\rm au} \left(\frac{r}{1\,\rm au}\right)^{-3/2} \exp\left\{\left(-\frac{r}{r_{\rm cut}}\right)\right\}, \tag{4.17}$$

where $\Sigma_{1\,\mathrm{au}}$ is the surface density at $r = 1\,\mathrm{au}$. In the equation, r_{cut} represents the cutoff radius that characterizes the disk size. There are various contradicting observation results on disk radius. Some infrared observations have shown that the disk radii scale with stellar mass. Based on this, we assume $r_{\mathrm{cut}} = 30\,\mathrm{au}(M_*/1\,\mathrm{M}_\odot)$.

The surface density is normalized by $\Sigma_{1\,\mathrm{au}} \sim 1.7 \times 10^3\,\mathrm{g\,cm^{-2}}$ according to the model by Hayashi [1981]. In the solar-mass case, this corresponds to a disk mass of $M_{\mathrm{disk}} = 0.0117\,\mathrm{M}_\odot$ with $r_{\mathrm{cut}} = 30\,\mathrm{au}$. Observations of T Tauri stars suggest that the disk mass scales proportionally to the stellar mass [Ansdell et al., 2016, Andrews, 2020]. However, there is significant variation in the disk masses even with the same stellar mass [Andrews and Williams, 2005, Ruíz-Rodríguez et al., 2018], spanning a few magnitudes of $10^{-2} \leq M_{\mathrm{disk}}/M_* \leq 10^{-4}$. It is important to note that these observations primarily target Class II stars. The disk mass of $M_{\mathrm{disk}} = 0.0117\,\mathrm{M}_\odot$ represents the higher end of the observed range. To investigate disk evolution from the early stages, we assume an initial disk mass as the higher-end value, $M_{\mathrm{disk}} = 0.0117(M_*/1\,\mathrm{M}_\odot)$ so that it is consistent with r_{cut}.

The calculation continues until either the disk mass decreases below $M_{\mathrm{disk}} < 10^{-10}\,\mathrm{M}_\odot$ or the disk age reaches $100\,\mathrm{Myr}$. The mass-loss rate decreases slightly throughout the disk dispersal. We confirmed that the results are not sensitive to the specific mass threshold. The termination time for the calculation remains consistent even when the threshold is increased to $< 10^{-5}\,\mathrm{M}_\odot$.

The dust dispersal timescale inferred from observations is typically the observable timescale of near infrared emission of dust grains. To compare our results with observations, we follow the method proposed by Kimura et al. [2016] to derive the near-infrared dust dispersal timescale for each simulation. In their model dust grains are observable when they have sufficient surface density and temperature. The observability criteria for wavelengths of 2–3 μm are defined as $\Sigma_{\mathrm{dust}} \geq 10^{-1}\,\mathrm{g\,cm^{-2}}$ and $T_{\mathrm{gas}} \geq 300\,\mathrm{K}$. The absorption coefficient is approximately $10\,\mathrm{cm^2\,g^{-1}}$ for small dust grains with sizes $\leq 10\,\mu\mathrm{m}$. The critical dust surface density is set to make the local optical depth equal to unity. The evolution of the gas surface density is calculated in the simulations. The dust-to-gas mass ratio is used to estimate the dust surface density from the gas surface density. We only need this ratio at the end, when most of the gas disperses. Gorti et al. [2009] performed disk evolution simulations with limited disk dispersal processes and a simplified dust evolution model. They found that the dust-to-gas mass ratio at $1.5\,\mathrm{Myr}$ is approximately 0.03 at $r = 30\,\mathrm{au}$, which matches the typical survival radius of the gas disk in our simulations. We adopt 0.03 as the dust-to-gas mass ratio in the final stage of disk dispersal and assume that it is constant throughout the disk for simplicity.

4.3 Results

We conducted one-dimensional long-term simulations of protoplanetary disk evolution, incorporating accretion, magnetohydrodynamic (MHD) winds, photoevaporation, and stellar evolution in a consistent manner. First, we focus on the case of a star with $M_* = 1\,\mathrm{M}_\odot$, analyzing the processes that drive disk dispersal and how they contribute

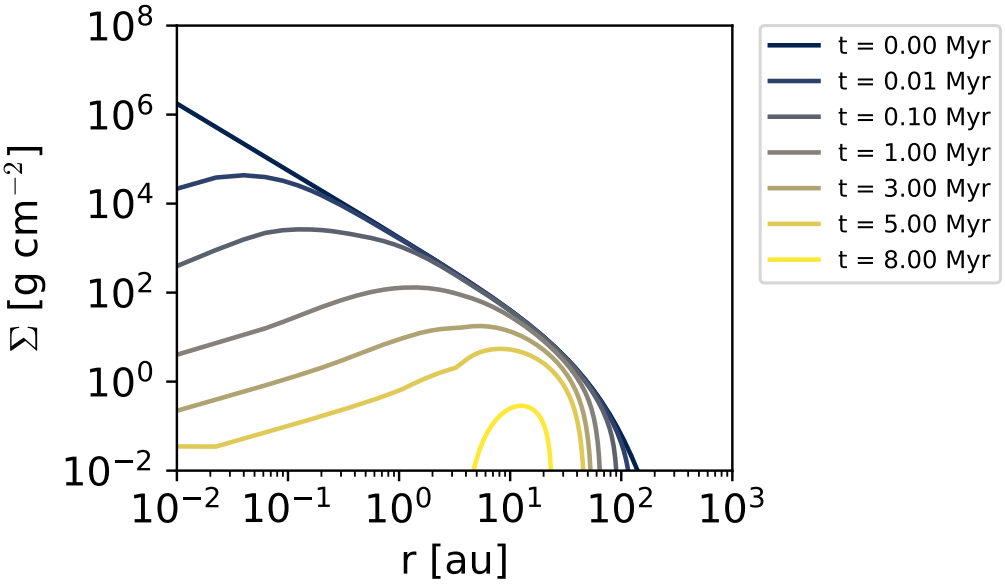

► **Figure. 4.1**

Snapshots of the surface density for the case of $M_* = 1\,\mathrm{M}_\odot$ are shown at ages of 0, 0.01, 0.1, 1, 3, 5, and $8\,\mathrm{Myr}$. The line color variations from navy to yellow represent the disk evolution over time. The disk loses mass primarily through accretion and MHD winds in the inner region. Photoevaporation is the dominant disk dispersal process in the outer region and contribute to decrease the disk radius. In the innermost region, the decrease in surface density is limited because of the upper limit on $\alpha_{\phi z}$.

over time. We examine the differences between various disk dispersal models and their implications for the overall evolution. To investigate the role of stellar mass, we performed a series of simulations across a wide range of stellar masses, from $0.1\,\mathrm{M}_\odot$ to $7\,\mathrm{M}_\odot$. This allowed us to examine the dependence of dispersal processes and disk evolution on stellar mass.

Finally, we discuss the effects of stellar evolution on disk dispersal, highlighting how variation in stellar luminosity and radiation over time influence the disk lifetime and structure.

4.3.1 Long-Term Evolution of Protoplanetary Disks

First, we will discuss the calculation result in the case of $M_* = 1\,\mathrm{M}_\odot$ and later in the case of $M_* = 3\,\mathrm{M}_\odot$. We employ the 'weak wind case' of $\epsilon_{\mathrm{rad}} = 0.9$, and weak viscosity of $\alpha_{r\phi} = 10^{-4}$ as a fiducial parameter. Recent observations suggest that disks have longer lifetimes than previous observations, so we choose these parameters aiming to reproduce the observed dust dispersal timescales.

Figure 4.1 shows a snapshot of the surface density at $0, 0.01, 0.1, 1, 3, 5, 8\,\mathrm{Myr}$, and

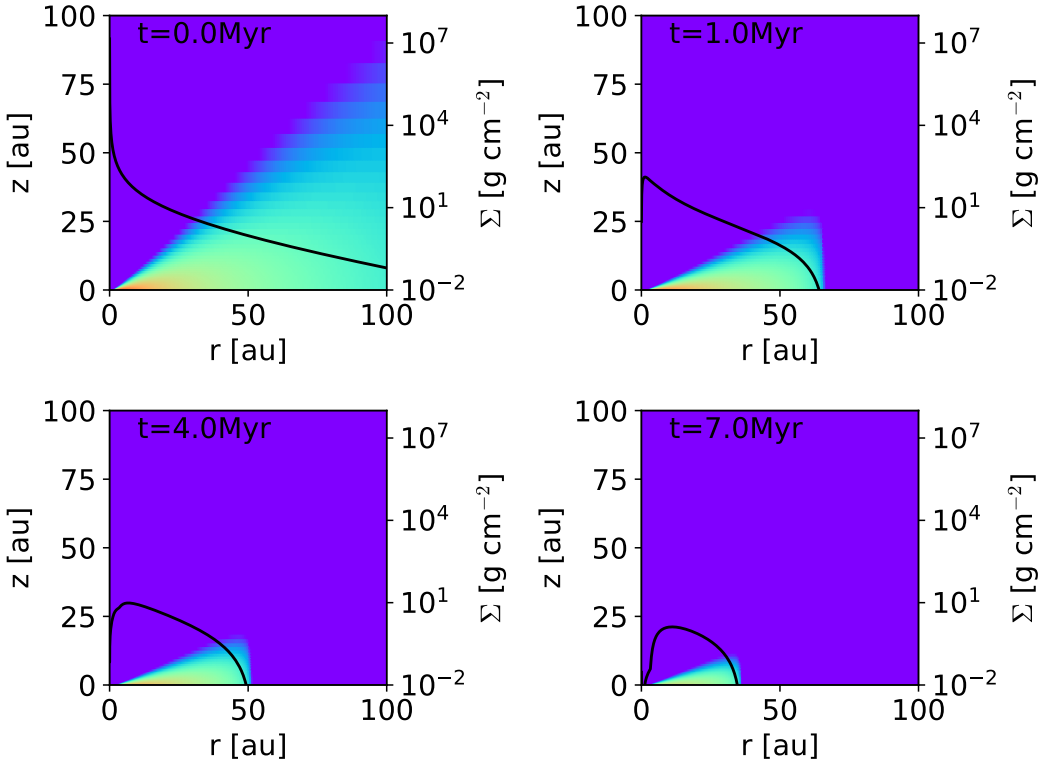

► **Figure. 4.2**

The snapshots of gas density and surface density in linear scale in the case of $M_* = 1\,\mathrm{M}_\odot$ at the age of $0, 1, 4, 7\,\mathrm{Myr}$. The color map shows the gas density distribution. The color variation from purple to red corresponds to the local gas density from 10^{-20} to $10^{-10}\,\mathrm{g\,cm^{-3}}$. The black line represents the surface density. The equations solve the evolution of surface density. The local gas density is derived by assuming hydrostatic equilibrium at each radius. This shows the more realistic picture obtained by observations.

Figure 4.2 shows a two-dimensional gas density distribution. The gas density distribution in (r, z) coordinates is derived by assuming hydrostatic equilibrium and is calculated as:

$$\rho(r,z) = \frac{\Sigma\Omega_{\rm K}}{\sqrt{2\pi}c_{\rm s}} \exp\left(-\frac{z^2}{2H^2}\right). \tag{4.18}$$

The scale height, H is determined based on the local temperature obtained in the simulation.

Accretion and MHD winds disperse gas in the vicinity of the star, while photoevaporation is a dominant disk dispersal process in the outer region. Due to the upper limit of $\overline{\alpha_{\phi z}}$, the mass-loss rate of MHD winds has a limitation in the vicinity of the star after the age of $\sim 5\,{\rm Myr}$, leading to a decrease in the total mass-loss rate near the central star. The vertical magnetic flux is assumed to be constant throughout the calculation. The winds remove the magnetic lines, and an upper limit of 1 is set for $\overline{\alpha_{\phi z}}$ to prevent the magnetic field-to-gas density ratio from becoming unrealistically high. Additional simulations confirm that both the dust dispersal timescale and gas dissipation timescale do not vary by varying the upper limit of $\overline{\alpha_{\phi z}}$ by 0.1 and 10 times.

Figure 4.2 shows the evolution of the disk gas density on a linear scale, which is more similar to what is observed. The disk radius decreases over time, and it looks like it is dispersing in the outside-in manner.

We determine the mass-loss rates for each process to identify the dominant process during disk evolution. The accretion rate to the central star is calculated by counting the amount of mass going into a specific radius and given by

$$\dot{M}_{\rm acc} = -2\pi(rv_r\Sigma), \tag{4.19}$$

The radius is set to the computational inner radius of $r_{\rm in} = 0.01\,{\rm au}$. The mass-loss rates of MHD winds and photoevaporation are given by

$$\begin{aligned} \dot{M}_{\rm w} &= \int_{r_{\rm in}}^{r'_{\rm out}} \dot{\Sigma}_{\rm w}\,{\rm d}r \\ \dot{M}_{\rm pe} &= \int_{r_{\rm in}}^{r'_{\rm out}} \dot{\Sigma}_{\rm pe}\,{\rm d}r. \end{aligned} \tag{4.20}$$

In the equations, $r_{\rm out}$ represents the disk radius, which is set to the location that the gas surface density becomes below $\Sigma < 10^{-2}\,{\rm g\,cm^{-2}}$.

Figure 4.3 shows the time evolution of the mass-loss rate of each process. Accretion is the dominant mass-loss process within the first $1.5\,{\rm Myr}$ even with the low viscous parameter of $\overline{\alpha_{r\phi}} = 10^{-4}$. After that, photoevaporation becomes the primary driver of mass loss. The contributions to the time-integrated mass loss of accretion, MHD winds, and photoevaporation are 47.7%, 21.9%, and 30.3%, respectively. As seen in Figure 4.3, the mass-loss rates of all the processes decrease over time. Both the accretion rate and the mass-loss profile by MHD winds are proportional to the gas surface density, Σ. The

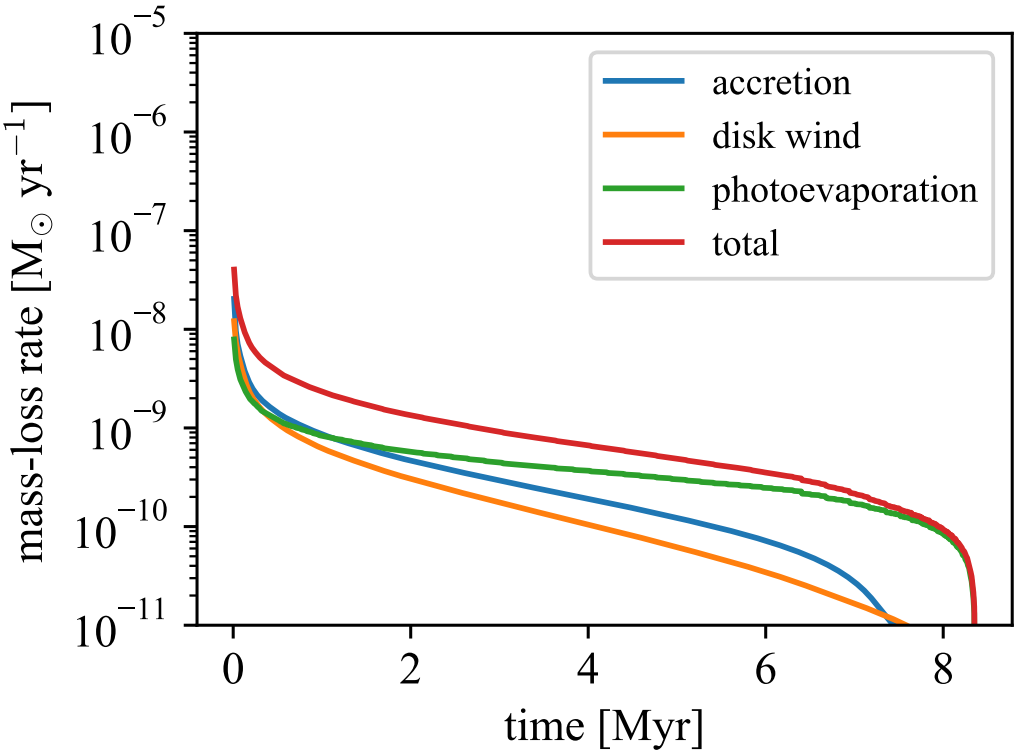

► **Figure. 4.3**

The mass-loss rates for each disk dispersal process: accretion (blue), MHD winds (orange), photoevaporation (green), and their total (red). Accretion is the primary dispersal process during the first few $1.5\,\mathrm{Myr}$ but eventually overtaken by photoevaporation. Both the mass-loss rates by accretion and MHD winds decrease over time because they are proportional to the surface density. Photoevaporation rate also decreases because of the truncation of the disk and the gradual decrease in FUV luminosity.

dependence on the gas surface density leads to a decrease in mass-loss rates over time as the disk dispersal proceeds.

The mass-loss rate of photoevaporation also slightly decreases over time for two reasons. First, the disk radius decreases because of the effective mass loss by photoevaporation. Since photoevaporation driven by FUV photons is efficient in the outer region, the decrease in disk radius leads to a low photoevaporation rate. Secondly, the FUV luminosity of chromospheric origin, which is the most dominant component of the total FUV luminosity, decreases as the star evolves on the Hayashi track. The total FUV luminosity decreases by 50% from $1\,\mathrm{Myr}$ to $2.5\,\mathrm{Myr}$. Since the photoevaporation mass loss rate follows $\dot{M}_{\rm pe} \propto L_{\rm FUV}^{0.55}$ [Komaki et al., 2021], the photoevaporation rate decreases by $\sim 30\%$ during this period.

Our goal is to understand the observed dust dispersal timescale, which corresponds to how long dust grains remain detectable. This allows a direct comparison with observations. However, since gas constitutes the majority of the disk and determines its evolution, we also estimate the disk gas dissipation timescale.

The disk mass decreases over time. The decrease in disk mass is fitted by a vertical sigmoid function given by

$$\begin{aligned} \log_{10} M_{\rm disk} &= a \log\left(\frac{1-x}{x}\right) + d \\ x &= \frac{(t/1\,\mathrm{Myr}) - b}{c}, \end{aligned} \tag{4.21}$$

where a, b, c, d are fitting parameters. We obtain the gas dissipation timescale by $b+c$ based on fit to the one-dimensional calculation. The gas dissipation timescale is $8.4\,\mathrm{Myr}$, longer than the dust dispersal timescale of $3.6\,\mathrm{Myr}$. The difference in timescales is attributed to the fact that the gas dissipation timescale corresponds to the timescale in which all of the disk gas completely disperses, while the dust dispersal timescale corresponds to when the surface density becomes lower than a specific density. The comparison implies a limitation in understanding disk evolution solely through observations of dust grains.

The disk observable criterion is defined when any region in the disk satisfies $\Sigma_{\rm dust} \geq 10^{-1}, \mathrm{g}, \mathrm{cm}^{-2}$ and $T_{\rm gas} \geq 300, \mathrm{K}$. The criterion is sensitive to the dust surface density, which is calculated by multiplying the assumed dust-to-gas mass ratio by the gas surface density. We discuss the impact of the assumed dust-to-gas mass ratio in Chapter 4.5.

We now closely study the calculation result in a $M_* = 3\,\mathrm{M}_\odot$ case. In this scenario, stellar evolution brings about a significant change to disk evolution.

Figure 4.4 shows the mass-loss rate of each dispersal process around a $M_* = 3\,\mathrm{M}_\odot$ star. The disk loses its mass by accretion, MHD winds in the inner disk, and photoevaporation in the outer disk. The dominant disk dispersal process changes at the last stage of disk dispersal. Photoevaporation replaces accretion and becomes the most dominant disk dispersal process at $1.3\,\mathrm{Myr}$. The transition occurs when the central star reaches the main sequence.

Figure 4.5 shows the evolution of FUV luminosity during the calculation. In the first $1.6\,\mathrm{Myr}$, the chromospheric origin is the dominant source of the FUV luminosity, but it is

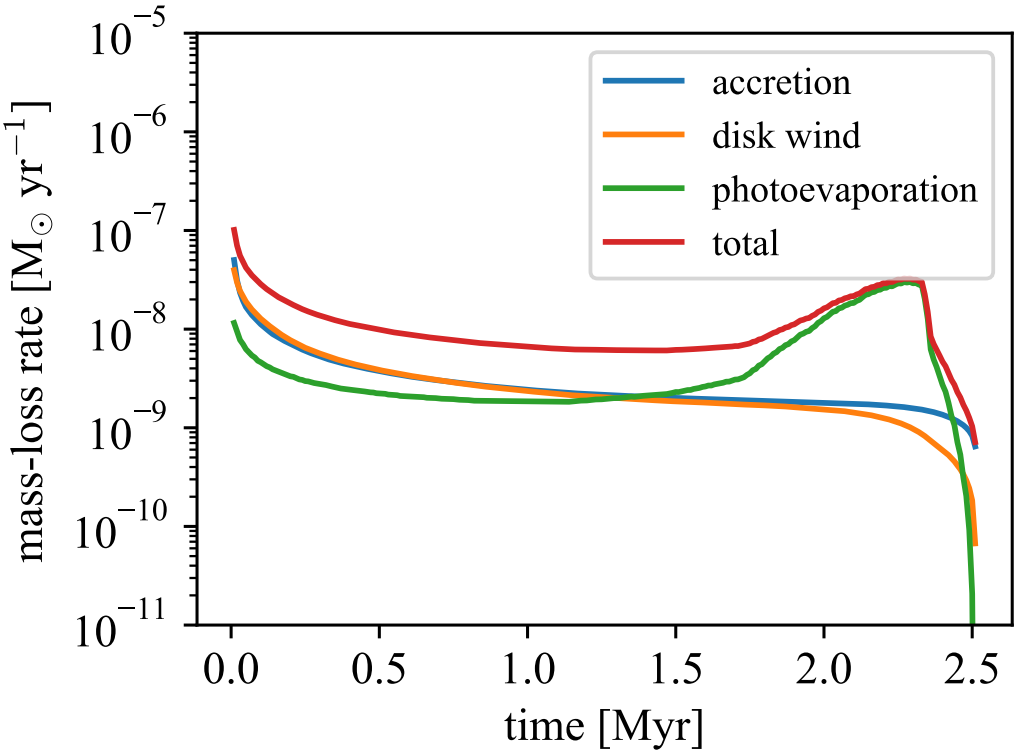

► **Figure. 4.4**

The mass-loss rates for each disk dispersal process in the case of $M_* = 3\,\mathrm{M}_\odot$: accretion (blue), MHD winds (orange), photoevaporation (green), and their total (red). Accretion and MHD winds dominate as the primary dispersal processes during the first $1\,\mathrm{Myr}$ but are eventually overtaken by photoevaporation. The photoevaporation rate increases significantly around $2\,\mathrm{Myr}$, when the star reaches the main sequence. This enhanced photoevaporation efficiently clears the disk gas, leading to rapid dispersal in the final stages of disk evolution.

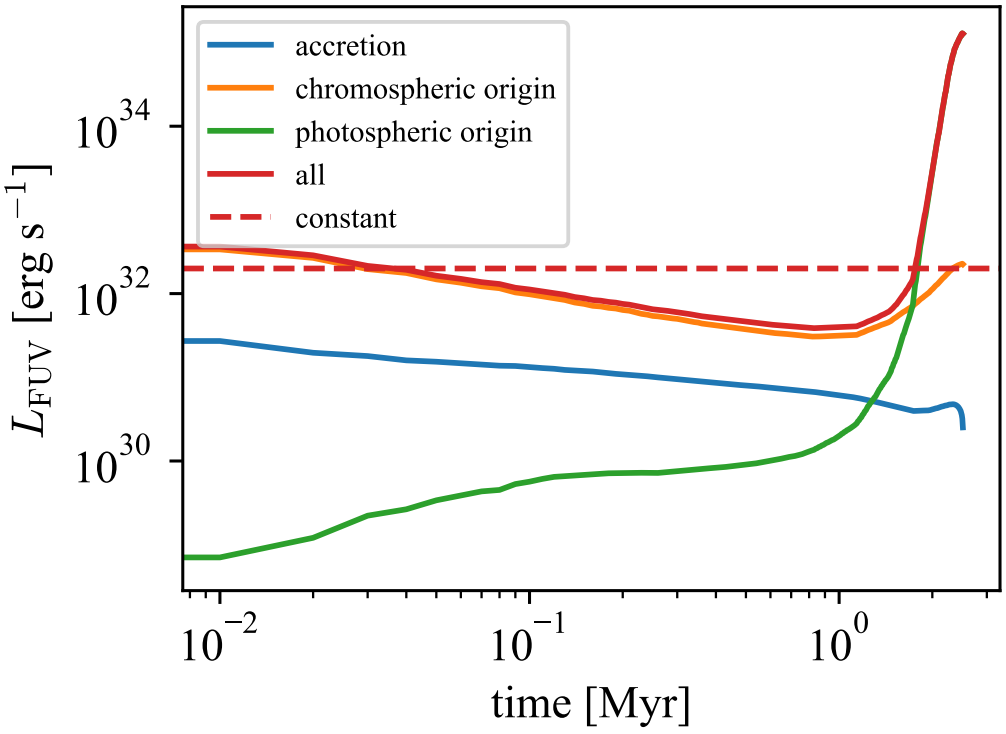

► **Figure. 4.5**

The FUV luminosities from different origins in the case of $M_* = 3\,\mathrm{M}_\odot$: accretion-origin (blue), chromospheric-origin (orange), photospheric-origin (green), and the total (red). During the first $1.6\,\mathrm{Myr}$, the chromosphere-origin is the primary source of FUV luminosity. The photospheric-origin becomes the main FUV luminosity after the star reaches the main-sequence because the effective temperature exceeds $10^4\,\mathrm{K}$.

replaced by the photospheric origin. When the star reaches main-sequence, the effective temperature exceeds $30000\,\mathrm{K}$, and the FUV luminosity increases accordingly. The total FUV luminosity increases by a factor of 10^3, which corresponds to the increase in the photoevaporation rate by a factor of ~ 45, derived from the relation of $\dot{M}_{\rm pe} \propto L_{\rm FUV}^{0.55}$ [Komaki et al., 2021].

Intermediate-mass stars do not have a convective zone on the stellar surface in the main-sequence phase. The inactive outer layer results in low X-ray luminosity due to the lack of magnetic activity on the surface. Therefore, X-ray luminosity drops when the central star reaches main-sequence. Our simulation considers the change in photoevaporation rate as a result of the evolution of the FUV luminosity, while the constant X-ray luminosity is assumed over time. Komaki et al. [2021] performed photoevaporation simulations varying X-ray luminosity by two magnitudes to clarify the dependence of photoevaporation on X-ray radiation. The obtained relation is $\dot{M}_{\rm pe} \propto L_{\rm X\text{-}ray}^{0.26}$, which is not as significant as the FUV luminosity. Considering that FUV photons are the dominant heating source on the base of photoevaporative flows, we expect that decreasing X-ray luminosity will have a limited impact.

Stellar evolution enhances photoevaporation and significantly impacts disk evolution around intermediate-mass stars, consistent with Kunitomo et al. [2021]. Their study incorporates photoevaporation as the combined effect of FUV, EUV, and X-ray-driven mass loss. Our simulations further confirm the critical role of stellar evolution in disk evolution using a more detailed photoevaporation model which comprehensively incorporates FUV, EUV, and X-ray photons.

4.3.2 Dependence of Disk Evolution on Stellar Mass

We performed a series of long-term disk evolution simulations, varying the stellar mass in the range of 0.1–$7\,\mathrm{M}_\odot$. Figure 4.6 shows the dust dispersal timescales of all ranges of masses, and has a peak around $\sim 2\,\mathrm{M}_\odot$.

For cases with $M_* \geq 2\,\mathrm{M}_\odot$, the central star reaches the main sequence before the disk gas disperses. A massive star with $M_* \geq 5\,\mathrm{M}_\odot$ reaches the main sequence, and its surrounding disk undergoes strong photoevaporation from intense FUV radiation. In these models, the central star reaches the main sequence within $1\,\mathrm{Myr}$, which causes the disk to be under the influence of strong radiation for a more extended period of time. The primary dispersal process is photoevaporation, and more than 40% of the disk mass is lost by photoevaporation. On the other hand, disks around low-mass stars have shorter dust dispersal timescales compared to intermediate-mass stars. This rapid disk dispersal is attributed to the low initial disk mass and the reduced temperature due to the low bolometric luminosity. We assume that dust grains are observable in the infrared where the temperature exceeds $300\,\mathrm{K}$ and dust surface density exceeds $0.1\,\mathrm{g\,cm^{-2}}$. In a $M_* = 0.1\,\mathrm{M}_\odot$ case, this criterion sets a strict limitation on the area where the disk is observable, and it is mainly $r < 0.3\,\mathrm{au}$. In our simulation, the gas temperature is derived considering stellar radiation and viscous heating. The temperature profile is determined mainly by stellar radiation, following $L_{\rm bol}^{1/4}$. The low luminosity directly affects the dust dispersal timescale

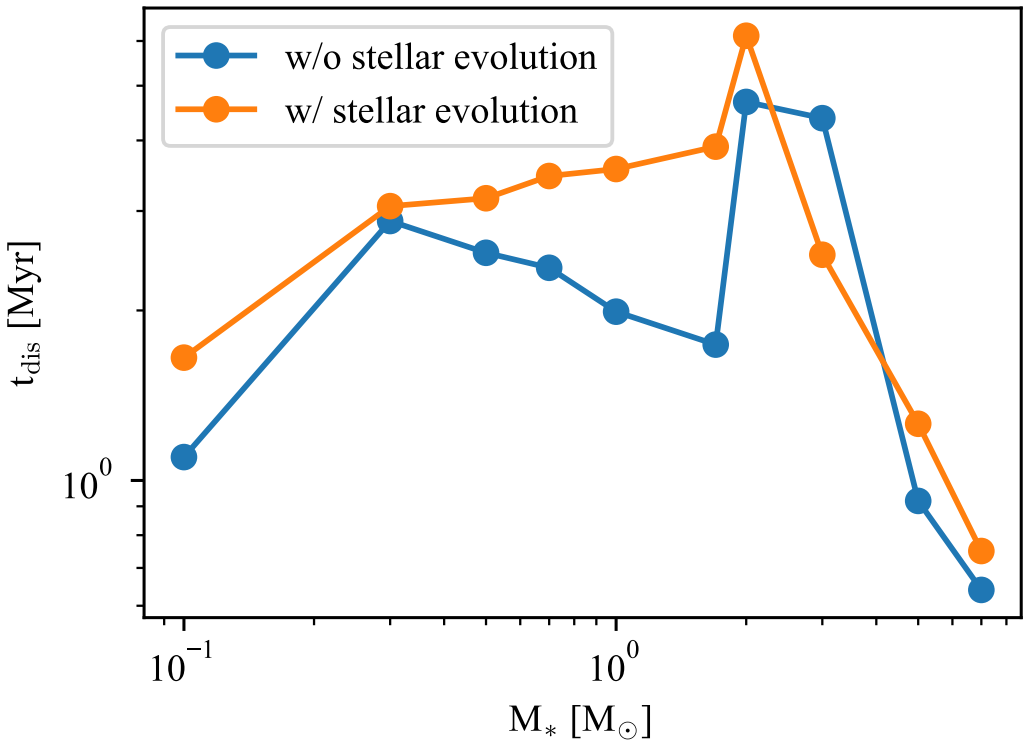

► **Figure. 4.6**

The dust dispersal timescale for each stellar mass calculated by simulations with stellar evolution (orange) and without stellar evolution (blue). A distinct difference is found around from solar to intermediate-mass stars. For low-mass to solar-mass stars, the star spends more time to reach main-sequence than disk dispersal. During this period, the FUV luminosity decreases along the Hayashi track throughout the whole lifetime. Around stars larger than intermediate-mass, the star reaches the main sequence before the disk disperses and the disk is exposed to intense FUV radiation at the final stage of disk dispersal. This result highlights the limitation of using constant FUV luminosity throughout disk evolution.

around a low-mass star. Because of the high temperature sensitivity on stellar bolometric luminosity, the observable area of stars with $M_* \geq 2\,\mathrm{M}_\odot$ expands because of the increase in bolometric luminosity as the star reaches the main-sequence. In a $M_* = 2\,\mathrm{M}_\odot$ case, the observable radius expands by a factor of 1.5 during the last $1.5\,\mathrm{Myr}$. The balance between enhanced photoevaporation and heating by bolometric luminosity determines the dust dispersal timescale. These two effects make disks around a $M_* = 2\,\mathrm{M}_\odot$ star observable for longer time compared to the other mass cases.

4.3.3 Impact of Stellar Evolution

Stellar evolution is first incorporated into disk evolution simulations by Kunitomo et al. [2021]. They incorporate the maximum photoevaporation rate among FUV, EUV, and X-ray, which is derived from previous research focusing on each heating source. We derive the surface mass-loss profile of photoevaporation from a two-dimensional radiation hydrodynamics simulation incorporating all FUV, EUV, and X-ray radiation simultaneously. Our calculation is the first to incorporate a realistic photoevaporation profile into a disk evolution simulation considering FUV heating. A disk evolution simulation with a whole package of disk dispersal processes enables us to clarify the precise role of stellar evolution in disk dispersal.

To assess the impact of stellar evolution, we perform disk evolution simulations with constant luminosity during the calculation. We assume the luminosity at the age of $\sim 1\,\mathrm{Myr}$ because it is the typical accretion timescale, just as many previous researches assumed. Three origins of FUV radiation are considered in the calculation: accretion, chromospheric origin, and photospheric origin. We calculate the accreted gas mass at each time step to estimate the FUV luminosity. In a calculation without stellar evolution, we assume that the accretion rate is constant with $\dot{M}_{\mathrm{acc}} = 1.0 \times 10^{-8} (M_*/\,\mathrm{M}_\odot)\,\mathrm{M}_\odot\,\mathrm{yr}^{-1}$ during the calculation.

Figure 4.6 shows the dust dispersal timescale of both with and without stellar evolution cases. It has an outstanding peak around $\sim 2\,\mathrm{M}_\odot$ in the case without including stellar evolution. The mass-loss rate of photoevaporation is low because of the relatively low X-ray luminosity around intermediate-mass stars. Intermediate-mass stars do not have a convective zone on their stellar surfaces, which results in low X-ray luminosity. This results in a relatively low mass-loss rate of photoevaporation around intermediate-mass stars.

The most significant difference is around the stars in the $0.5\,\mathrm{M}_\odot \leq M_* \leq 1\,\mathrm{M}_\odot$. When stellar evolution is considered, the dust dispersal timescales are longer, and the difference is attributed to distinct FUV luminosity. The luminosity of these types of stars decreases throughout the disk dispersal because the central star is on the Hayashi track. Moreover, the FUV luminosity is overestimated in the calculation without stellar luminosity. When calculating the FUV luminosity of accretion origin, the accretion rate of $\dot{M}_{\mathrm{acc}} = 1.0 \times 10^{-8} (M_*/\,\mathrm{M}_\odot)\,\mathrm{M}_\odot\,\mathrm{yr}^{-1}$ is assumed, which is higher by a factor of 10 compared to that calculated with stellar evolution (see Figure 4.3). The overestimated accretion rate leads to enhanced photoevaporation and an underestimation of the dust dispersal timescale.

In the case of $M_* = 3\,\mathrm{M}_\odot$, the dust dispersal timescale decreases by $1.9\,\mathrm{Myr}$ when stellar evolution is incorporated. The short lifetime is because the mass-loss rate of

photoevaporation is greatly enhanced when the central star reaches the main sequence. A star reaches the main sequence before the disk disperses in the case of $M_* \geq 2\,\mathrm{M}_\odot$. In the case of $M_* > 3\,\mathrm{M}_\odot$, a star reaches the main-sequence before $1\,\mathrm{Myr}$, and the luminosity of the main-sequence star is used in the calculation without stellar evolution. Therefore, there is little difference between the calculations with and without stellar evolution.

Comprehensive long-term disk evolution simulations show that disk dispersal is susceptible to change in FUV luminosity due to stellar evolution, especially around solar to intermediate-mass stars. We discuss that a simple estimate of stellar luminosity, using the value at the age of $1\,\mathrm{Myr}$ throughout the simulation, cannot reproduce realistic disk dispersal.

4.3.4 Uncertainties in Disk Dispersal Models

There is still a discussion about which disk dispersal model can better depict disk evolution and be more consistent with observations. Specifically, previous research suggests several models: 'strong wind case' or 'weak wind case' for MHD winds, variations in magnetic field strength including the absence of magnetic fields (no-B-field case). We perform long-term disk evolution simulations with different disk evolution models to further investigate the impacts of each disk dispersal process.

Strong MHD Winds

We have performed the 'weak wind case' of MHD winds for the fiducial calculation. We perform a series of long-term disk evolution simulations with the 'strong wind case.' In this model, all the energy lost by the wind torque and some of the energy released by viscosity are transferred to MHD winds. The dimensionless mass flux by MHD winds and the energy flux of heating in the disk is given by

$$\begin{aligned} C_{\mathrm{w},e} &= \max\left[\frac{2}{r^3\Omega(\rho c_\mathrm{s})_\mathrm{mid}}\frac{\partial}{\partial r}\left(r^2\Sigma\overline{\alpha_{r\phi}}c_\mathrm{s}^2\right) + \frac{2c_\mathrm{s}}{r\Omega}\overline{\alpha_{\phi z}}, 0\right] \\ F_\mathrm{rad} &= \max\left[-\frac{1}{r}\frac{\partial}{\partial r}\left(r^2\Sigma\Omega\overline{\alpha_{r\phi}}c_\mathrm{s}^2\right), 0\right]. \end{aligned} \tag{4.22}$$

The derivation of this equation is shown in Appendix C. The viscous parameter is still set to $\overline{\alpha_{r\phi}} = 10^{-4}$. The disks disperse more rapidly than in fiducial models in all the stellar mass cases. MHD winds are the main disk dispersal process except for $M_* = 7\,\mathrm{M}_\odot$. In the case of $M_* = 1\,\mathrm{M}_\odot$, approximately 60% of the disk is dispersed by MHD winds. In the case of $M_* = 7\,\mathrm{M}_\odot$, photoevaporation is the main disk dispersal process. The star reaches the main-sequence at the age of $\sim 0.2\,\mathrm{Myr}$; therefore, a disk experiences strong photoevaporation for a long time. The dust dispersal timescale is longest at $M_* = 3\,\mathrm{M}_\odot$ of $\sim 2\,\mathrm{Myr}$. The stellar mass dependence of dust dispersal timescale is similar to that obtained in the fiducial model and is more highlighted in this scenario. The dust dispersal timescale is longest at $M_* = 3\,\mathrm{M}_\odot$ because the observable region is more extended because of the high temperature by efficient heating by bolometric luminosity. The surface density

is highest at a few to a few tens of au because MHD winds disperse the inner disk, the outer disk is dispersed by photoevaporation, and the middle is left behind. As the stellar mass increases, the bolometric luminosity increases. In the case of $M_* = 3\,\mathrm{M}_\odot$, the observable region contains the peak in the surface density. Therefore, the dust dispersal timescale is almost equal to the gas dissipation timescale and becomes the highest among the various mass cases.

We also conduct simulations without including stellar evolution, and the dust dispersal timescale remains unchanged. This is because disk dispersal in the inner region is primarily driven by MHD winds. Since the dust dispersal timescale reflects the observable timescale of the inner disk, variations in photoevaporation caused by stellar evolution have minimal impact.

Dependence on Magnetic Fields

We also perform disk evolution simulations without magnetic fields by setting $\overline{\alpha_{\phi z}} = 0$ and excluding MHD winds. There is a discussion on how effective magnetic fields contribute to disk dispersal. We already assume a relatively low viscous parameter of $\overline{\alpha_{r\phi}} = 10^{-4}$. We still assume $\overline{\alpha_{r\phi}} = 10^{-4}$ because turbulence can cause a minimum effect of viscosity.

The disk around low-mass stars of $0.1\,\mathrm{M}_\odot$ does not completely disperse within $100\,\mathrm{Myr}$. In all ranges of stellar mass, the ratio of mass lost by photoevaporation increases, enhancing the relative importance of photoevaporation. Therefore, the FUV luminosity variation due to stellar evolution is more essential in this model. The significant change in dust dispersal timescale around $0.1\,\mathrm{M}_\odot$ stars suggests that disk dispersal is more sensitive to the strength of magnetic fields around low-mass stars, which are the main components of stellar clusters according to the IMF.

There are two causes for the accretion motion. The first is the redistribution of angular momentum due to viscosity, and the second is gas accretion onto the star as MHD winds carry away angular momentum. The accretion motion is primarily driven by angular momentum loss caused by wind torque, highlighting the importance of wind torque in understanding accretion processes. In the fiducial case, the accretion rate increases with stellar mass, following $\propto M_*^{0.92}$ at the age of $1\,\mathrm{Myr}$, which is lower than the observed relation of $\propto M_*^2$. This discrepancy suggests that the wind torque and the strength of the magnetic fields may be overestimated around low-mass stars in our calculation, indicating that the actual wind torque could be weaker for such stars.

Difference in Photoevaporation Profile

In our calculation, we derive the surface mass-loss profile of photoevaporation based on radiation hydrodynamic simulation, which incorporates all FUV, EUV, and X-ray photons. Our work is the first disk evolution simulation that incorporates a realistic mass-loss profile of photoevaporation. Previous theoretical research performed disk evolution simulations with the photoevaporation rate calculated as a maximum or sum of the mass-loss rates by each FUV, EUV, or X-ray-driven gas flow. In some previous studies, the effect of

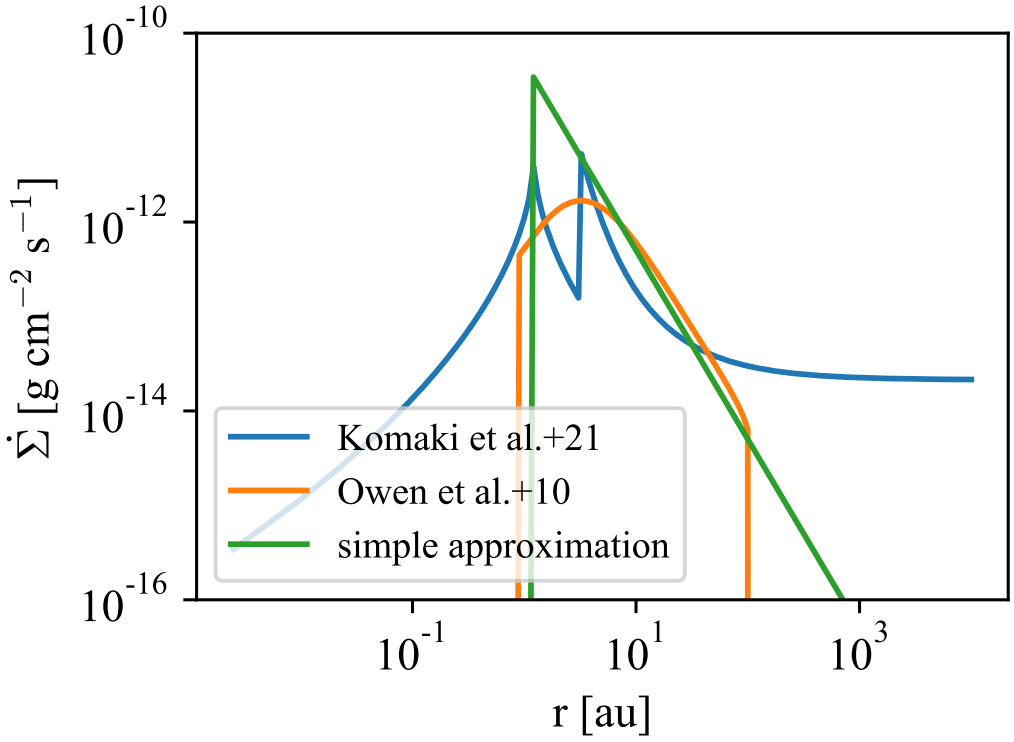

► **Figure. 4.7**

The surface mass-loss profiles due to photoevaporation are shown as calculated by Komaki et al. [2021], Owen et al. [2010], and a simple approximation of Owen et al. [2010]. In the profiles by Owen et al. [2010], the surface mass-loss rate decreases with radius approximately as r^{-2}. In contrast, the profile by Komaki et al. [2021] maintains a nearly constant value of $\sim 3 \times 10^{-14}\,\mathrm{g\,s^{-1}\,cm^{-2}}$ in the outer region. This is attributed to efficient FUV-driven photoevaporation in the outer region.

FUV radiation is omitted based on the assumption that its lower energy compared to EUV and X-ray photons makes it less important for driving photoevaporation. Recent photoevaporation simulations showed that FUV photons penetrate the disk and heat the gas via photoelectric heating on dust grains. X-ray photons also contribute to the photoelectric effect because electrons emitted by X-ray ionization decrease the electric charges of dust grains (see Eq. 3.9). Previous researches used photoevaporation mass-loss profiles based on simulations without FUV photons. For example, the mass-loss profile of Owen et al. [2012] is often used as in Kunitomo et al. [2021].

Figure 4.7 shows three surface mass-loss profiles of photoevaporation: the fiducial model, calculated by Owen et al. [2012], and the simple fit for the Owen et al. [2012] model. To clarify the impact of the difference in the mass-loss profile, we multiply 3.1×10^{-10} by the profile so that the mass-loss rate by photoevaporation within $100\,\mathrm{au}$ matches that of

our fiducial model. The most significant difference is the number of peaks in the profiles. The profile given by Komaki et al. [2021] has two peaks corresponding to the launching radius due to EUV and FUV radiation. The simple fit for Owen et al. [2012] is given by

$$\dot{\Sigma}_{\rm pe,s} = 3.2 \times 10^{-12}\,{\rm g\,s^{-1}\,cm^{-2}} \left(\frac{L_{\rm X-ray}}{10^{30}\,{\rm erg\,s^{-1}}}\right)\left(\frac{r}{2.5\,{\rm au}}\right)^{-2}. \tag{4.23}$$

We perform a long-term disk evolution simulation with the simple fit of photoevaporation. The simple model is used instead of the Owen et al. [2012] model because that profile only covers $[0.82\,{\rm au}, 100\,{\rm au}]$. In our calculation, the initial gas radius is set to $r_{\rm out} \sim 140\,{\rm au}$, and the profile of Owen et al. [2012] does not cover the whole region.

Figure 4.8 illustrates the gas density distribution reconstructed based on the simulation. The disk has a more expanded structure when the simple photoevaporation profile is assumed. This is because two profiles (fiducial and simple) have different functions of r toward the outer region. The profile of Komaki et al. [2021] maintains the constant surface mass-loss profile of $\sim 3.0 \times 10^{-14}\,{\rm g\,s^{-1}\,cm^{-2}}$, while the surface mass-loss rate decreases toward the outer region, following r^{-2} in the simple fit model. Although the mass loss due to photoevaporation is different in the outer region, the choice of the photoevaporation model does not affect the dust dispersal timescale. The dust dispersal timescale reflects the observable timescale of the inner region, and the impact of photoevaporation is limited. The difference in photoevaporation in the outer region does not affect the dust dispersal timescale, but it still affects the extent of the gas distribution. We argue that it is essential to consider a realistic profile of photoevaporation to obtain a realistic distribution of disk material, which provides possible locations of planet formation.

4.3.5 Other Processes Affecting Disk Evolution

External Photoevaporation

The observations toward star-forming regions with massive stars show that disks near O-type or B-type stars tend to have lower masses and smaller radii. This rapid disk dispersal is often attributed to external photoevaporation caused by intense radiation from nearby early-type stars. Previous simulations of stellar cluster evolution suggest that the efficiency of external photoevaporation depends on the stellar density and the proximity to massive stars. These findings imply that external photoevaporation is significant in environments with strong FUV fields, with its efficiency varying across different systems.

To focus on the general processes of disk evolution, our fiducial model excludes external photoevaporation. However, understanding the diverse disk properties observed requires exploring the contribution of external photoevaporation to disk dispersal.

Haworth and Clarke [2019] conducted radiation hydrodynamics simulations and found that external photoevaporation is most effective in the outer disk regions. These regions are optically thin and less gravitationally bound to the central star. Their study provides total mass-loss rates but not the surface mass-loss profiles. To estimate the surface mass-loss

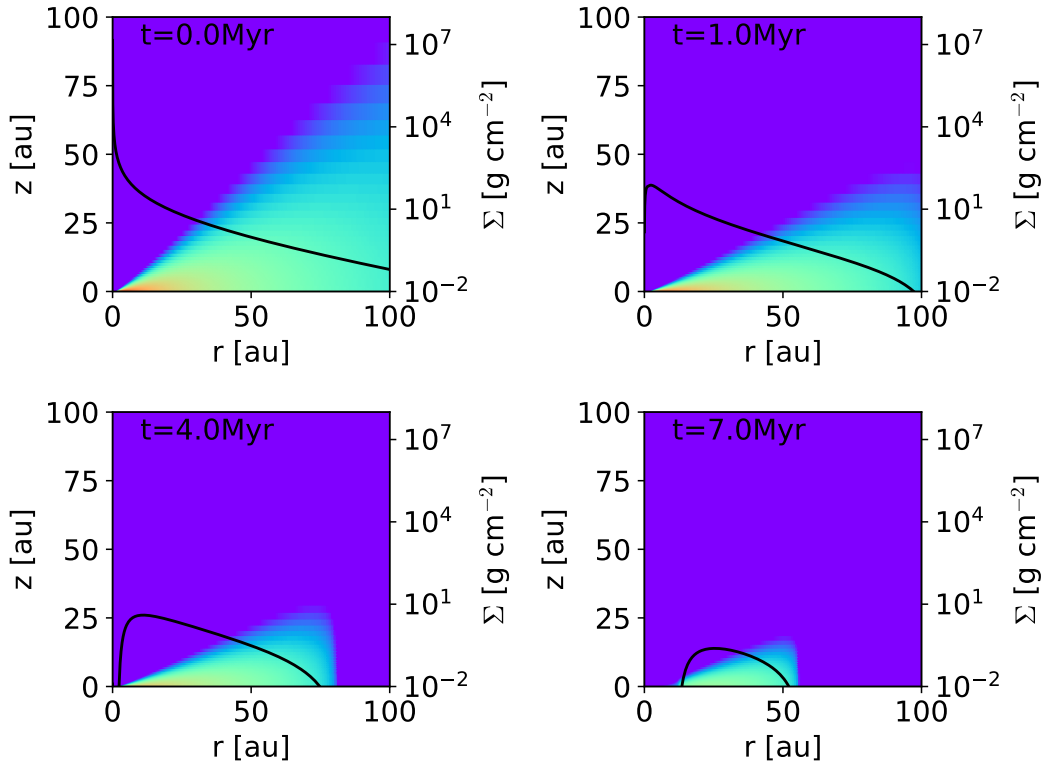

► **Figure. 4.8**

The snapshots of gas density and surface density in linear scale in the case of $M_* = 1\,\mathrm{M}_\odot$ at the age of $0, 1, 4, 7\,\mathrm{Myr}$ from the simulation which uses photoevaporation model by Owen et al. [2010]. The color map shows the gas density distribution. The color variation from purple to red corresponds to the local gas density from 10^{-20} to $10^{-10}\,\mathrm{g\,cm^{-3}}$. The black line represents the surface density. The equations solve the evolution of surface density. The local gas density is derived by assuming hydrostatic equilibrium at each radius. The radius decreases because of photoevaporation, but the decrease is not rapid compared to simulations considering photoevaporation profile by Komaki et al. [2021]. A high surface mass-loss rate around $\sim 2.5\,\mathrm{au}$ contributes to forming a cavity near the central star.

profile, we follow the approach of Weder et al. [2023], assuming:

$$\dot{\Sigma}_{\rm pe,ext} = \begin{cases} 0 \ \ (r < 0.9 r_{\rm out}) \\ \frac{\dot{M}_{\rm pe,ext}}{\pi\left(r_{\rm out}^2 - (0.9 r_{\rm out})^2\right)} \ \ (r \geq 0.9 r_{\rm out}) \end{cases}, \tag{4.24}$$

where $\dot{M}_{\rm pe,ext}$ is the mass-loss rate due to external photoevaporation from Haworth and Clarke [2019]. We assume the outer 10% of the disk radius contributes entirely to external photoevaporation.

To investigate the impact of external photoevaporation, we incorporate this surface mass-loss profile into our fiducial model. Simulations are performed with various FUV fluxes in the range of 10 to $10^5\,G_0$, while keeping other parameters unchanged. In environments with FUV fluxes below $10^4\,G_0$, the external photoevaporation rate does not exceed internal photoevaporation. For instance, the FUV flux from the central star at $r = 100\,{\rm au}$ is $100\,G_0$. The disk disperses rapidly lower than $100\,{\rm au}$. As the disk radius decreases, the region corresponding to the outer 10% of the radius moves inward. In this area, the FUV field from the central star surpasses the external FUV field, reducing the efficiency of external photoevaporation. Consequently, external photoevaporation becomes inefficient when the external FUV field is below $10^4\,G_0$.

Our simulations confirm that external photoevaporation becomes significant only under specific environmental conditions. We incorporate both internal and external photoevaporation by summing their contributions. However, this approach might overestimate mass-loss rates since outgoing gas can attenuate radiation, reducing efficiency. For future studies, it is essential to perform comprehensive radiation hydrodynamics simulations that include FUV radiation from both the central star and nearby massive stars.

Reduced Photoevaporation by Wind Shielding

We consider the main disk dispersal processes of accretion, MHD winds, and photoevaporation simultaneously but do not incorporate the interaction between them. Ercolano et al. [2009] suggested that dense winds originating from the inner disk can shield radiation from the central star, thereby inhibiting photoevaporation. As discussed in Chapter 3, we concluded that when the photoelectric effect is suppressed by lowering the dust-to-gas mass ratio, X-ray radiation and H_2 pumping begin to play a role in gas heating.

We have explicitly tested the shielding effect by running an additional simulation. We incorporate wind shielding by assuming that photoevaporation is completely turned off if the column density within $1 r_{\rm g}$ exceeds $10^{20}\,{\rm cm}^{-2}$ in the $M_* = 1\,{\rm M}_\odot$ case. This criterion is set to correspond to the location of the photoevaporative wind base (see Chapter 3.3.1). Although photoevaporation does not clear the gas in the first $0.7\,{\rm Myr}$, the estimated disk lifetime is unchanged in the case of $M_* = 1\,{\rm M}_\odot$. This is because photoevaporation is primarily effective in the outer disk, while the dust dispersal timescale, observable period in the near-infrared, is more focused on the inner disk. In contrast, the gas dissipation

timescale becomes longer by $10\,\mathrm{Myr}$ compared to the simulation without shielding.

Photoevaporation is completely turned off when the column density exceeds the criterion, which is an extreme assumption. As discussed in Chapter 3, H_2 pumping and X-ray photons become the dominant heating source when the photoelectric effect is reduced owing to less amount of dust. Therefore, the long gas dissipation timescale serves only as a longer limit of the disk lifetime.

4.4 The Evolution of Disk Fraction

4.4.1 Disk Fractions of Various Star-Forming Regions

Disks are observed more as a group than as an individual. The disk fraction is the most commonly used quantity to indicate the evolution stage of a stellar cluster. So far in this chapter, we have focused on the disk dispersal of a standard individual disk. This section discusses the difference in disk evolution due to the variation in disk parameters and the consequent disk fraction of a star-forming region. We also investigate the impact of stellar evolution on the disk fraction.

In the previous section, we focus on the stellar mass dependence of disk evolution. However, the disk evolution path is not determined solely by stellar mass; it is actually influenced by various physical parameters. The observations of star-forming regions have found a dispersion in disk mass and disk radius. These parameters could affect the disk dispersal process as well as stellar mass. We perform disk evolution simulations varying disk mass and radius in a wide range. Then, we assume a star-forming region with 10,000 systems and estimate the dust dispersal timescale of each system to calculate the disk fraction over time. Our work is the first calculation that incorporates accretion, MHD winds, photoevaporation, and stellar evolution in a consistent manner, so it is significant to evaluate the impact of each process on the disk fraction more precisely.

4.4.2 Methods

The observations toward star-forming regions showed a considerable variation in disk mass, ranging for two magnitudes, and in disk radius even within the same type of stars. The observed disk fraction means the disk survival rate among disks in various environments. In our simulation, we consider disk dispersal as the result of a combination of three major processes: accretion, MHD winds, and photoevaporation. We expect that the balance of these processes changes as we vary the physical parameters. Infrared observations showed that the disk lifetime varies by the stellar mass, and therefore theoretical studies have focused on the stellar mass dependence of disk dispersal. In the previous section, we have already clarified the stellar-mass dependence of disk dispersal. In this section, we perform disk evolution simulations varying the disk mass and radius to understand the difference in disk dispersal by physical parameters.

We first conduct one-dimensional long-term disk evolution simulations with varying disk

M_*	0.1, 0.3, 0.5, 0.7, 1.0, 1.7, 2.0, 3.0, 5.0, 7.0 $\mathrm{M}_\odot$
$M_{\rm disk}$	0.1, 0.3, 1.0, 3.0, 10 $\times 0.0117 M_*$
$R_{\rm disk}$	0.3, 0.7, 1.0, 1.3, 1.7 $\times (M_*/1\,\mathrm{M}_\odot) 30\,\mathrm{au}$

► **Table. 4.2** The list of stellar mass, disk mass, and disk radius we used for the simulations.

mass and disk radius for each stellar mass of 0.1–$1\,\mathrm{M}_\odot$. We vary the disk mass in the range of 0.0117×0.1–$10 M_*$, 10 times lower and higher compared to the fiducial value. We vary the disk radius in the range of 0.3–$1.7 \times 30\,\mathrm{au}(M_*/1\,\mathrm{M}_\odot)$. A list of physical parameters is shown in Table 3.2. We perform 250 disk evolution simulations with a combination of stellar mass, disk mass, and disk radius parameters.

Disk observations are conducted toward star-forming regions, and there have been a number of statistical analyses of disk evolution as in a group. Since the disk fraction is one of the limited features obtained from disk observations, it provides an important way to compare our model with observations. We calculate the disk fraction by setting an ideal stellar cluster. We generate a mock stellar cluster with 10000 systems in it. We choose a large number of stars, 10000, to focus on the general evolution of disk fraction in a statistically complete manner. To recreate the diversity in the region, various disks with various physical parameters (stellar mass, disk mass, and disk radius) are considered.

We generate 10,000 systems as cluster members, and the parameters of each system are chosen by Monte-Carlo sampling. Since it is computationally expensive to perform a long-term disk evolution simulation for each of the 10,000 disks, we estimate the dust dispersal timescale of each disk by interpolating the dust dispersal timescale of 250 disks shown above. The number of surviving disks in the system is counted over time to trace the evolution of the disk fraction. In order to make sure Monte-Carlo sampling reproduces the dust dispersal timescale, we randomly choose four sets of parameters and perform long-term disk evolution simulations with the parameter sets. Then, we calculate the dust dispersal timescale and compare it to the estimated value, which is interpolated from the results of the 250 disks. The difference was at most $0.65\,\mathrm{Myr}$, less than 10% of the original timescale.

We assume that the distribution of stellar mass follows the IMF suggested by Kroupa [2002], which is given by

$$\begin{aligned} \xi(m) &\propto m^{-\alpha} \\ \alpha &= 1.3 \,(0.1\,\mathrm{M}_\odot < m \leq 0.5\,\mathrm{M}_\odot) \\ \alpha &= 2.3 \,(0.5\,\mathrm{M}_\odot < m). \end{aligned} \tag{4.25}$$

We set the lower limit to $0.1\,\mathrm{M}_\odot$ because that roughly corresponds to the observation limit [Michel et al., 2021]. We do not consider disks around massive stars with $M_* > 7\,\mathrm{M}_\odot$. As the IMF shows, there is more weight on lower-mass stars, limiting the number of massive stars. Since disks around massive stars have short lifetimes, the absence of massive stars

has a limited effect on the disk fraction.

The observations toward class 0 and class I disks show that the dispersion in disk mass is expressed as $\sigma = 0.35$ dex in a log-normal Gaussian distribution [Tychoniec et al., 2018]. Because of this large dispersion, it is difficult to infer the dependence of disk mass on stellar mass. Some research concluded that disk mass increases proportionally to stellar mass as $M_{\rm disk} \propto M_*$ [Ansdell et al., 2016, Andrews, 2020]. In contrast, other research does not find a clear relation between stellar mass and disk mass [Ruíz-Rodríguez et al., 2018]. Another research even found a more steep relation between stellar mass and disk mass, given as $M_{\rm disk} \propto M_*^{1.8}$ [Pascucci et al., 2016]. In our calculation, we assume a proportional relation because we later compare our results with the observations by Ansdell et al. [2016].

The same can be said about the disk radius, but the situation is more complicated because there is no certain way to determine the disk radius. This is because the gas is thin in the outer region, and we cannot clearly define the disk radius. Observationally, Cieza et al. [2021] used ALMA data from Ophiuchus and defined the disk radius as the position within which 90% of the observed energy is emitted. The radius of the observed disk varies in the range of 53–$256\,{\rm au}$. On the other hand, Eisner et al. [2018] fitted the observed flux distribution with the Gaussian distribution. They obtain the cut-off radius of $r_{\rm cut} = 10$–$30\,{\rm au}$. They found the dependence of disk radius on stellar mass, while the others do not [Hendler et al., 2020]. For simplicity, we assume that the disk radius is proportional to the stellar mass. The dispersion is given as $\sigma = 0.1$ dex in a log-normal Gaussian distribution [Tobin et al., 2020]. The observed disks are mainly in the stage of class 0 and class I. Observing disks at a relatively early stage provides information on the initial stage of disk evolution. This is beneficial for our calculation, which aims to understand disk dispersal from the very beginning.

Figure 4.9 shows the distribution of stellar mass, disk mass, and disk radius, which is chosen by Monte-Carlo sampling. The calculated dust dispersal timescales of 250 disks and 10000 disks for the generated stellar cluster are also shown in Figure 4.10.

Several previous works have shown the observed evolution of disk fractions. We compare our results with those of the observations and discuss them in the following sections.

4.4.3 Diverse Evolution of Protoplanetary Disks

We performed long-term disk evolution simulations with 250 different parameter sets. We discussed the stellar-mass dependence in the previous section. Now, we want to focus on the distinct disk evolution as a result of the varied disk mass and radius.

The estimated dust dispersal timescale increases more drastically with increased disk mass than with disk radius. Around a $M_* = 1\,{\rm M}_\odot$ star, the dust dispersal timescale increases as the disk mass increases following $\propto M_{\rm disk}^{0.40}$ because there is more gas to disperse. Since the criterion for the dust dispersal timescale contains $\Sigma_{\rm dust} \geq 0.1\,{\rm g\,cm^{-2}}$, it takes a longer time for the surface density to decrease to a certain value. Still, the dust dispersal timescale does not increase by a factor of 10 when the initial disk mass is set to be 10 times larger than the fiducial value because the mass-loss rates by accretion and MHD winds also

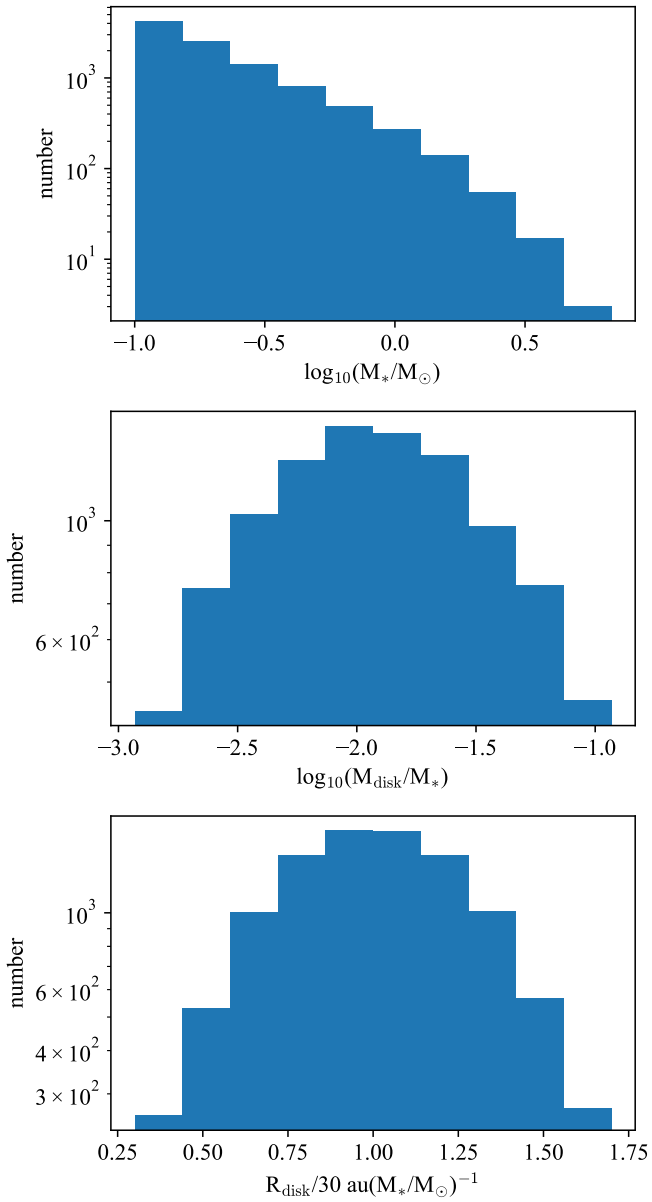

► **Figure. 4.9**

The distributions of stellar mass, disk mass, and disk radius adopted in our calculation are shown for a sample of 10,000 disks. The stellar mass distribution follows the Initial Mass Function (IMF), while the disk mass and disk radius are assumed to follow Gaussian distributions. The standard deviations for disk mass and disk radius are set to $\sigma = 0.35$ dex and $\sigma = 0.1$ dex, respectively.

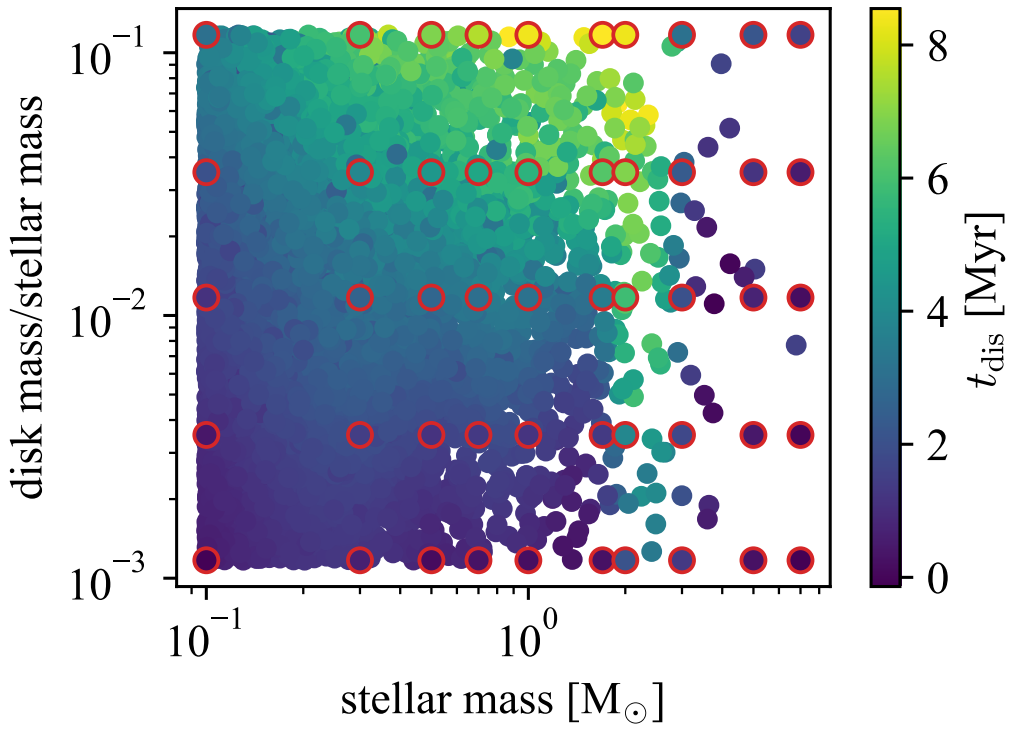

► **Figure. 4.10**

The parameter sets of stellar mass and disk mass for 10,000 disks are shown. The color scale represents the dust dispersal timescale. The color variation from black to yellow corresponds to the dust dispersal timescale from 0 to $8\,\mathrm{Myr}$. The plots with red circles indicate the dust dispersal timescales calculated based on simulations for 250 parameter sets. These simulation results are used to interpolate the dust dispersal timescales for the 10000 samples.

increase. Both mass-loss profiles depend on the surface density; therefore, the mass-loss rates increase as the initial disk mass increases. The dust dispersal timescale represents the observable timescale of the inner region, covering a few au, where accretion and MHD winds primarily drive gas dispersal.

The mass-loss rate of photoevaporation is also enhanced because the main source of FUV radiation is accretion-origin, and the FUV luminosity increases as the accretion rate increases because of the high surface density. In the fiducial case, the main component of FUV luminosity is the chromospheric origin, but it is replaced by the accretion origin when the initial disk mass is increased by a factor of 10. The main FUV component is the energy released by accretion until the age of $15\,\mathrm{Myr}$, but it is replaced by the chromospheric origin as the accretion rate decreases over time. Previous research has assumed that the main FUV component is energy liberated by accretion. However, this is not true in the fiducial case and only applies to models with high initial disk mass. We highlight the importance of calculating the FUV luminosity based on stellar evolution at each time step when performing long-term disk evolution.

In the case of $M_* = 3\,\mathrm{M}_\odot$, the dust dispersal timescale does not increase with the increase in disk mass as in the case of $M_* = 1\,\mathrm{M}_\odot$. It takes a longer time to disperse gas for a massive disk. The central star reaches the main sequence at $\sim 2.5\,\mathrm{Myr}$, exposing the disk to intense FUV radiation for extended periods. The disk disperses quickly after that, so the dust dispersal timescale does not increase as the initial disk mass increases. As a result, the dust dispersal timescale increases with the disk mass, following $\propto M_{\mathrm{disk}}^{0.17}$. It is essential to compare the timings when the star reaches the main sequence and when the disk completely disperses.

The dust dispersal timescale does not show a clear correlation with the disk radius as with the disk mass. As the disk cut-off radius increases, the disk has a more extended structure, which increases the mass-loss rate due to photoevaporation because it is dominant in the outer region. When the disk radius is small, the gas is more concentrated near the central star. Since surface mass-loss profiles of both accretion and MHD winds are proportional to the local surface density, the dust dispersal timescale is unchanged as the initial disk radius decreases. In our calculation, the initial magnetic fields depend on the initial surface density, and the magnetic lines are preserved throughout the simulation. The surface density of the innermost radius of $r = 0.01\,\mathrm{au}$ increases by 6% when the disk cut-off radius is reduced to 30% of the fiducial value, and consequently, the impact of varying the disk radius is minimal.

4.4.4 Evolution of Disk Fraction

Figure 4.11 shows the evolution track of the disk fraction along with recent observation results compiled by Pfalzner et al. [2022]. They sort out stellar clusters by whether the region is a dense cluster or a sparse cluster. The disk fractions of dense clusters are plotted in green, and those of sparse clusters are plotted in red. The disk fractions of dense clusters are low because the disks are sited in an intense radiation field and, therefore, are dispersed quickly by photoevaporation.

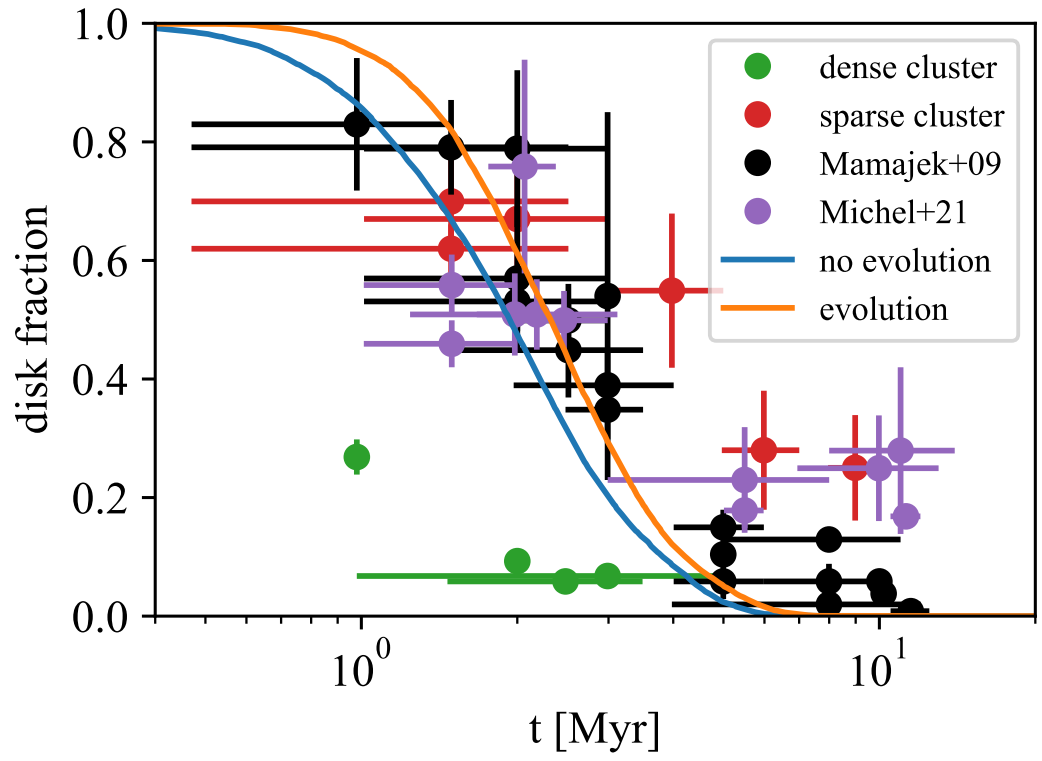

► **Figure. 4.11**

The disk fraction evolution over time. The blue and orange lines represent the results of calculations with and without stellar evolution, respectively. The plots represent the observed disk fraction toward each stellar cluster. The black and purple plots represent observations by Mamajek [2009] and Michel et al. [2021]. The red and green plots represent the observation results toward sparse and dense clusters compiled by Pfalzner et al. [2022]. The disk fractions of dense clusters are thought to be low because of the influence of FUV field flux from nearby stars, which enhances photoevaporation. The change in stellar luminosity due to transition to the main sequence affects the dust dispersal timescale from solar to intermidiate-mass stars. This effect is reflected in the evolution of disk fraction.

The calculated disk fraction decreases rapidly within $\sim 3\,\mathrm{Myr}$. The decline in disk fraction within a few million years is in agreement with observational data. Since our calculations exclude external photoevaporation to focus on a more generalized disk evolution process, it is significant that our model successfully reproduces the observed trends in sparse clusters. Because the standard IMF predicts that a large number of stars are low-mass stars, the disk fraction strongly reflects the disk survival rate around low-mass stars. Figure 4.6 shows that disks around low-mass stars have short lifetimes within $t_{\mathrm{dis}} \sim 2\,\mathrm{Myr}$, which leads to a significant decrease in the disk fraction. However, the calculated disk fraction decreases after that and becomes below 1% until the age of $6.5\,\mathrm{Myr}$, while the observed disk fraction is still $\sim 20\%$ at the age of $10\,\mathrm{Myr}$. The purple plots in Figure 4.11 show the recent observation results of Michel et al. [2021]. They observed class III stars in nearby stellar clusters within $200\,\mathrm{pc}$. As Pfalzner et al. [2022] suggests, recent disk observations have less observation luminosity limits, which means more samples are collected and provides a more comprehensive statistical analysis. Several possible explanations are proposed for the difference in disk fraction at the later stage. Michel et al. [2021] suggests that the formation of dust rings can elongate the disk observable timescale up to $8\,\mathrm{Myr}$. Dust grains are trapped and form dust rings instead of accreting onto the central star. We assume a smooth distribution for the initial gas and dust distribution profile. Thanks to the high-resolution observations, mainly by ALMA, many disks were found to have substructures. Substructured disks are observed with brighter signalsMichel et al. [2021]. Including the effect of dust traps may align the disk fraction more closely with observations. The other reason is the difference in the stellar mass distribution. We assume that the stellar mass distribution follows the IMF suggested by Kroupa [2002]. However, the actual observations of star-forming regions show that the mass distribution of observed stars does not perfectly follow the IMF. Since the calculated disk fraction is determined by the survival rate of disks around the smallest star of $0.1\,\mathrm{M}_{\odot}$, the observation luminosity limit for faint sources can affect the disk fraction. The details are discussed in the next section.

Figure 4.11 also shows the difference in the calculated disk fraction between simulations with and without stellar evolution. We derived the evolution of the disk fraction without including stellar evolution to clarify the impact of stellar evolution. In the previous section, we clarified that the dust dispersal timescale is affected by the variation in FUV luminosity due to stellar evolution around solar to intermediate-mass stars.

It is worth examining whether there is any apparent difference in disk fraction between models with and without stellar evolution. We derived the evolution of the disk fraction in the same way as in the calculation with stellar evolution. We first performed disk evolution simulations with 250 sets of parameters. Then, we estimate the dust dispersal timescale of 10000 disks whose physical parameters are chosen by Monte-Carlo sampling. The disk fraction decreases more rapidly than the model with stellar evolution. When stellar evolution is incorporated, the disk fraction increases by $\sim 20\%$ at the age of $2\,\mathrm{Myr}$. The dust dispersal timescale increases for $0.5\,\mathrm{M}_{\odot} \leq M_{*} \leq 1\,\mathrm{M}_{\odot}$. The disk fraction is determined mainly by the dust dispersal timescales for low-mass stars. The change in disk fraction between calculations with and without stellar evolution is relatively small compared to the

error bars in observations. It is still necessary to incorporate stellar evolution to understand the individual disk evolution of solar to intermediate-mass stars.

The comparison of disk fractions suggests the dependence of the disk lifetime on stellar mass. We sort out disks by central stellar mass and calculate the disk fraction of each group. We classify the groups into low-mass stars ($M_* < 1\,\mathrm{M}_\odot$), intermediate-mass stars ($1\,\mathrm{M}_\odot \leq M_* \leq 3\,\mathrm{M}_\odot$), and massive stars ($M_* > 3\,\mathrm{M}_\odot$). The evolution of the disk fraction of each group is shown in Figure 4.12. Figure 4.12 also shows the results of the observations by Ribas et al. [2015]. They observed eleven star-forming regions and sorted the systems by their age and mass. The boundary is $M_* = 2\,\mathrm{M}_\odot$ and $3\,\mathrm{Myr}$. Since our calculation shows that the dust dispersal timescale peaks around $M_* = 2\,\mathrm{M}_\odot$, the stellar mass distribution is crucial if the disk fraction of massive stars is lower than that of low-mass stars, as suggested by previous observations.

We performed disk evolution simulations with other disk dispersal models, such as the model with strong winds and no-B-field cases. Comparison between simulations with each model suggests that the disks around low-mass stars are more sensitive to the disk model. When MRI is inactive, the dust dispersal timescale exceeds $100\,\mathrm{Myr}$. There is still a debate about how much MRI is active and what the effective turbulence parameter should be. The calculated disk fraction of low-mass stars may be underestimated.

4.4.5 Comparison with Observations

We assume the general stellar mass distribution of IMF because we want to understand the general characteristics of the evolution of the disk fraction. The observed stellar mass distribution varies by each system. As seen in the previous section, the stellar mass has a great impact on determining the major disk dispersal process and resulting dust dispersal timescale. Therefore, it is necessary to use the individual set of parameters for the observed disks to compare the disk fractions with the observations. We choose two star-forming regions, Lupus and eta Cha, which are relatively young and old regions. Then, we calculate the disk fraction with the observed stellar mass distribution. While we choose stellar mass based on observations, the disk mass and disk radius are set to be fiducial values of $M_{\mathrm{disk}} = 0.0117(M_*/1\,\mathrm{M}_\odot)\,\mathrm{M}_\odot$ and $r_{\mathrm{cut}} = 30(M_*/1\,\mathrm{M}_\odot)\,\mathrm{au}$. The dust dispersal timescale of each disk is estimated by interpolating 250 disks, which are derived by performing simulations varying stellar mass, disk mass, and disk radius with a weak wind model. In the following section, we discuss the derived disk fraction and understand the observed trend in disk fraction.

The first target is Lupus. Lupus is a relatively young star-forming region with an average age of 1–$3\,\mathrm{Myr}$ [Ansdell et al., 2016]. The disks are mainly classified as in the evolutional stage of class II. Ansdell et al. [2018] has thoroughly researched disks in Lupus. Although Ansdell et al. [2018] identified 91 disks in the region, we employed 76 disks out of them because the stellar mass of these systems is already confirmed by Alcalá et al. [2014]. The number of stars increases as the stellar mass decreases, and this trend roughly aligns with the IMF. We calculate the evolution of disk fraction incorporating the combination of stellar mass.

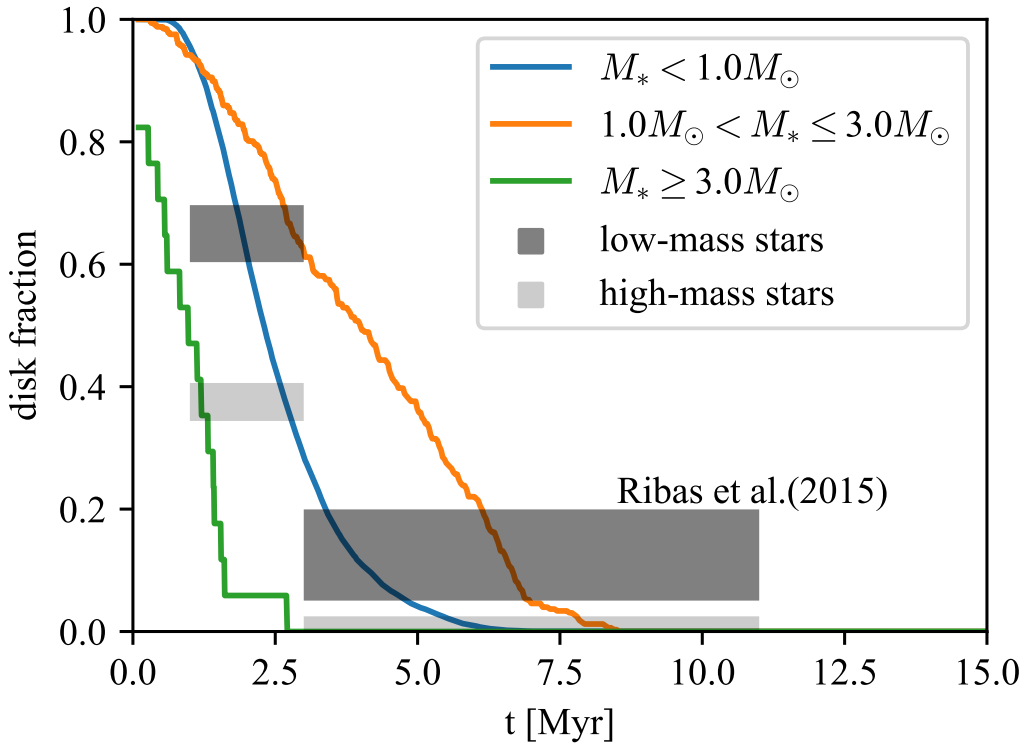

► **Figure. 4.12**

The disk fractions of each group: low-mass ($M_* < 1\,\mathrm{M}_\odot$), intermediate-mass ($1\,\mathrm{M}_\odot \leq M_* \leq 3\,\mathrm{M}_\odot$), and high-mass ($M_* > 3\,\mathrm{M}_\odot$). The disk fraction of high-mass stars is lower than other groups and this trend aligns with the observations. The disk fraction of intermediate-mass stars is the highest because of the long dust dispersal timescale around $\sim 2\,\mathrm{M}_\odot$. The box shows the disk fractions obtained by observation toward 11 star-forming regions Ribas et al. [2015]. They classified the stars by their ages and masses. The disk fraction of low-mass stars ($M_* < 2\,\mathrm{M}_\odot$) is shown in dark gray and that of low-mass stars ($M_* \geq 2\,\mathrm{M}_\odot$) is shown in light gray. The age criterion is set at $3\,\mathrm{Myr}$. Observations confirm that the disk fraction of high-mass stars drops to zero at an earlier age than for low-mass stars, suggesting a rapid decrease in disk fraction around high-mass stars.

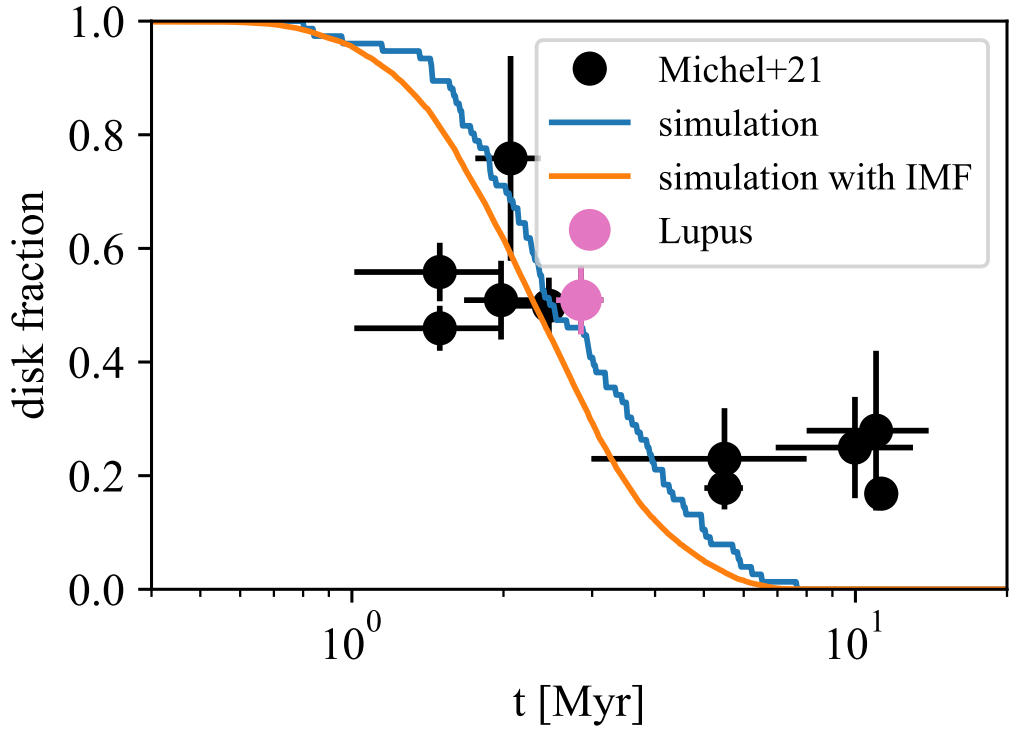

► **Figure. 4.13**

The time evolution of disk fraction derived from the simulations using the stellar mass distribution observed in Lupus (blue) and of the IMF (orange). Observed disk fractions for various stellar clusters are plotted [Michel et al., 2021], with Lupus highlighted in pink. The difference in stellar mass distribution results in variations in disk fraction evolution. Simulations using the observed Lupus stellar mass distribution better match the observed value, emphasizing the importance of considering stellar mass distribution when comparing disk fractions across different clusters.

Figure 4.13 shows the comparison between the observed disk fraction and the calculated disk fraction with the observed stellar mass distribution. The figure also shows the disk fraction of 10000 disks, calculated with the designated IMF. The calculated disk fraction shows good alignment with the observation.

The second target is η Cha [Lyo et al., 2004, Bell et al., 2015]. η Cha is a star-forming region at the age of 8–$14\,\mathrm{Myr}$ and the distance is $94\,\mathrm{pc}$ away from the Earth. The number of observed disks is 18: 1 class I, 5 class II, and 12 class III. The region reaches the last phase of disk dispersal judging from the age. However, the disk fraction is $28 \pm 14\%$, which is high for a region of such age. We calculate the evolution of disk fraction incorporating the combination of stellar mass.

Figure 4.14 shows the comparison between the observed disk fraction and the calculated disk fraction with the observed stellar mass distribution in η Cha. The figure also shows the disk fraction of 10000 disks, which is calculated with the assumption of the IMF. The calculated evolution of disk fraction is bumpy because the number of stars in the system is only 18. The disk fraction increases by 25% at the age of $3\,\mathrm{Myr}$ when the stellar mass distribution is set to reproduce the observed distribution of η Cha. The disks observed for an extended time of $10\,\mathrm{Myr}$ are attributed to the formation of substructures such as rings and gaps. Once the substructure is formed, it accumulates dust grains and keeps the disk observable for a long time.

Two comparisons with observations toward each system show the impact of assumed stellar mass distribution. The mass distribution of the IMF is assumed in our calculation, while the number of stars in the smallest mass bin is not the largest in the observation toward η Cha. Since the dust dispersal timescale of $M_* = 0.1\,\mathrm{M}_\odot$ is within $2\,\mathrm{Myr}$, the lack of low-mass stars in observation results in the higher disk fraction. This effect becomes even more apparent when the sample number is low. Previous research has treated the disk fraction of each cluster equally, assuming that all regions have the same initial conditions, but this is not always true. Our result indicates that the variation of physical parameters, such as stellar mass distribution, should be considered when analyzing the observed features.

4.5 Low-Metallicity Case

4.5.1 Low Disk Fraction in Low-Metallicity Environments

Observations of stellar clusters in low-metallicity regions showed a lower disk fraction compared to nearby star-forming regions. This indicates that disk dispersal processes are more effective in low-metallicity environments.

Theoretical studies have explored how reduced metallicity influences photoevaporation. Nakatani et al. [2018b] performed radiation hydrodynamics simulations across a metallicity range of 0.001–$3\,\mathrm{Z}_\odot$. Their results show that the mass-loss rate peaks at $Z = 0.03\,\mathrm{Z}_\odot$. The reduced abundance of dust grains leads to lower dust opacity, while the efficiency of the photoelectric effect decreases as the metallicity declines. Similar findings were reported

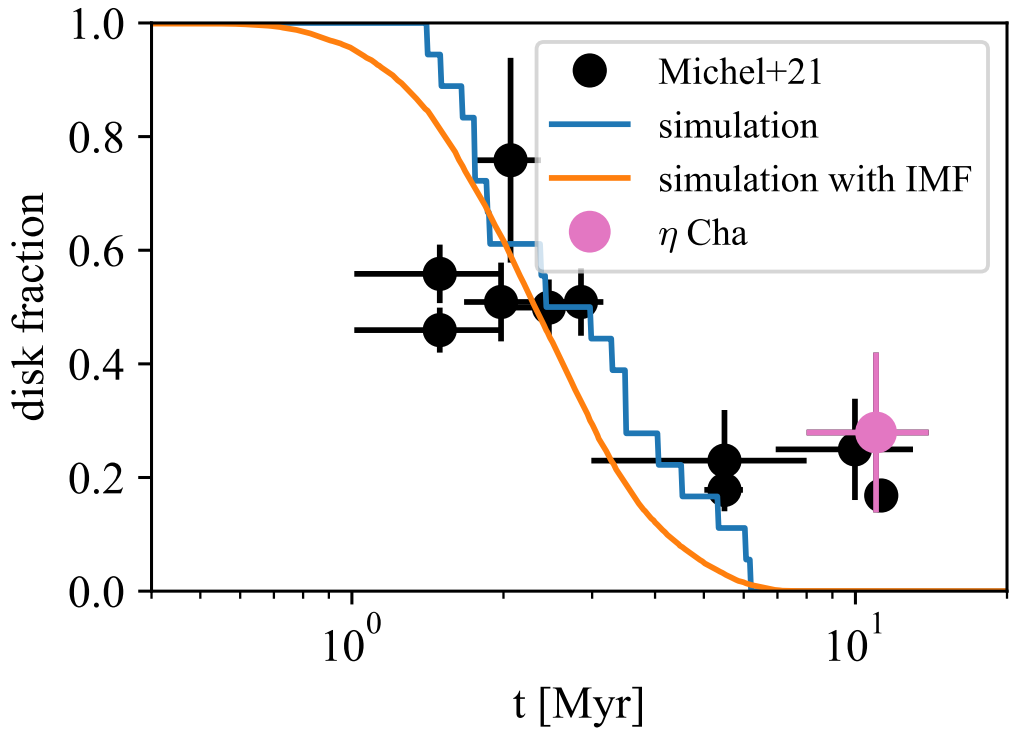

► **Figure. 4.14**

The time evolution of disk fraction derived from the simulations using the stellar mass distribution observed in η Cha (blue) and of the IMF (orange). Observed disk fractions for various stellar clusters [Michel et al., 2021] are plotted, with η Cha highlighted in pink. Differences in stellar mass distribution lead to variations in disk fraction evolution. Simulations using the observed stellar mass distribution of η Cha align more closely with the observed value. However, the high disk fraction observed at the final stage cannot be explained solely by changes in stellar mass distribution. The high disk fraction at the final stage is attributed to the formation of dust substructures.

by Wölfer et al. [2019]. At the same time, Pfalzner et al. [2022] highlights the role of observational selection bias in distant stellar clusters, suggesting that observed disk fractions may be influenced by observational limits rather than intrinsic differences. It remains under discussion whether disks in low-metallicity environments undergo distinct evolutionary processes.

Previous theoretical studies focused only on how changes in disk material lead to distinct disk dispersal. Since stars and disks form from the same molecular cloud, stars in such environments are expected to have lower metallicity. Stars with lower metallicity evolve faster to the main sequence because reduced opacity enhances energy transport and emission. For stars with $M_* \geq 3\,\mathrm{M}_\odot$, this transition significantly increases FUV luminosity, leading to rapid disk dispersal. These disks are exposed to strong FUV radiation early in their evolution. In contrast, solar-mass stars do not reach the main sequence during simulations, and their luminosity decreases gradually along the Hayashi track.

Whether a star reaches the main sequence before its disk disperses is a key factor in determining the role of stellar evolution in disk dispersal. A shorter pre-main-sequence phase can change the relative importance of photoevaporation in disk evolution. To investigate this, we conduct long-term disk evolution simulations with $Z = 0.1\,\mathrm{Z}_\odot$, focusing on the mechanisms that shorten dust dispersal timescales in low-metallicity environments. Our work is the first to explore the effects of a low-metallicity environment on disk dispersal.

4.5.2 Methods

We perform disk evolution simulations with $Z = 0.1\,\mathrm{Z}_\odot$ to investigate disk dispersal in low-metallicity environments. In the Galaxy, metallicity decreases gradually from the inner to the outer regions, ranging from 3 to $0.1\,\mathrm{Z}_\odot$. Observations often focus on the outer Galaxy to study disk fractions in low-metallicity environments. Based on this, our study specifically examines the case of $Z = 0.1\,\mathrm{Z}_\odot$.

Our method combines two simulation approaches introduced in earlier chapters. First, we conduct radiation hydrodynamics simulations of photoevaporation with $Z = 0.1\,\mathrm{Z}_\odot$ for stellar masses of $M_* = 0.5, 1, 3\,\mathrm{M}_\odot$. These stellar masses represent low-mass, solar-mass, and intermediate-mass stars, allowing us to evaluate the effects of low metallicity across different types of stars. In these simulations, we solve radiative transfer, hydrodynamics, and non-equilibrium thermochemistry to derive the surface mass-loss rate caused by photoevaporation. This rate is calculated in the same manner as described in Chapter 3.3.3.

Next, we incorporate the derived surface mass-loss rate into long-term disk evolution simulations. These simulations include accretion, MHD winds, and photoevaporation as key disk dispersal processes. The detailed methodology for long-term simulations is provided in Chapter 4.2. We assume the 'weak wind case' for MHD winds and use a low viscosity parameter, $\overline{\alpha_{r\phi}} = 10^{-4}$ because this setup aligns best with observed disk fractions in solar-metallicity environments.

Previous studies on disk dispersal in low-metallicity environments have mainly focused on enhanced photoevaporation. However, photoevaporation is only one of several processes causing disk dispersal. It is important to verify whether the trends observed

in photoevaporation studies hold when all major disk dispersal processes are considered comprehensively.

To estimate the dust dispersal timescale, we use the same criterion as in the solar metallicity case. Our simulations provide the evolution of gas surface density, while observations often focus on dust distribution. The dust surface density is derived by multiplying the gas surface density by the dust-to-gas mass ratio. For the solar metallicity case, we assume $\mathcal{D} = 0.03$ at the final stage of disk dispersal, based on simplified simulations that include both gas and dust components [Gorti et al., 2015].

In low-metallicity environments, the evolution path of dust grains may differ, making the dust-to-gas mass ratio at the final stage less certain. For our simulations, we assume $\mathcal{D} = 0.003$, which is ten times lower than in the solar metallicity case. Later, we discuss how this assumption influences the derived dust dispersal timescales.

Three major differences distinguish the low-metallicity case from the solar metallicity case: the stellar evolution modeled by MESA, the photoevaporation mass-loss profile, and the assumed dust-to-gas mass ratio at the final stage.

4.5.3 Results

We first introduce the results of radiation hydrodynamics simulations for metallicities in the range of 0.01–$1\,\mathrm{Z}_\odot$. Figure 4.15 shows the photoevaporation mass-loss rate for each metallicity case, scaled to the solar metallicity case. The plot represents a time-averaged value from 840 to 8400 years to minimize the impact of initial numerical turbulence. The photoevaporation rate is calculated as the gas mass crossing the spherical surface at $r = 100\,\mathrm{au} \times (M_*/\,\mathrm{M}_\odot)$ (see Eq. 3.20). The metallicity dependence of the photoevaporation rate varies with stellar mass.

For the low-mass case of $M_* = 0.5\,\mathrm{M}_\odot$, the photoevaporation mass-loss rate remains nearly constant across all metallicities. As metallicity decreases, the dust grain abundance also decreases proportionally. This reduction lowers the gas heating efficiency by the photoelectric effect. In the solar metallicity case, FUV photons are the primary heating source through the photoelectric effect. At lower metallicities, X-ray photons replace FUV photons as the main heating source, maintaining a consistent mass-loss rate.

For the solar-mass case of $M_* = 1\,\mathrm{M}_\odot$, the mass-loss rate peaks at $Z = 0.1\,\mathrm{Z}_\odot$. At this metallicity, the photoelectric effect remains the dominant heating process on the disk surface. The reduced opacity due to fewer dust grains allows FUV photons to penetrate deeper into the disk, driving dense gas flows and increasing the mass-loss rate. Below $Z = 0.1\,\mathrm{Z}_\odot$, the mass-loss rate declines because the reduced dust abundance renders the photoelectric effect less effective. In this case, X-ray photons become the dominant heating source. These results agree with Nakatani et al. [2018b], the first study to examine the metallicity dependence of photoevaporation. A key distinction in our work is the inclusion of H_2 pumping in the chemical network. As shown in Chapter 3, the heating contribution from H_2 pumping is comparable to that from X-ray photons, which explains the consistency with prior simulations.

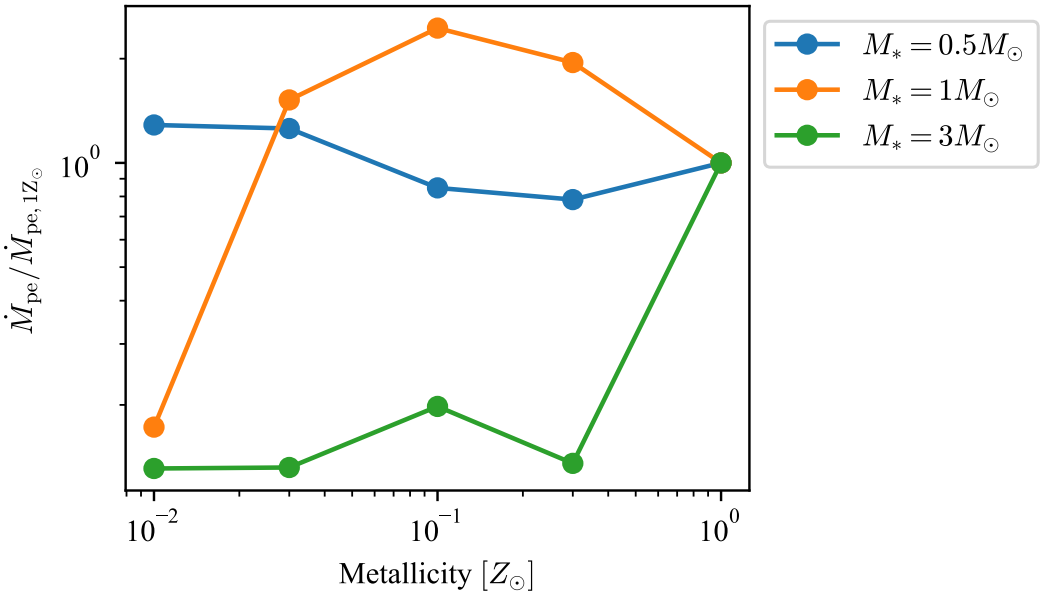

► **Figure. 4.15**

The photoevaporation mass loss rate of $M_* = 0.5\,\mathrm{M}_\odot$ (blue), $M_* = 1\,\mathrm{M}_\odot$ (orange), $M_* = 3\,\mathrm{M}_\odot$ (green) varying the metallicity in the range of 10^{-2}–$1\,\mathrm{Z}_\odot$. In the case of $M_* = 0.5\,\mathrm{M}_\odot$, the mass-loss rate stays constant because X-ray photons replace FUV photons as the dominant heating source. In the case of $M_* = 1\,\mathrm{M}_\odot$, the mass-loss rate peaks at $Z = 0.1\,\mathrm{Z}_\odot$ because of low attenuation caused by reduced dust abundance. In the case of $M_* = 3\,\mathrm{M}_\odot$, the mass-loss rate is low for $Z < 1\,\mathrm{Z}_\odot$ because intermediate-mass stars have low X-ray luminosity.

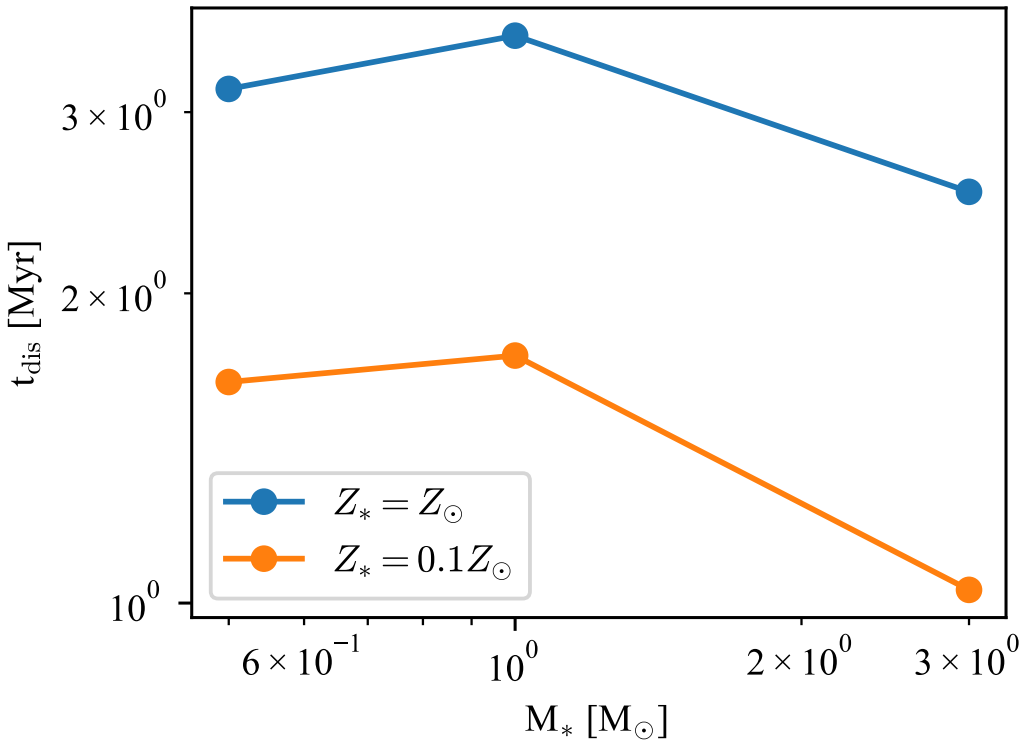

► **Figure. 4.16**

The dust dispersal timescales of $M_* = 0.5, 1, 3\,\mathrm{M}_\odot$ with solar metallicity (blue) and 10 times lower metallicity (orange) calculated by long-term disk evolution simulations. The dust dispersal timescales are shorter in low-metallicity cases for all stellar masses, with values below $2\,\mathrm{Myr}$. These short timescales are consistent with observations indicating a low disk fraction and rapid disk dispersal in low-metallicity environments.

For the intermediate-mass case of $M_* = 3\,\mathrm{M}_\odot$, the mass-loss rate decreases as the metallicity is reduced from solar values. The reduced efficiency of the photoelectric effect directly lowers the mass-loss rate. Across all metallicities below solar, X-ray photons are the dominant heating source, leading to a reduced mass-loss rate. The dependence of photoevaporation on metallicity varies with stellar mass, primarily because of differences in the relative efficiency of X-ray heating.

We also perform disk evolution simulations for $Z = 0.1\,\mathrm{Z}_\odot$. Figure 4.16 shows the dust dispersal timescales for both solar and low-metallicity cases. For all stellar masses considered ($M_* = 0.5, 1, 3\,\mathrm{M}_\odot$), the dust dispersal timescale is shorter in low-metallicity environments. The timescale is within $2\,\mathrm{Myr}$ for all cases.

To identify factors that shorten the dust dispersal timescale in low-metallicity environments, we perform additional disk simulations. These simulations isolate the effects of each metallicity-related update: stellar evolution, surface mass-loss rate, and

	stellar parameters	$\dot{\Sigma}_{\rm pe}$	$\mathcal{D}$
$Z = \mathrm{Z}_\odot$ case	$Z = \mathrm{Z}_\odot$	$Z = \mathrm{Z}_\odot$	$Z = \mathrm{Z}_\odot$
$Z = 0.1\,\mathrm{Z}_\odot$ case	$Z = 0.1\,\mathrm{Z}_\odot$	$Z = 0.1\,\mathrm{Z}_\odot$	$Z = 0.1\,\mathrm{Z}_\odot$
case A	$Z = 0.1\,\mathrm{Z}_\odot$	$Z = \mathrm{Z}_\odot$	$Z = \mathrm{Z}_\odot$
case B	$Z = \mathrm{Z}_\odot$	$Z = 0.1\,\mathrm{Z}_\odot$	$Z = \mathrm{Z}_\odot$
case C	$Z = \mathrm{Z}_\odot$	$Z = \mathrm{Z}_\odot$	$Z = 0.1\,\mathrm{Z}_\odot$

► **Table. 4.3** The list of stellar mass, disk mass, and disk radius we used for the simulations. Case A, B, C correspond to the additional simulations in which one of the three parameters is set to $Z = 0.1\,\mathrm{Z}_\odot$ value in order to investigate the cause of short dust dispersal timescale.

the dust-to-gas mass ratio at the final stage. Each parameter is updated individually to the $Z = 0.1\,\mathrm{Z}_\odot$ value. The parameter sets for each calculation are listed in Table 4.3.

Figure 4.17 shows the dust dispersal timescales for the simulations in which each parameter is individually updated to the $Z = 0.1\,\mathrm{Z}_\odot$ value.

For $M_* = 0.5\,\mathrm{M}_\odot$, the dust dispersal timescale is the same as in the solar-metallicity case, when the stellar parameters and the surface mass loss profile are updated to the $Z = 0.1\,\mathrm{Z}_\odot$ values. The stellar luminosity gradually decreases along the Hayashi track, and the star does not reach the main sequence before the disk disperses. The photoevaporation rate shows little variation with metallicity and does not significantly impact overall disk dispersal. The lower dust-to-gas mass ratio in the final stage shortens the dust dispersal timescale. Disks around low-mass stars in low-metallicity environments become less observable as a result of dust deficiency, but the absence of dust grains does not strongly influence disk evolution. Observations of Hα emission lines from accreting gas in the Small Magellanic Cloud (SMC) indicate that gas dissipation timescales are not shorter in low-metallicity environments. This aligns with our finding that dust disks become unobservable earlier than the gas components.

For $M_* = 1\,\mathrm{M}_\odot$, the dust dispersal timescale decreases because of enhanced photoevaporation and a lower dust-to-gas mass ratio. Low metallicity accelerates stellar evolution by enabling efficient radiative energy transfer, allowing the star to reach the Henyey track before the disk disperses. The effective temperature increases during this phase, but this increase does not significantly alter the dust dispersal timescale. The chromospheric-origin FUV radiation dominates, with FUV photons penetrating deeper into the disk in the $Z = 0.1\,\mathrm{Z}_\odot$ case. These photons drive dense photoevaporative flows, particularly in the outer regions, which contribute substantially to disk dispersal.

For $M_* = 3\,\mathrm{M}_\odot$, stellar evolution has the greatest impact on the dust dispersal timescale. The star reaches the main sequence within $0.5\,\mathrm{Myr}$, and its FUV luminosity increases by three orders of magnitude. Initially, chromospheric radiation dominates FUV emission, but after transitioning to the main sequence, photospheric radiation becomes the primary source. The photoevaporation rate, proportional to $L_{\rm FUV}^{0.55}$, increases by a factor of 45. After the transition to the main sequence, photoevaporation becomes the dominant dispersal process and rapidly clear the disk gas, especially in the outer regions. The final dust-to-gas

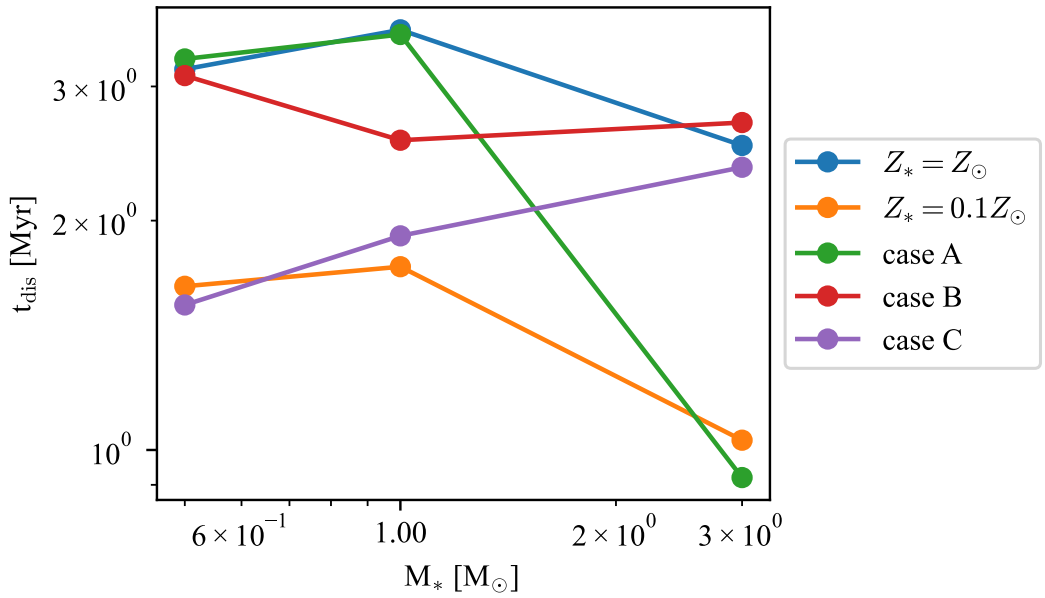

► **Figure. 4.17**

The dust dispersal timescales of $M_* = 0.5, 1, 3\,M_\odot$ with solar metallicity (blue), 10 times lower metallicity (orange), and additional calculation: case A (green), case B (red), and case C (purple). The details of each simulation paarmeter is shown in Table 3. The additional simulations investigate the specific factors causing shorter dust dispersal timescales in low-metallicity environments. Each parameter (stellar properties, photoevaporation profile, and dust-to-gas mass ratio) is adjusted to the low-metallicity value individually. The reasons for the shorter dust dispersal timescales differ by stellar mass. For intermediate-mass stars, the transition to the main sequence accelerates gas dispersal because of changes in stellar parameters. For low-mass and solar-mass stars, the reduction in dust-to-gas mass ratio influences the shorter dust dispersal timescale. For solar-mass stars, the enhanced photoevaporation also contribute to the rapid disk dispersal.

mass ratio has a minimal effect on the dust dispersal timescales. The gas temperature is primarily determined by stellar irradiation and increases with stellar mass. The high bolometric luminosity leads to high temperatures, increasing the observable region because the criterion includes $T_{\rm gas} \geq 300\,{\rm K}$. This expands the region to several to tens of au, where gas remains until the final dispersal stage. The broad observable area makes the dust dispersal timescale nearly equal to the gas dissipation timescale.

Our results show shorter dust dispersal timescales in low-metallicity environments across all stellar masses. While the dominant mechanisms vary, this trend aligns with observations showing disk dispersal within a few million years [Yasui et al., 2010]. Recent observations suggest that intermediate-mass stars in low-metallicity environments maintain disk fractions similar to those in solar-metallicity regions [Yasui, 2021]. This discrepancy may stem from not considering the evolution of X-ray luminosity. As stars reach the main sequence, the FUV luminosity increases while the X-ray luminosity decreases because of the loss of an active convective zone. X-ray photons provide free electrons that enhance the photoelectric heating efficiency. A reduction in X-ray luminosity lowers the photoevaporation rate, extending the dust dispersal timescale for intermediate-mass stars. Although X-ray heating is not the dominant process, a significant decrease in X-ray luminosity could lead to a low photoevaporation rate and a longer dust dispersal timescale, potentially explaining the observed trend around intermediate-mass stars.

Higher-mass stars reach the main sequence more quickly. For example, a $M_* = 7\,{\rm M}_\odot$ star undergoes a transition within $10^5\,{\rm yr}$, leading to intense photoevaporation from an earlier stage. Disks around high-mass stars are likely to disperse even faster in low-metallicity environments than in solar-metallicity cases. In our solar metallicity simulations, disks around $M_* = 7\,{\rm M}_\odot$ stars already disperse within $1\,{\rm Myr}$. In low-metallicity environments, the timescale is expected to be even shorter, leaving little time for planet formation.

Observations show higher gas giant occurrence rates in high-metallicity environments. Stars in such environments evolve more slowly, exposing their disks to reduced photoevaporation for longer periods. This slower evolution likely leads to extended dust dispersal timescales around low to intermediate-mass stars, providing more time for planet formation.

4.5.4 Implications for Disk Fraction

Disk evolution simulations for stars of various masses in low-metallicity environments suggest that the dust dispersal timescale is shorter for all stellar masses compared to solar-metallicity environments. Long-term simulations show that the dust dispersal timescale is consistently within $2\,{\rm Myr}$ for all masses. This trend differs from that observed in solar-metallicity environments. The disk fraction is predicted to decline steeply within $2\,{\rm Myr}$ because of the weak dependence of the dust dispersal timescale on stellar mass, which aligns with the findings of Yasui et al. [2010].

The number of disk obsrvations in low-metallicity environments is limited. Additional observations are needed to better understand the evolution of the disk fraction in these

environments.

4.6 Chapter Summary

We have performed long-term disk evolution simulations that consider accretion, magnetohydrodynamics winds, and photoevaporation for the first time. Additionally, we assess the impact of FUV luminosity evolution during the transition to the main sequence. Key findings from our study are summarized below:

- Viscous accretion primarily disperses gas in the inner regions, while photoevaporation dominates gas dispersal in the outer regions. The efficient photoevaporation in the outer region is a unique feature of the FUV photoevaporation model by Komaki et al. [2021].
- MHD winds are less effective in directly dispersing gas, but induce significant accretion by removing angular momentum from the disk, leading to greater mass loss through accretion than through the winds themselves.
- For a $3\,\mathrm{M}_\odot$ star, the FUV luminosity increases by a factor of 100 when the star reaches the main sequence at approximately $2.5\,\mathrm{Myr}$, driving efficient photoevaporation and rapid gas dispersal.
- The dust dispersal timescale, which corresponds to the observable timescale in the infrared, peaks at approximately $6\,\mathrm{Myr}$ for a $2\,\mathrm{M}_\odot$ star among 0.1–$7\,\mathrm{M}_\odot$. This occurs because the star does not reach the main sequence within the gas dissipation timescale, preventing enhanced photoevaporation. Instead, during the Henyey track, the bolometric luminosity increases, expanding the observable region with $T > 300\,\mathrm{K}$ by a factor of 1.5 in the final $1\,\mathrm{Myr}$.
- By incorporating stellar luminosity evolution, our simulations provide a more realistic estimate of the dust dispersal timescale around solar to intermediate-mass stars.
- The dust dispersal timescale decreases with decreasing stellar mass, contrary to observational trends. This discrepancy can be attributed to the magnetic field strength, as shown by simulations in which the gas fails to disperse without magnetic fields in the $M_* = 0.1\,\mathrm{M}_\odot$ case.
- Variations in surface mass-loss rates across photoevaporation models do not significantly affect the dust dispersal timescale, but do determine the gas dissipation timescale. Our latest model, which consistently incorporates FUV photoevaporation, is crucial for understanding gas evolution in the outer disk regions.

Disks are often observed as part of star-forming regions and analyzed statistically. Disk fraction provides insights into the evolutionary stage of the region. To compare our simulations to observations, we derived disk fraction evolution for 10,000 disks using a

stellar cluster model. Stellar mass, disk mass, and disk radius were assigned through Monte Carlo sampling, and the dust dispersal timescale was estimated for each system.

- The calculated disk fraction matches observed values in the first few million years, but underestimates it afterward
- The disk fraction depends on the assumed disk evolution model and the stellar mass distribution in a star-forming region. The disk fraction becomes higher by 20% at $2\,\mathrm{Myr}$ when luminosity change by stellar evolution is included, which brings the disk fraction closer to observations.
- We successfully reproduce the disk fraction of Lupus using the same stellar mass distribution observed in Lupus, but our model fails to explain the disk fraction higher than 20% observed in η Cha, emphasizing the importance of simulations that solve dust evolution and the gas component.

Observations in the outer galaxy reveal lower disk fractions in low-metallicity environments. Previous studies suggest that enhanced photoevaporation in these environments, because of reduced attenuation, may accelerate disk dispersal. Since photoevaporation is only one component of disk dispersal, it is unclear how its enhancement affects overall disk dispersal when all processes are considered. We conducted disk evolution simulations with $Z_* = 0.1\,\mathrm{Z}_\odot$ for $M_* = 0.5, 1, 3\,\mathrm{M}_\odot$. The dust dispersal timescales are shorter for all stellar masses, but the causes vary by stellar mass.

- The dust dispersal timescales become half of the values in solar metallicity environments, consistent with the observations.
- The specific mechanisms that cause the shortened lifetimes vary with stellar mass. For low-mass stars, disks become unobservable due to dust abundance being reduced by a factor of 10. For solar-mass stars, the photoevaporation mass-loss rate increases by a factor of 2, leading to accelerated gas dispersal. For high-mass stars, intense FUV radiation from an early transition to the main sequence (before $1\,\mathrm{Myr}$) drives rapid disk dispersal.
- These results highlight the importance of understanding disk dispersal within the broader context of star-disk evolution.

We perform long-term disk evolution simulations with a complete set of all the major disk dispersal processes. We perform disk evolution simulations with a variety set of disk parameters such as stellar mass, initial disk mass, and disk radius. These results are applicable to understanding disk evolution in various environments.

5

Long-Term Evolution of Dust and Gas: Impacts on Photoevaporation

Figures

5.1 Introduction to Dust Grains in Disks

Disk observations often focus on dust grains, which comprise only a small portion of the disk material by mass. However, the physical dynamics within the disk is dominated by the gas evolution. Many previous studies on disk evolution focus solely on gas dispersal and estimate the distribution of dust grains using the dust-to-gas mass ratio observed in the ISM. However, dust grains undergo several unique processes on relatively short timescales. The commonly used dust-to-gas mass ratio is not applicable to disks at every stage of evolution. This makes it challenging to infer the overall distribution of disk material based on dust observations alone.

Long-term gas evolution simulations show that photoevaporation effectively removes gas from the outer region. At the same time, theoretical studies on dust evolution reveal that dust grains coagulate and undergo intense radial drift toward the central star, reducing the dust-to-gas mass ratio in the outer regions. Photoevaporation depends on the efficient heating of the gas. Radiative hydrodynamic simulations show that this heating is primarily caused by the photoelectric effect on dust grains owing to FUV photons. This process depends strongly on the FUV luminosity and the amount of dust grains present. When dust grains are depleted in the outer regions, the photoevaporation efficiency may decrease significantly. This research aims to gain a more realistic understanding of the photoevaporation process. The coagulation of dust grains marks the onset of planet formation. Several pathways for planetesimal formation have been proposed, such as gravitational instability and streaming instability. These processes require a sufficiently high dust-to-gas mass ratio to become effective. Understanding the distribution of dust grains in a gas disk that undergoes dispersal is crucial.

Previous studies have attempted to clarify the time evolution of dust size and spatial distribution. Because of computational complexity and limitations, most research has not incorporated detailed gas evolution, although gas density significantly affects dust size distribution via turbulence and gas velocity influences dust spatial distribution via radial drift.

In this section, we present long-term disk evolution simulations that consider both gas and dust components. We include accretion, MHD winds, and photoevaporation for gas dispersal processes. For dust size evolution, we incorporate collisional growth and fragmentation. For dust radial evolution, we include radial drift, diffusion, and entrainment by photoevaporative gas flows. Additionally, we account for how changes in the dust-to-gas mass ratio affect photoevaporation. This is the first study to consider the feedback of dust evolution on gas evolution.

5.2 Methods

We solve the long-term evolution of both gas and dust components around a solar-mass, solar-metallicity star. For gas dispersal processes, we include accretion, MHD winds, and photoevaporation. The detailed methodology is provided in Chapter 4.2; we introduce an overview. The governing equation is given by

$$\frac{\partial \Sigma}{\partial t} + \frac{1}{r}\frac{\partial}{\partial r}\left(r\Sigma v_r\right) + \dot{\Sigma}_{\rm w} + \dot{\Sigma}_{\rm pe} = 0,$$

where $\dot{\Sigma}_{\rm w}$ and $\dot{\Sigma}_{\rm pe}$ represent the surface mass-loss rates due to MHD winds and photoevaporation. For MHD winds, we assume a 'weak wind' model in which 10% of the energy from accretion launches MHD winds, and the rest heats the gas. This model aligns closely with the observed dust dispersal timescales. The surface mass-loss rate due to photoevaporation is derived from radiation hydrodynamic simulations.

The evolution of the dust surface density is given by:

$$\frac{\partial \Sigma_{\rm d}}{\partial t} + \frac{1}{r}\frac{\partial}{\partial r}\left(r\Sigma_{\rm d}u_{\rm d}\right) - \frac{1}{r}\frac{\partial}{\partial r}\left[r\Sigma D_{\rm d}\frac{\partial}{\partial r}\left(\frac{\Sigma_{\rm d}}{\Sigma}\right)\right] + \dot{\Sigma}_{\rm ent} = 0, \tag{5.1}$$

where $\dot{\Sigma}_{\rm ent}$ is the mass-loss rate of dust grains due to entrainment by gas flows. The second term describes the radial drift toward the central star. The difference in velocities between gas and dust, caused by their interaction, results in the deviation of the dust velocity from the Keplerian motion. Gas moves sub-Keplerian because of pressure and also moves toward the star via viscous accretion. The gas velocity deviations from Keplerian motion are given by:

$$r\Sigma v'_{{\rm gas},r} = -\frac{2}{r\Omega_{\rm K}}\left[\frac{\partial}{\partial r}(r^2\Sigma\alpha c_{\rm s}^2) + r^2\alpha_z(\rho c_{\rm s}^2)_{\rm mid}\right] \tag{5.2}$$

for the radial direction, and:

$$v'_{{\rm gas},\phi} = \frac{1}{2}\frac{c_{\rm s}^2}{v_{\rm K}}\frac{\partial \ln P}{\partial \ln r}, \tag{5.3}$$

for the azimuthal direction, where $v_{\rm K}$ is the Keplerian velocity. In the ϕ direction, gas pressure gradients cause deviations from the Keplerian motion, typically resulting in a headwind felt by dust grains.

The dust velocity deviations from Keplerian motion $(v'_{{\rm dust},r}, v'_{{\rm dust},\phi})$ are calculated by solving the equations of motion for radial and angular momentum:

$$\begin{aligned} v'_{{\rm dust},r} &= \frac{2St}{St^2+1} v'_{{\rm gas},\phi} + \frac{1}{St^2+1} v'_{{\rm gas},r} \\ v'_{{\rm dust},\phi} &= \frac{1}{St^2+1} v'_{{\rm gas},\phi} - \frac{1}{2}\frac{St}{St^2+1} v'_{{\rm gas},r}, \end{aligned} \tag{5.4}$$

where St is the Stokes number, a dimensionless parameter representing the coupling between gas and dust.

The Stokes number is given by:

$$St = \begin{cases} \frac{\pi a \rho_{\rm dust}}{2\Sigma} & \text{(Epstein regime)} \\ \frac{2}{9}\sqrt{\frac{\pi}{8}}\frac{a^2 \rho_{\rm dust} \Omega_{\rm K}}{c_{\rm s} \rho \lambda_{\rm gas}} & \text{(Stokes regime)}, \end{cases} \tag{5.5}$$

where a, $\rho_{\rm dust}$, ρ, and $\lambda_{\rm gas}$ represent the dust grain radius, solid density of dust, gas density, and gas mean free path, respectively. The Epstein regime applies to small dust grains ($a < \lambda_{\rm gas}$), where dust is well-coupled with gas. In the Stokes regime ($a > \lambda_{\rm gas}$), dust grains are less affected by gas motion. Both regimes are covered in our calculation.

The third term in the dust evolution equation represents diffusion. The diffusion coefficient for dust is given by Youdin and Lithwick [2007] as:

$$D_{\rm d} = \frac{1}{St^2+1} D_{\rm g}, \tag{5.6}$$

where $D_{\rm g}$ is the gas diffusion coefficient, derived under the assumption of Keplerian motion.

Dust grains go through coagulation and fragmentation by collisions with each other. The dust grains eventually grow to sizes on the order of cm. There are several possible reactions followed by collisions between dust grains; sticking, fragmentation, erosion, and bouncing. Sticking occurs when two grains collide and combine to form a larger particle. Fragmentation occurs when grains collide at high velocities and shatter into smaller pieces. Erosion is a process in which small grains chip larger grains, and bouncing is that colliding grains separate without any change in size Windmark et al. [2012]. The relative velocity of the dust grains determines which of these processes occurs. The boundary between sticking and fragmentation is defined by the fragmentation velocity. Experiments suggest that this velocity ranges between 10^2–$10^3\,\mathrm{cm\,s^{-1}}$, depending on the dust composition, such as silicate or water ice. For simplicity, we assume a constant fragmentation velocity of $10^2\,\mathrm{cm\,s^{-1}}$ across the entire disk.

It is important to calculate the relative velocities of dust grains in detail because they vary with particle size. Simulations using only two dust size models fail to capture the dust size distribution properly because fragmentation limits vary are not traced comprehensively.

In this calculation, dust grains are considered in a wide range from 10^{-16} to $10^{4}\,\mathrm{g}$, divided into 150 logarithmic bins. The solid density is set to $1.67\,\mathrm{g\,cm^{-3}}$. The size range corresponds to the radii from $2.4 \times 10^{-6}\,\mathrm{cm}$ to $11.26\,\mathrm{cm}$, allowing us to obtain a realistic dust size distribution.

The relative velocity between grains of different sizes is calculated based on five processes: Brownian motion, azimuthal drift, radial drift, settling toward the midplane, and turbulence. The method from Stammler and Birnstiel [2022] is used to compute these velocities. The total relative velocity is expressed as:

$$v_{ij}^{\mathrm{rel}} = \sqrt{(v_{ij}^{\mathrm{rel,brown}})^2 + (v_{ij}^{\mathrm{rel,azi}})^2 + (v_{ij}^{\mathrm{rel,rad}})^2 + (v_{ij}^{\mathrm{rel,sett}})^2 + (v_{ij}^{\mathrm{rel,turb}})^2} \tag{5.7}$$

where i and j refer to the size bins of the two colliding grains. The terms $v_{ij}^{\mathrm{rel,brown}}$, $v_{ij}^{\mathrm{rel,azi}}$, $v_{ij}^{\mathrm{rel,rad}}$, $v_{ij}^{\mathrm{rel,sett}}$, and $v_{ij}^{\mathrm{rel,turb}}$ represent the relative velocities due to Brownian motion, azimuthal drift, radial drift, settling, and turbulence.

The relative velocity from Brownian motion is determined by the reduced mass and is given by:

$$v_{ij}^{\mathrm{rel,brown}} = \sqrt{\frac{8 k_{\mathrm{B}} T (m_i + m_j)}{\pi m_i m_j}}, \tag{5.8}$$

where m_i and m_j are the masses of grains in bins i and j. The relative velocity arises among the dust grains of the same size.

Radial drift, azimuthal drift, and settling velocities depend on grain size. Larger grains experience stronger settling toward the midplane. The settling velocity is:

$$u_{\mathrm{sett}} = -z \Omega_{\mathrm{K}} St. \tag{5.9}$$

which depends on the height z above the midplane. The vertical distribution of dust grains is controlled by a balance between settling and diffusion:

$$\frac{\partial \rho_{\mathrm{dust}}}{\partial t} + \frac{\partial}{\partial z}\left(\rho_{\mathrm{dust}} u_{\mathrm{sett}} - D_{\mathrm{d}} \rho \frac{\partial}{\partial z}\left(\frac{\rho_{\mathrm{dust}}}{\rho}\right)\right) = 0, \tag{5.10}$$

where ρ_{gas} and ρ_{dust} are the gas and dust local densities. Assuming $St \ll 1$, the dust scale height H_{d} can be expressed using the gas scale height H:

$$H_{\mathrm{d}} = \sqrt{\frac{\alpha}{\alpha + St}} H. \tag{5.11}$$

The relative velocity due to settling is calculated using Eq. 5.9 and Eq. 5.10. The velocity difference caused by turbulence, $v_{ij}^{\mathrm{rel,turb}}$, is calculated following the theoretical calculation with the assumption of Kolmogorov law by Ormel and Cuzzi [2007].

Dust grains collide with velocities derived as explained above. Several outcomes are possible after collisions: sticking, fragmentation, erosion, and bouncing. When the collision velocity is low, the dust grains stick together to form a larger particle. At higher velocities, dust grains shatter into many smaller particles. When one grain is much larger than the

other, the smaller grain chips the larger one, which is called erosion. The final possible outcome is bouncing, where grains collide, but no change occurs in their size. Simulations suggest that bouncing is rare for grains smaller than 100μm and can be neglected [Wada et al., 2011]. We do not include bouncing in this calculation.

The boundary velocity that separates sticking and fragmentation is called fragmentation velocity, $v_{\rm frag}$. Experiments and theoretical studies suggest $v_{\rm frag} = 10^2\,{\rm cm\,s^{-1}}$ for silicate grains [Blum and Münch, 1993, Poppe et al., 2000, Leinhardt and Stewart, 2009]. Dust grains consist of various compounds such as silicates, carbonates, water ice, and ammonia. The fragmentation velocity depends on the grain composition. Because water and carbonates have specific snowlines where their states change between solid and gas, grain composition also depends on disk position. For simplicity, we assume a constant $v_{\rm frag} = 10^2\,{\rm cm\,s^{-1}}$ throughout the disk. Whether a collision results in fragmentation or erosion depends on the size ratio of the colliding grains. If the radius ratio exceeds 10, the collision results in erosion; otherwise, it leads to fragmentation.

The reaction rates for sticking and fragmentation (or erosion) are given by:

$$\begin{aligned} R^{\rm f}_{ij} &= \sigma_{\rm geo}\Delta\bar{v}p^{\rm f}_{ij} \\ R^{\rm s}_{ij} &= \sigma_{\rm geo}\Delta\bar{v}p^{\rm s}_{ij}, \end{aligned} \tag{5.12}$$

where $\sigma_{\rm geo}$ is the geometric cross-section of the colliding particles. The subscript f refers to fragmentation, and s refers to sticking. While collision outcomes are determined by relative velocity, the transition between sticking and fragmentation is smooth. Probability functions $p^{\rm f}_{ij}$ and $p^{\rm s}_{ij}$ define the likelihood of each outcome. The dust density is assumed to be constant at $1.67\,{\rm g\,cm^{-3}}$ throughout the calculation. After a sticking event, the newly formed particle is assigned to a size bin corresponding to its mass. If its mass falls between two bins, it is distributed proportionally to maintain mass conservation. For fragmentation, experimental results show that the resulting size distribution follows $n(m){\rm d}m \propto m^{-11/6}{\rm d}m$. We use this relation to distribute the fragments. The dust size range covers 10^{-16}–$10^4\,{\rm g}$, corresponding to dust radii of 0.024μm–$11\,{\rm cm}$ in our simulations. Observations of the interstellar medium suggest dust grains range from 0.005μm to 1μm, with a power-law distribution of -3.5 in the 0.005μm to 0.25μm range. We assume that the initial dust size distribution follows a power-law of -3.5 in the range of 0.024μm–1μm. We set the lower limit at 0.024μm to reduce computational load and include grains up to cm sizes to investigate planet formation.

The theoretical maximum size of dust grains, called the fragmentation radius $a_{\rm frag}$, is the size where relative velocity equals the fragmentation velocity. By assuming turbulence dominates the relative velocity, $a_{\rm frag}$ is given by:

$$\begin{aligned} a_{\rm frag} &= \frac{2\Sigma}{\pi\alpha_{\rm t}\rho_{\rm dust}}\frac{v^2_{\rm frag}}{c^2_{\rm s}} \\ &\sim 3.8\,{\rm cm}\left(\frac{\Sigma}{10\,{\rm g\,cm^{-2}}}\right)\left(\frac{c_{\rm s}}{10^4\,{\rm cm\,s^{-1}}}\right)^{-2}. \end{aligned} \tag{5.13}$$

This gives the maximum grain size, balancing coagulation and fragmentation. Our

calculation includes this range, ensuring realistic size distribution.

The MRN distribution is assumed in the range of 0.024–1μm as the initial condition. Since our calculation aims to follow disk evolution from the beginning, we set the upper limit to 1μm, which is the common upper limit obtained in the interstellar medium. We exclude dust grains smaller than 0.024μm because of computational limitations. According to the MRN distribution, small dust grains in the range of 0.005–0.024μm account for 9% of the total dust mass in the 0.005–1μm range. We set the initial dust disk mass to 0.01×0.9 of the gas disk mass.

To obtain a realistic understanding of photoevaporation, we include stellar evolution and the decline of small dust grains in our calculation. Previous dust growth simulations show that the size distribution of small dust grains ($< 0.1\mu$m) is dominated by fragmentation and follows a power-law relation. This means that once the abundance of one size bin is known, the abundance in other bins and the total mass of small grains ($< 0.01\mu$m) can be inferred. We calculate the local abundance of small dust grains at $a = 0.024\mu$m and estimate the total amount of grains smaller than $a = 0.024\mu$m. Comparing this value to the MRN distribution, we estimate the practical dust-to-gas mass at each radius.

The photoevaporation rates for dust-to-gas mass ratios in the range 10^{-4}–10^{-1} are fitted as:

$$\dot{M}_{\rm pe} = 6.4 \times 10^{-0.23(\log_{10}\mathcal{D})^2 - 0.73(\log_{10}\mathcal{D}) - 10}\,{\rm M}_\odot\,{\rm yr}^{-1}. \tag{5.14}$$

As shown in Chapter 3, photoevaporative flows are driven by the heating from the photoelectric effect of dust grains when $\mathcal{D} \geq 10^{-3}$. However, the photoevaporation rate does not continue to decrease below $\mathcal{D} = 10^{-3}$ because H_2 pumping and X-ray photons take over as the main heating sources and drive photoevaporative flows. Therefore, we set a lower limit of $1.0 \times 10^{-10}\,{\rm M}_\odot\,{\rm yr}^{-1}$ for the mass-loss rate. The ratio of the photoevaporation rate calculated with the local dust-to-gas mass ratio to the fiducial rate at $\mathcal{D} = 0.01$ is parameterized, and the surface mass-loss profile is given by:

$$\dot{\Sigma}_{\rm pe} = \beta \times \zeta(r)\dot{\Sigma}_{\rm pe,ini}, \tag{5.15}$$

where $\dot{\Sigma}_{\rm pe,ini}$ represents the photoevaporation rate with fiducial stellar luminosity and $\mathcal{D} = 0.01$. In the equation, β represents a scaling parameter for FUV luminosity. The parameter $\zeta(r)$ is calculated by interpolating the practical dust-to-gas mass ratio for the mass-loss rate and normalizing it by the fiducial surface mass-loss rate at $\mathcal{D} = 10^{-2}$.

Dust entrainment is also included. Small dust grains are mixed with gas and entrained by gas flows. When the drag force acting on the dust grains exceeds gravity, the dust grains are carried away with the gas. A boundary dust radius, $a_{\rm ent}$, determines whether dust is entrained. Hydrodynamics simulations suggest that dust grains smaller than 10μm are lost with photoevaporative flows around T Tauri stars. We calculate $a_{\rm ent}$ at each position and time step, allowing only grains smaller than this boundary to be lost. It is assumed that the dust and gas are well-mixed, so their proportions in the wind match those in the disk.

We perform long-term disk evolution simulations for both gas and dust components. For the fiducial case, we use $M_* = 1\,{\rm M}_\odot$, $\mathcal{D} = 0.01$, and $M_{\rm disk} = 0.0117 M_*$. We also perform

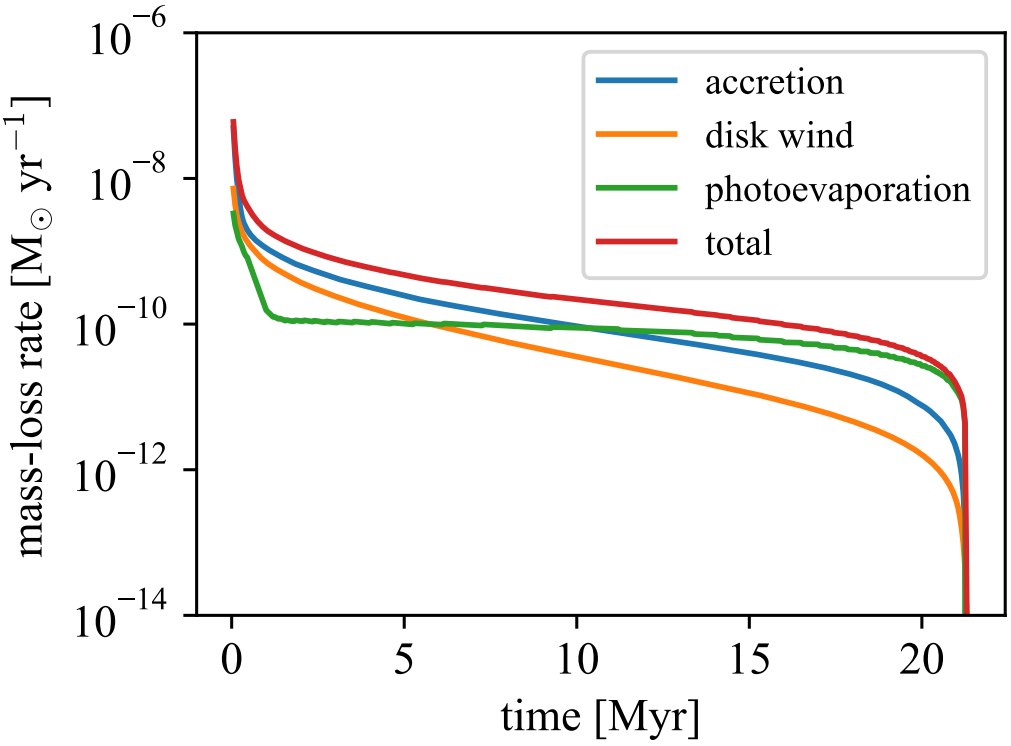

► **Figure. 5.1**

The time evolution of mass-loss rate due to accretion (blue), MHD winds (orange), photoevaporation (green), and the total (red). Accretion is the dominant disk dispersal process in the first $10\,\mathrm{Myr}$, the dominant dispersal process is replaced by photoevaporation. The mass-loss rate by photoevaporation decreases in the first $1\,\mathrm{Myr}$ because of the rapid clearance of dust grains.

simulations without dust entrainment and for a lower metallicity of $Z = 0.1\,\mathrm{Z}_\odot$ to study dust abundance and photoevaporation in low-metallicity environments.

5.3 Results

In this section, we discuss the realistic photoevaporation in an evolving disk. This is the first simulation to incorporate all three major disk gas dispersal processes while considering dust growth and surface density evolution.

5.3.1 Variations and Impacts on Photoevaporation

Figure 5.1 shows the time evolution of the mass-loss rate for each disk dispersal process: accretion, MHD winds, and photoevaporation. Figure 5.2 compares the photoevaporation

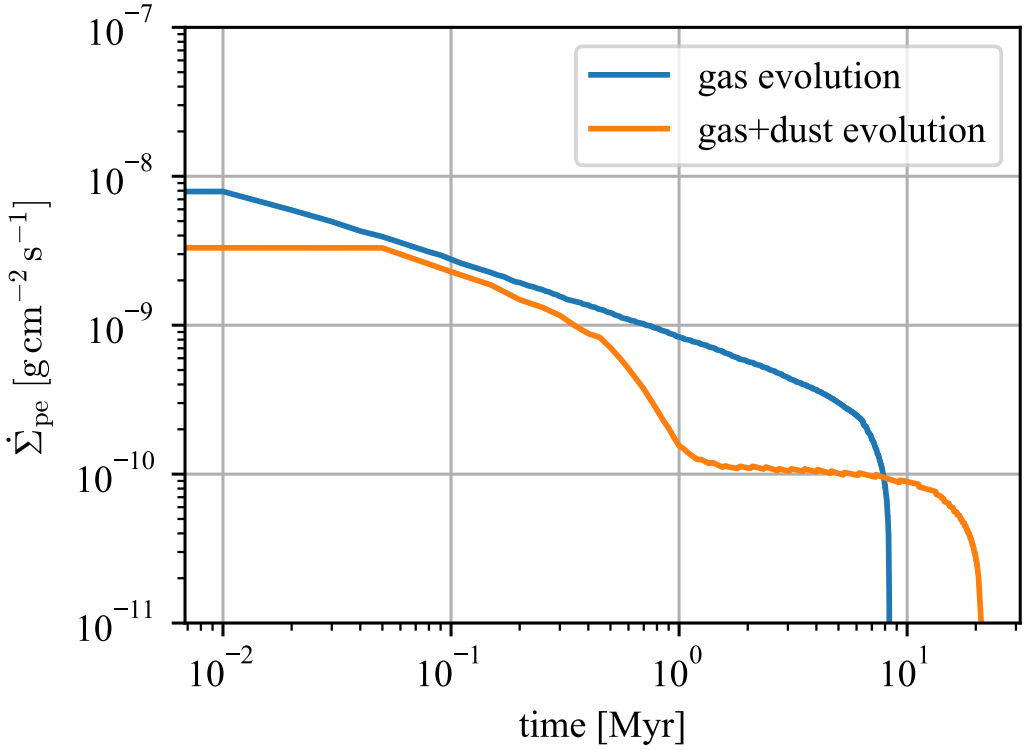

► **Figure. 5.2**

The time evolution of photoevaporation rate in calculations without dust components (blue) and with dust components (orange). In the calculation considering dust evolution, the amount of dust grains decreases within $1\,\mathrm{Myr}$. The practical dust-to-gas mass ratio is 10^{-4} throughout the disk and the photoevaporation rate is the value at the dust-deficient limit. The decreased photoevaporation rate elongates the gas dissipation timescale by a factor of 2.5, while the dust dispersal timescale does not vary. This confirms that photoevaporation is a process efficient in the outer region.

rates between simulations with and without dust evolution. Accretion is the dominant process within the first $10\,\mathrm{Myr}$, but after that, photoevaporation becomes the main dispersal process. This transition from accretion to photoevaporation is consistent with simulations in which only the evolution of the gas surface density is solved. However, the transition is delayed in simulations that include dust evolution because the photoevaporation rate is lower. The reduced photoevaporation rate is attributed to the low dust-to-gas mass ratio of small dust grains.

The dust-to-gas mass ratio remains approximately at its initial value of $\sim 10^{-2}$ during the first million years, but drops to $\sim 10^{-4}$ over the next few millions of years. We estimate the dust dispersal timescale using the same criteria introduced in Chapter 4.2.6. Dust grains are considered observable when two conditions are satisfied: $\Sigma_{\mathrm{dust}} \geq 0.1\,\mathrm{g\,cm^{-2}}$ and $T_{\mathrm{gas}} \geq 300\,\mathrm{K}$. The rapid decline in the dust-to-gas mass ratio results in a short dust dispersal timescale of $2.5\,\mathrm{Myr}$, even though the gas dissipation timescale is longer in simulations with dust evolution.

Figure 5.3 shows the dust size distribution at $r = 1, 10, 30, 100\,\mathrm{au}$ at the age of 0.1 and $1\,\mathrm{Myr}$. There are two main reasons for the rapid decrease in the dust-to-gas mass ratio throughout the disk. The first is dust coagulation and accretion. The dust grains grow to sizes of $\sim 0.1\,\mathrm{cm}$ through coagulation. These larger grains are accreted onto the star and are cleared within $1\,\mathrm{Myr}$. The second is dust-size redistribution. Several physical parameters, such as gas surface density, temperature, and turbulence, influence the dust size distribution. Birnstiel et al. [2010] demonstrated that gas surface density plays a more crucial role than dust surface density. The low gas surface density leads to higher relative dust velocities because of increased Stokes parameters. The dust collisions are more likely to result in fragmentation than coagulation. This is suggested by the relation between the fragmentation radius and the gas surface density following $a_{\mathrm{frag}} \propto \Sigma$ (see Eq. 5.13). The large grains are no longer created.

To estimate the realistic local photoevaporation rate, we calculate the practical dust-to-gas mass ratio, which is derived by determining the ratio of small dust grain surface density to gas surface density and comparing it to the corresponding ISM value. The practical dust-to-gas mass ratio drops below 10^{-4} within a million years across the disk. This decline in small dust grains reduces the photoevaporation rate.

The reduced photoevaporation rate leads to a longer gas dissipation timescale. However, this is not the only observable change by incorporating dust evolution in the calculation. A notable difference is observed in the disk radius. Figure 5.4 illustrates the disk gas radius in simulations with and without dust evolution. The disk radius is defined as the location where the gas surface density is below $10^{-2}\,\mathrm{g\,cm^{-2}}$. Although the decrease in disk radius is more rapid in the simulation without dust evolution, the disk radius increases to $130\,\mathrm{au}$ because of viscous spreading in the simulation with dust evolution. A lower photoevaporation rate results in a larger disk gas radius. Photoevaporation is the primary gas dispersal process in the outer regions of the disk.

Figure 5.2 shows the photoevaporation rate over time. When dust evolution is included, the practical dust-to-gas mass ratio reduces the photoevaporation rate by a factor of ~ 5.3.

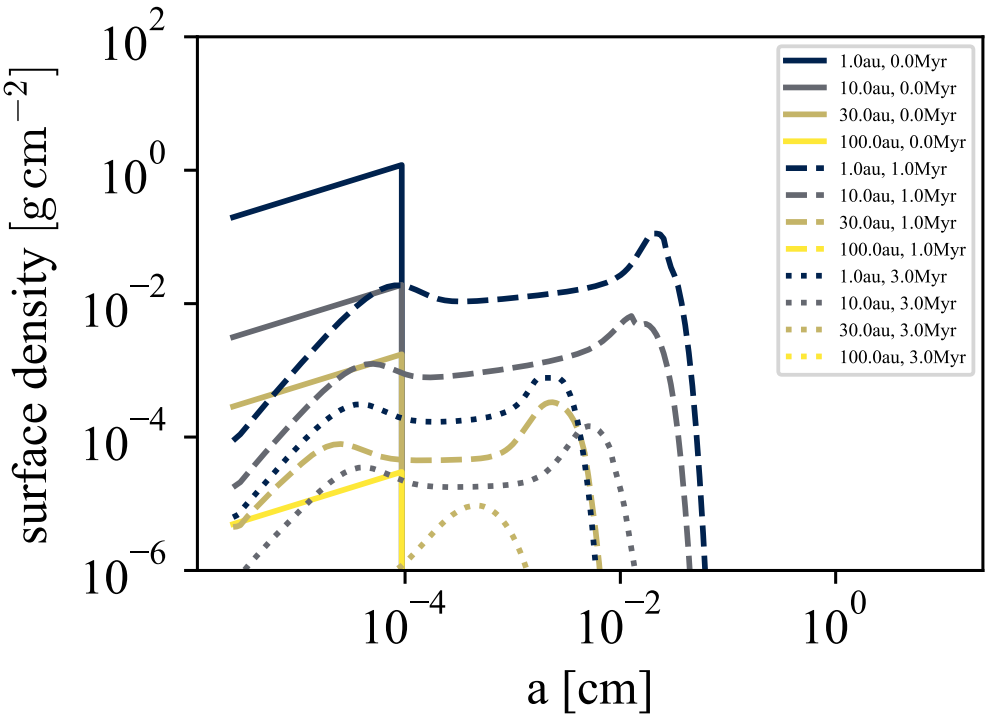

► **Figure. 5.3**

The dust size distribution at $r = 1, 10, 30, 100\,\mathrm{au}$ at the age of 0.1 (solid line) and $1\,\mathrm{Myr}$ (dotted line). The color variation corresponds to the location: $r = 1\,\mathrm{au}$ (navy), $r = 10\,\mathrm{au}$ (gray), $r = 30\,\mathrm{au}$ (cloudy yellow), $r = 100\,\mathrm{au}$ (yellow). The maximum dust size decreases rapidly at $r = 1\,\mathrm{au}$ as $\sim 0.1\,\mathrm{cm}$ size dust grains accrete on to the star and that size dust are not created because of the decreased gas surface density (see Eq. 5.13).

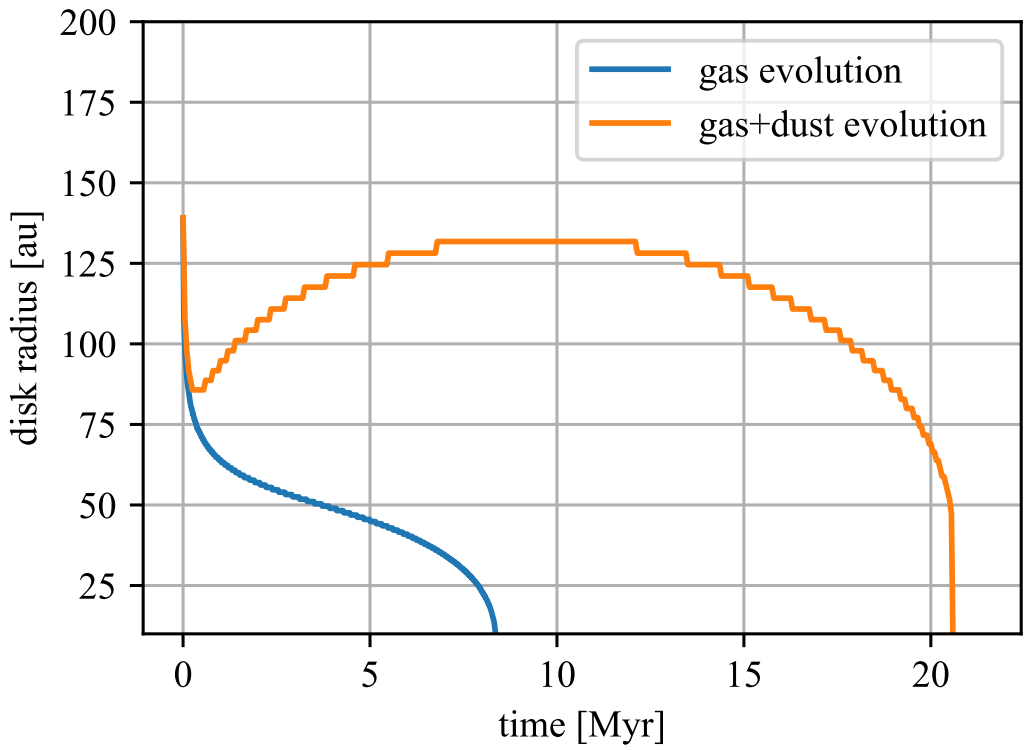

► **Figure. 5.4**

The time evolution of disk gas radius in the simulations without solving dust evolution (blue) and solving dust evolution (orange). In the calculation without dust evolution, the radius decreases monotonically because photoevaporation contributes to mass-loss from the outer region. In contrast, in the calculation with dust evolution, the disk gas once decreases because of photoevaporation but increases after that. The increase is caused by redistribution of angular momentum due to viscosity and inefficient photoevaporation in the outer region. The low photoevaporation rate leads to longer lifetime in the calculation considering dust evolution.

This reduction is less than the expected value of $2.7 \times 10^{-9}/1.0 \times 10^{-10} \sim 27$, which is derived from the photoevaporation rate at $\mathcal{D} = 10^{-2}$ and the lower limit. This discrepancy arises because of the larger gas disk radius. A lower photoevaporation rate contributes to a larger disk radius because photoevaporation is the dominant process in the outer disk. The mass-loss rate by photoevaporation is given by

$$\dot{M}_{\rm pe} = \int_{r_{\rm in}}^{r_{\rm out}} \dot{\Sigma}_{\rm pe}\, {\rm d}r.$$

The mass-loss rate increases with disk radius. This explains why the mass-loss rate remains relatively high, even when the practical dust-to-gas mass ratio is $\sim 10^{-4}$.

The dust dispersal timescale does not change significantly when considering the local abundance of small dust grains. This is because the dust dispersal timescale corresponds to the dispersal of the inner region, where the impact of changes in photoevaporation is less significant. However, it is important to note that gas dispersal is sensitive to the lower limit of the photoevaporation rate set for cases with a low dust-to-gas mass ratio. We set this lower limit to $1.0 \times 10^{-10}\,{\rm M}_\odot\,{\rm yr}^{-1}$. As discussed in Chapter 3, disk gas in these cases is mainly heated by H_2 pumping and X-ray photons. For intermediate-mass stars, such as a $3\,{\rm M}_\odot$ star, the X-ray luminosity drops to $\sim 10^{28.7}\,{\rm erg\,s}^{-1}$ after the star reaches the main sequence. This low X-ray luminosity cannot sustain a high mass-loss rate of photoevaporation. Nakatani et al. [2021] showed that the photoevaporation rates decrease to $\sim 2.0 \times 10^{-11}\,{\rm M}_\odot\,{\rm yr}^{-1}$ around A-type stars when there are no small dust grains capable of photoelectric heating. In such cases, the dust dispersal timescale is expected to be longer.

To study the effect of MHD winds on dust evolution, we also perform disk evolution simulations without magnetic fields. We still assume a viscous parameter of $\overline{\alpha_{r\phi}} = 10^{-4}$ because a minimal level of turbulence maintains viscosity. Without magnetic fields, disk dispersal is delayed because MHD winds contribute to efficient accretion by taking angular momentum.

Taki et al. [2021] investigated the effects of MHD winds on dust growth. Our fiducial calculation aligns with their weak turbulence + weak mass loss + Σ-dependent case, showing a dust-to-gas mass ratio of $\sim 10^{-4}$ across most of the disk, consistent with our findings. However, at $r \sim 1\,{\rm au}$, their calculations show ${\rm km}$-sized dust grains, which differ from our results. This discrepancy arises because their calculations exclude fragmentation. As the gas surface density decreases, the fragmentation limit shifts toward smaller grain sizes, preventing steady growth to larger grains during the later stages of disk dispersal. This highlights the critical role of fragmentation in limiting dust growth.

We do not observe pressure bumps even though the surface density profile does not strictly follow a negative power-law relation with radius. This is because the temperature profile follows $r^{-1/2}$, primarily determined by irradiation from the central star. Our temperature calculation incorporates both stellar irradiation and viscous heating, with stellar irradiation dominating the thermal structure. Taki et al. [2021] similarly considers only stellar irradiation, resulting in comparable temperature profiles. The assumption of an optically thin disk impacts the calculation of the temperature profile.

Our simulation calculates a vertically averaged temperature as a function of radius. In contrast, the radiative hydrodynamic simulations discussed in Chapter 3 separately calculate the gas and dust temperatures in a two-dimensional way, and these results suggest that the gas temperature reaches 300–400 K on the disk surface, while $\sim$ 50 K in the midplane in a wide radial range. This vertical temperature gradient could lead to a shallower pressure gradient in the midplane.

Temperature also plays a crucial role in dust size distribution. The relative velocity of dust grains, which governs their growth or fragmentation, is largely determined by gas turbulence characterized by local sound speed. A decrease in sound speed at the midplane may promote coagulation over fragmentation. Birnstiel et al. [2011] demonstrated that the fragmentation radius increases by a factor of ~ 5 when the gas temperature decreases by a factor of 10. Our primary focus is on the spatial distribution of small dust grains that contribute to gas heating via the photoelectric effect, and these grains are well-mixed with gas and do not settle to the midplane like larger grains. However, future disk evolution simulations that incorporate vertical temperature variation will be essential to fully understand the evolution of dust grains from fragmentation to planetesimal formation.

We confirm that the dust-to-gas mass ratio remains close to its initial value of $\sim 10^{-2}$ during the first million years but decreases by a factor of 100 over the subsequent few million years. The radial drift velocity of dust grains at the fragmentation radius is $\sim 10\,\mathrm{cm\,s^{-1}}$ within 60 au. Beyond this radius, the density profile becomes steeper due to the cut-off, leading to higher radial drift velocities for dust grains. Multi-wavelength observations suggest that the dust dispersal timescale does not depend on the wavelength used for observations, which corresponds to the temperature of dust grains. This indicates that the dust dispersal timescale is uniform across disk positions. To compare our simulation results with observations, we calculate the evolution of dust grains over a wide range of radii and derive the local mass-loss timescale from the simulations. The mass flux of dust grains with a specific size i due to radial drift and diffusion is given by:

$$J_{\mathrm{d},i} = \Sigma_{\mathrm{d}} u_{\mathrm{d}} - \Sigma D_{\mathrm{d}} \frac{\partial}{\partial r}\left(\frac{\Sigma_{\mathrm{d}}}{\Sigma}\right) \tag{5.16}$$

The surface mass-loss rate of dust grains with size i is derived as

$$\dot{\Sigma}_{\mathrm{d},i} = -\frac{1}{r}\frac{\partial}{\partial r}\left(r J_{\mathrm{d},i}\right). \tag{5.17}$$

We define the local mass-loss timescale as the period required for all dust grains of all sizes to disperse. For dust grains of a specific size i, the timescale is given by:

$$t_{\mathrm{dis},i} = \frac{\Sigma_{\mathrm{d}}}{\Sigma_i \dot{\Sigma}_{\mathrm{d},i}}. \tag{5.18}$$

Figure 5.5 shows the derived local mass-loss timescale. Although observations at various wavelengths indicate a consistent dust dispersal timescale, our results show that the local mass-loss timescale varies, peaking at 0.8 Myr at $r = 60$ au. We also note that

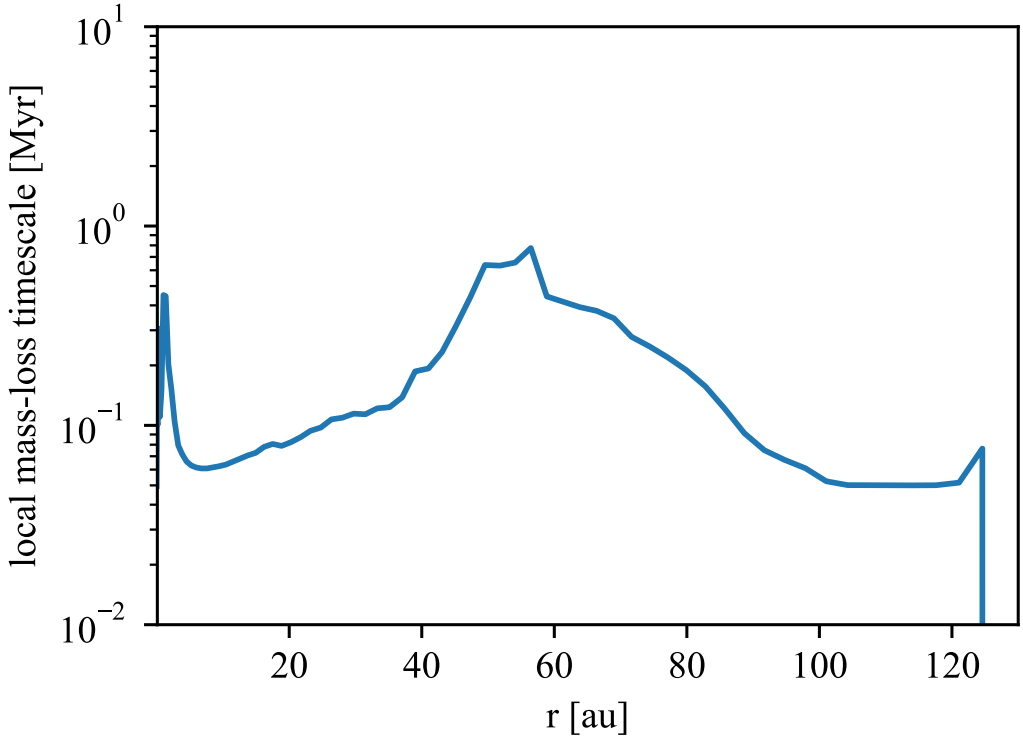

► **Figure. 5.5**

The local mass-loss timescale at $1\,\mathrm{Myr}$. This timescale is derived by accounting for radial drift and diffusion. The local surface mass-loss rate is calculated as the sum of the surface mass-loss rates for each dust size. The local mass-loss timescale reaches a peak of $0.8\,\mathrm{Myr}$ at $r = 60\,\mathrm{au}$. It should be noted that the total surface mass-loss rate may be overestimated because larger dust grains, which are removed quickly, still contribute to the mass-loss rate calculation.

the photoevaporation rate decreases over time due to the diminishing amount of small dust grains. Consequently, the local mass-loss timescale is expected to be longer in the outer regions of the disk.

5.3.2 Dust Entrainment and Its Effect on Dust Abundance

Dust entrainment occurs when gas flows carry away small dust grains as they are well mixed with the gas. Since photoevaporation is mainly driven by heating from the photoelectric effect on dust grains, the amount of small dust grains is crucial for disk evolution, especially in the outer regions where photoevaporation is most effective.

We performed additional simulations without dust entrainment and without dust growth, each to estimate the impact of each process. Figure 5.6 shows the evolution of photoevaporation rates, and Figure 5.7 illustrates the time evolution of the disk radius. Dust growth removes small grains through coagulation. In scenarios where dust growth is not included, the photoevaporation rate remains the highest, sustaining $10^{-9}\,\mathrm{M}_\odot\,\mathrm{yr}^{-1}$ for $3\,\mathrm{Myr}$.

In calculations without dust entrainment, the photoevaporation rate is nearly the same as in scenarios with entrainment, despite a smaller disk radius. This is because the practical dust-to-gas mass ratio at the outer radius is higher without entrainment. Dust entrainment removes small grains in photoevaporative winds, but in this scenario, the practical dust-to-gas mass ratio remains around 10^{-2} at the outermost radius, maintaining the mass-loss rate by photoevaporation.

The dust dispersal timescale is $2.55\,\mathrm{Myr}$ and does not change when dust entrainment is considered. Within $50\,\mathrm{au}$, the dust-to-gas mass ratio remains the same. In the inner regions, disk dispersal is dominated by accretion and MHD winds, resulting in similar dust surface densities and equivalent dust dispersal timescales.

We assume that photoevaporative gas flows primarily drive dust entrainment. However, MHD winds can also contribute to dust entrainment. The surface mass-loss rate of MHD winds is proportional to the local surface density, so the mass-loss rate is concentrated in the inner disk. At $r = 1\,\mathrm{au}$ and $1\,\mathrm{Myr}$, the dust size distribution peaks around $0.3\,\mathrm{cm}$. Only μm size dust grains are entrained by gas flows. As a result, we expect that dust loss due to MHD winds has a minimal impact on the overall disk dispersal and the dust dispersal timescale.

In the calculation without dust growth, the time evolution of photoevaporation does not differ from that in the simulation without considering dust grains at all, where the dust size distribution of the ISM is employed. This comparison highlights the impact of dust growth on dust spatial distribution.

The disk radius decreases over time as the gas disperses. The sustained photoevaporation rate contributes to disperse gas in the outer region, leading to a decrease in the disk radius. The dust dispersal timescale is $3.05\,\mathrm{Myr}$, while the gas dissipation timescale is $6.7\,\mathrm{Myr}$. Following the ISM, we assume an initial dust size distribution where all dust grains are smaller than $1\,\mu$m. Without strong radial drift toward the star, the

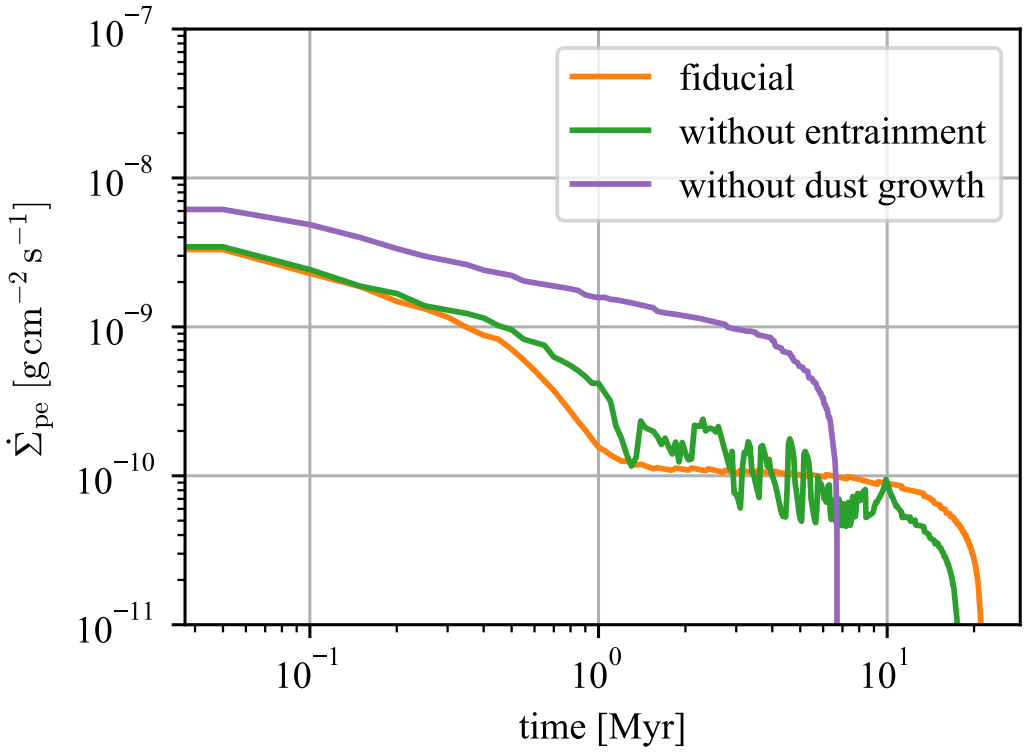

► **Figure. 5.6**

The time evolution of photoevaporation rates in the calculations considering both entrainment and dust growth (orange), without considering entrainment (green), and without considering dust growth (purple). The photoevaporation rate does not vary when entrainment is omitted as a result of balance between sustained practical dust-to-gas mass ratio in the outer region and reduced disk radius due to photoevaporation. In the scenario where dust growth is omitted, the practical dust-to-gas mass ratio does not decrease from 10^{-2} because small um-size dust grains are not removed by dust growth. This results in a sustained photoevaporation rate even though the disk radius decreases because of efficient mass loss by photoevaporation.

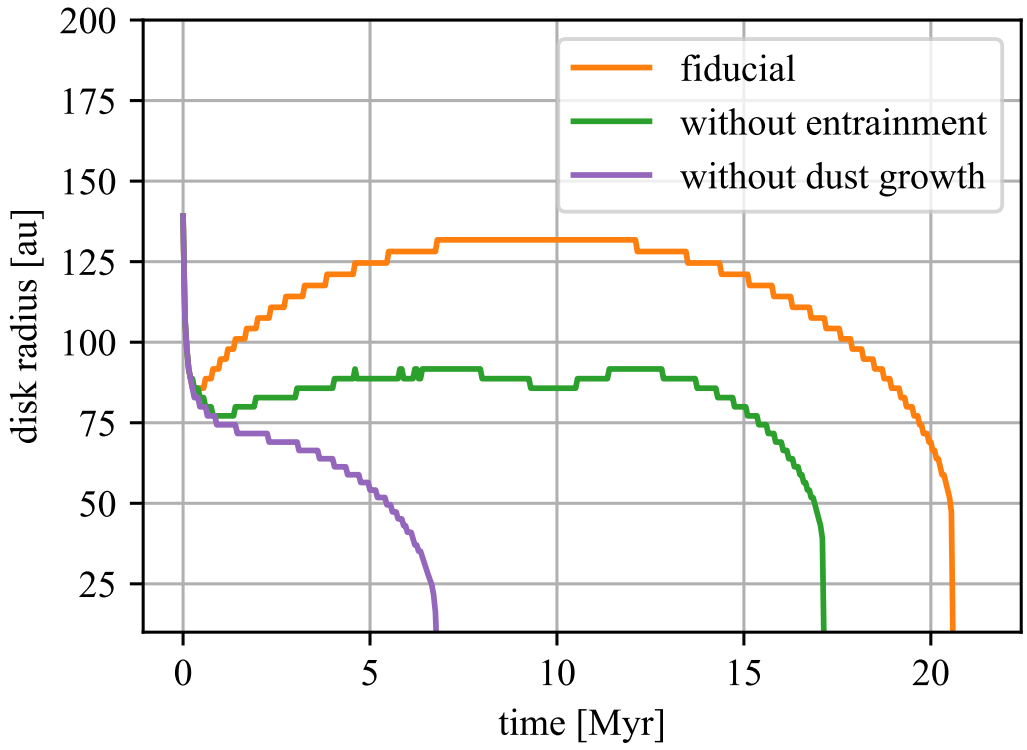

► **Figure. 5.7**

The time evolution of photoevaporation rates in the calculations considering both entrainment and dust growth (orange), without considering entrainment (green), and without considering dust growth (purple). In the calculation without entrainment, the disk radius is constant at $r_{\rm out} \sim 85\,{\rm au}$ because of a balance between spreading by viscosity and mass-loss by photoevaporation. In the calculation without dust growth, the disk radius decreases rapidly by efficient photoevaporation.

dust-to-gas mass ratio increases from 10^{-2} and exceeds one by $5\,\mathrm{Myr}$. This high dust-to-gas mass ratio extends the dust dispersal timescale.

By comparing simulations with and without dust growth and entrainment, we identify the impact of each process. Dust coagulation removes the dust from the disk, affecting both the dust dispersal timescale and the gas radius. Dust entrainment disperses small grains at the outermost radius, resulting in a larger gas radius because of less effective photoevaporation. However, dust entrainment does not significantly affect the gas and dust evolution in the inner region, so the dust dispersal timescale remains unchanged. We argue that incorporating dust growth is essential to understanding the dust dispersal timescale. Dust entrainment should also be included to accurately reproduce the gas distribution.

5.3.3 Effects of Low Metallicity on Dust and Gas Evolution

To better understand disk dispersal in a low-metallicity environment, we perform long-term disk evolution simulations of gas and dust grains with $Z = 0.1\,\mathrm{Z}_\odot$ around a $M_* = 1\,\mathrm{M}_\odot$ star.

Because the dust size distribution depends more on the gas surface density than on the dust surface density, the ratio of coagulated dust grains does not vary with the dust-to-gas mass ratio. The grown dust grains are quickly removed by radial drift, so the fraction of dust cleared from the disk does not depend on the local dust surface density.

In Chapter 4.5, where we discuss disk dispersal in low-metallicity environments, we assume that the dust-to-gas mass ratio remains low at the final stage of disk dispersal. The results of our disk evolution simulation, which includes both gas and dust grains, confirm that this assumption is valid.

5.3.4 Implications for Protoplanetary Disk Fraction

The dust dispersal timescale decreases by $1\,\mathrm{Myr}$ around a $M_* = 1\,\mathrm{M}_\odot$ star. This reduction is caused by the low abundance of dust grains. The initial dust size distribution is set to match the distribution observed in the ISM. In the simulation, we assume that the dust particle density is constant at $1.67\,\mathrm{g\,cm^{-3}}$ throughout the calculation. Recent studies of dust collisions suggest that dust grains can coagulate with porosity, allowing them to grow without experiencing strong radial drift. This process prevents $1\,\mathrm{cm}$-sized dust grains from quickly moving to the central star on a timescale of $100\,\mathrm{yr}$. Including this effect would result in a higher dust-to-gas mass ratio and would likely extend the dust dispersal timescale. The shift in the disk fraction would be less than $1\,\mathrm{Myr}$, leading to a lower overall disk fraction.

This underscores the importance of incorporating dust evolution in disk evolution calculations. The shorter dust dispersal timescale observed around low- to solar-mass stars in low-metallicity environments can largely be attributed to the scarcity of dust grains. Many studies of disk evolution have primarily focused on the evolution of the gas surface density, often assuming a constant dust-to-gas mass ratio of 0.01 as seen in the ISM.

It is also worth noting that the disk surface is heated by radiation from the central star. In the long-term disk evolution simulations, we calculate the temperature averaged in the z-direction. Radiation hydrodynamic simulations of photoevaporation show that

the temperature can reach a few hundred K. Given that the gas dissipation timescale is generally longer than the dust dispersal timescale, it is possible that the dust dispersal timescale approaches the gas dissipation timescale.

5.4 Chapter Summary

Photoevaporation is an important process that contributes to disk dispersal. Previous theoretical research highlights its importance, as mass loss from photoevaporation enables a disk to fully disperse. Radiation hydrodynamic simulations of photoevaporation incorporating FUV, EUV, and X-ray photons show that FUV photons mainly heat the gas through the photoelectric effect on dust grains. Dust grains undergo different physical processes compared to gas, leading to a locally varied dust-to-gas mass ratio. Previous studies mainly focused on understanding either dust or gas evolution in a disk, therefore the other one is incorporated with simple assumptions and approximations. Our work aims to reproduce a realistic photoevaporation profile while considering dust evolution for the first time.

We perform long-term disk evolution simulations that include both gas and dust components consistently. We consider coagulation, fragmentation, radial drift, diffusion, and entrainment for dust evolution. Dust growth and radial drift contribute to dust clearance in the disk and thus influence the dust dispersal timescale. The rapid radial velocity greater than $10\,\mathrm{cm\,s^{-1}}$ reduces the abundance of small dust grains to the level of 0.01 of the ISM value in a million years, leading to the low photoevaporation rate. In contrast, dust entrainment does not affect the dust dispersal timescale, as photoevaporation remains efficient in the outer region. Reducing small dust grains decreases the photoevaporation rate and results in a larger gas disk, aligning well with observations by Ansdell et al. [2018]. The evolution of dust grains has been expected to lead to a low photoevaporation rate, but our work is the first to show the impact quantitatively. We argue that the abundance of dust grains of μm size is critical for the spatial distribution of the gas, since photoevaporation determines the outer edge of the gas disk, emphasizing the great importance of modeling photoevaporation in a realistic manner.

6

Summary and Conclusion

More than 5000 planets have been discovered. These planets exhibit diversity in physical properties, such as stellar mass, planet mass, and orbital period. A protoplanetary disk is a circumstellar structure composed of gas and dust grains and a natal environment for planets. The diversity of planets is thought to result from different disk evolution pathways. Since planets are formed from disk material, understanding disk evolution is crucial for studying planet formation. This study aims to understand the gas and dust dispersal and evolution and provide the possible position and timing for planet formation to occur.

Disks are observed in groups within star-forming regions. The disk fraction, which is the ratio of stars with surrounding disks, is often used to describe the evolutionary stage of these regions. Observations of nearby stellar clusters suggest that the disk fraction decreases within a few million years, indicating that individual dust dispersal timescales are also a few million years.

Theoretical studies identify three major gas dispersal processes in disks: accretion, magnetohydrodynamical (MHD) winds, and photoevaporation. Accretion explains the power-law surface density profile observed in disks. Photoevaporation is essential for dispersing disks within a limited time by driving mass-loss from the outer regions. Radiation hydrodynamic simulations show that FUV photons heat the disk gas through the photoelectric effect on dust grains. This highlights the importance of FUV luminosity and dust abundance for disk dispersal. Komaki [2022] conducted photoevaporation simulations with varying FUV luminosities by two magnitudes and derived the relation $\dot{M}_{\rm pe} \propto L_{\rm FUV}^{0.55}$.

In Chapter 3, we perform radiation hydrodynamic simulations varying the dust-to-gas mass ratio in the range of 10^{-6}–10^{-1}. The simulations solve radiative transfer, hydrodynamics, and non-equilibrium thermochemistry simultaneously while FUV, EUV, and X-ray photons are incorporated as high-energy photons from the central star. When $\mathcal{D} \geq 10^{-2}$, the photoelectric effect by FUV photons dominates gas heating at the photoevaporative base. In the case of $\mathcal{D} = 10^{-3}$, the heating from the photoelectric effect, H_2 pumping, and X-ray ionization contribute equally. When $\mathcal{D} < 10^{-3}$, the photoelectric effect becomes inefficient and H_2 pumping heats the inner regions, while X-ray photons heat

the outer regions. The mass-loss rate decreases with lower dust-to-gas mass ratios but does not continue to decrease because H_2 pumping and X-ray heating are independent of dust abundance. This study quantitatively demonstrates, for the first time, the dependence of the photoevaporative mass-loss rate on the dust-to-gas mass ratio, establishing an essential connection between dust evolution and gas dispersal. As the primary cooling mechanism at the photoevaporative base in dust-deficient disks is O I line cooling, we emphasize that the gas temperature profile in such disks cannot be approximated by the low-metallicity case. We also derive the surface mass-loss profile of photoevaporation for various dust-to-gas mass ratios, which makes it applicable to disk evolution simulations.

Photoevaporation is one of the major disk dispersal processes, but understanding the entire mechanism requires incorporating all of the processes. In Chapter 4, we perform long-term disk evolution simulations for a wide stellar mass range of 0.1–$7\,\mathrm{M}_\odot$. The simulations include accretion, MHD winds, and photoevaporation, along with stellar evolution that updates stellar parameters over time. The surface mass-loss profile for photoevaporation is derived using two-dimensional radiation hydrodynamics simulations that account for FUV, EUV, and X-ray photons as high-energy radiation from the central star. This is the first disk evolution simulation to include a realistic and comprehensive photoevaporation profile. We confirm that differences in the radial dependence of photoevaporation models lead to variations in the gas dissipation timescale. This highlights the importance of using realistic photoevaporation models to understand the evolution of gas distribution and reveals the limitations of earlier models. Stellar evolution significantly impacts solar to intermediate-mass stars. This finding aligns with the results of Kunitomo et al. [2021], and we demonstrate that this trend holds true when all major disk dispersal processes are considered comprehensively for the first time. For solar-mass stars, the FUV luminosity decreases along the Hayashi track, as the main source of FUV radiation is chromospheric. This gradual decrease challenges the assumption of constant FUV luminosity in simulations. Intermediate-mass stars reach the main sequence within a few million years, which is shorter than the typical dust dispersal timescale. The transition to the main sequence causes a sharp increase in FUV luminosity, enhancing photoevaporation and leading to rapid disk dispersal. In contrast, disks around low-mass stars of $M_* < 2\,\mathrm{M}_\odot$ disperse before the star reaches the main sequence.

Disks are observed in groups within star-forming regions. Many observations focus on stellar clusters, and the disk fraction is a common parameter for describing cluster evolution. To compare our simulations with observations, we calculated the evolution of the disk fraction by modeling a stellar cluster with variations in stellar mass, disk mass, and radius. We successfully explain the observed decrease in disk fraction within the first few million years using our disk dispersal model, which incorporates major disk dispersal processes for the first time. Including stellar evolution in the simulations significantly affects the evolution of the disk fraction. While the assumed IMF primarily indicates that low-mass stars are main components, changes in the dust dispersal timescale for solar and intermediate-mass stars still impact the overall disk fraction evolution. This underscores the importance of accurately modeling FUV luminosity evolution. Using the

latest photoevaporation model, we demonstrate that the efficiency of photoevaporation depends on the timing of a star reaching the main sequence relative to the disk dispersal phase.

Observations of the outer galaxy suggest that disk fractions are lower and dust dispersal timescales are shorter in low-metallicity environments. This rapid dispersal has been linked to enhanced photoevaporation due to reduced dust attenuation. To explore this, we performed radiation hydrodynamics simulations and long-term disk evolution calculations for $Z = 0.1\,\mathrm{Z}_\odot$ around $M_* = 0.5, 1, 3\,\mathrm{M}_\odot$ stars in Chapter 4.5. Previous works have generally attributed the low disk fraction to an enhanced photoevaporation rate. For the first time, we quantitatively investigate the specific reasons behind the low disk fraction using numerical calculations. Our findings reveal that the reasons for short dust dispersal timescales vary depending on stellar mass. For low-mass stars, disk dispersal is unaffected by metallicity, but the low dust abundance makes disks unobservable at earlier stages. For solar-mass stars, enhanced photoevaporation and reduced dust abundance shorten the dust dispersal timescale. For intermediate-mass stars, the transition to the main sequence significantly increases FUV luminosity, leading to high photoevaporation rates and shorter dust dispersal timescales. The resulting dust dispersal timescale is within $2\,\mathrm{Myr}$, causing the disk fraction to drop rapidly, consistent with observations.

Photoevaporation is strongly influenced by FUV luminosity and the abundance of dust grains. Dust grains evolve differently from gas components. Since gas constitutes the majority of disk mass, previous theoretical studies have focused primarily on gas evolution and its effects on dust. Although photoevaporation is driven by the photoelectric effect on dust grains caused by FUV photons, the impact of dust evolution on gas evolution has not been included in simulations.

In Chapter 5, we perform disk evolution simulations that solve for both gas and dust surface densities. Dust collisional coagulation and fragmentation are considered for dust growth, while radial drift, diffusion, and entrainment by photoevaporative gas flows are included for dust spatial evolution. We present the latest disk evolution model, incorporating variation in the photoevaporation rate due to the depletion of small dust grains through a consistent simulation approach. Previous studies have attempted to understand photoevaporation during the later stages of disk evolution by making assumptions about dust size or gas distribution, leading to results that are strongly influenced by these assumptions. Our study addresses this issue by performing comprehensive disk evolution simulations that account for the interactions between gas and dust. The dust dispersal timescale decreases because of dust growth, which enhances the radial drift toward the central star. The change in dust dispersal timescale is not the only notable effect of including dust evolution in the simulation. The disk radius extends beyond $100\,\mathrm{au}$ when dust growth and entrainment are incorporated because of the reduced photoevaporation rate in the outer region. This extended disk radius aligns more closely with the observational data. Photoevaporation remains the dominant process during the final stage of disk dispersal and is responsible for the complete clearance of the disk gas.

Through this work, we clarify how photoevaporation depends on dust abundance and

present a realistic photoevaporative mass-loss profile that accounts for the gas distribution in the outer radius. These findings provide a more detailed understanding of the photoevaporation process.

7

Future Prospects

Photoevaporation is a gas dispersal process caused by high-energy photons such as FUV, EUV, and X-ray photons emitted from the star. There is an ongoing discussion about which of FUV, EUV, and X-ray radiation is the most dominant heating source for the disk gas. In Chapter 3, we showed that photoevaporation is driven by heating by H_2 pumping and X-ray photons in dust-deficient disks. In the calculation, we assume that the de-excitation of electronically excited H_2 is the only path to generate vibrationally excited H_2 in the ground state (represented by H_2^*). The excitation to electronically excited H_2 is caused by Lyman-Werner photons with $11.2\,\mathrm{eV} \leq h\nu \leq 13.6\,\mathrm{eV}$ which is a fraction of whole FUV radiation spectrum ($6\,\mathrm{eV} \leq h\nu \leq 13.6\,\mathrm{eV}$). This means that the efficiency of H_2 pumping depends on the spectral energy distribution in FUV radiation.

In our simulations, radiative transfer is solved along with hydrodynamics, but the spectral energy distribution is assumed to be smooth and unchanged. This simplification excludes effects such as variations in photon availability at specific wavelengths. As shown in Chapter 5, the dust-to-gas mass ratio in the outer disk decreases to 10^{-4}, which reduces the photoevaporation rate and increases the disk radius. This underscores the need for detailed photoevaporation simulations in dust-deficient disks with updated spectral energy distribution.

Observational studies suggest that up to 80% of FUV radiation is emitted via Lyα emission lines. Ercolano et al. [2021] proposed that the spectral energy distribution of X-ray photons significantly influences photoevaporation, as soft X-rays deposit energy more effectively in the gas, raising its temperature. A similar effect likely applies to FUV-driven photoevaporation. Both observational and theoretical studies highlight the importance of incorporating spectral evolution into photoevaporation models.

Our simulations incorporate three major disk dispersal processes: accretion, MHD winds, and photoevaporation. Radiation hydrodynamic simulations allow us to model realistic fluxes at various locations, considering the attenuation of high-energy photons by a photoevaporative gas. Ercolano et al. [2008] compared simulations that include hydrodynamics with those assuming hydrostatic equilibrium. They found that the

attenuation of high-energy photons by evaporating gas reduces the mass-loss rate by an order of magnitude. In our study, the surface mass-loss rate due to photoevaporation is derived from radiation hydrodynamics simulations, accounting for attenuation by evaporating gas. However, the shielding effects of MHD winds are not explicitly included.

In Chapter 4.3, we performed additional simulations in which photoevaporation was turned off when the column density of the MHD winds exceeded $10^{20}\,\mathrm{cm}^{-2}$. This approach simplifies disk morphology and applies only to FUV-driven photoevaporation at the photoevaporative base. In dust-deficient disks, X-ray photons dominate heating in the outer region. Detailed photoevaporation simulations are needed to accurately model the temperature structures and resulting mass-loss rates.

Recent observations provide detailed insights into gas surface density distributions. Since gas constitutes 99% of the disk mass, these observations are crucial for understanding the surface density profile and its evolution. Recent theoretical studies on planet formation showed that a high dust-to-gas mass ratio can trigger planet formation. It is necessary to understand the gas distribution as well as the dust distribution.

We believe that the upgrade of ALMA and the initiation of the Square Kilometer Array (SKA) will provide more detailed structures of disk gas, including thin outer regions. Our calculation showed that both gas and dust distributions cannot be reproduced without solving equations for both at the same time. We clarified that the gas distribution is highly sensitive to the photoevaporation rate in the outer region.

Our ultimate goal is to construct an evolution model of disk materials because they are the ingredients of planets. Recent observations use simple viscous accretion models for fitting and estimating parameters such as viscosity, initial disk radius, and mass. By building a new model, we aim to propose a better method to estimate the disk parameters. Since the disk in the earliest stage is difficult to observe, this would help us to understand disks in the Class 0 or I stages. We would like to connect our research to planetesimal formation simulations by providing gas distributions at each phase. There remains a gap in theoretical research between disk dispersal and planet formation.

We showed that the photoevaporation rate also varies with the FUV luminosity, which depends on stellar mass. We performed disk evolution simulations that include gas and dust evolution in a consistent manner, including the interaction between them. We ran the simulation around a $M_* = 1\,\mathrm{M}_\odot$ star. In the future, it will be necessary to perform gas and dust simulations around various stellar masses.

Upgrading the dust coagulation calculation is also needed. In our calculation, we assumed the solid density of dust is constant throughout the disk, but recent simulations show that dust grains grow with porosity inside them. This model with porosity enables dust grains to grow beyond the cm size, overcoming strong radial drift. It is necessary to combine updated dust evolution models with gas dispersal models. Realistic simulations of dust and gas will provide disk material distributions and suggest the most likely locations for planet formation.

Acknowledgement

First, I would like to express my gratitude to my supervisor, Prof. Naoki Yoshida, for his continuous support and guidance throughout my research. His patience and encouragement have inspired me to think creatively and emphasized the importance of staying focused—like a bird on a perch—despite my terrier-like attention span.

I am deeply thankful to Dr. Riouhei Nakatani and Prof. Rolf Kuiper for providing invaluable codes and engaging in fruitful discussions. I am also grateful to Dr. Hiroto Mitani for his insightful comments and thoughtful feedback.

I would also like to express my appreciation to everyone around me, those who have taught me kindness, and those who, through our differences, have shown me valuable lessons about the kind of person I strive to be. I have learned so much from people I admire and, surprisingly, from those I do not. For all these lessons, I am truly thankful.

Finally, I express my thanks to my family for supporting my life.

This work has been supported by FoPM and JSPS. The numerical computations for the two-dimensional radiation hydrodynamic simulations in Chapters 2, 3, and 4 were carried out on the Cray XC50 at the Center for Computational Astrophysics, National Astronomical Observatory of Japan.

Appendix A: Chemical Reactions

In this section, we introduce the chemical reactions that we incorporate in photoevaporation simulations [Tielens and Hollenbach, 1985, Draine and Bertoldi, 1996, Lee et al., 1996, Shapiro and Kang, 1987, Omukai, 2000]. All coefficients are given in cgs units.

reaction	coefficient		
$H + e^- \longrightarrow H^+ + 2\,e^-$	k_1	$=$	$\exp\left[-32.71396786\right.$ $+13.536556\,\ln T_{\rm eV}$ $-5.73932875\,(\ln T_{\rm eV})^2$ $+1.56315498\,(\ln T_{\rm eV})^3$ $-0.2877056\,(\ln T_{\rm eV})^4$ $+3.4825597\times10^{-2}\,(\ln T_{\rm eV})^5$ $-2.6319617\times10^{-3}\,(\ln T_{\rm eV})^6$ $-1.11954395\times10^{-4}\,(\ln T_{\rm eV})^7$ $\left.-2.03914985\times10^{-6}\,(\ln T_{\rm eV})^8\right]$
$H^+ + e^- \longrightarrow H + \gamma$	$R_{\rm rec}$	$=$	$\exp\left[-28.6130338\right.$ $-0.72411256\,\ln T_{\rm eV}$ $-2.02604473\times10^{-2}\,(\ln T_{\rm eV})^2$ $-2.38086188\times10^{-3}\,(\ln T_{\rm eV})^3$ $-3.21260521\times10^{-4}\,(\ln T_{\rm eV})^4$ $-1.42150291\times10^{-5}\,(\ln T_{\rm eV})^5$ $+4.98910892\times10^{-6}\,(\ln T_{\rm eV})^6$ $+5.75561414\times10^{-7}\,(\ln T_{\rm eV})^7$ $-1.85676704\times10^{-8}\,(\ln T_{\rm eV})^8$ $\left.-3.07113524\times10^{-9}\,(\ln T_{\rm eV})^9\right]$
$H + e^- \longrightarrow H^- + \gamma$	k_7	$=$	$1.4\times10^{-18}T^{0.928}\exp\left[-T/1.62\times10^4\right]$
$H^- + H \longrightarrow H_2 + e^-$	k_8	$=$	$4.0\times10^{-9}T^{-0.17}\ \ (T>300)$ $1.5\times10^{-9}\ \ (T<300)$
$H + H^+ \longrightarrow {H_2}^+ + \gamma$	k_9	$=$	$10^{[-19.38-1.523\log_{10}T+1.118(\log_{10}T)^2-0.1269(\log_{10}T)^3]}$
${H_2}^+ + H \longrightarrow H_2 + H^+$	k_{10}	$=$	6.4×10^{-10}
$H_2 + H^+ \longrightarrow {H_2}^+ + H$	k_{11}	$=$	$3.0\times10^{-10}\exp\left[-2.1050\times10^4/T\right]$
$H_2 + e^- \longrightarrow H + H + e^-$	k_{12}	$=$	$4.4\times10^{-10}T^{0.35}\exp\left[-1.02\times10^5/T\right]$
$H_2 + H \longrightarrow H + H + H$	k_{13}	$=$	$k_{\rm H}^{1-a}k_{\rm L}^{a}$ $k_{\rm L}=1.12\times10^{-10}\exp\left[-7.035\times10^4/T\right]$

			$k_{\rm K} = 6.5 \times 10^{-7} T^{-1/2} \exp[-5.2 \times 10^4/T]$
			$[1 - \exp(-6000/T)]$
			$a = (1 + n/n_{\rm cr})^{-1} \log_{10}(n_{\rm cr})$
			$= 4.0 - 0.416 \log_{10}(T/10^4) - 0.327 \left(\log_{10}(T/10^4)\right)$
$H^- + e^- \longrightarrow H + e^- + e^-$	k_{14}	=	$\exp[-18.01849334$
			$+2.3608552 \ln T_{\rm eV}$
			$-0.28274430 (\ln T_{\rm eV})^2$
			$+1.62331664 \times 10^{-2} (\ln T_{\rm eV})^3$
			$-3.36501203 \times 10^{-2} (\ln T_{\rm eV})^4$
			$+1.17832978 \times 10^{-2} (\ln T_{\rm eV})^5$
			$-1.65619470 \times 10^{-3} (\ln T_{\rm eV})^6$
			$+1.06827520 \times 10^{-4} (\ln T_{\rm eV})^7$
			$-2.63128581 \times 10^{-6} (\ln T_{\rm eV})^8]$
$H^- + H^+ \longrightarrow H + H$	k_{15}	=	$5.7 \times 10^{-6} T^{-1/2} + 6.3 \times 10^{-8}$
			$-9.2 \times 10^{-11} T^{1/2} + 4.4 \times 10^{-13} T$
$H^- + H^+ \longrightarrow H_2^+ + e^-$	k_{16}	=	$6.9 \times 10^{-9} T^{-0.35}$ $(T < 8000)$
			$9.6 \times 10^{-7} T^{-0.9}$ $(T > 8000)$
$H_2^+ + e^- \longrightarrow H + H$	k_{17}	=	$2.0 \times 10^{-7} T^{-1/2}$
$H_2^+ + H^- \longrightarrow H_2 + H$	k_{18}	=	$2.3 \times 10^{-7} (T/300)^{-1/2}$
$H + H + H \longrightarrow H_2 + H$	k_{19}	=	$5.5 \times 10^{-29} T^{-1}$
$H + H + H_2 \longrightarrow 2\,H_2$	k_{20}	=	$k_{19}/8$
$H_2 + H_2 \longrightarrow H_2 + H + H$	k_{21}	=	$k_{\rm H}^{1-a} k_{\rm L}^a$
			$k_{\rm L} = 1.18 \times 10^{-10} \exp[-6.95 \times 10^4/T]$
			$k_{\rm H} = 8.125 \times 10^{-8} T^{-1/2} \exp[-5.2 \times 10^4/T]$ $\times [1 - \exp(-6.0 \times 10^3/T)]$
			$a = (1 + n/n_{\rm cr})^{-1} \log_{10}(n_{\rm cr})$
			$= 4.845 - 1.3 \log_{10}(T/10^4) + 1.62 \left(\log_{10}(T/10^4)\right)^2$
$H + H \longrightarrow H^+ + e^- + H$	k_{22}	=	$1.7 \times 10^{-4} k_1$
$H + H \longrightarrow H_2$	$k_{\rm dust}$	=	$6.0 \times 10^{-17} (T/300^{1/2}) f_a (Z/Z_\odot)$
			$\times \left[1 + 4.0 \times 10^2 (T + T_{\rm dust})^{1/2} + 2.0 \times 10^{-3} T + 8.0 \times 10^{-6} T^2\right]^{-1}$
			$f_a = \left[1 + \exp(7.5 \times 10^2 (1/75 - 1/T_{\rm dust}))\right]^{-1}$
$H_2^* + H \longrightarrow H_2 + H$	$k_{\rm de,\,H}$	=	$1.8 \times 10^{-13} T^{1/2} \exp[-1000/T]$
$H_2^* + H_2 \longrightarrow H_2 + H_2$	$k_{\rm de,\,H_2}$	=	$2.3 \times 10^{-13} T^{1/2} \exp[-18000/(T + 1200)]$
$H_2^* \longrightarrow H_2$	$A(H_2^*)$	=	2.0×10^{-7}
$H + \gamma \longrightarrow H^+ + e^-$	$P_{\rm ion}$		Eq. 3.2
$H_2 + \gamma \longrightarrow H_2^+$	$R_{\rm H_2,\,ion}$	=	$[6.2 \times 10^{-18} E - 9.4 \times 10^{-17}] F_{\rm EUV}$ $(15.42 < E < 16.5)$
			$[1.4 \times 10^{-18} E - 1.48 \times 10^{-17}] F_{\rm EUV}$ $(16.5 < E < 17.7)$

			$2.5 \times 10^{-14} E^{-2.71}$ $(E > 17.7)$
			$E = E_{\rm EX}/1\,{\rm eV}$
$H_2 + \gamma \longrightarrow H + H$	$R_{\rm H_2,\,diss}$	$=$	$3.4 \times 10^{-11} f_{\rm shield} G_0 \exp[-2.5 A_{\rm V}]$
$H_2 + \gamma \longrightarrow H_2^*$	$R_{\rm H_2,\,pump}$	$=$	$3.06 \times 10^{-10} f_{\rm shield} G_0 \exp[-2.5 A_{\rm V}]$
$H_2^* + \gamma \longrightarrow H + H$	$R_{\rm H_2^*,\,diss}$	$=$	$1.0 \times 10^{-11} f_{\rm shield} G_0 \exp[-2.5 A_{\rm V}]$
$CO + \gamma \longrightarrow C^+ + O$	$R_{\rm CO,\,diss}$		see Lee et al. [1996]
$C^+ + O \longrightarrow CO$	$R_{\rm CO,\,form}$		see Nelson and Langer [1997] and Nomura and Millar [2005]

In the equation, $T = T_{\rm gas}/1\,{\rm K}$ represents the gas temperature in the Kelvin unit, while $T_{\rm eV} = T_{\rm gas}/1\,{\rm eV}$ denotes the temperature in electron volt unit. The dust temperature is given by $T_{\rm dust}$. $E_{\rm EX}$ represents the photon energy in electron volt units.

Appendix B: Disk Evolution Equations with Viscosity

In this section, we will derive the time evolution equation of surface density under the influence of viscosity. We derive the equation from the equations of a viscous gas. We use 3 dimensional cylindrical coordinates, (r, ϕ, z) The basic equations for viscous gas are given by

$$\frac{\partial \rho}{\partial t} + \nabla \cdot \rho \mathbf{v} = 0$$
$$\rho \frac{D\mathbf{v}}{Dt} = -\nabla P - \rho \frac{GM}{r^3}\mathbf{r} + \nabla \cdot \sigma$$
$$\frac{\partial E}{\partial t} + \nabla \cdot (H\mathbf{v}) = -\rho v_r \frac{GM_*}{r^2} + \rho(\Gamma - \Lambda)$$

The first equation represents the continuity equation. The second equation is the Euler equation, where σ denotes the stress tensor. The third equation represents the conservation of energy, with E and H denoting the energy and enthalpy per unit volume, respectively, and Γ and Λ representing the heating and cooling rates per unit volume.

The equation of continuity is written as below using coordinates,

$$\frac{\partial \rho}{\partial t} + \frac{1}{r}\frac{\partial}{\partial r}(r\rho v_r) + \frac{1}{r}\frac{\partial}{\partial \phi}(\rho v_\phi) + \frac{\partial}{\partial z}(\rho v_z) = 0$$

We assume that the disk is axisymmetric around the z-axis and that the disk is vertically thin, and the differential of $\partial/\partial\phi$ and v_z can be ignored. Under these assumptions, the equation simplifies to:

$$\frac{\partial \rho}{\partial t} + \frac{1}{r}\frac{\partial}{\partial r}(r\rho v_r) = 0.$$

In the simulation, we ignore the vertical structure of the disk and instead solve for the surface density. By integrating the governing equations along the z-axis, the surface density equation is given by:

$$\frac{\partial \Sigma}{\partial t} + \frac{1}{r}\frac{\partial}{\partial r}(r\Sigma v_r) = 0. \tag{B1}$$

On the other hand, Euler equation in ϕ-direction is given by

$$\rho\frac{\partial v_\phi}{\partial t}+\rho\left(v_r\frac{\partial v_\phi}{\partial r}+\frac{v_\phi}{r}\frac{\partial v_\phi}{\partial \phi}+v_z\frac{\partial v_\phi}{\partial z}+\frac{v_r v_\phi}{r}\right)=\frac{1}{r}\frac{\partial}{\partial r}(r\sigma_{r\phi})+\frac{1}{r}\frac{\partial \sigma_{\phi\phi}}{\partial \phi}+\frac{\partial \sigma_{\phi z}}{\partial z}+\frac{\sigma_{r\phi}}{r}$$
$$\sigma_{r\phi}=\mu\left(\frac{1}{r}\frac{\partial v_r}{\partial \phi}+r\frac{\partial}{\partial r}\left(\frac{v_\phi}{r}\right)\right)$$

This equation is simplified under the assumptions that the disk is axisymmetric and vertically thin. The Euler equation is then rewritten as:

$$\begin{aligned}\rho\frac{\partial v_\phi}{\partial t}+\rho\left(v_r\frac{\partial v_\phi}{\partial r}+\frac{v_r v_\phi}{r}\right)&=\frac{1}{r}\frac{\partial}{\partial r}(r\sigma_{r\phi})+\frac{\sigma_{r\phi}}{r}\\&=\frac{1}{r^2}\frac{\partial}{\partial r}(r^2\sigma_{r\phi}).\end{aligned}$$

The stress tensor in ϕ-direction is also simplified as

$$\sigma_{r\phi}\sim\mu r\frac{\partial\Omega}{\partial r},$$

where Ω is the angular velocity. By combining these two relations, the Euler equation required for describing disk evolution is finally given by:

$$\rho\frac{\partial v_\phi}{\partial t}+\rho\left(v_r\frac{\partial v_\phi}{\partial r}+\frac{v_r v_\phi}{r}\right)=\frac{1}{r^2}\frac{\partial}{\partial r}\left(\mu r^3\frac{\partial\Omega}{\partial r}\right).$$

The equation is arranged for evolution of surface density by integrating along z-axis and is given by

$$\Sigma\frac{\partial v_\phi}{\partial t}+\Sigma v_r\frac{\partial v_\phi}{\partial r}+\frac{\Sigma v_r v_\phi}{r}=\frac{1}{r^2}\frac{\partial}{\partial r}\left(\nu\Sigma r^3\frac{\partial\Omega}{\partial r}\right).$$

The left-hand side of the equation can be simplified by incorporating the continuity equation. The resulting equation is given by:

$$\frac{\partial}{\partial t}(\Sigma r^2\Omega)+\frac{1}{r}\frac{\partial}{\partial r}(r^3\Sigma v_r\Omega)=\frac{1}{2\pi r}\frac{\partial}{\partial r}\left(2\pi r^3\nu\Sigma\frac{\partial\Omega}{\partial r}\right). \tag{B2}$$

In the equation, the term in $()$ in the right-hand side denotes the torque exerted by the gas, and the equation describes angular momentum transport. This indicates that the transfer of torque occurs through the exchange of angular momentum with the nearby gas.

We assume that the angular velocity, Ω, remains constant over time. By combining equations (B1) and (B2), we obtain the equation describing the accretion motion, which is given by:

$$2\pi r\Sigma v_r=\frac{\frac{\partial}{\partial r}(2\pi r^3\nu\Sigma\frac{\partial\Omega}{\partial r})}{\frac{\partial}{\partial r}(r^2\Omega)}. \tag{B3}$$

The right-hand side, $2\pi R\Sigma v_r$, represents the accreted mass at a specific radius, r.

The equation describing the time evolution of surface density is obtained by rewriting

Equation (B3) with Equation (B1), and is given by:

$$\frac{\partial \Sigma}{\partial t} = -\frac{1}{r}\frac{\partial}{\partial r}\left[\frac{\frac{\partial}{\partial r}(r^3 \nu \Sigma \frac{\partial \Omega}{\partial r})}{\frac{\partial}{\partial r}(r^2 \Omega)}\right]$$

The equation express the time evolution of surface density due to viscous accretion. The motion of the disk gas follows Keplerian rotation. By introducing Ω_{K} (the Keplerian angular velocity), the equation can be rewritten as:

$$\frac{\partial \Sigma}{\partial t} = \frac{3}{r}\frac{\partial}{\partial r}\left[r^{\frac{1}{2}}\frac{\partial}{\partial r}(r^{\frac{1}{2}}\nu\Sigma)\right].$$

This equation describes the evolution of surface density under the effects of viscous accretion.

To simplify and better understand the essence of the surface density equation, we introduce the following new parameters:

$$x = 2\sqrt{r} \;\; f = \frac{3}{2}\Sigma x$$

The equation for surface density evolution can be rewritten as:

$$\frac{\partial f}{\partial t} = \frac{12}{x^2}\frac{\partial^2 f}{\partial x^2}.$$

This equation is a diffusion equation, indicating that the disk surface density evolves according to diffusion due to viscosity.

Appendix C: Disk Evolution Equations with Viscosity and MHD Winds

In this section, we derive the equation that governs the evolution of the disk surface density while considering the effects of magnetic fields. We then derive the coefficients that describe magnetohydrodynamic (MHD) winds. The equations are expressed in three-dimensional cylindrical coordinates (r, ϕ, z). In this case, the basic equations for viscous gas are given by

$$\frac{\partial \rho}{\partial t} + \nabla \cdot \rho \mathbf{v} = 0$$
$$\rho \frac{D\mathbf{v}}{Dt} = -\nabla P - \rho \frac{GM}{r^3}\mathbf{r} + \nabla \cdot \sigma + \frac{1}{4\pi}\nabla\left(\frac{\mathbf{T}}{4\pi}\right) - \frac{1}{8\pi}\nabla B^2$$
$$\frac{\partial}{\partial t}\left(E + \rho\Phi + \frac{B^2}{8\pi}\right) + \nabla \cdot \left(H\mathbf{v} + \rho\Phi\mathbf{v} + \frac{\mathbf{B} \times (\mathbf{v} \times \mathbf{B})}{4\pi} + \mathbf{F}\right) = 0.$$

The first equation is the continuity equation. The second equation represents the Euler equation. In the equation, B denotes magnetic fields, and $\mathbf{T}$ represents the momentum tensor due to magnetic effects and is given by

$$T = \begin{pmatrix} B_r^2 - B^2/2 & B_r B_\phi & B_r B_z \\ B_r B_\phi & B_\phi^2 - B^2/2 & B_\phi B_z \\ B_r B_z & B_\phi B z & B_z^2 - B^2/2 \end{pmatrix}.$$

The third equation is the equation of energy conservation. In the equation, Φ and $\mathbf{F}$ represent the potential energy and energy exchange with external sources through heat.

The first equation is simplified as follows by assuming axisymmetry around the z-axis:

$$\frac{\partial \rho}{\partial t} + \frac{1}{r}\frac{\partial}{\partial r}(r\rho v_r) + \frac{\partial}{\partial z}(\rho v_z) = 0.$$

In this case, we consider mass loss by MHD winds, by which the gas flows are launched into the upper air by magnetic centrifugal forces. The gas has a velocity in the z-direction due to the MHD winds, satisfying $v_z \neq 0$. By integrating the equation along the z-axis, the resulting equation for surface density is given as:

$$\frac{\partial \Sigma}{\partial t} + \frac{1}{r}\frac{\partial}{\partial r}(r\Sigma v_r) + (\rho v_z)_{\rm w} = 0. \tag{C1}$$

The subscript w indicates the gas motion driven by MHD winds.

The Euler equation in the ϕ-direction is approximated similarly. Unlike the previous section, which considers only viscous accretion with a specified viscous parameter, we attribute the viscosity to the interaction between gas and magnetic fields as well as the torque caused by differential motion between adjacent gas layers. Thus, the Euler equation is given by:

$$\rho\frac{\partial v_\phi}{\partial t}+\rho(\mathbf{v}\cdot\nabla)v_\phi+\rho\frac{v_\phi v_r}{r}=\frac{1}{4\pi}\left(\frac{1}{r^2}\frac{\partial}{\partial r}(r^2B_rB_\phi)+\frac{\partial(B_\phi B_z)}{\partial z}\right).$$

The left-hand side of the equation is simplified by combining it with the continuity equation and is given by:

$$\frac{\partial(\rho v_\phi)}{\partial t}+\frac{1}{r^2}\frac{\partial}{\partial r}(r^2\rho v_r v_\phi)+\frac{\partial}{\partial z}(\rho v_\phi v_z)=\frac{1}{4\pi r^2}\frac{\partial}{\partial r}(r^2B_rB_\phi)+\frac{1}{4\pi}\frac{\partial(B_\phi B_z)}{\partial z}.$$

This is rewritten by multiplying r on both sides:

$$\frac{\partial(\rho r v_\phi)}{\partial t}+\frac{1}{r}\frac{\partial}{\partial r}\left(r^2\left(\rho v_r v_\phi-\frac{B_rB_\phi}{4\pi}\right)\right)+\frac{\partial}{\partial z}\left(r\left(\rho v_\phi v_z-\frac{B_\phi B_z}{4\pi}\right)\right)=0. \tag{C2}$$

Basically, the gas velocity follows Keplerian motion, and gas velocity in the ϕ-direction is approximated to the Keplerian velocity. We introduce a new parameter, δv_ϕ, which represents the deviation from the Keplerian motion:

$$v_\phi=r\Omega_{\rm K}+\delta v_\phi,$$

where $\Omega_{\rm K}$ represents Keplerian angular velocity. Equation (C2) is rewritten by

$$\begin{aligned}\frac{\partial(\rho r v_\phi)}{\partial t}&+\rho v_r\frac{\partial}{\partial r}(rv_{\rm K})+\rho v_z\frac{\partial}{\partial z}(rv_{\rm K})\\&+\frac{1}{r}\frac{\partial}{\partial r}\left(r^2\left(\rho v_r\delta v_\phi-\frac{B_rB_\phi}{4\pi}\right)\right)+\frac{\partial}{\partial z}\left(r\left(\rho\delta v_\phi v_z-\frac{B_\phi B_z}{4\pi}\right)\right)=0\end{aligned} \tag{C3}$$

This equation describes the evolution of local density due to stress caused by velocity differences between adjacent gas and interactions with magnetic fields. The viscosity parameters, $\alpha_{r\phi}$ and $\alpha_{\phi z}$, describe the efficiency of angular momentum transport in a steady state where $\partial/\partial t=0$. The viscous parameters are derived by comparing to the original definition by Shakura and Sunyaev [1973].

$$\begin{aligned}\alpha_{r\phi}\rho c_{\rm s}^2&\equiv\rho v_r\delta v_\phi-\frac{B_rB_\phi}{4\pi}\\\alpha_{\phi z}\rho c_{\rm s}^2&\equiv\rho v_z\delta v_\phi-\frac{B_\phi B_z}{4\pi}.\end{aligned}$$

Equation (C3) is rewritten using this prescription as follows:

$$\frac{\partial(\rho r v_\phi)}{\partial t} + \frac{1}{r}\frac{\partial}{\partial r}\left(\rho r^2\left(v_r r\Omega_{\rm K} + \alpha_{r\phi}c_{\rm s}^2\right)\right) + \frac{\partial}{\partial z}\left(r\left(\rho v_z r\Omega_{\rm K} + \alpha_{\phi z}\rho c_{\rm s}^2\right)\right) = 0.$$

This equation describes the evolution of the local gas density. It is converted into an equation for surface density by integrating along the z-axis as:

$$\frac{\partial(\Sigma r^2 v_\phi)}{\partial t} + \frac{\partial}{\partial r}\left(\Sigma r^2\left(v_r r\Omega_{\rm K} + \overline{\alpha_{r\phi}}c_{\rm s}^2\right)\right) + r^2\left((\rho v_z)_{\rm w} r\Omega_{\rm K} + \alpha_{\phi z}(\rho c_{\rm s}^2)_{\rm mid}\right) = 0 \qquad \text{(C4)}$$

This equation describes the evolution of surface density, including gas outflows driven by MHD winds. In the equation, $\overline{\alpha_{r\phi}}$ is the viscous parameter normalized by the local surface density and is given by

$$\overline{\alpha_{r\phi}} = \frac{\int \rho\alpha_{r\phi}{\rm d}z}{\Sigma}.$$

The subscript 'w' indicates that the gas motion in the z-direction originates from MHD winds. The subscript 'mid' denotes that the value is taken at the disk midplane.

The continuity equation multiplied by $r^2 v_\phi$ is given by

$$\frac{\partial}{\partial t}(\Sigma r^2 v_\phi) + (r^2\Omega_{\rm K})\frac{\partial}{\partial r}(r\Sigma v_r) + r^3\Omega_{\rm K}(\rho v_z)_{\rm w} = 0. \qquad \text{(C5)}$$

By comparing equations (C4) and (C5), we derive the following equation under the assumption that the sum of the second and third terms remains equivalent:

$$(r\Sigma v_r)\frac{\partial}{\partial r}(r^2\Omega_{\rm K}) + \frac{\partial}{\partial r}(r^2\Sigma\overline{\alpha_{r\phi}}c_{\rm s}^2) + r^2\overline{\alpha_{\phi z}}(\rho c_{\rm s}^2)_{\rm mid} = 0.$$

Then the velocity in r-direction is given by

$$v_r = -\frac{2}{r^2\Sigma\Omega_{\rm K}}\left[\frac{\partial}{\partial r}(r^2\Sigma\overline{\alpha_{r\phi}}c_{\rm s}^2) + r^2\overline{\alpha_{\phi z}}(\rho c_{\rm s}^2)_{\rm mid}\right]$$

The first term represents the accretion motion due to viscosity, while the second term represents the gas motion toward the star driven by angular momentum loss through disk torque induced by magnetic activity. The equation of surface density is then given by

$$\frac{\partial\Sigma}{\partial t} - \frac{1}{r}\frac{\partial}{\partial r}\left[\frac{2}{r\Omega_{\rm K}}\left(\frac{\partial}{\partial r}(r^2\Sigma\overline{\alpha_{r\phi}}c_{\rm s}^2) + r^2\overline{\alpha_{\phi z}}(\rho c_{\rm s}^2)_{\rm mid}\right)\right] + C_{\rm w}(\rho c_{\rm s})_{\rm mid} = 0,$$

where C_{mw} is a non-dimensional parameter representing mass loss by MHD winds normalized by the value at the midplane. This equation is solved in our simulation.

The coefficient C_{mw} is derived from the energy conservation equation. The energy

equation in cylindrical coordinates is given by:

$$\begin{aligned}
&\frac{\partial}{\partial t}\left(\frac{1}{2}\rho\mathbf{v}^2+\frac{P}{\gamma-1}+\rho\Phi+\frac{B^2}{8\pi}\right)\\
&\quad+\frac{1}{r}\frac{\partial}{\partial r}\left[r\left\{v_r\left(\frac{1}{2}\rho v^2+\frac{\gamma}{\gamma-1}P+\rho\Phi+\frac{1}{4\pi}(B_\phi^2+B_z^2)\right)-\frac{B_r}{4\pi}(v_\phi B_\phi+v_z B_z)+F_r\right\}\right]\\
&\quad+\frac{\partial}{\partial z}\left[v_z\left(\frac{1}{2}\rho v^2+\frac{\gamma}{\gamma-1}P+\rho\Phi+\frac{1}{4\pi}(B_r^2+B_\phi^2)\right)-\frac{B_z}{4\pi}(v_r B_r+v_\phi B_\phi)+F_z\right]=0.
\end{aligned}\tag{C6}$$

The gas motion is approximated as Keplerian motion. Under this assumption, $r\Omega_{\rm K}\gg v_r, v_z, c_{\rm s}=\sqrt{P/\rho}, B/\sqrt{4\pi\rho}$ serve as a good approximations. As a result, Equation (C6) can be simplified. The first term is given by

$$\begin{aligned}
\frac{\partial}{\partial t}\left(\frac{1}{2}\rho\mathbf{v}^2+\frac{P}{\gamma-1}+\rho\Phi+\frac{B^2}{8\pi}\right)&\sim\frac{\partial}{\partial t}\left(\frac{1}{2}\rho\mathbf{v}^2+\rho\Phi\right)\\
&\sim\frac{\partial}{\partial t}\left(\frac{1}{2}\rho(\rho\Omega_{\rm K}+\delta v_\phi)^2-\rho r^2\Omega_{\rm K}^2\right)\\
&\sim\frac{\partial}{\partial t}\left(-\frac{1}{2}\rho r^2\Omega_{\rm K}^2\right).
\end{aligned}$$

Using the assumptions above, the second term is given by:

$$\begin{aligned}
&\frac{1}{r}\frac{\partial}{\partial r}\left[r\left\{v_r\left(\frac{1}{2}\rho v^2+\frac{\gamma}{\gamma-1}P+\rho\Phi+\frac{1}{4\pi}(B_\phi^2+B_z^2)\right)-\frac{B_r}{4\pi}(v_\phi B_\phi+v_z B_z)+F_r\right\}\right]\\
\sim&\frac{1}{r}\frac{\partial}{\partial r}\left[r\left\{v_r\left(\frac{1}{2}\rho v^2+\rho\Phi\right)-\frac{1}{4\pi}v_\phi B_r B_\phi+F_r\right\}\right]\\
\sim&\frac{1}{r}\frac{\partial}{\partial r}\left[r\left\{v_r\left(-\frac{1}{2}\rho r^2\Omega_{\rm K}^2+\rho r\Omega_{\rm K}\delta v_\phi\right)-\frac{1}{4\pi}v_\phi B_r B_\phi+F_r\right\}\right]\\
=&\frac{1}{r}\frac{\partial}{\partial r}\left[r\left\{-\frac{1}{2}\rho v_r r^2\Omega_{\rm K}^2+\rho r\Omega_{\rm K}\left(v_r\delta v_\phi-\frac{B_r B_\phi}{4\pi\rho}\right)+F_r\right\}\right]\\
=&\frac{1}{r}\frac{\partial}{\partial r}\left[r\left\{-\frac{1}{2}\rho v_r r^2\Omega_{\rm K}^2+\rho r\Omega_{\rm K}\alpha_{r\phi}c_{\rm s}^2+F_r\right\}\right].
\end{aligned}$$

The third term is given by

$$\frac{\partial}{\partial z}\left(v_z\rho E_{\rm w}+F_z\right)\equiv\frac{\partial}{\partial z}\left[v_z\left(\frac{1}{2}\rho v^2+\frac{\gamma}{\gamma-1}P+\rho\Phi+\frac{1}{4\pi}(B_r^2+B_\phi^2)\right)-\frac{B_z}{4\pi}(v_r B_r+v_\phi B_\phi)+F_z\right],$$

where $E_{\rm w}$ represents the energy carried away by MHD winds per unit mass. The energy equation is then simplified as

$$\frac{\partial}{\partial t}\left(-\frac{1}{2}\rho r^2\Omega_{\rm K}^2\right)+\frac{1}{r}\frac{\partial}{\partial r}\left[r\left\{-\frac{1}{2}\rho v_r r^2\Omega_{\rm K}^2+\rho r\Omega_{\rm K}\alpha_{r\phi}c_{\rm s}^2+F_r\right\}\right]+\frac{\partial}{\partial z}\left(v_z\rho E_{\rm w}+F_z\right)=0.\tag{C7}$$

This describes the balance among energy transported by accretion motion, energy carried

away by MHD winds, and energy released as heat from the disk surface. The surface density equation is derived by integrating Equation (C7) along the z-direction and is given by:

$$\frac{\partial}{\partial t}\left(-\frac{1}{2}\Sigma r^2\Omega_{\rm K}^2\right)+\frac{1}{r}\frac{\partial}{\partial r}\left[r\left\{-\frac{1}{2}\Sigma v_r r^2\Omega_{\rm K}^2+\Sigma r\Omega_{\rm K}\overline{\alpha_{r\phi}}c_{\rm s}^2\right\}\right]+(\rho v_z)_{\rm w}E_{\rm w}+F_{\rm rad}=0.$$

In the equation, the energy release is represented by a single term, $F_{\rm rad}$. The term involving $\partial/\partial t$ is eliminated by applying the continuity equation multiplied by $r^2\Omega_{\rm K}^2/2$. The resulting equation is:

$$\frac{1}{2}r\Sigma v_r\Omega_{\rm K}^2+\frac{1}{r}\frac{\partial}{\partial r}(\Sigma r^2\Omega_{\rm K}\overline{\alpha_{r\phi}}c_{\rm s}^2)+\left(\frac{1}{2}r^2\Omega_{\rm K}^2+E_{\rm w}\right)(\rho v_z)_{\rm w}+F_{\rm rad}=0.$$

Using the description of v_r given by (C3), the equation is rearranged as:

$$\left(\frac{1}{2}r^2\Omega_{\rm K}^2+E_{\rm w}\right)C_{\rm w}(\rho c_{\rm s})_{\rm mid}+F_{\rm rad}$$
$$=\frac{\Omega_{\rm K}}{r}\left[\frac{\partial}{\partial r}(r^2\Sigma\overline{\alpha_{r\phi}}c_{\rm s}^2)+r^2\overline{\alpha_{\phi z}}(\rho c_{\rm s}^2)_{\rm mid}\right]-\frac{1}{r}\frac{\partial}{\partial r}(\Sigma r^2\Omega_{\rm K}\overline{\alpha_{r\phi}}c_{\rm s}^2).$$

This equation represents the total energy lost through radiation and carried away by MHD winds but does not specify the fraction of energy used to drive MHD winds. Since MHD winds are driven by wind torque, the term with $\overline{\alpha_{\phi z}}$ is often associated with the driving mechanism for these winds.

Interestingly, the shearing box simulation by Suzuki et al. [2010] showed that MHD winds can still launch gas flows even when the wind torque is completely turned off, $\overline{\alpha_{\phi z}}=0$. This suggests that the MHD wind coefficient, $C_{\rm w}$, must also account for contributions from the term involving $\overline{\alpha_{r\phi}}$.

Two primary formulations for $C_{\rm w}$ exist, commonly referred to as the 'strong wind case' and the 'weak wind case.' In the equations, $E_{\rm w}$ denotes the energy carried by MHD wind gas per unit mass. For gas to escape the system, the condition $E_{\rm w}\geq 0$ must be met. In our calculations, we adopt the minimum energy condition, $E_{\rm w}=0$, for simplicity. The two formulations are described below.

- strong wind case
  All the gravitational energy released is used to drive MHD winds, while the energy from viscous heating is emitted as radiation. In this model, the parameters for mass loss by MHD winds and radiation from the disk are given by:

$$C_{\rm w}=\frac{2}{r^3\Omega_{\rm K}(\rho c_{\rm s})_{\rm mid}}\frac{\partial}{\partial r}(r^2\Sigma\overline{\alpha_{r\phi}}c_{\rm s}^2)+\frac{2c_{\rm s}}{r\Omega_{\rm K}}\overline{\alpha_{r\phi}}$$
$$F_{\rm rad}=-\frac{1}{r}\frac{\partial}{\partial r}(\Sigma r^2\Omega_{\rm K}\overline{\alpha_{r\phi}}c_{\rm s}^2).$$

- weak wind case
  Only a portion of the energy liberated through accretion is used to drive MHD winds.

We define the fraction of the total energy (released via accretion and viscous heating) allocated to radiation as $\epsilon_{\rm rad}$. Based on this assumption, the parameters for mass loss due to disk winds and radiation from the disk are expressed as:

$$C_{\rm w} = (1-\epsilon_{\rm rad})\left[\frac{2}{r\Omega_{\rm K}}\overline{\alpha_{\phi z}}c_{\rm s} + 3\sqrt{2\pi}\frac{\overline{\alpha_{r\phi}}c_{\rm s}^2}{r^2\Omega_{\rm K}^2}\right]$$
$$F_{\rm rad} = \epsilon_{\rm rad}\left[\frac{1}{\sqrt{2\pi}}r\Omega_{\rm K}^2\Sigma\overline{\alpha_{\phi z}}c_{\rm s} + \frac{3}{2}\Sigma\Omega_{\rm K}\overline{\alpha_{r\phi}}c_{\rm s}^2\right].$$

In previous studies, $\epsilon_{\rm rad} = 0.9$ is the commonly adopted for the 'weak wind case.' This model leads to a longer disk lifetime, aligning more closely with the observations. In our calculations, we use the 'weak wind model' as the fiducial model.

References

Charles P. Abod, Jacob B. Simon, Rixin Li, Philip J. Armitage, Andrew N. Youdin, and Katherine A. Kretke. The Mass and Size Distribution of Planetesimals Formed by the Streaming Instability. II. The Effect of the Radial Gas Pressure Gradient. ApJ, 883(2): 192, October 2019. doi: 10.3847/1538-4357/ab40a3. 29

J. M. Alcalá, A. Natta, C. F. Manara, L. Spezzi, B. Stelzer, A. Frasca, K. Biazzo, E. Covino, S. Randich, E. Rigliaco, L. Testi, F. Comerón, G. Cupani, and V. D'Elia. X-shooter spectroscopy of young stellar objects. IV. Accretion in low-mass stars and substellar objects in Lupus. A&A, 561:A2, January 2014. doi: 10.1051/0004-6361/201322254. 18, 19, 85

J. M. Alcalá, C. F. Manara, A. Natta, A. Frasca, L. Testi, B. Nisini, B. Stelzer, J. P. Williams, S. Antoniucci, K. Biazzo, E. Covino, M. Esposito, F. Getman, and E. Rigliaco. X-shooter spectroscopy of young stellar objects in Lupus. Accretion properties of class II and transitional objects. A&A, 600:A20, April 2017. doi: 10.1051/0004-6361/201629929. 18

R. D. Alexander, C. J. Clarke, and J. E. Pringle. Photoevaporation of protoplanetary discs - I. Hydrodynamic models. MNRAS, 369(1):216–228, June 2006a. doi: 10.1111/j.1365-2966.2006.10293.x. 20

R. D. Alexander, C. J. Clarke, and J. E. Pringle. Photoevaporation of protoplanetary discs - II. Evolutionary models and observable properties. MNRAS, 369(1):229–239, June 2006b. doi: 10.1111/j.1365-2966.2006.10294.x. 20, 24

ALMA Partnership, C. L. Brogan, L. M. Pérez, T. R. Hunter, W. R. F. Dent, A. S. Hales, R. E. Hills, S. Corder, E. B. Fomalont, C. Vlahakis, Y. Asaki, D. Barkats, A. Hirota, J. A. Hodge, C. M. V. Impellizzeri, R. Kneissl, E. Liuzzo, R. Lucas, N. Marcelino, S. Matsushita, K. Nakanishi, N. Phillips, A. M. S. Richards, I. Toledo, R. Aladro, D. Broguiere, J. R. Cortes, P. C. Cortes, D. Espada, F. Galarza, D. Garcia-Appadoo, L. Guzman-Ramirez, E. M. Humphreys, T. Jung, S. Kameno, R. A. Laing, S. Leon, G. Marconi, A. Mignano, B. Nikolic, L. A. Nyman, M. Radiszcz, A. Remijan, J. A. Rodón, T. Sawada, S. Takahashi, R. P. J. Tilanus, B. Vila Vilaro, L. C. Watson, T. Wiklind, E. Akiyama, E. Chapillon, I. de Gregorio-Monsalvo, J. Di Francesco, F. Gueth, A. Kawamura, C. F. Lee, Q. Nguyen Luong, J. Mangum, V. Pietu, P. Sanhueza, K. Saigo, S. Takakuwa, C. Ubach, T. van Kempen,

A. Wootten, A. Castro-Carrizo, H. Francke, J. Gallardo, J. Garcia, S. Gonzalez, T. Hill, T. Kaminski, Y. Kurono, H. Y. Liu, C. Lopez, F. Morales, K. Plarre, G. Schieven, L. Testi, L. Videla, E. Villard, P. Andreani, J. E. Hibbard, and K. Tatematsu. The 2014 ALMA Long Baseline Campaign: First Results from High Angular Resolution Observations toward the HL Tau Region. ApJ, 808(1):L3, July 2015. doi: 10.1088/2041-8205/808/1/L3. 13

Alexa R. Anderson, Jonathan P. Williams, Nienke van der Marel, Charles J. Law, Luca Ricci, John J. Tobin, and Simin Tong. Protostellar and Protoplanetary Disk Masses in the Serpens Region. ApJ, 938(1):55, October 2022. doi: 10.3847/1538-4357/ac8ff0. 14

Ph. André, A. Men'shchikov, S. Bontemps, V. Könyves, F. Motte, N. Schneider, P. Didelon, V. Minier, P. Saraceno, D. Ward-Thompson, J. di Francesco, G. White, S. Molinari, L. Testi, A. Abergel, M. Griffin, Th. Henning, P. Royer, B. Merín, R. Vavrek, M. Attard, D. Arzoumanian, C. D. Wilson, P. Ade, H. Aussel, J. P. Baluteau, M. Benedettini, J. Ph. Bernard, J. A. D. L. Blommaert, L. Cambrésy, P. Cox, A. di Giorgio, P. Hargrave, M. Hennemann, M. Huang, J. Kirk, O. Krause, R. Launhardt, S. Leeks, J. Le Pennec, J. Z. Li, P. G. Martin, A. Maury, G. Olofsson, A. Omont, N. Peretto, S. Pezzuto, T. Prusti, H. Roussel, D. Russeil, M. Sauvage, B. Sibthorpe, A. Sicilia-Aguilar, L. Spinoglio, C. Waelkens, A. Woodcraft, and A. Zavagno. From filamentary clouds to prestellar cores to the stellar IMF: Initial highlights from the Herschel Gould Belt Survey. A&A, 518:L102, July 2010. doi: 10.1051/0004-6361/201014666. 3

Sean M. Andrews. Observations of Protoplanetary Disk Structures. ARA&A, 58:483–528, August 2020. doi: 10.1146/annurev-astro-031220-010302. 14, 60, 79

Sean M. Andrews and Jonathan P. Williams. Circumstellar Dust Disks in Taurus-Auriga: The Submillimeter Perspective. ApJ, 631(2):1134–1160, October 2005. doi: 10.1086/432712. 60

Sean M. Andrews, D. J. Wilner, A. M. Hughes, Chunhua Qi, and C. P. Dullemond. Protoplanetary Disk Structures in Ophiuchus. ApJ, 700(2):1502–1523, August 2009. doi: 10.1088/0004-637X/700/2/1502. 19

Sean M. Andrews, David J. Wilner, Zhaohuan Zhu, Tilman Birnstiel, John M. Carpenter, Laura M. Pérez, Xue-Ning Bai, Karin I. Öberg, A. Meredith Hughes, Andrea Isella, and Luca Ricci. Ringed Substructure and a Gap at 1 au in the Nearest Protoplanetary Disk. ApJ, 820(2):L40, April 2016. doi: 10.3847/2041-8205/820/2/L40. 13

Peter Anninos, Yu Zhang, Tom Abel, and Michael L. Norman. Cosmological hydrodynamics with multi-species chemistry and nonequilibrium ionization and cooling. New A, 2(3):209–224, August 1997. doi: 10.1016/S1384-1076(97)00009-2. 39

M. Ansdell, J. P. Williams, N. van der Marel, J. M. Carpenter, G. Guidi, M. Hogerheijde, G. S. Mathews, C. F. Manara, A. Miotello, A. Natta, I. Oliveira, M. Tazzari, L. Testi, E. F. van Dishoeck, and S. E. van Terwisga. ALMA Survey of Lupus Protoplanetary Disks. I. Dust

and Gas Masses. ApJ, 828(1):46, September 2016. doi: 10.3847/0004-637X/828/1/46. 14, 17, 60, 79, 85

M. Ansdell, J. P. Williams, C. F. Manara, A. Miotello, S. Facchini, N. van der Marel, L. Testi, and E. F. van Dishoeck. An ALMA Survey of Protoplanetary Disks in the σ Orionis Cluster. AJ, 153(5):240, May 2017. doi: 10.3847/1538-3881/aa69c0. 14, 26

M. Ansdell, J. P. Williams, L. Trapman, S. E. van Terwisga, S. Facchini, C. F. Manara, N. van der Marel, A. Miotello, M. Tazzari, M. Hogerheijde, G. Guidi, L. Testi, and E. F. van Dishoeck. ALMA Survey of Lupus Protoplanetary Disks. II. Gas Disk Radii. ApJ, 859(1): 21, May 2018. doi: 10.3847/1538-4357/aab890. 85, 117

Philip J. Armitage, Jacob B. Simon, and Rebecca G. Martin. Two Timescale Dispersal of Magnetized Protoplanetary Disks. ApJ, 778(1):L14, November 2013. doi: 10.1088/2041-8205/778/1/L14. 19

Nicole Arulanantham, M. K. McClure, Klaus Pontoppidan, Tracy L. Beck, J. A. Sturm, D. Harsono, A. C. A. Boogert, M. Cordiner, E. Dartois, M. N. Drozdovskaya, C. Espaillat, G. J. Melnick, J. A. Noble, M. E. Palumbo, Y. J. Pendleton, H. Terada, and E. F. van Dishoeck. JWST MIRI MRS Images of Disk Winds, Water, and CO in an Edge-on Protoplanetary Disk. ApJ, 965(1):L13, April 2024. doi: 10.3847/2041-8213/ad35c9. 20

D. Arzoumanian, Ph. André, P. Didelon, V. Könyves, N. Schneider, A. Men'shchikov, T. Sousbie, A. Zavagno, S. Bontemps, J. di Francesco, M. Griffin, M. Hennemann, T. Hill, J. Kirk, P. Martin, V. Minier, S. Molinari, F. Motte, N. Peretto, S. Pezzuto, L. Spinoglio, D. Ward-Thompson, G. White, and C. D. Wilson. Characterizing interstellar filaments with Herschel in IC 5146. A&A, 529:L6, May 2011. doi: 10.1051/0004-6361/201116596. 3

Yusuke Aso, Nagayoshi Ohashi, Yuri Aikawa, Masahiro N. Machida, Kazuya Saigo, Masao Saito, Shigehisa Takakuwa, Kengo Tomida, Kohji Tomisaka, and Hsi-Wei Yen. ALMA Observations of the Protostar L1527 IRS: Probing Details of the Disk and the Envelope Structures. ApJ, 849(1):56, November 2017. doi: 10.3847/1538-4357/aa8264. 13

Jaehan Bae, Lee Hartmann, Zhaohuan Zhu, and Charles Gammie. The Long-term Evolution of Photoevaporating Protoplanetary Disks. ApJ, 774(1):57, September 2013. doi: 10.1088/0004-637X/774/1/57. 24

Jaehan Bae, Zhaohuan Zhu, and Lee Hartmann. On the Formation of Multiple Concentric Rings and Gaps in Protoplanetary Disks. ApJ, 850(2):201, December 2017. doi: 10.3847/1538-4357/aa9705. 14

Xue-Ning Bai and James M. Stone. Local Study of Accretion Disks with a Strong Vertical Magnetic Field: Magnetorotational Instability and Disk Outflow. ApJ, 767(1):30, April 2013a. doi: 10.1088/0004-637X/767/1/30. 20, 55

Xue-Ning Bai and James M. Stone. Wind-driven Accretion in Protoplanetary Disks. I. Suppression of the Magnetorotational Instability and Launching of the Magnetocentrifugal Wind. ApJ, 769(1):76, May 2013b. doi: 10.1088/0004-637X/769/1/76. 20

Xue-Ning Bai and James M. Stone. Magnetic Flux Concentration and Zonal Flows in Magnetorotational Instability Turbulence. ApJ, 796(1):31, November 2014. doi: 10.1088/0004-637X/796/1/31. 14

E. L. O. Bakes and A. G. G. M. Tielens. The Photoelectric Heating Mechanism for Very Small Graphitic Grains and Polycyclic Aromatic Hydrocarbons. ApJ, 427:822, June 1994. doi: 10.1086/174188. 10, 37

Isabelle Baraffe, Derek Homeier, France Allard, and Gilles Chabrier. New evolutionary models for pre-main sequence and main sequence low-mass stars down to the hydrogen-burning limit. A&A, 577:A42, May 2015. doi: 10.1051/0004-6361/201425481. 6

A. Bayo, D. Barrado, J. Stauffer, M. Morales-Calderón, C. Melo, N. Huélamo, H. Bouy, B. Stelzer, M. Tamura, and R. Jayawardhana. Spectroscopy of very low mass stars and brown dwarfs in the Lambda Orionis star forming region. I. Enlarging the census down to the planetary mass domain in Collinder 69. A&A, 536:A63, December 2011. doi: 10.1051/0004-6361/201116617. 17

A. Bayo, D. Barrado, N. Huélamo, M. Morales-Calderón, C. Melo, J. Stauffer, and B. Stelzer. Spectroscopy of very low-mass stars and brown dwarfs in the Lambda Orionis star-forming region. II. Rotation, activity and other properties of spectroscopically confirmed members of Collinder 69. A&A, 547:A80, November 2012. doi: 10.1051/0004-6361/201219374. 17

Steven V. W. Beckwith, Anneila I. Sargent, Rolf S. Chini, and Rolf Guesten. A Survey for Circumstellar Disks around Young Stellar Objects. AJ, 99:924, March 1990. doi: 10.1086/115385. 14

Cameron P. M. Bell, Tim Naylor, N. J. Mayne, R. D. Jeffries, and S. P. Littlefair. Pre-main-sequence isochrones - II. Revising star and planet formation time-scales. MNRAS, 434(1):806–831, September 2013. doi: 10.1093/mnras/stt1075. 6

Cameron P. M. Bell, Eric E. Mamajek, and Tim Naylor. A self-consistent, absolute isochronal age scale for young moving groups in the solar neighbourhood. MNRAS, 454(1):593–614, November 2015. doi: 10.1093/mnras/stv1981. 88

Edwin Bergin, Nuria Calvet, Paola D'Alessio, and Gregory J. Herczeg. The Effects of UV Continuum and Lyα Radiation on the Chemical Equilibrium of T Tauri Disks. ApJ, 591(2):L159–L162, July 2003. doi: 10.1086/377148. 7, 10

T. J. Bethell and Edwin A. Bergin. Photoelectric Cross-sections of Gas and Dust in Protoplanetary Disks. ApJ, 740(1):7, October 2011. doi: 10.1088/0004-637X/740/1/7. 8

T. Birnstiel, C. P. Dullemond, and F. Brauer. Gas- and dust evolution in protoplanetary disks. A&A, 513:A79, April 2010. doi: 10.1051/0004-6361/200913731. 27, 107

T. Birnstiel, C. W. Ormel, and C. P. Dullemond. Dust size distributions in coagulation/fragmentation equilibrium: numerical solutions and analytical fits. A&A, 525:A11, January 2011. doi: 10.1051/0004-6361/201015228. 111

T. Birnstiel, H. Klahr, and B. Ercolano. A simple model for the evolution of the dust population in protoplanetary disks. A&A, 539:A148, March 2012. doi: 10.1051/0004-6361/201118136. 27

Tilman Birnstiel, Cornelis P. Dullemond, Zhaohuan Zhu, Sean M. Andrews, Xue-Ning Bai, David J. Wilner, John M. Carpenter, Jane Huang, Andrea Isella, Myriam Benisty, Laura M. Pérez, and Shangjia Zhang. The Disk Substructures at High Angular Resolution Project (DSHARP). V. Interpreting ALMA Maps of Protoplanetary Disks in Terms of a Dust Model. ApJ, 869(2):L45, December 2018. doi: 10.3847/2041-8213/aaf743. 14

Jürgen Blum and Michael Münch. Experimental Investigations on Aggregate-Aggregate Collisions in the Early Solar Nebula. Icarus, 106(1):151–167, November 1993. doi: 10.1006/icar.1993.1163. 103

Alice S. Booth, Benoît Tabone, John D. Ilee, Catherine Walsh, Yuri Aikawa, Sean M. Andrews, Jaehan Bae, Edwin A. Bergin, Jennifer B. Bergner, Arthur D. Bosman, Jenny K. Calahan, Gianni Cataldi, L. Ilsedore Cleeves, Ian Czekala, Viviana V. Guzmán, Jane Huang, Charles J. Law, Romane Le Gal, Feng Long, Ryan A. Loomis, François Ménard, Hideko Nomura, Karin I. Öberg, Chunhua Qi, Kamber R. Schwarz, Richard Teague, Takashi Tsukagoshi, David J. Wilner, Yoshihide Yamato, and Ke Zhang. Molecules with ALMA at Planet-forming Scales (MAPS). XVI. Characterizing the Impact of the Molecular Wind on the Evolution of the HD 163296 System. ApJS, 257(1):16, November 2021. doi: 10.3847/1538-4365/ac1ad4. 20

Ryan D. Boyden and Josh A. Eisner. Protoplanetary Disks in the Orion Nebula Cluster: Gas-disk Morphologies and Kinematics as Seen with ALMA. ApJ, 894(1):74, May 2020. doi: 10.3847/1538-4357/ab86b7. 26

F. Brauer, C. P. Dullemond, A. Johansen, Th. Henning, H. Klahr, and A. Natta. Survival of the mm-cm size grain population observed in protoplanetary disks. A&A, 469(3): 1169–1182, July 2007. doi: 10.1051/0004-6361:20066865. 14

F. Brauer, C. P. Dullemond, and Th. Henning. Coagulation, fragmentation and radial motion of solid particles in protoplanetary disks. A&A, 480(3):859–877, March 2008. doi: 10.1051/0004-6361:20077759. 27, 29

César Briceño, Nuria Calvet, Jesús Hernández, A. Katherina Vivas, Cecilia Mateu, Juan José Downes, Jaqueline Loerincs, Alice Pérez-Blanco, Perry Berlind, Catherine Espaillat, Lori Allen, Lee Hartmann, Mario Mateo, and III Bailey, John I. The CIDA Variability Survey of Orion OB1. II. Demographics of the Young, Low-mass Stellar Populations. AJ, 157(2):85, February 2019. doi: 10.3847/1538-3881/aaf79b. 16

R. Burn, A. Emsenhuber, J. Weder, O. Völkel, H. Klahr, T. Birnstiel, B. Ercolano, and C. Mordasini. Toward a population synthesis of disks and planets. I. Evolution of dust with entrainment in winds and radiation pressure. A&A, 666:A73, October 2022. doi: 10.1051/0004-6361/202243262. 27

N. Calvet, P. D'Alessio, D. M. Watson, R. Franco-Hernández, E. Furlan, J. Green, P. M. Sutter, W. J. Forrest, L. Hartmann, K. I. Uchida, L. D. Keller, B. Sargent, J. Najita, T. L. Herter, D. J. Barry, and P. Hall. Disks in Transition in the Taurus Population: Spitzer IRS Spectra of GM Aurigae and DM Tauri. ApJ, 630(2):L185–L188, September 2005. doi: 10.1086/491652. 13

Nuria Calvet and Erik Gullbring. The Structure and Emission of the Accretion Shock in T Tauri Stars. ApJ, 509(2):802–818, December 1998. doi: 10.1086/306527. 7

Nuria Calvet, James Muzerolle, César Briceño, Jesus Hernández, Lee Hartmann, José Luis Saucedo, and Karl D. Gordon. The Mass Accretion Rates of Intermediate-Mass T Tauri Stars. AJ, 128(3):1294–1318, September 2004. doi: 10.1086/422733. 54

John M. Carpenter, Eric E. Mamajek, Lynne A. Hillenbrand, and Michael R. Meyer. Evidence for Mass-dependent Circumstellar Disk Evolution in the 5 Myr Old Upper Scorpius OB Association. ApJ, 651(1):L49–L52, November 2006. doi: 10.1086/509121. 16

D. Cesarsky, J. Lequeux, A. Abergel, M. Perault, E. Palazzi, S. Madden, and D. Tran. Infrared spectrophotometry of M 17 with ISOCAM. A&A, 315:L309–L312, November 1996. 10

Kan Chen and Min-Kai Lin. How Efficient Is the Streaming Instability in Viscous Protoplanetary Disks? ApJ, 891(2):132, March 2020. doi: 10.3847/1538-4357/ab76ca. 29

F. J. Ciesla. Two-dimensional transport of solids in viscous protoplanetary disks. Icarus, 200(2):655–671, April 2009. doi: 10.1016/j.icarus.2008.12.009. 14

Lucas A. Cieza, Matthias R. Schreiber, Gisela A. Romero, Jonathan P. Williams, Alberto Rebassa-Mansergas, and Bruno Merín. The Nature of Transition Circumstellar Disks. III. Perseus, Taurus, and Auriga. ApJ, 750(2):157, May 2012. doi: 10.1088/0004-637X/750/2/157. 19

Lucas A. Cieza, Camilo González-Ruilova, Antonio S. Hales, Paola Pinilla, Dary Ruíz-Rodríguez, Alice Zurlo, Simón Casassus, Sebastián Pérez, Hector Cánovas, Carla Arce-Tord, Mario Flock, Nicolas Kurtovic, Sebastian Marino, Pedro H. Nogueira, Laura

Perez, Daniel J. Price, David A. Principe, and Jonathan P. Williams. The Ophiuchus DIsc Survey Employing ALMA (ODISEA) - III. The evolution of substructures in massive discs at 3-5 au resolution. MNRAS, 501(2):2934–2953, February 2021. doi: 10.1093/mnras/staa3787. 79

C. J. Clarke and J. E. Pringle. The diffusion of contaminant through an accretion disc. MNRAS, 235:365–373, November 1988. doi: 10.1093/mnras/235.2.365. 26

C. J. Clarke, A. Gendrin, and M. Sotomayor. The dispersal of circumstellar discs: the role of the ultraviolet switch. MNRAS, 328(2):485–491, December 2001. doi: 10.1046/j.1365-8711.2001.04891.x. 20, 24, 39

Gavin A. L. Coleman and Thomas J. Haworth. Dispersal of protoplanetary discs: how stellar properties and the local environment determine the pathway of evolution. MNRAS, 514(2):2315–2332, August 2022. doi: 10.1093/mnras/stac1513. 2

Francisca Concha-Ramírez, Martijn J. C. Wilhelm, Simon Portegies Zwart, and Thomas J. Haworth. External photoevaporation of circumstellar discs constrains the time-scale for planet formation. MNRAS, 490(4):5678–5690, October 2019. doi: 10.1093/mnras/stz2973. 26

Francisca Concha-Ramírez, Martijn J. C. Wilhelm, Simon Portegies Zwart, Sierk E. van Terwisga, and Alvaro Hacar. Effects of stellar density on the photoevaporation of circumstellar discs. MNRAS, 501(2):1782–1790, February 2021. doi: 10.1093/mnras/staa3669. 26

Jeffrey N. Cuzzi, Robert C. Hogan, and Karim Shariff. Toward Planetesimals: Dense Chondrule Clumps in the Protoplanetary Nebula. ApJ, 687(2):1432–1447, November 2008. doi: 10.1086/591239. 29

S. E. Dahm and L. A. Hillenbrand. Spitzer Observations of NGC 2362: Primordial Disks at 5 Myr. AJ, 133(5):2072–2086, May 2007. doi: 10.1086/512156. 16

S. E. Dahm and Theodore Simon. The T Tauri Star Population of the Young Cluster NGC 2264. AJ, 129(2):829–855, February 2005. doi: 10.1086/426326. 6

Paola D'Alessio, Nuria Calvet, and Lee Hartmann. Accretion Disks around Young Objects. III. Grain Growth. ApJ, 553(1):321–334, May 2001. doi: 10.1086/320655. 14

Paola D'Alessio, Nuria Calvet, Lee Hartmann, Ramiro Franco-Hernández, and Hermelinda Servín. Effects of Dust Growth and Settling in T Tauri Disks. ApJ, 638(1):314–335, February 2006. doi: 10.1086/498861. 12, 14

Steven J. Desch and Neal J. Turner. High-temperature Ionization in Protoplanetary Disks. ApJ, 811(2):156, October 2015. doi: 10.1088/0004-637X/811/2/156. 19

Ruobing Dong, Shengtai Li, Eugene Chiang, and Hui Li. Multiple Disk Gaps and Rings Generated by a Single Super-Earth. ApJ, 843(2):127, July 2017. doi: 10.3847/1538-4357/aa72f2. 14

B. T. Draine and Frank Bertoldi. Structure of Stationary Photodissociation Fronts. ApJ, 468: 269, September 1996. doi: 10.1086/177689. 37, 38, 127

B. T. Draine and H. M. Lee. Optical Properties of Interstellar Graphite and Silicate Grains. ApJ, 285:89, October 1984. doi: 10.1086/162480. 10

C. P. Dullemond, D. Hollenbach, I. Kamp, and P. D'Alessio. Models of the Structure and Evolution of Protoplanetary Disks. In Bo Reipurth, David Jewitt, and Klaus Keil, editors, *Protostars and Planets V*, page 555, January 2007. doi: 10.48550/arXiv.astro-ph/0602619. 11

J. A. Eisner, J. M. Bally, A. Ginsburg, and P. D. Sheehan. Protoplanetary Disks in the Orion OMC1 Region Imaged with ALMA. ApJ, 826(1):16, July 2016. doi: 10.3847/0004-637X/826/1/16. 14

J. A. Eisner, H. G. Arce, N. P. Ballering, J. Bally, S. M. Andrews, R. D. Boyden, J. Di Francesco, M. Fang, D. Johnstone, J. S. Kim, R. K. Mann, B. Matthews, I. Pascucci, L. Ricci, P. D. Sheehan, and J. P. Williams. Protoplanetary Disk Properties in the Orion Nebula Cluster: Initial Results from Deep, High-resolution ALMA Observations. ApJ, 860(1):77, June 2018. doi: 10.3847/1538-4357/aac3e2. 26, 79

Alexandre Emsenhuber, Christoph Mordasini, Remo Burn, Yann Alibert, Willy Benz, and Erik Asphaug. The New Generation Planetary Population Synthesis (NGPPS). II. Planetary population of solar-like stars and overview of statistical results. A&A, 656:A70, December 2021. doi: 10.1051/0004-6361/202038863. 24, 25

Alexandre Emsenhuber, Remo Burn, Jesse Weder, Kristina Monsch, Giovanni Picogna, Barbara Ercolano, and Thomas Preibisch. Toward a population synthesis of disks and planets. II. Confronting disk models and observations at the population level. A&A, 673: A78, May 2023. doi: 10.1051/0004-6361/202244767. 27

Barbara Ercolano, Jeremy J. Drake, John C. Raymond, and Cathie C. Clarke. X-Ray-Irradiated Protoplanetary Disk Atmospheres. I. Predicted Emission-Line Spectrum and Photoevaporation. ApJ, 688(1):398–407, November 2008. doi: 10.1086/590490. 22, 49, 51, 123

Barbara Ercolano, Cathie J. Clarke, and Jeremy J. Drake. X-Ray Irradiated Protoplanetary Disk Atmospheres. II. Predictions from Models in Hydrostatic Equilibrium. ApJ, 699(2): 1639–1649, July 2009. doi: 10.1088/0004-637X/699/2/1639. 23, 76

Barbara Ercolano, Giovanni Picogna, Kristina Monsch, Jeremy J. Drake, and Thomas Preibisch. The dispersal of protoplanetary discs - II: photoevaporation models with

observationally derived irradiating spectra. MNRAS, 508(2):1675–1685, December 2021. doi: 10.1093/mnras/stab2590. 22, 23, 24, 49, 123

C. Espaillat, P. D'Alessio, J. Hernández, E. Nagel, K. L. Luhman, D. M. Watson, N. Calvet, J. Muzerolle, and M. McClure. Unveiling the Structure of Pre-transitional Disks. ApJ, 717 (1):441–457, July 2010. doi: 10.1088/0004-637X/717/1/441. 14

C. Espaillat, J. Muzerolle, J. Najita, S. Andrews, Z. Zhu, N. Calvet, S. Kraus, J. Hashimoto, A. Kraus, and P. D'Alessio. An Observational Perspective of Transitional Disks. In Henrik Beuther, Ralf S. Klessen, Cornelis P. Dullemond, and Thomas Henning, editors, *Protostars and Planets VI*, pages 497–520, January 2014. doi: 10.2458/azu_uapress_9780816531240-ch022. 13

T. L. Esplin and K. L. Luhman. A Survey for New Stars and Brown Dwarfs in the Ophiuchus Star-forming Complex. AJ, 159(6):282, June 2020. doi: 10.3847/1538-3881/ab8dbd. 7

Stefano Facchini, Cathie J. Clarke, and Thomas G. Bisbas. External photoevaporation of protoplanetary discs in sparse stellar groups: the impact of dust growth. MNRAS, 457 (4):3593–3610, April 2016. doi: 10.1093/mnras/stw240. 28

M. Fang, R. van Boekel, R. R. King, Th. Henning, J. Bouwman, Y. Doi, Y. K. Okamoto, V. Roccatagliata, and A. Sicilia-Aguilar. Star formation and disk properties in Pismis 24. A&A, 539:A119, March 2012. doi: 10.1051/0004-6361/201015914. 17

Marco Fatuzzo and Fred C. Adams. UV Radiation Fields Produced by Young Embedded Star Clusters. ApJ, 675(2):1361–1374, March 2008. doi: 10.1086/527469. 26

Cécile Favre, L. Ilsedore Cleeves, Edwin A. Bergin, Chunhua Qi, and Geoffrey A. Blake. A Significantly Low CO Abundance toward the TW Hya Protoplanetary Disk: A Path to Active Carbon Chemistry? ApJ, 776(2):L38, October 2013. doi: 10.1088/2041-8205/776/2/L38. 11

D. Fedele, M. E. van den Ancker, Th. Henning, R. Jayawardhana, and J. M. Oliveira. Timescale of mass accretion in pre-main-sequence stars. A&A, 510:A72, February 2010. doi: 10.1051/0004-6361/200912810. 16, 19

D. Fedele, M. Tazzari, R. Booth, L. Testi, C. J. Clarke, I. Pascucci, A. Kospal, D. Semenov, S. Bruderer, Th. Henning, and R. Teague. ALMA continuum observations of the protoplanetary disk AS 209. Evidence of multiple gaps opened by a single planet. A&A, 610:A24, February 2018. doi: 10.1051/0004-6361/201731978. 19

Gregory A. Feiden. Magnetic inhibition of convection and the fundamental properties of low-mass stars. III. A consistent 10 Myr age for the Upper Scorpius OB association. A&A, 593:A99, September 2016. doi: 10.1051/0004-6361/201527613. 7

E. Flaccomio, F. Damiani, G. Micela, S. Sciortino, Jr. Harnden, F. R., S. S. Murray, and S. J. Wolk. Chandra X-Ray Observation of the Orion Nebula Cluster. II. Relationship between

X-Ray Activity Indicators and Stellar Parameters. ApJ, 582(1):398–409, January 2003. doi: 10.1086/344536. 8

K. M. Flaherty and J. Muzerolle. Evidence for Early Circumstellar Disk Evolution in NGC 2068/71. AJ, 135(3):966–983, March 2008. doi: 10.1088/0004-6256/135/3/966. 19

Kevin Flaherty, A. Meredith Hughes, Jacob B. Simon, Chunhua Qi, Xue-Ning Bai, Alyssa Bulatek, Sean M. Andrews, David J. Wilner, and Ágnes Kóspál. Measuring Turbulent Motion in Planet-forming Disks with ALMA: A Detection around DM Tau and Nondetections around MWC 480 and V4046 Sgr. ApJ, 895(2):109, June 2020. doi: 10.3847/1538-4357/ab8cc5. 19

Kevin M. Flaherty, A. Meredith Hughes, Katherine A. Rosenfeld, Sean M. Andrews, Eugene Chiang, Jacob B. Simon, Skylar Kerzner, and David J. Wilner. Weak Turbulence in the HD 163296 Protoplanetary Disk Revealed by ALMA CO Observations. ApJ, 813(2):99, November 2015. doi: 10.1088/0004-637X/813/2/99. 19

Kevin M. Flaherty, A. Meredith Hughes, Sanaea C. Rose, Jacob B. Simon, Chunhua Qi, Sean M. Andrews, Ágnes Kóspál, David J. Wilner, Eugene Chiang, Philip J. Armitage, and Xue-ning Bai. A Three-dimensional View of Turbulence: Constraints on Turbulent Motions in the HD 163296 Protoplanetary Disk Using DCO^+. ApJ, 843(2):150, July 2017. doi: 10.3847/1538-4357/aa79f9. 19

Andreea S. Font, Ian G. McCarthy, Doug Johnstone, and David R. Ballantyne. Photoevaporation of Circumstellar Disks around Young Stars. ApJ, 607(2):890–903, June 2004. doi: 10.1086/383518. 21, 48

Logan Francis and Nienke van der Marel. Dust-depleted Inner Disks in a Large Sample of Transition Disks through Long-baseline ALMA Observations. ApJ, 892(2):111, April 2020. doi: 10.3847/1538-4357/ab7b63. 13

R. Franz, G. Picogna, B. Ercolano, S. Casassus, T. Birnstiel, Ch. Rab, and S. Pérez. Dust entrainment in photoevaporative winds: Synthetic observations of transition disks. A&A, 659:A90, March 2022. doi: 10.1051/0004-6361/202142785. 20

S. Fromang, H. Latter, G. Lesur, and G. I. Ogilvie. Local outflows from turbulent accretion disks. A&A, 552:A71, April 2013. doi: 10.1051/0004-6361/201220016. 20

Benjamin J. Fulton, Erik A. Petigura, Andrew W. Howard, Howard Isaacson, Geoffrey W. Marcy, Phillip A. Cargile, Leslie Hebb, Lauren M. Weiss, John Asher Johnson, Timothy D. Morton, Evan Sinukoff, Ian J. M. Crossfield, and Lea A. Hirsch. The California-Kepler Survey. III. A Gap in the Radius Distribution of Small Planets. AJ, 154(3):109, September 2017. doi: 10.3847/1538-3881/aa80eb. 28

Daniele Galli and Francesco Palla. The chemistry of the early Universe. A&A, 335:403–420, July 1998. doi: 10.48550/arXiv.astro-ph/9803315. 39

P. A. B. Galli, H. Bouy, J. Olivares, N. Miret-Roig, L. M. Sarro, D. Barrado, A. Berihuete, E. Bertin, and J. C. Cuillandre. Chamaeleon DANCe. Revisiting the stellar populations of Chamaeleon I and Chamaeleon II with Gaia-DR2 data. A&A, 646:A46, February 2021. doi: 10.1051/0004-6361/202039395. 6

Charles F. Gammie. Layered Accretion in T Tauri Disks. ApJ, 457:355, January 1996. doi: 10.1086/176735. 19

P. Garaud. Growth and Migration of Solids in Evolving Protostellar Disks. I. Methods and Analytical Tests. ApJ, 671(2):2091–2114, December 2007. doi: 10.1086/523090. 27

B. Scott Gaudi, Michael Meyer, and Jessie Christiansen. The Demographics of Exoplanets. In Nikku Madhusudhan, editor, *ExoFrontiers; Big Questions in Exoplanetary Science*, pages 2–1. IOP Publishing, 2021. doi: 10.1088/2514-3433/abfa8fch2. 28

V. C. Geers, J. C. Augereau, K. M. Pontoppidan, C. P. Dullemond, R. Visser, J. E. Kessler-Silacci, II Evans, N. J., E. F. van Dishoeck, G. A. Blake, A. C. A. Boogert, J. M. Brown, F. Lahuis, and B. Merín. C2D Spitzer-IRS spectra of disks around T Tauri stars. II. PAH emission features. A&A, 459(2):545–556, November 2006. doi: 10.1051/0004-6361:20064830. 34

V. C. Geers, E. F. van Dishoeck, R. Visser, K. M. Pontoppidan, J. C. Augereau, E. Habart, and A. M. Lagrange. Spatially extended polycyclic aromatic hydrocarbons in circumstellar disks around T Tauri and Herbig Ae stars. A&A, 476(1):279–289, December 2007. doi: 10.1051/0004-6361:20078466. 34

Konstantin Gerbig, Ruth A. Murray-Clay, Hubert Klahr, and Hans Baehr. Requirements for Gravitational Collapse in Planetesimal Formation—The Impact of Scales Set by Kelvin-Helmholtz and Nonlinear Streaming Instability. ApJ, 895(2):91, June 2020. doi: 10.3847/1538-4357/ab8d37. 29

Peter Goldreich and William R. Ward. The Formation of Planetesimals. ApJ, 183: 1051–1062, August 1973. doi: 10.1086/152291. 29

Daniel A. Gole, Jacob B. Simon, Rixin Li, Andrew N. Youdin, and Philip J. Armitage. Turbulence Regulates the Rate of Planetesimal Formation via Gravitational Collapse. ApJ, 904(2):132, December 2020. doi: 10.3847/1538-4357/abc334. 29

U. Gorti and D. Hollenbach. Photoevaporation of Circumstellar Disks By Far-Ultraviolet, Extreme-Ultraviolet and X-Ray Radiation from the Central Star. ApJ, 690(2):1539–1552, January 2009. doi: 10.1088/0004-637X/690/2/1539. 22, 23, 57

U. Gorti, C. P. Dullemond, and D. Hollenbach. Time Evolution of Viscous Circumstellar Disks due to Photoevaporation by Far-Ultraviolet, Extreme-Ultraviolet, and X-ray Radiation from the Central Star. ApJ, 705(2):1237–1251, November 2009. doi: 10.1088/0004-637X/705/2/1237. 24, 33, 60

U. Gorti, D. Hollenbach, and C. P. Dullemond. The Impact of Dust Evolution and Photoevaporation on Disk Dispersal. ApJ, 804(1):29, May 2015. doi: 10.1088/0004-637X/804/1/29. 2, 27, 91

David F. Gray. *The Observation and Analysis of Stellar Photospheres*. Cambridge University Press, 2005. doi: 10.1017/CBO9781316036570. 6

Scott G. Gregory, Fred C. Adams, and Claire L. Davies. The influence of radiative core growth on coronal X-ray emission from pre-main-sequence stars. MNRAS, 457(4): 3836–3858, April 2016. doi: 10.1093/mnras/stw259. 8

M. G. Guarcello, J. J. Drake, N. J. Wright, J. F. Albacete-Colombo, C. Clarke, B. Ercolano, E. Flaccomio, V. Kashyap, G. Micela, T. Naylor, N. Schneider, S. Sciortino, and J. S. Vink. Photoevaporation and close encounters: how the environment around Cygnus OB2 affects the evolution of protoplanetary disks. *arXiv e-prints*, art. arXiv:1605.01773, May 2016. doi: 10.48550/arXiv.1605.01773. 26

M. G. Guarcello, K. Biazzo, J. J. Drake, G. Micela, L. Prisinzano, S. Sciortino, F. Damiani, E. Flaccomio, C. Neiner, and N. J. Wright. Dispersal timescale of protoplanetary disks in the low-metallicity young cluster Dolidze 25. A&A, 650:A157, June 2021. doi: 10.1051/0004-6361/202140361. 17

Erik Gullbring, Lee Hartmann, Cesar Briceño, and Nuria Calvet. Disk Accretion Rates for T Tauri Stars. ApJ, 492(1):323–341, January 1998. doi: 10.1086/305032. 7

Jr. Haisch, Karl E., Elizabeth A. Lada, and Charles J. Lada. Disk Frequencies and Lifetimes in Young Clusters. ApJ, 553(2):L153–L156, June 2001. doi: 10.1086/320685. 15, 16

Kenji Hamaguchi, Shigeo Yamauchi, and Katsuji Koyama. X-Ray Study of Herbig Ae/Be Stars. ApJ, 618(1):360–384, January 2005. doi: 10.1086/423192. 8

Lee Hartmann, Nuria Calvet, Erik Gullbring, and Paola D'Alessio. Accretion and the Evolution of T Tauri Disks. ApJ, 495(1):385–400, March 1998. doi: 10.1086/305277. 18, 19

Lee Hartmann, Paola D'Alessio, Nuria Calvet, and James Muzerolle. Why Do T Tauri Disks Accrete? ApJ, 648(1):484–490, September 2006. doi: 10.1086/505788. 54

Lee Hartmann, Gregory Herczeg, and Nuria Calvet. Accretion onto Pre-Main-Sequence Stars. ARA&A, 54:135–180, September 2016. doi: 10.1146/annurev-astro-081915-023347. 24

Thomas J. Haworth and Cathie J. Clarke. The first multidimensional view of mass loss from externally FUV irradiated protoplanetary discs. MNRAS, 485(3):3895–3908, May 2019. doi: 10.1093/mnras/stz706. 74, 76

Thomas J. Haworth and James E. Owen. The observational anatomy of externally photoevaporating planet-forming discs - I. Atomic carbon. MNRAS, 492(4):5030–5040, March 2020. doi: 10.1093/mnras/staa151. 20

Thomas J. Haworth, Cathie J. Clarke, Wahidur Rahman, Andrew J. Winter, and Stefano Facchini. The FRIED grid of mass-loss rates for externally irradiated protoplanetary discs. MNRAS, 481(1):452–466, November 2018. doi: 10.1093/mnras/sty2323. 26

Thomas J. Haworth, Gavin A. L. Coleman, Lin Qiao, Andrew D. Sellek, and Kanaar Askari. FRIED v2: a new grid of mass-loss rates for externally irradiated protoplanetary discs. MNRAS, 526(3):4315–4334, December 2023. doi: 10.1093/mnras/stad3054. 26

C. Hayashi. Structure of the Solar Nebula, Growth and Decay of Magnetic Fields and Effects of Magnetic and Turbulent Viscosities on the Nebula. *Progress of Theoretical Physics Supplement*, 70:35–53, January 1981. doi: 10.1143/PTPS.70.35. 59, 60

Nathanial Hendler, Ilaria Pascucci, Paola Pinilla, Marco Tazzari, John Carpenter, Renu Malhotra, and Leonardo Testi. The Evolution of Dust Disk Sizes from a Homogeneous Analysis of 1-10 Myr old Stars. ApJ, 895(2):126, June 2020. doi: 10.3847/1538-4357/ab70ba. 79

Gregory J. Herczeg and Lynne A. Hillenbrand. UV Excess Measures of Accretion onto Young Very Low Mass Stars and Brown Dwarfs. ApJ, 681(1):594–625, July 2008. doi: 10.1086/586728. 18, 19

Gregory J. Herczeg, Jeffrey L. Linsky, Jeff A. Valenti, Christopher M. Johns-Krull, and Brian E. Wood. The Far-Ultraviolet Spectrum of TW Hydrae. I. Observations of H_2 Fluorescence. ApJ, 572(1):310–325, June 2002. doi: 10.1086/339731. 49

Gregory J. Herczeg, Brian E. Wood, Jeffrey L. Linsky, Jeff A. Valenti, and Christopher M. Johns-Krull. The Far-Ultraviolet Spectra of TW Hydrae. II. Models of H_2 Fluorescence in a Disk. ApJ, 607(1):369–383, May 2004. doi: 10.1086/383340. 7, 10, 49

Gregory J. Herczeg, Jeffrey L. Linsky, Frederick M. Walter, Gösta F. Gahm, and Christopher M. Johns-Krull. The Origins of Fluorescent H_2 Emission From T Tauri Stars. ApJS, 165(1):256–282, July 2006. doi: 10.1086/503558. 49

Jesús Hernández, Nuria Calvet, C. Briceño, L. Hartmann, A. K. Vivas, J. Muzerolle, J. Downes, L. Allen, and R. Gutermuth. Spitzer Observations of the Orion OB1 Association: Disk Census in the Low-Mass Stars. ApJ, 671(2):1784–1799, December 2007. doi: 10.1086/522882. 12

Jesús Hernández, Lee Hartmann, Nuria Calvet, R. D. Jeffries, R. Gutermuth, J. Muzerolle, and J. Stauffer. A Spitzer View of Protoplanetary Disks in the γ Velorum Cluster. ApJ, 686(2):1195–1208, October 2008. doi: 10.1086/591224. 15, 16

L. A. Hillenbrand, A. Bauermeister, and R. J. White. An Assessment of HR Diagram Constraints on Ages and Age Spreads in Star-Forming Regions and Young Clusters. In G. van Belle, editor, *14th Cambridge Workshop on Cool Stars, Stellar Systems, and the Sun*, volume 384 of *Astronomical Society of the Pacific Conference Series*, page 200, April 2008. doi: 10.48550/arXiv.astro-ph/0703642. 6

Lynne A. Hillenbrand, Stephen E. Strom, Frederick J. Vrba, and Jocelyn Keene. Herbig Ae/Be Stars: Intermediate-Mass Stars Surrounded by Massive Circumstellar Accretion Disks. ApJ, 397:613, October 1992. doi: 10.1086/171819. 16

David Hollenbach and Christopher F. McKee. Molecule Formation and Infrared Emission in Fast Interstellar Shocks. III. Results for J Shocks in Molecular Clouds. ApJ, 342:306, July 1989. doi: 10.1086/167595. 38

David Hollenbach, Doug Johnstone, Susana Lizano, and Frank Shu. Photoevaporation of Disks around Massive Stars and Application to Ultracompact H II Regions. ApJ, 428:654, June 1994. doi: 10.1086/174276. 22

Andrew W. Howard. Observed Properties of Extrasolar Planets. *Science*, 340(6132): 572–576, May 2013. doi: 10.1126/science.1233545. 28

Andrew W. Howard, Geoffrey W. Marcy, Stephen T. Bryson, Jon M. Jenkins, Jason F. Rowe, Natalie M. Batalha, William J. Borucki, David G. Koch, Edward W. Dunham, III Gautier, Thomas N., Jeffrey Van Cleve, William D. Cochran, David W. Latham, Jack J. Lissauer, Guillermo Torres, Timothy M. Brown, Ronald L. Gilliland, Lars A. Buchhave, Douglas A. Caldwell, Jørgen Christensen-Dalsgaard, David Ciardi, Francois Fressin, Michael R. Haas, Steve B. Howell, Hans Kjeldsen, Sara Seager, Leslie Rogers, Dimitar D. Sasselov, Jason H. Steffen, Gibor S. Basri, David Charbonneau, Jessie Christiansen, Bruce Clarke, Andrea Dupree, Daniel C. Fabrycky, Debra A. Fischer, Eric B. Ford, Jonathan J. Fortney, Jill Tarter, Forrest R. Girouard, Matthew J. Holman, John Asher Johnson, Todd C. Klaus, Pavel Machalek, Althea V. Moorhead, Robert C. Morehead, Darin Ragozzine, Peter Tenenbaum, Joseph D. Twicken, Samuel N. Quinn, Howard Isaacson, Avi Shporer, Philip W. Lucas, Lucianne M. Walkowicz, William F. Welsh, Alan Boss, Edna Devore, Alan Gould, Jeffrey C. Smith, Robert L. Morris, Andrej Prsa, Timothy D. Morton, Martin Still, Susan E. Thompson, Fergal Mullally, Michael Endl, and Phillip J. MacQueen. Planet Occurrence within 0.25 AU of Solar-type Stars from Kepler. ApJS, 201(2):15, August 2012. doi: 10.1088/0067-0049/201/2/15. 28

David P. Huenemoerder, Norbert S. Schulz, Paola Testa, Anthony Kesich, and Claude R. Canizares. X-Ray Emission and Corona of the Young Intermediate-Mass Binary θ^1 Ori E. ApJ, 707(2):942–953, December 2009. doi: 10.1088/0004-637X/707/2/942. 8

R. Hueso and T. Guillot. Evolution of protoplanetary disks: constraints from DM Tauri and GM Aurigae. A&A, 442(2):703–725, November 2005. doi: 10.1051/0004-6361:20041905. 56

Anna L. H. Hughes and Philip J. Armitage. Particle Transport in Evolving Protoplanetary Disks: Implications for Results from Stardust. ApJ, 719(2):1633–1653, August 2010. doi: 10.1088/0004-637X/719/2/1633. 27

T. O. Husser, S. Wende-von Berg, S. Dreizler, D. Homeier, A. Reiners, T. Barman, and P. H. Hauschildt. A new extensive library of PHOENIX stellar atmospheres and synthetic spectra. A&A, 553:A6, May 2013. doi: 10.1051/0004-6361/201219058. 7, 59

Mark A. Hutchison, Guillaume Laibe, and Sarah T. Maddison. On the maximum grain size entrained by photoevaporative winds. MNRAS, 463(3):2725–2734, December 2016a. doi: 10.1093/mnras/stw2191. 28

Mark A. Hutchison, Daniel J. Price, Guillaume Laibe, and Sarah T. Maddison. On dust entrainment in photoevaporative winds. MNRAS, 461(1):742–759, September 2016b. doi: 10.1093/mnras/stw1126. 28

J. Igea and A. E. Glassgold. X-Ray Ionization of the Disks of Young Stellar Objects. ApJ, 518 (2):848–858, June 1999. doi: 10.1086/307302. 8

Andrea Isella, Greta Guidi, Leonardo Testi, Shangfei Liu, Hui Li, Shengtai Li, Erik Weaver, Yann Boehler, John M. Carperter, Itziar De Gregorio-Monsalvo, Carlo F. Manara, Antonella Natta, Laura M. Pérez, Luca Ricci, Anneila Sargent, Marco Tazzari, and Neal Turner. Ringed Structures of the HD 163296 Protoplanetary Disk Revealed by ALMA. Phys. Rev. Lett., 117(25):251101, December 2016. doi: 10.1103/PhysRevLett.117.251101. 13

A. V. Ivlev, V. V. Akimkin, and P. Caselli. Ionization and Dust Charging in Protoplanetary Disks. ApJ, 833(1):92, December 2016. doi: 10.3847/1538-4357/833/1/92. 10

Emmanuel Jacquet, Steven Balbus, and Henrik Latter. On linear dust-gas streaming instabilities in protoplanetary discs. MNRAS, 415(4):3591–3598, August 2011. doi: 10.1111/j.1365-2966.2011.18971.x. 29

John Asher Johnson, Kimberly M. Aller, Andrew W. Howard, and Justin R. Crepp. Giant Planet Occurrence in the Stellar Mass-Metallicity Plane. PASP, 122(894):905, August 2010. doi: 10.1086/655775. 28

Doug Johnstone, David Hollenbach, and John Bally. Photoevaporation of Disks and Clumps by Nearby Massive Stars: Application to Disk Destruction in the Orion Nebula. ApJ, 499 (2):758–776, May 1998. doi: 10.1086/305658. 22

M. Kama, S. Bruderer, M. Carney, M. Hogerheijde, E. F. van Dishoeck, D. Fedele, A. Baryshev, W. Boland, R. Güsten, A. Aikutalp, Y. Choi, A. Endo, W. Frieswijk, A. Karska, P. Klaassen, E. Koumpia, L. Kristensen, S. Leurini, Z. Nagy, J. P. Perez Beaupuits, C. Risacher, N. van der Marel, T. A. van Kempen, R. J. van Weeren, F. Wyrowski, and U. A. Yıldız. Observations and modelling of CO and [C I] in protoplanetary disks. First detections

of [C I] and constraints on the carbon abundance. A&A, 588:A108, April 2016a. doi: 10.1051/0004-6361/201526791. 11

M. Kama, S. Bruderer, E. F. van Dishoeck, M. Hogerheijde, C. P. Folsom, A. Miotello, D. Fedele, A. Belloche, R. Güsten, and F. Wyrowski. Volatile-carbon locking and release in protoplanetary disks. A study of TW Hya and HD 100546. A&A, 592:A83, August 2016b. doi: 10.1051/0004-6361/201526991. 46

Kazuhiro D. Kanagawa, Takayuki Muto, and Hidekazu Tanaka. Dust Rings as a Footprint of Planet Formation in a Protoplanetary Disk. ApJ, 921(2):169, November 2021. doi: 10.3847/1538-4357/ac282b. 14

Joel H. Kastner, David P. Huenemoerder, Norbert S. Schulz, Claude R. Canizares, and David A. Weintraub. Evidence for Accretion: High-Resolution X-Ray Spectroscopy of the Classical T Tauri Star TW Hydrae. ApJ, 567(1):434–440, March 2002. doi: 10.1086/338419. 8

A. Kataoka, H. Tanaka, S. Okuzumi, and K. Wada. Static compression of porous dust aggregates. A&A, 554:A4, June 2013a. doi: 10.1051/0004-6361/201321325. 30

Akimasa Kataoka, Hidekazu Tanaka, Satoshi Okuzumi, and Koji Wada. Fluffy dust forms icy planetesimals by static compression. A&A, 557:L4, September 2013b. doi: 10.1051/0004-6361/201322151. 30

Ch. Keller and H. P. Gail. Radial mixing in protoplanetary accretion disks. VI. Mixing by large-scale radial flows. A&A, 415:1177–1185, March 2004. doi: 10.1051/0004-6361:20034629. 14

Grant M. Kennedy and Scott J. Kenyon. Stellar Mass Dependent Disk Dispersal. ApJ, 695 (2):1210–1226, April 2009. doi: 10.1088/0004-637X/695/2/1210. 16

Shigeo S. Kimura, Masanobu Kunitomo, and Sanemichi Z. Takahashi. From birth to death of protoplanetary discs: modelling their formation, evolution and dispersal. MNRAS, 461 (2):2257–2265, September 2016. doi: 10.1093/mnras/stw1531. 24, 25, 60

C. Knight, E. Peeters, A. G. G. M. Tielens, and W. D. Vacca. Characterizing the PAH emission in the Orion Bar. MNRAS, 509(3):3523–3546, January 2022. doi: 10.1093/mnras/stab3047. 10

Arieh Koenigl. Disk Accretion onto Magnetic T Tauri Stars. ApJ, 370:L39, March 1991. doi: 10.1086/185972. 24

Eiichiro Kokubo and Shigeru Ida. Formation of Protoplanet Systems and Diversity of Planetary Systems. ApJ, 581(1):666–680, December 2002. doi: 10.1086/344105. 28

Komaki. Dispersal mechanism of proto-planetary disks. Master's Thesis, The University of Tokyo, 2022. URL https://www-utap.phys.s.u-tokyo.ac.jp/Theses/M_Komaki.pdf. 23, 42, 51, 57, 58, 119

Ayano Komaki, Riouhei Nakatani, and Naoki Yoshida. Radiation Hydrodynamics Simulations of Protoplanetary Disks: Stellar Mass Dependence of the Disk Photoevaporation Rate. ApJ, 910(1):51, March 2021. doi: 10.3847/1538-4357/abe2af. 23, 33, 41, 57, 65, 68, 73, 74, 75, 97

Ayano Komaki, Rolf Kuiper, and Naoki Yoshida. The Effect of Ultraviolet Photon Pumping of H_2 in Dust-deficient Protoplanetary Disks. ApJ, 963(2):81, March 2024. doi: 10.3847/1538-4357/ad21f1. 57

V. Könyves, Ph. André, A. Men'shchikov, P. Palmeirim, D. Arzoumanian, N. Schneider, A. Roy, P. Didelon, A. Maury, Y. Shimajiri, J. Di Francesco, S. Bontemps, N. Peretto, M. Benedettini, J. Ph. Bernard, D. Elia, M. J. Griffin, T. Hill, J. Kirk, B. Ladjelate, K. Marsh, P. G. Martin, F. Motte, Q. Nguyên Luong, S. Pezzuto, H. Roussel, K. L. J. Rygl, S. I. Sadavoy, E. Schisano, L. Spinoglio, D. Ward-Thompson, and G. J. White. A census of dense cores in the Aquila cloud complex: SPIRE/PACS observations from the Herschel Gould Belt survey. A&A, 584:A91, December 2015. doi: 10.1051/0004-6361/201525861. 3

Pavel Kroupa. The Initial Mass Function of Stars: Evidence for Uniformity in Variable Systems. *Science*, 295(5552):82–91, January 2002. doi: 10.1126/science.1067524. 3, 78, 84

Masanobu Kunitomo, Takeru K. Suzuki, and Shu-ichiro Inutsuka. Dispersal of protoplanetary discs by the combination of magnetically driven and photoevaporative winds. MNRAS, 492(3):3849–3858, March 2020. doi: 10.1093/mnras/staa087. 2, 20, 24

Masanobu Kunitomo, Shigeru Ida, Taku Takeuchi, Olja Panić, James M. Miley, and Takeru K. Suzuki. Photoevaporative Dispersal of Protoplanetary Disks around Evolving Intermediate-mass Stars. ApJ, 909(2):109, March 2021. doi: 10.3847/1538-4357/abdb2a. 2, 22, 24, 58, 68, 70, 73, 120

Charles J. Lada. Star formation: from OB associations to protostars. In Manuel Peimbert and Jun Jugaku, editors, *Star Forming Regions*, volume 115 of *IAU Symposium*, page 1, January 1987. 13

Charles J. Lada, August A. Muench, K. L. Luhman, Lori Allen, Lee Hartmann, Tom Megeath, Philip Myers, Giovanni Fazio, Kenneth Wood, James Muzerolle, George Rieke, Nick Siegler, and Erick Young. Spitzer Observations of IC 348: The Disk Population at 2-3 Million Years. AJ, 131(3):1574–1607, March 2006. doi: 10.1086/499808. 16

H. H. Lee, R. P. A. Bettens, and E. Herbst. Fractional abundances of molecules in dense interstellar clouds: A compendium of recent model results. A&AS, 119:111–114, October 1996. 127, 129

Zoë M. Leinhardt and Sarah T. Stewart. Full numerical simulations of catastrophic small body collisions. Icarus, 199(2):542–559, February 2009. doi: 10.1016/j.icarus.2008.09.013. 103

G. Lesur, J. Ferreira, and G. I. Ogilvie. The magnetorotational instability as a jet launching mechanism. A&A, 550:A61, February 2013. doi: 10.1051/0004-6361/201220395. 20

Geoffroy Lesur, Matthew W. Kunz, and Sébastien Fromang. Thanatology in protoplanetary discs. The combined influence of Ohmic, Hall, and ambipolar diffusion on dead zones. A&A, 566:A56, June 2014. doi: 10.1051/0004-6361/201423660. 20

Kurt Liffman. The Gravitational Radius of an Irradiated Disk. PASA, 20(4):337–339, January 2003. doi: 10.1071/AS03019. 21

Johan E. Lindberg, Jes K. Jørgensen, Christian Brinch, Troels Haugbølle, Edwin A. Bergin, Daniel Harsono, Magnus V. Persson, Ruud Visser, and Satoshi Yamamoto. ALMA observations of the kinematics and chemistry of disc formation. A&A, 566:A74, June 2014. doi: 10.1051/0004-6361/201322651. 13

G. Lodato, L. Rampinelli, E. Viscardi, C. Longarini, A. Izquierdo, T. Paneque-Carreño, L. Testi, S. Facchini, A. Miotello, B. Veronesi, and C. Hall. Dynamical mass measurements of two protoplanetary discs. MNRAS, 518(3):4481–4493, January 2023. doi: 10.1093/mnras/stac3223. 14

S. H. Lubow and G. D'Angelo. Gas Flow across Gaps in Protoplanetary Disks. ApJ, 641(1): 526–533, April 2006. doi: 10.1086/500356. 14

D. Lynden-Bell and J. E. Pringle. The evolution of viscous discs and the origin of the nebular variables. MNRAS, 168:603–637, September 1974. doi: 10.1093/mnras/168.3.603. 18

A. Ran Lyo, Warrick A. Lawson, Eric D. Feigelson, and Lisa A. Crause. Population and dynamical state of the η Chamaeleontis sparse young open cluster. MNRAS, 347(1): 246–254, January 2004. doi: 10.1111/j.1365-2966.2004.07194.x. 88

Hiroshi Maeshima, Takao Nakagawa, Takuya Kojima, Satoshi Takita, and Jungmi Kwon. Dust dissipation timescales in the intermediate and outer regions of protoplanetary disks. PASJ, 73(6):1589–1603, December 2021. doi: 10.1093/pasj/psab095. 16

Eric E. Mamajek. Initial Conditions of Planet Formation: Lifetimes of Primordial Disks. In Tomonori Usuda, Motohide Tamura, and Miki Ishii, editors, *Exoplanets and Disks: Their Formation and Diversity*, volume 1158 of *American Institute of Physics Conference Series*, pages 3–10. AIP, August 2009. doi: 10.1063/1.3215910. 15, 16, 83

C. F. Manara, G. Rosotti, L. Testi, A. Natta, J. M. Alcalá, J. P. Williams, M. Ansdell, A. Miotello, N. van der Marel, M. Tazzari, J. Carpenter, G. Guidi, G. S. Mathews, I. Oliveira, T. Prusti, and E. F. van Dishoeck. Evidence for a correlation between mass accretion rates onto young stars and the mass of their protoplanetary disks. A&A, 591: L3, June 2016. doi: 10.1051/0004-6361/201628549. 11, 18

C. F. Manara, L. Testi, G. J. Herczeg, I. Pascucci, J. M. Alcalá, A. Natta, S. Antoniucci, D. Fedele, G. D. Mulders, T. Henning, S. Mohanty, T. Prusti, and E. Rigliaco. X-shooter

study of accretion in Chamaeleon I. II. A steeper increase of accretion with stellar mass for very low-mass stars? A&A, 604:A127, August 2017. doi: 10.1051/0004-6361/201630147. 18, 19

C. F. Manara, A. Natta, G. P. Rosotti, J. M. Alcalá, B. Nisini, G. Lodato, L. Testi, I. Pascucci, L. Hillenbrand, J. Carpenter, A. Scholz, D. Fedele, A. Frasca, G. Mulders, E. Rigliaco, C. Scardoni, and E. Zari. X-shooter survey of disk accretion in Upper Scorpius. I. Very high accretion rates at age > 5 Myr. A&A, 639:A58, July 2020. doi: 10.1051/0004-6361/202037949. 19

Rita K. Mann, James Di Francesco, Doug Johnstone, Sean M. Andrews, Jonathan P. Williams, John Bally, Luca Ricci, A. Meredith Hughes, and Brenda C. Matthews. ALMA Observations of the Orion Proplyds. ApJ, 784(1):82, March 2014. doi: 10.1088/0004-637X/784/1/82. 26

J. S. Mathis, W. Rumpl, and K. H. Nordsieck. The size distribution of interstellar grains. ApJ, 217:425–433, October 1977. doi: 10.1086/155591. 10

Michel Mayor and Didier Queloz. A Jupiter-mass companion to a solar-type star. Nature, 378(6555):355–359, November 1995. doi: 10.1038/378355a0. 28

Mark J. McCaughrean and C. Robert O'Dell. Direct Imaging of Circumstellar Disks in the Orion Nebula. AJ, 111:1977, May 1996. doi: 10.1086/117934. 21

Arnaud Michel, Nienke van der Marel, and Brenda C. Matthews. Bridging the Gap between Protoplanetary and Debris Disks: Separate Evolution of Millimeter and Micrometer-sized Dust. ApJ, 921(1):72, November 2021. doi: 10.3847/1538-4357/ac1bbb. 16, 78, 83, 84, 87, 89

A. Mignone, G. Bodo, S. Massaglia, T. Matsakos, O. Tesileanu, C. Zanni, and A. Ferrari. PLUTO: A Numerical Code for Computational Astrophysics. ApJS, 170(1):228–242, May 2007. doi: 10.1086/513316. 34

A. Miotello, E. F. van Dishoeck, M. Kama, and S. Bruderer. Determining protoplanetary disk gas masses from CO isotopologues line observations. A&A, 594:A85, October 2016. doi: 10.1051/0004-6361/201628159. 11

A. Miotello, E. F. van Dishoeck, J. P. Williams, M. Ansdell, G. Guidi, M. Hogerheijde, C. F. Manara, M. Tazzari, L. Testi, N. van der Marel, and S. van Terwisga. Lupus disks with faint CO isotopologues: low gas/dust or high carbon depletion? A&A, 599:A113, March 2017. doi: 10.1051/0004-6361/201629556. 11, 46

C. Mordasini, Y. Alibert, and W. Benz. Extrasolar planet population synthesis. I. Method, formation tracks, and mass-distance distribution. A&A, 501(3):1139–1160, July 2009a. doi: 10.1051/0004-6361/200810301. 25

C. Mordasini, Y. Alibert, W. Benz, and D. Naef. Extrasolar planet population synthesis. II. Statistical comparison with observations. A&A, 501(3):1161–1184, July 2009b. doi: 10.1051/0004-6361/200810697. 25

Shoji Mori and Satoshi Okuzumi. Electron Heating in Magnetorotational Instability: Implications for Turbulence Strength in the Outer Regions of Protoplanetary Disks. ApJ, 817(1):52, January 2016. doi: 10.3847/0004-637X/817/1/52. 19

R. Morishima. Gap opening beyond dead zones by photoevaporation. MNRAS, 420(4): 2851–2858, March 2012. doi: 10.1111/j.1365-2966.2011.19940.x. 24

Gijs D. Mulders, Ilaria Pascucci, and Dániel Apai. A Stellar-mass-dependent Drop in Planet Occurrence Rates. ApJ, 798(2):112, January 2015. doi: 10.1088/0004-637X/798/2/112. 28

James Muzerolle, Lynne Hillenbrand, Nuria Calvet, César Briceño, and Lee Hartmann. Accretion in Young Stellar/Substellar Objects. ApJ, 592(1):266–281, July 2003. doi: 10.1086/375704. 19, 54

James Muzerolle, Kevin L. Luhman, César Briceño, Lee Hartmann, and Nuria Calvet. Measuring Accretion in Young Substellar Objects: Approaching the Planetary Mass Regime. ApJ, 625(2):906–912, June 2005. doi: 10.1086/429483. 54

James Muzerolle, Lori E. Allen, S. Thomas Megeath, Jesús Hernández, and Robert A. Gutermuth. A Spitzer Census of Transitional Protoplanetary Disks with AU-scale Inner Holes. ApJ, 708(2):1107–1118, January 2010. doi: 10.1088/0004-637X/708/2/1107. 15

Y. Nakagawa, K. Nakazawa, and C. Hayashi. Growth and sedimentation of dust grains in the primordial solar nebula. Icarus, 45(3):517–528, March 1981. doi: 10.1016/0019-1035(81)90018-X. 14

Taishi Nakamoto and Yoshitsugo Nakagawa. Formation, Early Evolution, and Gravitational Stability of Protoplanetary Disks. ApJ, 421:640, February 1994. doi: 10.1086/173678. 56

Riouhei Nakatani, Takashi Hosokawa, Naoki Yoshida, Hideko Nomura, and Rolf Kuiper. Radiation Hydrodynamics Simulations of Photoevaporation of Protoplanetary Disks by Ultraviolet Radiation: Metallicity Dependence. ApJ, 857(1):57, April 2018a. doi: 10.3847/1538-4357/aab70b. 23, 33, 34

Riouhei Nakatani, Takashi Hosokawa, Naoki Yoshida, Hideko Nomura, and Rolf Kuiper. Radiation Hydrodynamics Simulations of Photoevaporation of Protoplanetary Disks. II. Metallicity Dependence of UV and X-Ray Photoevaporation. ApJ, 865(1):75, September 2018b. doi: 10.3847/1538-4357/aad9fd. 23, 33, 44, 57, 88, 91

Riouhei Nakatani, Hiroshi Kobayashi, Rolf Kuiper, Hideko Nomura, and Yuri Aikawa. Photoevaporation of Grain-depleted Protoplanetary Disks around Intermediate-mass Stars: Investigating the Possibility of Gas-rich Debris Disks as Protoplanetary Remnants. ApJ, 915(2):90, July 2021. doi: 10.3847/1538-4357/ac0137. 57, 110

A. Natta, L. Testi, J. Muzerolle, S. Randich, F. Comerón, and P. Persi. Accretion in brown dwarfs: An infrared view. A&A, 424:603–612, September 2004. doi: 10.1051/0004-6361:20040356. 19

A. Natta, L. Testi, and S. Randich. Accretion in the ρ-Ophiuchi pre-main sequence stars. A&A, 452(1):245–252, June 2006. doi: 10.1051/0004-6361:20054706. 19

Richard P. Nelson and William D. Langer. The Dynamics of Low-Mass Molecular Clouds in External Radiation Fields. ApJ, 482(2):796–826, June 1997. doi: 10.1086/304167. 35, 129

Richard P. Nelson, Oliver Gressel, and Orkan M. Umurhan. Linear and non-linear evolution of the vertical shear instability in accretion discs. MNRAS, 435(3):2610–2632, November 2013. doi: 10.1093/mnras/stt1475. 19

H. Nomura and T. J. Millar. Molecular hydrogen emission from protoplanetary disks. A&A, 438(3):923–938, August 2005. doi: 10.1051/0004-6361:20052809. 10, 129

H. Nomura, Y. Aikawa, M. Tsujimoto, Y. Nakagawa, and T. J. Millar. Molecular Hydrogen Emission from Protoplanetary Disks. II. Effects of X-Ray Irradiation and Dust Evolution. ApJ, 661(1):334–353, May 2007. doi: 10.1086/513419. 36, 50

Karin I. Öberg, Chunhua Qi, Jeffrey K. J. Fogel, Edwin A. Bergin, Sean M. Andrews, Catherine Espaillat, Tim A. van Kempen, David J. Wilner, and Ilaria Pascucci. The Disk Imaging Survey of Chemistry with SMA. I. Taurus Protoplanetary Disk Data. ApJ, 720(1):480–493, September 2010. doi: 10.1088/0004-637X/720/1/480. 10

C. R. O'Dell and Zheng Wen. Postrefurbishment Mission Hubble Space Telescope Images of the Core of the Orion Nebula: Proplyds, Herbig-Haro Objects, and Measurements of a Circumstellar Disk. ApJ, 436:194, November 1994. doi: 10.1086/174892. 21

C. R. O'Dell, Zheng Wen, and Xihai Hu. Discovery of New Objects in the Orion Nebula on HST Images: Shocks, Compact Sources, and Protoplanetary Disks. ApJ, 410:696, June 1993. doi: 10.1086/172786. 9, 21

Nagayoshi Ohashi, Kazuya Saigo, Yusuke Aso, Yuri Aikawa, Shin Koyamatsu, Masahiro N. Machida, Masao Saito, Sanemichi Z. Takahashi, Shigehisa Takakuwa, Kengo Tomida, Kohji Tomisaka, and Hsi-Wei Yen. Formation of a Keplerian Disk in the Infalling Envelope around L1527 IRS: Transformation from Infalling Motions to Kepler Motions. ApJ, 796(2):131, December 2014. doi: 10.1088/0004-637X/796/2/131. 13

Satoshi Okuzumi. Electric Charging of Dust Aggregates and its Effect on Dust Coagulation in Protoplanetary Disks. ApJ, 698(2):1122–1135, June 2009. doi: 10.1088/0004-637X/698/2/1122. 10

Satoshi Okuzumi, Hidekazu Tanaka, Hiroshi Kobayashi, and Koji Wada. Rapid Coagulation of Porous Dust Aggregates outside the Snow Line: A Pathway to Successful Icy Planetesimal Formation. ApJ, 752(2):106, June 2012. doi: 10.1088/0004-637X/752/2/106. 29

Isa Oliveira, Klaus M. Pontoppidan, Bruno Merín, Ewine F. van Dishoeck, Fred Lahuis, Vincent C. Geers, Jes K. Jørgensen, Johan Olofsson, Jean-Charles Augereau, and Joanna M. Brown. A Spitzer Survey of Protoplanetary Disk Dust in the Young Serpens Cloud: How do Dust Characteristics Evolve with Time? ApJ, 714(1):778–798, May 2010. doi: 10.1088/0004-637X/714/1/778. 34

Kazuyuki Omukai. Protostellar Collapse with Various Metallicities. ApJ, 534(2):809–824, May 2000. doi: 10.1086/308776. 127

Kazuyuki Omukai, Takashi Hosokawa, and Naoki Yoshida. Low-metallicity Star Formation: Prestellar Collapse and Protostellar Accretion in the Spherical Symmetry. ApJ, 722(2):1793–1815, October 2010. doi: 10.1088/0004-637X/722/2/1793. 39

C. W. Ormel and J. N. Cuzzi. Closed-form expressions for particle relative velocities induced by turbulence. A&A, 466(2):413–420, May 2007. doi: 10.1051/0004-6361:20066899. 102

Donald E. Osterbrock. *Astrophysics of gaseous nebulae and active galactic nuclei*. University Science Books, 1989. 38

Donald E. Osterbrock and Gary J. Ferland. *Astrophysics of gaseous nebulae and active galactic nuclei*. University Science Books, 2006. 36

J. E. Owen, B. Ercolano, C. J. Clarke, and R. D. Alexander. Radiation-hydrodynamic models of X-ray and EUV photoevaporating protoplanetary discs. MNRAS, 401(3):1415–1428, January 2010. doi: 10.1111/j.1365-2966.2009.15771.x. 24, 37, 46, 73, 75

James E. Owen, Cathie J. Clarke, and Barbara Ercolano. On the theory of disc photoevaporation. MNRAS, 422(3):1880–1901, May 2012. doi: 10.1111/j.1365-2966.2011.20337.x. 73, 74

Richard J. Parker, Hayley L. Alcock, Rhana B. Nicholson, Olja Panić, and Simon P. Goodwin. External Photoevaporation of Protoplanetary Disks: Does Location Matter? ApJ, 913(2):95, June 2021. doi: 10.3847/1538-4357/abf4cc. 26

I. Pascucci and M. Sterzik. Evidence for Disk Photoevaporation Driven by the Central Star. ApJ, 702(1):724–732, September 2009. doi: 10.1088/0004-637X/702/1/724. 20

I. Pascucci, L. Testi, G. J. Herczeg, F. Long, C. F. Manara, N. Hendler, G. D. Mulders, S. Krijt, F. Ciesla, Th. Henning, S. Mohanty, E. Drabek-Maunder, D. Apai, L. Szűcs, G. Sacco, and J. Olofsson. A Steeper than Linear Disk Mass-Stellar Mass Scaling Relation. ApJ, 831(2): 125, November 2016. doi: 10.3847/0004-637X/831/2/125. 19, 79

I. Pascucci, S. Cabrit, S. Edwards, U. Gorti, O. Gressel, and T. K. Suzuki. The Role of Disk Winds in the Evolution and Dispersal of Protoplanetary Disks. In S. Inutsuka, Y. Aikawa, T. Muto, K. Tomida, and M. Tamura, editors, *Protostars and Planets VII*, volume 534 of *Astronomical Society of the Pacific Conference Series*, page 567, July 2023. doi: 10.48550/arXiv.2203.10068. 20

Ilaria Pascucci, Andrea Banzatti, Uma Gorti, Min Fang, Klaus Pontoppidan, Richard Alexander, Giulia Ballabio, Suzan Edwards, Colette Salyk, Germano Sacco, Ettore Flaccomio, Geoffrey A. Blake, Andres Carmona, Cassandra Hall, Inga Kamp, Hans Ulrich Käufl, Gwendolyn Meeus, Michael Meyer, Tyler Pauly, Simon Steendam, and Michael Sterzik. The Evolution of Disk Winds from a Combined Study of Optical and Infrared Forbidden Lines. ApJ, 903(2):78, November 2020. doi: 10.3847/1538-4357/abba3c. 20

Sudeshna Patra, Jessy Jose, and Neal J. Evans. Does Metallicity Affect the Protoplanetary Disk Fraction? Answers from the Outer Milky Way. ApJ, 970(1):88, July 2024. doi: 10.3847/1538-4357/ad4996. 17

Bill Paxton, Lars Bildsten, Aaron Dotter, Falk Herwig, Pierre Lesaffre, and Frank Timmes. Modules for Experiments in Stellar Astrophysics (MESA). ApJS, 192(1):3, January 2011. doi: 10.1088/0067-0049/192/1/3. 5, 58

Mark J. Pecaut and Eric E. Mamajek. The star formation history and accretion-disc fraction among the K-type members of the Scorpius-Centaurus OB association. MNRAS, 461(1): 794–815, September 2016. doi: 10.1093/mnras/stw1300. 16

Erik A. Petigura, Geoffrey W. Marcy, Joshua N. Winn, Lauren M. Weiss, Benjamin J. Fulton, Andrew W. Howard, Evan Sinukoff, Howard Isaacson, Timothy D. Morton, and John Asher Johnson. The California-Kepler Survey. IV. Metal-rich Stars Host a Greater Diversity of Planets. AJ, 155(2):89, February 2018. doi: 10.3847/1538-3881/aaa54c. 28

Susanne Pfalzner, Manuel Steinhausen, and Karl Menten. Short Dissipation Times of Proto-planetary Disks: An Artifact of Selection Effects? ApJ, 793(2):L34, October 2014. doi: 10.1088/2041-8205/793/2/L34. 16

Susanne Pfalzner, Shahrzad Dehghani, and Arnaud Michel. Most Planets Might Have More than 5 Myr of Time to Form. ApJ, 939(1):L10, November 2022. doi: 10.3847/2041-8213/ac9839. 15, 16, 18, 82, 83, 84, 90

Giovanni Picogna, Barbara Ercolano, and Catherine C. Espaillat. The dispersal of protoplanetary discs - III. Influence of stellar mass on disc photoevaporation. MNRAS, 508(3):3611–3619, December 2021. doi: 10.1093/mnras/stab2883. 23, 46

P. Pinilla, M. Benisty, and T. Birnstiel. Ring shaped dust accumulation in transition disks. A&A, 545:A81, September 2012. doi: 10.1051/0004-6361/201219315. 14

Paola Pinilla, Ilaria Pascucci, and Sebastian Marino. Hints on the origins of particle traps in protoplanetary disks given by the M_{dust} - $M_\star$ relation. A&A, 635:A105, March 2020. doi: 10.1051/0004-6361/201937003. 19

C. Pinte, W. R. F. Dent, F. Ménard, A. Hales, T. Hill, P. Cortes, and I. de Gregorio-Monsalvo. Dust and Gas in the Disk of HL Tauri: Surface Density, Dust Settling, and Dust-to-gas Ratio. ApJ, 816(1):25, January 2016. doi: 10.3847/0004-637X/816/1/25. 19

J. B. Pollack, C. P. McKay, and B. M. Christofferson. A calculation of the Rosseland mean opacity of dust grains in primordial solar system nebulae. Icarus, 64(3):471–492, December 1985. doi: 10.1016/0019-1035(85)90069-7. 56

James B. Pollack, David Hollenbach, Steven Beckwith, Damon P. Simonelli, Ted Roush, and Wesley Fong. Composition and Radiative Properties of Grains in Molecular Clouds and Accretion Disks. ApJ, 421:615, February 1994. doi: 10.1086/173677. 35

Torsten Poppe, Jürgen Blum, and Thomas Henning. Analogous Experiments on the Stickiness of Micron-sized Preplanetary Dust. ApJ, 533(1):454–471, April 2000. doi: 10.1086/308626. 103

Thomas Preibisch, Yong-Cheol Kim, Fabio Favata, Eric D. Feigelson, Ettore Flaccomio, Konstantin Getman, Giusi Micela, Salvatore Sciortino, Keivan Stassun, Beate Stelzer, and Hans Zinnecker. The Origin of T Tauri X-Ray Emission: New Insights from the Chandra Orion Ultradeep Project. ApJS, 160(2):401–422, October 2005. doi: 10.1086/432891. 8

Chunhua Qi, David J. Wilner, Nuria Calvet, Tyler L. Bourke, Geoffrey A. Blake, Michiel R. Hogerheijde, Paul T. P. Ho, and Edwin Bergin. CO J = 6-5 Observations of TW Hydrae with the Submillimeter Array. ApJ, 636(2):L157–L160, January 2006. doi: 10.1086/500241. 10

Chunhua Qi, Karin I. Öberg, David J. Wilner, Paola D'Alessio, Edwin Bergin, Sean M. Andrews, Geoffrey A. Blake, Michiel R. Hogerheijde, and Ewine F. van Dishoeck. Imaging of the CO Snow Line in a Solar Nebula Analog. *Science*, 341(6146):630–632, August 2013. doi: 10.1126/science.1239560. 11

Chunhua Qi, Karin I. Öberg, Catherine C. Espaillat, Connor E. Robinson, Sean M. Andrews, David J. Wilner, Geoffrey A. Blake, Edwin A. Bergin, and L. Ilsedore Cleeves. Probing CO and N_2 Snow Surfaces in Protoplanetary Disks with N_2H^+ Emission. ApJ, 882(2):160, September 2019. doi: 10.3847/1538-4357/ab35d3. 11

Roman R. Rafikov. Protoplanetary Disks as (Possibly) Viscous Disks. ApJ, 837(2):163, March 2017. doi: 10.3847/1538-4357/aa6249. 19

Álvaro Ribas, Bruno Merín, Hervé Bouy, and Luke T. Maud. Disk evolution in the solar neighborhood. I. Disk frequencies from 1 to 100 Myr. A&A, 561:A54, January 2014. doi: 10.1051/0004-6361/201322597. 16

Álvaro Ribas, Hervé Bouy, and Bruno Merín. Protoplanetary disk lifetimes vs. stellar mass and possible implications for giant planet populations. A&A, 576:A52, April 2015. doi: 10.1051/0004-6361/201424846. 16, 17, 28, 85, 86

L. Ricci, F. Trotta, L. Testi, A. Natta, A. Isella, and D. J. Wilner. The effect of local optically thick regions in the long-wave emission of young circumstellar disks. A&A, 540:A6, April 2012. doi: 10.1051/0004-6361/201118296. 14

A. J. W. Richert, K. V. Getman, E. D. Feigelson, M. A. Kuhn, P. S. Broos, M. S. Povich, M. R. Bate, and G. P. Garmire. Circumstellar disc lifetimes in numerous galactic young stellar clusters. MNRAS, 477(4):5191–5206, July 2018. doi: 10.1093/mnras/sty949. 6, 16, 17

Sabine Richling and Harold W. Yorke. Photoevaporation of Protostellar Disks. V. Circumstellar Disks under the Influence of Both Extreme-Ultraviolet and Far-Ultraviolet Radiation. ApJ, 539(1):258–272, August 2000. doi: 10.1086/309198. 21, 35, 37

Veronica Roccatagliata, Jeroen Bouwman, Thomas Henning, Mario Gennaro, Eric Feigelson, Jinyoung Serena Kim, Aurora Sicilia-Aguilar, and Warrick A. Lawson. Disk Evolution in OB Associations: Deep Spitzer/IRAC Observations of IC 1795. ApJ, 733(2):113, June 2011. doi: 10.1088/0004-637X/733/2/113. 16

M. M. Romanova, G. V. Ustyugova, A. V. Koldoba, and R. V. E. Lovelace. Launching of conical winds and axial jets from the disc-magnetosphere boundary: axisymmetric and 3D simulations. MNRAS, 399(4):1802–1828, November 2009. doi: 10.1111/j.1365-2966.2009.15413.x. 24

M. P. Ronco, M. R. Schreiber, E. Villaver, O. M. Guilera, and M. M. Miller Bertolami. Planet formation around intermediate-mass stars. I. Different disc evolutionary pathways as a function of stellar mass. A&A, 682:A155, February 2024. doi: 10.1051/0004-6361/202347762. 14

Giovanni P. Rosotti, Richard Teague, Cornelis Dullemond, Richard A. Booth, and Cathie J. Clarke. The efficiency of dust trapping in ringed protoplanetary discs. MNRAS, 495(1):173–181, June 2020. doi: 10.1093/mnras/staa1170. 19

D. Ruíz-Rodríguez, L. A. Cieza, J. P. Williams, S. M. Andrews, D. A. Principe, C. Caceres, H. Canovas, S. Casassus, M. R. Schreiber, and J. H. Kastner. ALMA survey of circumstellar discs in the young stellar cluster IC 348. MNRAS, 478(3):3674–3692, August 2018. doi: 10.1093/mnras/sty1351. 60, 79

K. L. J. Rygl, M. Benedettini, E. Schisano, D. Elia, S. Molinari, S. Pezzuto, Ph. André, J. P. Bernard, G. J. White, D. Polychroni, S. Bontemps, N. L. J. Cox, J. Di Francesco, A. Facchini,

C. Fallscheer, A. M. di Giorgio, M. Hennemann, T. Hill, V. Könyves, V. Minier, F. Motte, Q. Nguyen-Luong, N. Peretto, M. Pestalozzi, S. Sadavoy, N. Schneider, L. Spinoglio, L. Testi, and D. Ward-Thompson. Recent star formation in the Lupus clouds as seen by Herschel. A&A, 549:L1, January 2013. doi: 10.1051/0004-6361/201219511. 13

S. Sabotta, M. Schlecker, P. Chaturvedi, E. W. Guenther, I. Muñoz Rodríguez, J. C. Muñoz Sánchez, J. A. Caballero, Y. Shan, S. Reffert, I. Ribas, A. Reiners, A. P. Hatzes, P. J. Amado, H. Klahr, J. C. Morales, A. Quirrenbach, Th. Henning, S. Dreizler, E. Pallé, M. Perger, M. Azzaro, S. V. Jeffers, A. Kaminski, M. Kürster, M. Lafarga, D. Montes, V. M. Passegger, and M. Zechmeister. The CARMENES search for exoplanets around M dwarfs. Planet occurrence rates from a subsample of 71 stars. A&A, 653:A114, September 2021. doi: 10.1051/0004-6361/202140968. 28

E. Sanchis, L. Testi, A. Natta, S. Facchini, C. F. Manara, A. Miotello, B. Ercolano, Th. Henning, T. Preibisch, J. M. Carpenter, I. de Gregorio-Monsalvo, R. Jayawardhana, C. Lopez, K. Mužić, I. Pascucci, A. Santamaría-Miranda, S. van Terwisga, and J. P. Williams. Measuring the ratio of the gas and dust emission radii of protoplanetary disks in the Lupus star-forming region. A&A, 649:A19, May 2021. doi: 10.1051/0004-6361/202039733. 27

Takayoshi Sano, Shu-ichiro Inutsuka, Neal J. Turner, and James M. Stone. Angular Momentum Transport by Magnetohydrodynamic Turbulence in Accretion Disks: Gas Pressure Dependence of the Saturation Level of the Magnetorotational Instability. ApJ, 605(1):321–339, April 2004. doi: 10.1086/382184. 19

Fernando Santoro and J. Michael Shull. Critical Metallicity and Fine-Structure Emission of Primordial Gas Enriched by the First Stars. ApJ, 643(1):26–37, May 2006. doi: 10.1086/501518. 38

Rebecca Schindhelm, Kevin France, Gregory J. Herczeg, Edwin Bergin, Hao Yang, Alexander Brown, Joanna M. Brown, Jeffrey L. Linsky, and Jeff Valenti. Lyα Dominance of the Classical T Tauri Far-ultraviolet Radiation Field. ApJ, 756(1):L23, September 2012. doi: 10.1088/2041-8205/756/1/L23. 7

Andrew D. Sellek, Richard A. Booth, and Cathie J. Clarke. The evolution of dust in discs influenced by external photoevaporation. MNRAS, 492(1):1279–1294, February 2020. doi: 10.1093/mnras/stz3528. 26, 28

Andrew D. Sellek, Tommaso Grassi, Giovanni Picogna, Christian Rab, Cathie J. Clarke, and Barbara Ercolano. Photoevaporation of protoplanetary discs with PLUTO+PRIZMO I. Lower X-ray-driven mass-loss rates due to enhanced cooling. *arXiv e-prints*, art. arXiv:2408.00848, August 2024. doi: 10.48550/arXiv.2408.00848. 23, 24, 49

N. I. Shakura and R. A. Sunyaev. Black holes in binary systems. Observational appearance. A&A, 24:337–355, January 1973. 18, 136

Paul R. Shapiro and Hyesung Kang. Hydrogen Molecules and the Radiative Cooling of Pregalactic Shocks. ApJ, 318:32, July 1987. doi: 10.1086/165350. 127

Kazunari Shibata and Tetsuya Magara. Solar Flares: Magnetohydrodynamic Processes. *Living Reviews in Solar Physics*, 8(1):6, December 2011. doi: 10.12942/lrsp-2011-6. 8

Y. Shimajiri, Ph. André, E. Ntormousi, A. Men'shchikov, D. Arzoumanian, and P. Palmeirim. Probing fragmentation and velocity sub-structure in the massive NGC 6334 filament with ALMA. A&A, 632:A83, December 2019. doi: 10.1051/0004-6361/201935689. 3

Frank Shu, Joan Najita, Eve Ostriker, Frank Wilkin, Steven Ruden, and Susana Lizano. Magnetocentrifugally Driven Flows from Young Stars and Disks. I. A Generalized Model. ApJ, 429:781, July 1994. doi: 10.1086/174363. 24

L. Siess, E. Dufour, and M. Forestini. An internet server for pre-main sequence tracks of low- and intermediate-mass stars. A&A, 358:593–599, June 2000. doi: 10.48550/arXiv.astro-ph/0003477. 6

Jacob B. Simon, Geoffroy Lesur, Matthew W. Kunz, and Philip J. Armitage. Magnetically driven accretion in protoplanetary discs. MNRAS, 454(1):1117–1131, November 2015. doi: 10.1093/mnras/stv2070. 19

D. R. Soderblom, L. A. Hillenbrand, R. D. Jeffries, E. E. Mamajek, and T. Naylor. Ages of Young Stars. In Henrik Beuther, Ralf S. Klessen, Cornelis P. Dullemond, and Thomas Henning, editors, *Protostars and Planets VI*, pages 219–241, January 2014. doi: 10.2458/azu_uapress_9780816531240-ch010. 6

Alice Somigliana, Claudia Toci, Giovanni Rosotti, Giuseppe Lodato, Marco Tazzari, Carlo F. Manara, Leonardo Testi, and Federico Lepri. On the time evolution of the M_d-$M_\star$ and $\dot{M}$-$M_\star$ correlations for protoplanetary discs: the viscous time-scale increases with stellar mass. MNRAS, 514(4):5927–5940, August 2022. doi: 10.1093/mnras/stac1587. 19

Alice Somigliana, Leonardo Testi, Giovanni Rosotti, Claudia Toci, Giuseppe Lodato, Rossella Anania, Benoît Tabone, Marco Tazzari, Ralf Klessen, Ugo Lebreuilly, Patrick Hennebelle, and Sergo Molinari. The evolution of the M_d–$M_\star$ and $\dot{M}$–$M_\star$ correlations traces protoplanetary disc dispersal. A&A, 689:A285, September 2024. doi: 10.1051/0004-6361/202450744. 19

Lyman Spitzer. *Physical processes in the interstellar medium*. A Wiley-Interscience Publication, 1978. doi: 10.1002/9783527617722. 39

Vito Squicciarini, Raffaele Gratton, Mariangela Bonavita, and Dino Mesa. Unveiling the star formation history of the Upper Scorpius association through its kinematics. MNRAS, 507 (1):1381–1400, October 2021. doi: 10.1093/mnras/stab2079. 7

Steven W. Stahler and Francesco Palla. *The Formation of Stars*. John Wiley & Sons, 2004. 5, 6

Sebastian M. Stammler and Tilman Birnstiel. DustPy: A Python Package for Dust Evolution in Protoplanetary Disks. ApJ, 935(1):35, August 2022. doi: 10.3847/1538-4357/ac7d58. 27, 102

Karen M. Strom, Stephen E. Strom, Suzan Edwards, Sylvie Cabrit, and Michael F. Skrutskie. Circumstellar Material Associated with Solar-Type Pre-Main-Sequence Stars: A Possible Constraint on the Timescale for Planet Building. AJ, 97:1451, May 1989. doi: 10.1086/115085. 13

Takeru K. Suzuki and Shu-ichiro Inutsuka. Disk Winds Driven by Magnetorotational Instability and Dispersal of Protoplanetary Disks. ApJ, 691(1):L49–L54, January 2009. doi: 10.1088/0004-637X/691/1/L49. 19

Takeru K. Suzuki, Takayuki Muto, and Shu-ichiro Inutsuka. Protoplanetary Disk Winds via Magnetorotational Instability: Formation of an Inner Hole and a Crucial Assist for Planet Formation. ApJ, 718(2):1289–1304, August 2010. doi: 10.1088/0004-637X/718/2/1289. 19, 139

Takeru K. Suzuki, Masahiro Ogihara, Alessandro Morbidelli, Aurélien Crida, and Tristan Guillot. Evolution of protoplanetary discs with magnetically driven disc winds. A&A, 596:A74, December 2016. doi: 10.1051/0004-6361/201628955. 20

B. Tabone, G. P. Rosotti, G. Lodato, P. J. Armitage, A. J. Cridland, and E. F. van Dishoeck. MHD disc winds can reproduce fast disc dispersal and the correlation between accretion rate and disc mass in Lupus. MNRAS, 512(1):L74–L79, May 2022a. doi: 10.1093/mnrasl/slab124. 20

Benoît Tabone, Giovanni P. Rosotti, Alexander J. Cridland, Philip J. Armitage, and Giuseppe Lodato. Secular evolution of MHD wind-driven discs: analytical solutions in the expanded α-framework. MNRAS, 512(2):2290–2309, May 2022b. doi: 10.1093/mnras/stab3442. 20

Sanemichi Z. Takahashi and Shu-ichiro Inutsuka. Two-component Secular Gravitational Instability in a Protoplanetary Disk: A Possible Mechanism for Creating Ring-like Structures. ApJ, 794(1):55, October 2014. doi: 10.1088/0004-637X/794/1/55. 14, 30

Sanemichi Z. Takahashi and Shu-ichiro Inutsuka. An Origin of Multiple Ring Structure and Hidden Planets in HL Tau: A Unified Picture by Secular Gravitational Instability. AJ, 152(6):184, December 2016. doi: 10.3847/0004-6256/152/6/184. 14

Tetsuo Taki, Koh Kuwabara, Hiroshi Kobayashi, and Takeru K. Suzuki. New Growth Mechanism of Dust Grains in Protoplanetary Disks with Magnetically Driven Disk Winds. ApJ, 909(1):75, March 2021. doi: 10.3847/1538-4357/abd79f. 110

A. Telleschi, M. Güdel, K. R. Briggs, M. Audard, and F. Palla. X-ray emission from T Tauri stars and the role of accretion: inferences from the XMM-Newton extended survey of the

Taurus molecular cloud. A&A, 468(2):425–442, June 2007. doi: 10.1051/0004-6361:20066565. 8

L. Testi, T. Birnstiel, L. Ricci, S. Andrews, J. Blum, J. Carpenter, C. Dominik, A. Isella, A. Natta, J. P. Williams, and D. J. Wilner. Dust Evolution in Protoplanetary Disks. In Henrik Beuther, Ralf S. Klessen, Cornelis P. Dullemond, and Thomas Henning, editors, *Protostars and Planets VI*, pages 339–361, January 2014. doi: 10.2458/azu_uapress_9780816531240-ch015. 11

L. Testi, A. Natta, C. F. Manara, I. de Gregorio Monsalvo, G. Lodato, C. Lopez, K. Muzic, I. Pascucci, E. Sanchis, A. Santamaria Miranda, A. Scholz, M. De Simone, and J. P. Williams. The protoplanetary disk population in the ρ-Ophiuchi region L1688 and the time evolution of Class II YSOs. A&A, 663:A98, July 2022. doi: 10.1051/0004-6361/202141380. 14

A. G. G. M. Tielens. Interstellar polycyclic aromatic hydrocarbon molecules. ARA&A, 46:289–337, September 2008. doi: 10.1146/annurev.astro.46.060407.145211. 10

A. G. G. M. Tielens and D. Hollenbach. Photodissociation regions. I. Basic model. ApJ, 291:722–746, April 1985. doi: 10.1086/163111. 35, 38, 127

John J. Tobin, Patrick D. Sheehan, S. Thomas Megeath, Ana Karla Díaz-Rodríguez, Stella S. R. Offner, Nadia M. Murillo, Merel L. R. van 't Hoff, Ewine F. van Dishoeck, Mayra Osorio, Guillem Anglada, Elise Furlan, Amelia M. Stutz, Nickalas Reynolds, Nicole Karnath, William J. Fischer, Magnus Persson, Leslie W. Looney, Zhi-Yun Li, Ian Stephens, Claire J. Chandler, Erin Cox, Michael M. Dunham, Łukasz Tychoniec, Mihkel Kama, Kaitlin Kratter, Marina Kounkel, Brian Mazur, Luke Maud, Lisa Patel, Laura Perez, Sarah I. Sadavoy, Dominique Segura-Cox, Rajeeb Sharma, Brian Stephenson, Dan M. Watson, and Friedrich Wyrowski. The VLA/ALMA Nascent Disk and Multiplicity (VANDAM) Survey of Orion Protostars. II. A Statistical Characterization of Class 0 and Class I Protostellar Disks. ApJ, 890(2):130, February 2020. doi: 10.3847/1538-4357/ab6f64. 29, 79

Claudia Toci, Giovanni Rosotti, Giuseppe Lodato, Leonardo Testi, and Leon Trapman. On the secular evolution of the ratio between gas and dust radii in protoplanetary discs. MNRAS, 507(1):818–833, October 2021. doi: 10.1093/mnras/stab2112. 27

Ryosuke T. Tominaga, Sanemichi Z. Takahashi, and Shu-ichiro Inutsuka. Revised Description of Dust Diffusion and a New Instability Creating Multiple Rings in Protoplanetary Disks. ApJ, 881(1):53, August 2019. doi: 10.3847/1538-4357/ab25ea. 30

L. Trapman, G. Rosotti, A. D. Bosman, M. R. Hogerheijde, and E. F. van Dishoeck. Observed sizes of planet-forming disks trace viscous spreading. A&A, 640:A5, August 2020. doi: 10.1051/0004-6361/202037673. 19

N. J. Turner, Man Hoi Lee, and T. Sano. Magnetic Coupling in the Disks around Young Gas Giant Planets. ApJ, 783(1):14, March 2014. doi: 10.1088/0004-637X/783/1/14. 19

Łukasz Tychoniec, John J. Tobin, Agata Karska, Claire Chandler, Michael M. Dunham, Robert J. Harris, Kaitlin M. Kratter, Zhi-Yun Li, Leslie W. Looney, Carl Melis, Laura M. Pérez, Sarah I. Sadavoy, Dominique Segura-Cox, and Ewine F. van Dishoeck. The VLA Nascent Disk and Multiplicity Survey of Perseus Protostars (VANDAM). IV. Free-Free Emission from Protostars: Links to Infrared Properties, Outflow Tracers, and Protostellar Disk Masses. ApJS, 238(2):19, October 2018. doi: 10.3847/1538-4365/aaceae. 79

Łukasz Tychoniec, Carlo F. Manara, Giovanni P. Rosotti, Ewine F. van Dishoeck, Alexander J. Cridland, Tien-Hao Hsieh, Nadia M. Murillo, Dominique Segura-Cox, Sierk E. van Terwisga, and John J. Tobin. Dust masses of young disks: constraining the initial solid reservoir for planet formation. A&A, 640:A19, August 2020. doi: 10.1051/0004-6361/202037851. 29, 53

Orkan M. Umurhan, Paul R. Estrada, and Jeffrey N. Cuzzi. Streaming Instability in Turbulent Protoplanetary Disks. ApJ, 895(1):4, May 2020. doi: 10.3847/1538-4357/ab899d. 29

Jeff A. Valenti, Adam A. Fallon, and Christopher M. Johns-Krull. An IUE Atlas of Pre-Main-Sequence Stars. III. Co-added Final Archive Spectra from the Long-Wavelength Cameras. ApJS, 147(2):305–336, August 2003. doi: 10.1086/375445. 59

Nienke van der Marel and Gijs D. Mulders. A Stellar Mass Dependence of Structured Disks: A Possible Link with Exoplanet Demographics. AJ, 162(1):28, July 2021. doi: 10.3847/1538-3881/ac0255. 15, 28

S. E. van Terwisga, E. F. van Dishoeck, R. K. Mann, J. Di Francesco, N. van der Marel, M. Meyer, S. M. Andrews, J. Carpenter, J. A. Eisner, C. F. Manara, and J. P. Williams. Protoplanetary disk masses in NGC 2024: Evidence for two populations. A&A, 640:A27, August 2020. doi: 10.1051/0004-6361/201937403. 26

Benedetta Veronesi, Teresa Paneque-Carreño, Giuseppe Lodato, Leonardo Testi, Laura M. Pérez, Giuseppe Bertin, and Cassandra Hall. A Dynamical Measurement of the Disk Mass in Elias 227. ApJ, 914(2):L27, June 2021. doi: 10.3847/2041-8213/abfe6a. 14

S. Vicente, O. Berné, A. G. G. M. Tielens, N. Huélamo, E. Pantin, I. Kamp, and A. Carmona. Polycyclic Aromatic Hydrocarbon Emission in the Proplyd HST10: What is the Mechanism behind Photoevaporation? ApJ, 765(2):L38, March 2013. doi: 10.1088/2041-8205/765/2/L38. 34

F. Villebrun, E. Alecian, G. Hussain, J. Bouvier, C. P. Folsom, Y. Lebreton, L. Amard, C. Charbonnel, F. Gallet, L. Haemmerlé, T. Böhm, C. Johns-Krull, O. Kochukhov, S. C. Marsden, J. Morin, and P. Petit. Magnetic fields of intermediate-mass T Tauri stars. I. Magnetic detections and fundamental stellar parameters. A&A, 622:A72, February 2019. doi: 10.1051/0004-6361/201833545. 8

Koji Wada, Hidekazu Tanaka, Toru Suyama, Hiroshi Kimura, and Tetsuo Yamamoto. The Rebound Condition of Dust Aggregates Revealed by Numerical Simulation of Their Collisions. ApJ, 737(1):36, August 2011. doi: 10.1088/0004-637X/737/1/36. 103

Catherine Walsh, T. J. Millar, and Hideko Nomura. Chemical Processes in Protoplanetary Disks. ApJ, 722(2):1607–1623, October 2010. doi: 10.1088/0004-637X/722/2/1607. 10

Lile Wang and Jeremy Goodman. Hydrodynamic Photoevaporation of Protoplanetary Disks with Consistent Thermochemistry. ApJ, 847(1):11, September 2017. doi: 10.3847/1538-4357/aa8726. 23, 33, 57

Haruka Washinoue, Shinsuke Takasao, and Kenji Furuya. Effect of Time-varying X-Ray Emission from Stellar Flares on the Ionization of Protoplanetary Disks. ApJ, 976(1):25, November 2024. doi: 10.3847/1538-4357/ad7fdf. 49, 51

Michael L. Weber, Barbara Ercolano, Giovanni Picogna, Lee Hartmann, and Peter J. Rodenkirch. The interpretation of protoplanetary disc wind diagnostic lines from X-ray photoevaporation and analytical MHD models. MNRAS, 496(1):223–244, July 2020. doi: 10.1093/mnras/staa1549. 20

Jesse Weder, Christoph Mordasini, and Alexandre Emsenhuber. Population study on MHD wind-driven disc evolution. Confronting theory and observation. A&A, 674:A165, June 2023. doi: 10.1051/0004-6361/202243453. 2, 24, 25, 55, 76

S. J. Weidenschilling. Aerodynamics of solid bodies in the solar nebula. MNRAS, 180: 57–70, July 1977. doi: 10.1093/mnras/180.2.57. 14

S. J. Weidenschilling and Jeffrey N. Cuzzi. Formation of Planetesimals in the Solar Nebula. In Eugene H. Levy and Jonathan I. Lunine, editors, *Protostars and Planets III*, page 1031, January 1993. 29

Joseph C. Weingartner and B. T. Draine. Dust Grain-Size Distributions and Extinction in the Milky Way, Large Magellanic Cloud, and Small Magellanic Cloud. ApJ, 548(1):296–309, February 2001. doi: 10.1086/318651. 14

Joseph C. Weingartner, B. T. Draine, and David K. Barr. Photoelectric Emission from Dust Grains Exposed to Extreme Ultraviolet and X-Ray Radiation. ApJ, 645(2):1188–1197, July 2006. doi: 10.1086/504420. 37

Russel J. White and Gibor Basri. Very Low Mass Stars and Brown Dwarfs in Taurus-Auriga. ApJ, 582(2):1109–1122, January 2003. doi: 10.1086/344673. 19

Russel J. White, A. M. Ghez, I. Neill Reid, and Greg Schultz. A Test of Pre-Main-Sequence Evolutionary Models across the Stellar/Substellar Boundary Based on Spectra of the Young Quadruple GG Tauri. ApJ, 520(2):811–821, August 1999. doi: 10.1086/307494. 6

Jonathan P. Williams and William M. J. Best. A Parametric Modeling Approach to Measuring the Gas Masses of Circumstellar Disks. ApJ, 788(1):59, June 2014. doi: 10.1088/0004-637X/788/1/59. 11

Jonathan P. Williams and Lucas A. Cieza. Protoplanetary Disks and Their Evolution. ARA&A, 49(1):67–117, September 2011. doi: 10.1146/annurev-astro-081710-102548. 13, 19

F. Windmark, T. Birnstiel, C. Güttler, J. Blum, C. P. Dullemond, and Th. Henning. Planetesimal formation by sweep-up: how the bouncing barrier can be beneficial to growth. A&A, 540:A73, April 2012. doi: 10.1051/0004-6361/201118475. 101

Andrew J. Winter, Myriam Benisty, and Sean M. Andrews. Planet Formation Regulated by Galactic-scale Interstellar Turbulence. ApJ, 972(1):L9, September 2024. doi: 10.3847/2041-8213/ad6d5d. 25

Lisa Wölfer, Giovanni Picogna, Barbara Ercolano, and Ewine F. van Dishoeck. Radiation-hydrodynamical models of X-ray photoevaporation in carbon-depleted circumstellar discs. MNRAS, 490(4):5596–5614, December 2019. doi: 10.1093/mnras/stz2939. 46, 57, 90

Nicholas J. Wright, Jeremy J. Drake, Eric E. Mamajek, and Gregory W. Henry. The Stellar-activity-Rotation Relationship and the Evolution of Stellar Dynamos. ApJ, 743 (1):48, December 2011. doi: 10.1088/0004-637X/743/1/48. 8

Hao Yang, Jeffrey L. Linsky, and Kevin France. HST/COS Spectra of DF Tau and V4046 Sgr: First Detection of Molecular Hydrogen Absorption Against the Lyα Emission Line. ApJ, 730(1):L10, March 2011. doi: 10.1088/2041-8205/730/1/L10. 49

Chikako Yasui. Spitzer Mid-infrared Study of Sh 2-208: Evolution of Protoplanetary Disks in Low-metallicity Environments. ApJ, 914(2):115, June 2021. doi: 10.3847/1538-4357/abf8b7. 13, 96

Chikako Yasui, Naoto Kobayashi, Alan T. Tokunaga, Masao Saito, and Chihiro Tokoku. The Lifetime of Protoplanetary Disks in a Low-metallicity Environment. ApJ, 705(1):54–63, November 2009. doi: 10.1088/0004-637X/705/1/54. 16

Chikako Yasui, Naoto Kobayashi, Alan T. Tokunaga, Masao Saito, and Chihiro Tokoku. Short Lifetime of Protoplanetary Disks in Low-metallicity Environments. ApJ, 723(1): L113–L116, November 2010. doi: 10.1088/2041-8205/723/1/L113. 15, 16, 17, 96

Chikako Yasui, Naoto Kobayashi, Alan T. Tokunaga, and Masao Saito. Rapid evolution of the innermost dust disc of protoplanetary discs surrounding intermediate-mass stars. MNRAS, 442(3):2543–2559, August 2014. doi: 10.1093/mnras/stu1013. 11, 17

Chikako Yasui, Naoto Kobayashi, Masao Saito, and Natsuko Izumi. Low-metallicity Young Clusters in the Outer Galaxy. II. Sh 2-208. AJ, 151(5):115, May 2016a. doi: 10.3847/0004-6256/151/5/115. 17

Chikako Yasui, Naoto Kobayashi, Alan T. Tokunaga, Masao Saito, and Natsuko Izumi. Low-metallicity Young Clusters in the Outer Galaxy. I. Sh 2-207. AJ, 151(3):50, March 2016b. doi: 10.3847/0004-6256/151/3/50. 17

H. W. Yorke and A. Welz. Photoevaporation of protostellar disks. I. The evolution of disks around early B stars. A&A, 315:555–564, November 1996. 21, 38

A. Youdin and A. Johansen. Protoplanetary Disk Turbulence Driven by the Streaming Instability: Linear Evolution and Numerical Methods. ApJ, 662(1):613–626, June 2007. doi: 10.1086/516729. 29

Andrew N. Youdin. On the Formation of Planetesimals Via Secular Gravitational Instabilities with Turbulent Stirring. ApJ, 731(2):99, April 2011. doi: 10.1088/0004-637X/731/2/99. 30

Andrew N. Youdin and Jeremy Goodman. Streaming Instabilities in Protoplanetary Disks. ApJ, 620(1):459–469, February 2005. doi: 10.1086/426895. 29

Andrew N. Youdin and Yoram Lithwick. Particle stirring in turbulent gas disks: Including orbital oscillations. Icarus, 192(2):588–604, December 2007. doi: 10.1016/j.icarus.2007.07.012. 101

Guo-Yin Zhang, Ph. André, A. Men'shchikov, and Ke Wang. Fragmentation of star-forming filaments in the X-shaped nebula of the California molecular cloud. A&A, 642:A76, October 2020. doi: 10.1051/0004-6361/202037721. 3

Shangjia Zhang, Zhaohuan Zhu, Jane Huang, Viviana V. Guzmán, Sean M. Andrews, Tilman Birnstiel, Cornelis P. Dullemond, John M. Carpenter, Andrea Isella, Laura M. Pérez, Myriam Benisty, David J. Wilner, Clément Baruteau, Xue-Ning Bai, and Luca Ricci. The Disk Substructures at High Angular Resolution Project (DSHARP). VII. The Planet-Disk Interactions Interpretation. ApJ, 869(2):L47, December 2018. doi: 10.3847/2041-8213/aaf744. 28

Wei Zhu and Subo Dong. Exoplanet Statistics and Theoretical Implications. ARA&A, 59:291–336, September 2021. doi: 10.1146/annurev-astro-112420-020055. 28

H. Zinnecker and Th. Preibisch. X-ray emission from Herbig Ae/Be stars: a ROSAT survey. A&A, 292:152–164, December 1994. 8